Université Libre de Bruxelles
Faculté des Sciences

Scalar boson decays to tau leptons : in the standard model and beyond

Thèse présentée par :

Cécile Caillol

En vue de l'obtention du grade de :

Docteur en Sciences

Bruxelles, avril 2016

Constitution du jury de thèse :

Giacomo Bruno (UCL)
Barbara Clerbaux (ULB), promoteur
Sridhara Dasu (University of Wisconsin Madison)
Albert De Roeck (CERN)
Jean-Marie Frère (ULB), président
Abdollah Mohammadi (Kansas State University), co-promoteur
Pascal Vanlaer (ULB), secrétaire

Abstract

This thesis presents a study of the scalar sector in the standard model (SM), as well as different searches for an extended scalar sector in theories beyond the standard model (BSM). All analyses have in common the fact that at least one scalar boson decays to a pair of tau leptons. The results exploit the data collected by the CMS detector during LHC Run-1, in proton-proton collisions with a center-of-mass energy of 7 or 8 TeV.

The particle discovered in 2012, H, looks compatible with a SM Brout-Englert-Higgs boson, but this statement is driven by the $H \to \gamma\gamma$ and $H \to ZZ$ decay modes. The $H \to \tau^+\tau^-$ decay mode is the most sensitive fermionic decay channel, and allows to test the Yukawa couplings of the new particle. The search for the SM scalar boson decaying to tau leptons, and produced in association with a massive vector boson W or Z, is described in this thesis. Even though a good background rejection can be achieved by selecting the leptons originating from the vector boson, Run-1 data are not sensitive to the small production cross sections predicted in the SM for the scalar boson. The combination with the gluon-gluon fusion and vector boson fusion production searches leads to an evidence for the decay of the H boson to tau leptons.

Many BSM models, such as the minimal supersymmetric SM (MSSM) or models with two scalar doublets (2HDM), predict the existence of several scalar bosons. The decays of these bosons to tau leptons can be enhanced in some scenarios depending on the model parameters, which makes the di-tau decay mode powerful to discover BSM physics. Four searches for an extended scalar sector are detailed in this thesis. The first analysis searches for a pseudoscalar boson with a mass between 220 and 350 GeV, decaying to an SM-like scalar boson and a Z boson, in the final state with two light leptons and two tau leptons. Second, a search for the exotic decay of the new particle H to a pair of light pseudoscalar bosons, which is still allowed by all measurements made up to now, in the final state with two muons and two tau leptons is performed. Third, a mass region almost never explored at the LHC is probed by the search of a light pseudoscalar, with a mass between 25 and 80 GeV, decaying to tau leptons and produced in association with b quarks. The last analysis describes the search for a heavy resonance in the MSSM, decaying to a pair of tau leptons. None of these analyses has found any hint of new physics beyond the SM, but stringent limits on the cross section of such signals could be set.

Résumé

Cette thèse présente une étude du secteur scalaire dans le cadre du modèle standard (MS), ainsi que la recherche d'un secteur scalaire étendu dans des théories au-delà du MS. Ces analyses ont en commun la désintégration d'au moins un des bosons scalaires en une paire de leptons taus. Les résultats sont basés sur les données collectées par le détecteur CMS pendant le Run-1 du LHC, lors de collisions proton-proton à une énergie dans le centre de masse de 7 ou 8 TeV.

La particule découverte en 2012, H, semble compatible avec un boson de Brout-Englert-Higgs du MS, mais ce constat se base essentiellement sur l'étude des modes de désintégration $H \to \gamma\gamma$ et $H \to ZZ$. Le mode de désintégration $H \to \tau^+\tau^-$ est le canal fermionique le plus sensible, et permet de tester les couplages de Yukawa du nouveau boson. Cette thèse décrit dans un premier temps la recherche du boson scalaire du MS se désintégrant en leptons taus et produit en association avec un boson vecteur massif W ou Z. Bien que les bruits de fond puissent être réduits en sélectionnant les leptons provenant de la désintégration des bosons vecteurs, les données du Run-1 ne sont pas sensibles aux petites sections efficaces de production prédites dans le SM pour le boson scalaire. Cependant, la combinaison avec les recherches du boson scalaire dans d'autres modes de production montre avec évidence l'existence de désintégrations du boson H en leptons taus.

De nombreux modèles au-delà du MS, tels que l'extension supersymétrique minimale du MS (MSSM) ou les modèles avec deux doublets scalaires (2HDM), prédisent l'existence de plusieurs bosons scalaires. La désintégration de ces bosons en leptons taus peut être favorisée dans certains scénarios en fonction des paramètres du modèle, ce qui rend ce mode de désintégration très puissant dans la recherche de nouvelle physique. Quatre recherches d'un secteur scalaire étendu au-delà du MS sont présentées dans cette thèse. La première analyse recherche un pseudoscalaire avec une masse entre 220 et 350 GeV, se désintégrant en un boson scalaire similaire à celui du MS et en un boson Z, dans l'état final avec deux leptons taus et deux leptons légers. La deuxième analyse explore la possibilité d'une désintégration exotique de la nouvelle particule, H, en deux bosons scalaires plus légers, ce qui est toujours autorisé par toutes les mesures faites à ce jour, dans l'état final avec deux muons et deux leptons taus. Dans le cadre de la troisième analyse, une région en masse quasiment inexplorée auparavant au LHC est testée par la recherche d'un pseudoscalaire avec une masse entre 25 et 80 GeV, se désintégrant en leptons taus et produit en association avec deux quarks b, dans le contexte des 2HDM. La dernière analyse recherche une résonance lourde se désintégrant en une paire de leptons taus dans le contexte du MSSM. Aucun indice de nouvelle physique n'a été trouvé dans aucune des analyses décrites ci-dessus, mais des limites strictes sur les sections efficaces des différents signaux ont été déterminées.

Acknowledgements

First, I would like to thank Barbara Clerbaux for supervising this work. At every moment she has been present, supportive, and has given me the best advice. This manuscript would not have been the same without her, and I want to thank her for the careful review of the previous versions.

I also want to thank Abdollah Mohammadi. He has taught me so many things, and has always tried to give me visibility and responsibilities, from the very beginning of my PhD. It has always been a pleasure to work with him, and I could not have imagined a better teammate to carry on this project.

I am grateful to the other jury members, Jean-Marie Frère, Pascal Vanlaer, Sridhara Dasu, Giacomo Bruno, and Albert De Roeck, for reading this thesis, and giving me their valuable comments.

This thesis was made possible with the help of many people working at CERN. In particular, I want to thank Christian Veelken for the time he patiently spent with me, to teach me about tau physics at CMS.

I had the invaluable opportunity to work one year at CERN ; and this certainly improved the quality of my work. For this, I want to thank Joe Incandela and the FPS committee.

My work at the IIHE and at CERN would not have been that pleasant without my colleagues. It is impossible to name everyone here, but special thanks go to the nicest office mates, Nastja and Didar, to the most efficient secretary, Audrey, to the most patient IT team, and to the best support at CERN, Jian.

And the last word goes to my parents and my sisters, whom always support me, and whom I cannot thank enough.

Contents

Introduction **1**

I Theoretical bases 5

1 The standard model of particle physics **7**
1.1 Elementary particles and forces . . . 7
1.2 Standard model Lagrangian . . . 9
1.3 Scalar sector . . . 12
1.4 Chapter summary . . . 18

2 Physics beyond the standard model **19**
2.1 Motivations for new physics . . . 19
2.2 Two-Higgs-doublet models . . . 22
2.3 Supersymmetry . . . 25
2.4 Two-Higgs-doublet models + a singlet . . . 31
2.5 Search for BSM physics in the scalar sector . . . 33
2.6 Precision measurements vs. direct discovery in the case of the SM+S . . . 35
2.7 Chapter summary and personal contributions . . . 37

3 Statistics **39**
3.1 Likelihood . . . 39
3.2 Maximum likelihood fit . . . 43
3.3 Exclusion limits . . . 43
3.4 Significance . . . 45
3.5 Goodness-of-fit test . . . 47
3.6 Boosted decision trees . . . 48
3.7 k-Nearest Neighbor classifier . . . 50
3.8 Chapter summary . . . 52

II Experimental bases 53

4 Experimental setup **55**
4.1 Large Hadron Collider . . . 55
4.2 Compact Muon Solenoid . . . 58
4.3 Chapter summary . . . 67

5 Event generation, simulation and reconstruction **69**
5.1 Event generation and simulation . . . 69
5.2 Object reconstruction and identification . . . 70
5.3 Chapter summary . . . 81

6 Tau lepton reconstruction and identification **83**
6.1 HPS algorithm description . . . 83
6.2 HPS algorithm performance in Run-1 . . . 89
6.3 HPS algorithm in Run-2 . . . 113
6.4 Chapter summary and personal contributions . . . 121

III SM physics analyses **123**

7 Search for the SM scalar in the $ZH \to \ell\ell\tau\tau$ channel **125**
7.1 Analysis overview . . . 125
7.2 Selection . . . 126
7.3 Background estimation . . . 129
7.4 Di-tau mass reconstruction . . . 135
7.5 Systematic uncertainties and simulation corrections . . . 136
7.6 Results . . . 141
7.7 Chapter summary and personal contributions . . . 146

8 Search for the SM scalar in the $WH \to e\mu\tau_h$ channel **147**
8.1 Selection . . . 147
8.2 Background estimation . . . 148
8.3 Results . . . 153
8.4 Chapter summary and personal contributions . . . 156

9 Combination of searches for the SM scalar boson decaying to taus **157**
9.1 Gluon-gluon fusion and vector boson fusion production modes . . . 157
9.2 Vector boson associated production . . . 158
9.3 Combination of all production modes . . . 158
9.4 Chapter summary and personal contributions . . . 162

IV BSM physics analyses **163**

10 Search for a heavy pseudoscalar boson A decaying to Zh in the $\ell\ell\tau\tau$ final state **165**
10.1 Differences with respect to the SM $ZH \to \ell\ell\tau\tau$ analysis . . . 165
10.2 Background estimation validation . . . 169
10.3 High $\not{E}_T$ excess . . . 170
10.4 Results . . . 171
10.5 Combination with $H \to hh \to bb\tau\tau$ . . . 174
10.6 Chapter summary and personal contributions . . . 177

11 Search for exotic decays of the SM-like scalar boson in the $\mu\mu\tau\tau$ final state **179**
11.1 Selection . . . 179
11.2 Background estimation and its validation . . . 183
11.3 Modeling of the experimental $m_{\mu\mu}$ distributions . . . 186
11.4 Uncertainties . . . 195
11.5 Results . . . 198

11.6 Interpretation and comparison with other CMS searches . . . 202
11.7 Chapter summary and personal contributions . . . 209

12 Search for a light pseudoscalar decaying to taus **211**
12.1 Analysis overview . . . 211
12.2 Selection . . . 213
12.3 Background estimation . . . 215
12.4 Systematic uncertainties . . . 219
12.5 Results . . . 222
12.6 Chapter summary and personal contributions . . . 226

13 Search for a heavy di-tau resonance in the MSSM **227**
13.1 Categorization . . . 227
13.2 $\tau_h\tau_h$ final state . . . 229
13.3 Differences from the light pseudoscalar boson search analysis in the $e\tau_h$, $\mu\tau_h$ and $e\mu$ final states . . . 234
13.4 Φ p_T reweighting . . . 237
13.5 Result interpretation . . . 237
13.6 Chapter summary and personal contributions . . . 240

V Status and prospects **241**

14 Overview of LHC results and prospects for future colliders **243**
14.1 Overview of CMS measurements in the scalar sector . . . 243
14.2 Overview of other SM and BSM results of the CMS experiment . . . 250
14.3 Future collider experiments . . . 251
14.4 Chapter summary . . . 254

Conclusion **255**

A Technical details about physics analyses **259**
A.1 Monte Carlo samples and collected datasets . . . 259
A.2 Triggers . . . 259

Introduction

The standard model (SM) of particle physics describes the elementary particles and their interactions through the electromagnetic, the weak and the strong forces. Experimental results from various high-energy experiments, such as the Large Electron-Positron Collider (LEP) at CERN between 1989 and 2000, the Tevatron at Fermilab between 1983 and 2011, and the Large Hadron Collider (LHC) at CERN from 2010, have shown up to now an amazing agreement with the predictions of the SM. The latest triumph of the theory is the discovery of a new scalar particle, compatible with the Brout-Englert-Higgs boson of the SM, in July 2012. This particle, the cornerstone and last missing piece of the SM, was introduced as a consequence of the electroweak symmetry breaking, in order to explain how elementary particles could obtain a mass without violating the gauge invariance of the theory. The physicists Francois Englert - working closely with deceased Robert Brout - and Peter Higgs were awarded the 2013 Physics Nobel Prize in acknowledgment of "the theoretical discovery of a mechanism that contributes to our understanding of the origin of mass of subatomic particles, and which recently was confirmed through the discovery of the predicted fundamental particle, by the ATLAS and CMS experiments at CERN's Large Hadron Collider". The data collected by the ATLAS and CMS experiments at CERN in 2011 and 2012, during the LHC Run-1, have permitted to study more precisely the properties and couplings of this new particle; all measurements indicate up to now that it is compatible within uncertainties with the scalar boson from the SM.

The discovery of a particle compatible with the scalar boson of the SM happened almost fifty years after its prediction in 1964, and was made possible by the high performance of the LHC, and of its two general-purpose experiments, ATLAS and CMS. The LHC, situated under the French-Swiss border, is a twenty-seven kilometer long circular proton-proton (pp) collider. Its Run-1 extended from 2010 to 2012, and permitted to collect roughly 25 fb^{-1} of data at a center-of-mass energy of 7 and 8 TeV; whereas Run-2 started in summer 2015 at a center-of-mass energy of 13 TeV after a long shutdown of the LHC. The search for the SM scalar boson was the main objective when designing the experiment.

In the SM, the scalar boson is produced via different mechanisms. Its largest production cross section at the LHC corresponds to the gluon-gluon fusion, whereas vector boson fusion production and the production in association with a vector boson have smaller cross sections. Although the gluon-gluon fusion production dominates, studying the other pro-

duction modes is important to test the compatibility of the discovered boson, H, with the SM scalar boson. Subdominant production modes can moreover have a larger sensitivity to the presence of a signal in the case where the H decay products are difficult to identify. For a mass of 125 GeV, as measured by the CMS and ATLAS experiments, a large variety of decay modes is opened, which provides experimentalists with a wide range of physics signatures to study. The discovery of the H boson in 2012 was led by the study of bosonic decay channels ($H \to \gamma\gamma$, $H \to W^{\pm}W^{\mp *}$ and $H \to ZZ^{*}$), but searching for its decay to fermions, essentially $H \to \tau^{+}\tau^{-}$ and $H \to b\bar{b}$, is important to test if the H Yukawa couplings are in agreement with the predictions of the SM. Fermionic decay channels, despite their large branching fractions, are less sensitive than bosonic decay channels because of the difficulty in identifying and reconstructing tau leptons and b quarks, and in separating the signal from large backgrounds.

Tau leptons are the only leptons heavy enough to decay semi-hadronically. In about two thirds of cases, tau leptons decay to a combination of charged and neutral hadrons, and to a tau neutrino. Muons and electrons produced in leptonic tau decays along with neutrinos cannot be distinguished from other muons or electrons produced promptly. Hadronically decaying tau leptons, τ_h, are reconstructed and identified in CMS with the Hadrons Plus Strips (HPS) algorithm, which combines trajectories measured in the tracker detector and energy deposits in the electromagnetic calorimeter to form τ_h candidates. The algorithm also provides handles to distinguish hadronically decaying taus from jets, electrons and muons; it typically identifies successfully 60% of hadronically decaying taus, while less than 1% of quark and gluon jets are misidentified as τ_h.

Although the SM is a remarkable theory that is not contradicted by the precision measurements made up to now, evidence for new physics beyond the SM (BSM physics) exists. Theorists have proposed models to address the shortcomings of the SM; many of these models predict the existence of an extended scalar sector. The minimal supersymmetric extension of the SM (MSSM), which addresses the hierarchy and the coupling unification problems among others, introduces a second scalar doublet in addition to the one predicted in the SM. This results, after symmetry breaking, in five scalar eigenstates: two charged Higgs bosons $H^{\pm}$, a light and a heavy CP-even (scalar) bosons h and H, and a CP-odd (pseudoscalar) boson A. One of the free parameters of the theory at tree level is the ratio of the vacuum expectation values of the two Higgs doublets, $\tan\beta$. At large values of $\tan\beta$, the most sensitive channel to uncover an eventual MSSM scalar sector is by far the decay of a heavy neutral scalar to a pair of tau leptons: $\Phi = H/A/h \to \tau^{+}\tau^{-}$. At low $\tan\beta$, the phenomenology is richer and different channels can contribute with comparable sensitivities. One of them is the decay of the heavy pseudoscalar A to a Z boson and the light neutral scalar h, where the h boson decays to tau leptons: $A \to Zh \to \ell^{+}\ell^{-}\tau^{+}\tau^{-}$. More generic BSM models that include the MSSM, are two-Higgs-doublet models (2HDM). In such models, the pseudoscalar A could be lighter than the neutral scalar h, making $bbA \to bb\tau^{+}\tau^{-}$ with low m_A a high-potential channel to discover an extended scalar sector. Finally, some models authorize the SM-like h boson to decay exotically to non-SM

particles, which is still allowed by all LHC measurements. A powerful channel is, under some assumptions, $h \to aa \to \mu^+\mu^-\tau^+\tau^-$, where a is a light pseudoscalar boson.

The Run-1 of the LHC not only led to the observation of a new particle compatible with the scalar boson of the SM, but also permitted to explore large regions of the parameter spaces of many BSM theories. The measurement of the properties of the new particle has not shown any disagreement with the predictions of the SM, and the ATLAS and CMS Collaborations have joined their efforts to determine the mass of this new particle with a great precision: 125.09 $\pm$ 0.21 (stat.) $\pm$ 0.11 (syst.) GeV. No evidence for the existence of an extended scalar sector has been observed, but some intriguing excesses ($H \to \mu^\pm\tau^\mp$ flavor violating decays, $t\bar{t}H$ production, ...) need more data to be confirmed. The Run-2 has permitted to collect about 3 fb^{-1} data at 13 TeV center-of-mass energy in 2015, which is not sufficient to equalize the sensitivity reached in Run-1 for scalar studies. The large amount of data collected at the LHC and High-Luminosity LHC (HL-LHC) in the coming years will allow for a large range of precision measurements and direct searches for new physics beyond the SM, and different future collider options are already being studied to take over from the LHC.

This thesis is devoted to the study of the scalar sector of the SM, and to the search for an extended scalar sector, with tau leptons in the final state. While Chapter 1 presents the SM, Chapter 2 introduces the motivations for BSM physics as well as some BSM models with an extended scalar sector. Some statistic tools useful to interpret the results of physics analyses are described in Chapter 3. The LHC and the CMS detector are presented in Chapter 4, and the simulations and physics object reconstruction in Chapter 5. The HPS algorithm, which reconstructs and identifies hadronically decaying tau leptons, is detailed in Chapter 6, and its performance is measured in data. Searches for the decay of the SM scalar boson to tau leptons are presented in Chapter 7 (ZH associated production), Chapter 8 ($WH \to e^\pm\mu^\pm\tau_h^\mp$) and Chapter 9 (combination of all production modes). The next chapters detail searches for BSM scalars decaying to tau leptons: MSSM pseudoscalar $A \to Zh \to \ell^+\ell^-\tau^+\tau^-$ in Chapter 10, exotic decays of the 125-GeV scalar $h \to aa \to \mu^+\mu^-\tau^+\tau^-$ in Chapter 11, light pseudoscalars in 2HDM $bbA \to bb\tau^+\tau^-$ in Chapter 12, and heavy MSSM resonances $\Phi = A/H/h \to \tau^+\tau^-$ in Chapter 13. The thesis ends with a discussion about the status of high energy physics after the first run of the LHC and the plans for future collider experiments, in Chapter 14. All the physics analyses detailed in this thesis exploit data collected by the CMS detector during Run-1, whereas the HPS algorithm performance is measured in data collected in both Run-1 and Run-2.

Part I

Theoretical bases

Chapter 1

The standard model of particle physics

The standard model (SM) of particles physics [1–7] describes the elementary particles and their interactions at the most fundamental level. It is a gauge theory based on the $SU(3) \times SU(2) \times U(1)$ symmetry group.

1.1 Elementary particles and forces

All interactions can be described by four forces: the strong force, the electromagnetic force, the weak force and the gravitational force. These forces are mediated by particles with an integer spin, bosons. The gravitational force, which can be neglected if the energy is lower than the Planck scale (1.22×10^{19} GeV), is not included in the SM. The mediators of the strong interaction are eight gluons, while the photon mediates the electromagnetic force, and the $W^{\pm}$ and Z bosons the weak force. The forces and some of their characteristics are detailed in Tab. 1.1.

Interaction	Range	Relative strength	Mediators
Strong	10^{-15} m	1	8 gluons (g)
Electromagnetic	∞	10^{-3}	photon (γ)
Weak	10^{-18} m	10^{-14}	W^+, W^-, Z
Gravitational	∞	10^{-43}	gravitons?

Table 1.1: Range, relative strength with respect to the strong force, and mediators of the four fundamental interactions. The gravitational force is not included in the SM, and gravitons are hypothetical particles.

The first elementary particle that was discovered is the electron [8]. The electron e belongs to the first generation of leptons, together with the electronic neutrino ν_e. The muon μ, and the muonic neutrino ν_μ constitute the second generation of leptons, whereas the tau τ and the tauic neutrino ν_τ form the third generation. The masses of the charged

leptons differ by four orders of magnitude between the first and third generations. Table 1.2 summarizes the leptons and their properties. The leptons are fermions and are constituents of matter. They do not interact strongly.

Generation	Particle	Charge	Mass (MeV)	Lifetime (s)
First	electron (e)	-q_e	0.51099	∞
	electronic neutrino (ν_e)	0	$\simeq 0$	∞
Second	muon (μ)	-q_e	105.67	2.20×10^{-6}
	muonic neutrino (ν_μ)	0	$\simeq 0$	∞
Third	tau (τ)	-q_e	1776.99	2.91×10^{-13}
	tauic neutrino (ν_τ)	0	$\simeq 0$	∞

Table 1.2: Properties of the leptons in the three generations. q_e represents the Coulomb charge. Neutrinos are known to have a tiny mass compared to the other SM particles, but non-zero. [9]

Quarks, like leptons, are fermions and can be categorized in three generations. The six quarks can interact via strong interaction and carry color charges. The top quark, which was discovered in 1995 at the Tevatron, is the heaviest SM particle, with a mass close to 173.2 GeV [1] [9]. The quarks and their properties are shown in Tab. 1.3.

Generation	Quark	Charge	Mass
First	up quark (u)	2/3 q_e	$2.3^{+0.7}_{-0.5}$ MeV
	down quark (d)	-1/3 q_e	$4.8^{+0.5}_{-0.3}$ MeV
Second	charm quark (c)	2/3 q_e	1.275 ± 0.025 GeV
	strange quark (s)	-1/3 q_e	95 ± 5 MeV
Third	top quark (t)	2/3 q_e	$173.21 \pm 0.51 \pm 0.71$ GeV
	bottom quark (b)	-1/3 q_e	4.66 ± 0.03 GeV

Table 1.3: Quarks and their properties. q_e represents the Coulomb charge. Up, down and strange quark masses correspond to current quark masses with $\mu = 2$ GeV, whereas other quark masses correspond to running masses in the $\overline{\text{MS}}$ scheme. [9]

Ordinary matter on earth is essentially composed of particles from the first generation: up and down quarks in the nucleus, and electrons in the electron cloud.

Finally, the last piece of the SM is the scalar boson, discovered in 2012, and responsible for the masses of the $W^\pm$ and Z bosons, and of the fermions.

1. In this thesis all masses and energies are expressed in natural units, where the speed of light and $\hbar$ are taken as equal to 1.

1.2 Standard model Lagrangian

The SM is a theory based on the $SU(3)_C \times SU(2)_L \times U(1)_Y$ gauge symmetry, where $SU(2)_L \times U(1)_Y$ describes the electroweak interaction and $SU(3)_C$ the strong interaction. The index C refers to the color, L to the left chiral nature of the $SU(2)$ coupling and Y to the weak hypercharge.

The gauge field associated to the symmetry group of electromagnetic interactions is B_μ, which corresponds to the generator Y. Three gauge fields, W_μ^1, W_μ^2 and W_μ^3 are associated to $SU(2)_L$ with three generators that can be expressed as half of the Pauli matrices:

$$T_1 = \frac{1}{2}\begin{pmatrix} 0 & 1 \\ 1 & 0 \end{pmatrix},\ T_2 = \frac{1}{2}\begin{pmatrix} 0 & -i \\ i & 0 \end{pmatrix},\ \text{and } T_3 = \frac{1}{2}\begin{pmatrix} 1 & 0 \\ 0 & -1 \end{pmatrix}. \tag{1.1}$$

The generators T^a satisfy the Lie algebra:

$$[T^a, T^b] = i\epsilon^{abc} T_c \text{ and } [T^a, Y] = 0, \tag{1.2}$$

where ϵ^{abc} is an antisymmetric tensor. Finally, in $SU(3)_C$, eight generators correspond to the eight gluon fields $G_\mu^{1\cdots 8}$. Unlike $SU(2)_L \times U(1)_Y$, $SU(3)_C$ is not chiral.

Quarks and leptons are described by matter fields that are organized in weak isodoublets or weak isosinglets, depending on their chirality. There are three generations of matter fields. Under $SU(3)_C$, quarks are color triplets while leptons are color singlets; quarks therefore carry a color index ranging between one and three, whereas leptons do not take part in strong interactions. Each generation i of fermions consists of these left-handed doublets and right-handed singlets [2]:

$$\ell_L = \begin{pmatrix} e_L \\ \nu_L \end{pmatrix},\ e_R, q_L = \begin{pmatrix} u_L \\ d_L \end{pmatrix},\ u_R,\ d_R. \tag{1.3}$$

After electroweak symmetry breaking, $SU(2)_L \times U(1)_Y$ is reduced to the $U(1)_{EM}$ symmetry group. The weak hypercharge Y carried by the matter fields is related to the electric charge Q and the weak isotopic charge T^3 with:

$$Y = Q - T^3. \tag{1.4}$$

The fermion content of the SM is summarized in Tab. 1.4, together with its representation under the different groups of symmetry.

The SM Lagrangian density can be decomposed as a sum of four different terms:

$$\mathcal{L}_{SM} = \mathcal{L}_{gauge} + \mathcal{L}_f + \mathcal{L}_{Yuk} + \mathcal{L}_\phi, \tag{1.5}$$

which are related respectively to the gauge, fermion, Yukawa and scalar sectors. The four Lagrangian terms are detailed below.

2. Right-handed neutrinos, ν_R, are sometimes also considered.

Field	$SU(3)_C$ representation	$SU(2)_L$ representation	y	t^3	q
u_{iL}	3	2	$\frac{1}{6}$	$\frac{1}{2}$	$\frac{2}{3}$
d_{iL}	3	2	$\frac{1}{6}$	$-\frac{1}{2}$	$-\frac{1}{3}$
ℓ_{iL}	1	2	$-\frac{1}{2}$	$-\frac{1}{2}$	-1
ν_{iL}	1	2	$-\frac{1}{2}$	$\frac{1}{2}$	0
u_{iR}	3	1	$\frac{2}{3}$	0	$\frac{2}{3}$
d_{iR}	3	1	$-\frac{1}{3}$	0	$-\frac{1}{3}$
ℓ_{iR}	1	1	-1	0	-1
ν_{iR}	1	1	0	0	0

Table 1.4: Fermion content of the SM, with representations under $SU(3)_C$ and $SU(2)_L$, hypercharge y, isospin t^3 and electric charge q. The index i refers to the fermion generation, while the indices L and R represent the left-handed or right-handed nature of the particle.

– The gauge Lagrangian density $\mathcal{L}_{gauge}$ regroups the gauge fields of all three symmetry groups:

$$\mathcal{L}_{gauge} = -\frac{1}{4}G^i_{\mu\nu}G^{\mu\nu i} - \frac{1}{4}W^i_{\mu\nu}W^{\mu\nu i} - \frac{1}{4}B_{\mu\nu}B^{\mu\nu}. \tag{1.6}$$

In this expression, the tensors are:

$$G^i_{\mu\nu} = \partial_\mu G^i_\nu - \partial_\nu G^i_\mu - g_s f_{ijk} G^j_\mu G^k_\nu, \text{ with } i,j,k = 1,...,8; \tag{1.7}$$

$$W^i_{\mu\nu} = \partial_\mu W^i_\nu - \partial_\nu W^i_\mu - g\epsilon_{ijk} W^j_\mu W^k_\nu, \text{ with } i,j,k = 1,...,3; \tag{1.8}$$

$$B_{\mu\nu} = \partial_\mu B_\nu - \partial_\nu B_\mu, \tag{1.9}$$

where g_S and g are the coupling constants associated to the $SU(3)_C$ and $SU(2)_L$ symmetry groups respectively.

– The fermionic part of the Lagrangian density consists of kinetic energy terms for quarks and leptons, namely:

$$\mathcal{L}_f = i\bar{q}_{iL}\not{D}q_{iL} + i\bar{u}_{iR}\not{D}u_{iR} + i\bar{d}_{iR}\not{D}d_{iR} + i\bar{\ell}_{iL}\not{D}\ell_{iL} + i\bar{e}_{iR}\not{D}e_{iR}. \tag{1.10}$$

The gauge-covariant derivatives are:

$$D^\mu q_{iL} = (\partial^\mu + \frac{i}{2}g_S G^\mu_a \lambda_a + \frac{i}{2}gW^\mu_b \sigma_b + \frac{i}{6}g'B^\mu)q_{iL}, \tag{1.11}$$

$$D^\mu u_{iR} = (\partial^\mu + \frac{i}{2}g_S G^\mu_a \lambda_a + \frac{2i}{3}g'B^\mu)u_{iR}, \tag{1.12}$$

$$D^\mu d_{iR} = (\partial^\mu + \frac{i}{2}g_S G^\mu_a \lambda_a - \frac{i}{3}g'B^\mu)d_{iR}, \tag{1.13}$$

$$D^\mu \ell_{iL} = (\partial^\mu + \frac{i}{2}gW^\mu_a \sigma_a - \frac{i}{2}g'B^\mu)\ell_{iL}, \tag{1.14}$$

$$D^\mu e_{iR} = (\partial^\mu - ig' B^\mu) e_{iR}, \tag{1.15}$$

where g' is the coupling constant associated to the $U(1)_Y$ symmetry group.

– The Yukawa Lagrangian density describes the interactions between the fermions and the scalar doublet ϕ, which give rise to fermion masses. The doublet ϕ is composed of two complex scalar fields; it can be written as $\phi = \begin{pmatrix} \phi^+ \\ \phi^0 \end{pmatrix}$. If one notes Y^u, Y^d and Y^e three general complex 3×3 matrices of dimensionless couplings, the Yukawa Lagrangian density can be written as:

$$\mathcal{L}_{Yuk} = -Y^u_{ij} \bar{q_{iL}} u_{jR} \tilde{\phi} - Y^d_{ij} \bar{q_{iL}} d_{jR} \phi - Y^e_{ij} \bar{\ell_{iL}} e_{jR} \phi + h.c., \tag{1.16}$$

where $\tilde{\phi}$ is defined as:

$$\tilde{\phi} = i\sigma_2 (\phi^\dagger)^t. \tag{1.17}$$

Without loss of generality, it is possible to choose a basis such that the Yukawa coupling matrices become diagonal, at the cost of intoducing the Babbibo-Kobayashi-Maskawa mixing matrix in the charged gauge couplings:

$$\hat{Y_e} = V_{eL} Y^e V^\dagger_{eR} = \mathrm{diag}(\lambda_e, \lambda_\mu, \lambda_\tau), \tag{1.18}$$

$$\hat{Y_u} = V_{uL} Y^u V^\dagger_{uR} = \mathrm{diag}(\lambda_u, \lambda_c, \lambda_t), \tag{1.19}$$

$$\hat{Y_d} = V_{dL} Y^d V^\dagger_{dR} = \mathrm{diag}(\lambda_d, \lambda_s, \lambda_b). \tag{1.20}$$

The Yukawa sector introduces a large number of free parameters in the SM.

– The scalar sector will be described at length in the next section, but one can already detail the Lagrangian density associated to the scalar sector, $\mathcal{L}_\phi$. It is composed of a kinematic and a potential components:

$$\mathcal{L}_\phi = (D^\mu \phi)^\dagger D_\mu \phi - V(\phi). \tag{1.21}$$

The potential $V(\phi)$ has the most general renormalizable [3] form invariant under $SU(2)_L \times U(1)_Y$:

$$V(\phi) = \mu^2 \phi^\dagger \phi + \lambda (\phi^\dagger \phi)^2. \tag{1.22}$$

To obtain the spontaneous electroweak symmetry breaking necessary to give mass to the W and Z bosons, the factor μ^2 has to be negative; and unitarity requires that it is real. Additionally, to preserve the vacuum stability, λ is a positive real number. The kinetic part includes the gauge covariant derivative, which is defined as:

$$D_\mu \phi = \left(\partial_\mu + ig \vec{T}.\vec{W}_\mu + \frac{ig'}{2} B_\mu \right) \phi. \tag{1.23}$$

3. Theories are usually defined as valid within certain thresholds. In quantum theories, because all particles can contribute to a process as virtual particles, all scales contribute, even to low-energy processes. A cut-off is often needed in the calculation. If the cut-off disappears from the final results (possibly by its absorption in a finite number of measured constants), the theory is called renormalizable.

1.3 Scalar sector

Mass terms for fermions and gauge fields are not present in $\mathcal{L}_{gauge}$ or $\mathcal{L}_f$, because only singlets under $SU(3)_C \times SU(2)_L \times U(1)_Y$ could acquire a mass with an interaction of the type $m^2\phi^\dagger\phi$ without breaking the gauge invariance. Electroweak symmetry breaking, leading to the Lagrangian term $\mathcal{L}_\phi$, is introduced to give mass terms to fermions and gauge fields [10–15].

1.3.1 Electroweak symmetry breaking

A scalar doublet is introduced in the SM:

$$\phi = \frac{1}{\sqrt{2}} \begin{pmatrix} \varphi_1 + i\varphi_2 \\ \varphi_3 + i\varphi_4 \end{pmatrix}. \tag{1.24}$$

As described in the previous section, the field potential has the generic form $V(\phi) = \mu^2\phi^\dagger\phi + \lambda(\phi^\dagger\phi)^2$, with $\mu^2 < 0$ and λ a positive integer. This choice of parameters gives the potential the shape of a "Mexican hat". While a local maximum of the potential is at the value zero, its minimum corresponds to a non-zero field. The field can be developed around one of its degenerate minima in an arbitrary direction of the electroweak symmetry breaking (EWSB):

$$\phi = \langle\phi\rangle + \widehat{\phi} = \begin{pmatrix} 0 \\ \frac{v}{\sqrt{2}} \end{pmatrix} + \widehat{\phi}. \tag{1.25}$$

where v is the vacuum expectation value (vev), measured to be about 246 GeV, and corresponds to $\sqrt{\frac{-\mu^2}{\lambda}}$. This solution leads to a closed continuous surface of minima in the radial direction. The second derivative of the potential in the radial direction is positive, while it is zero in the transverse directions. One deduces the existence of one massive particle, and three massless particles, called Goldstone bosons.

Given the existence of the field doublet ϕ, one can write the Yukawa coupling of the electron to this doublet with the following Lagrangian:

$$\mathcal{L}^e_{Yuk} = -\lambda_e \bar{\ell}_{1L}\phi e_{1R} + h.c. \xrightarrow{\text{EWSB}} -\lambda_e \frac{v}{\sqrt{2}} \bar{e}_{1L} e_{1R} + h.c. \tag{1.26}$$

A mass can now be given to the electron in the SM:

$$m_e = \frac{\lambda_e v}{\sqrt{2}}. \tag{1.27}$$

The covariant derivative of the ϕ field is given by:

$$D_\mu\phi = (\partial_\mu + igW^a_\mu T_a + i\frac{g'}{2}B_\mu)\phi \tag{1.28}$$

which leads to

$$|D_\mu\langle\phi\rangle|^2 = \frac{g^2v^2}{8}\left((W^1_\mu)^2 + (W^2_\mu)^2 + (-W^3_\mu + \frac{g'}{g}B_\mu)^2\right). \tag{1.29}$$

The vector bosons W^1 and W^2 therefore acquire a mass, given by:

$$m_{W1} = m_{W2} = \frac{gv}{2}. \tag{1.30}$$

The third term of equation (1.29) is a linear combination of W^3_μ and B_μ, and corresponds to a heavy boson field that is called Z_μ. Its massless orthogonal combination is called A_μ and corresponds to the photon field:

$$\begin{cases} Z_\mu = W^3_\mu \cos\theta_W - B_\mu \sin\theta_W \\ A_\mu = W^3_\mu \sin\theta_W + B_\mu \cos\theta_W \end{cases}. \tag{1.31}$$

The third term of equation (1.29) can be recovered for:

$$\tan\theta_W = \frac{g'}{g}. \tag{1.32}$$

The mass of the Z boson is thus related to the mass of the W bosons via the Weinberg angle θ_W, which can be determined experimentally [4]:

$$\frac{m_W}{m_Z} = \cos\theta_W. \tag{1.33}$$

The three Goldstone bosons get absorbed to give a mass to the W and Z bosons. This can be seen using the Higgs transformation:

$$\phi = \frac{1}{\sqrt{2}}\begin{pmatrix}\varphi_1 + i\varphi_2 \\ \varphi_3 + i\varphi_4\end{pmatrix} = e^{i\frac{\vec{\xi}(x).\vec{T}}{v}}\begin{pmatrix}0 \\ \frac{v+h(x)}{\sqrt{2}}\end{pmatrix}, \tag{1.34}$$

where one introduces the fields $\vec{\xi}(x)$ and $h(x)$ that vanish in the vacuum. Given the local gauge invariance, the following gauge transformation eliminates the degrees of freedom associated to the Goldstone bosons:

$$\phi' = e^{-i\frac{\vec{\xi}(x).\vec{T}}{v}}\phi. \tag{1.35}$$

One can rewrite the potential as:

$$V = \lambda\left(\phi^\dagger\phi - \frac{v^2}{2}\right)^2 - \lambda\frac{v^4}{4} \tag{1.36}$$

$$= \lambda\left(\frac{1}{2}(v+h)^2 - \frac{v^2}{2}\right)^2 - \lambda\frac{v^4}{4} \tag{1.37}$$

$$= \lambda v^2 h^2 + \lambda v h^3 + \frac{\lambda}{4}h^4 - \lambda\frac{v^4}{4}, \tag{1.38}$$

where the degrees of freedom associated to the three broken generators $\xi_a(x)$ have disappeared. The last equality gives rise to the mass of the h field:

$$m_H^2 = 2\lambda v^2 = -2\mu^2. \tag{1.39}$$

4. $\sin^2\theta_W \simeq 0.231$. [9]

The down quark can, like the electron, acquire a mass through Yukawa couplings to the ϕ doublet:

$$\mathcal{L}^{d}_{Yuk} = -\lambda_d \bar{q}_{1L} \phi d_{1R} + h.c. \xrightarrow{\text{EWSB}} -\lambda_d \frac{v}{\sqrt{2}} \bar{d}_{1L} d_{1R} + h.c. \tag{1.40}$$

The up quark cannot acquire a mass by directly coupling to ϕ. The most economical solution consists in making it couple to a transformation of ϕ: $\tilde{\phi}$ as defined in equation (1.17). The four degrees of freedom of the ϕ doublet, after absorption by the three Goldstone bosons, lead to one degree of freedom corresponding to the massive scalar boson of the SM, H.

The Brout-Englert-Higgs field couples universally to all quarks and leptons with a strength proportional to their masses, and to gauge bosons with a strength proportional to the square of their masses.

1.3.2 SM H production modes

The production modes of the SM scalar boson at the LHC are:

- The **gluon-gluon fusion** (ggH) production has the largest cross section at the LHC. It proceeds via a quark loop.
- The **vector boson fusion** (VBF) production has a cross section an order of magnitude below the ggH production. Two high-momentum quarks are present in the final state; they hadronize to form jets. The kinematic characteristics of these jets, such as their forward direction or their large invariant mass, make of the VBF production an interesting process to tag experimentally.
- The **associated production with a vector boson** (VH) consists in the production of a virtual boson V^* that splits into a real boson V and a boson H; it is sometimes called "Higgsstrahlung". The cross section is even smaller than in the VBF case, but the presence of leptons or quarks coming from vector boson decays help discriminating a scalar boson VH signal from backgrounds.
- The production in **association with a pair of top quarks** ($t\bar{t}H$) has such a small cross section that it was not accessible experimentally in Run-1, even with the SM background reduction obtained thanks to the presence of the two top quarks. CMS is expected to be sensitive to $t\bar{t}H$ production in Run-2, given the larger luminosity and the increase of center-of-mass energy, which especially benefits this production mode.

The Feynman diagrams of the three dominant production modes of the SM scalar boson at the LHC are shown in Fig. 1.1, and their respective cross sections at a center-of-mass energy of 8 TeV as well as the total H boson production cross sections at center-of-mass energies of 7, 8 and 14 TeV are illustrated in Fig. 1.2.

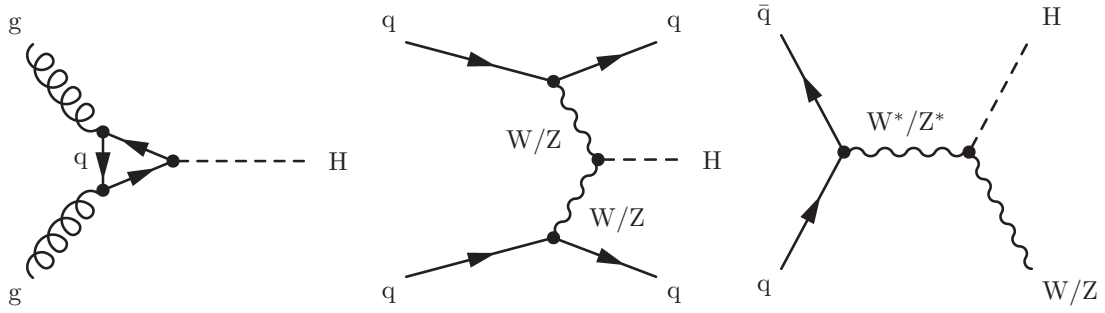

Figure 1.1: Dominant Feynman diagrams for the SM scalar boson production at the LHC: gluon-gluon fusion (left), vector boson fusion production (center) and associated production with a vector boson (right). [16]

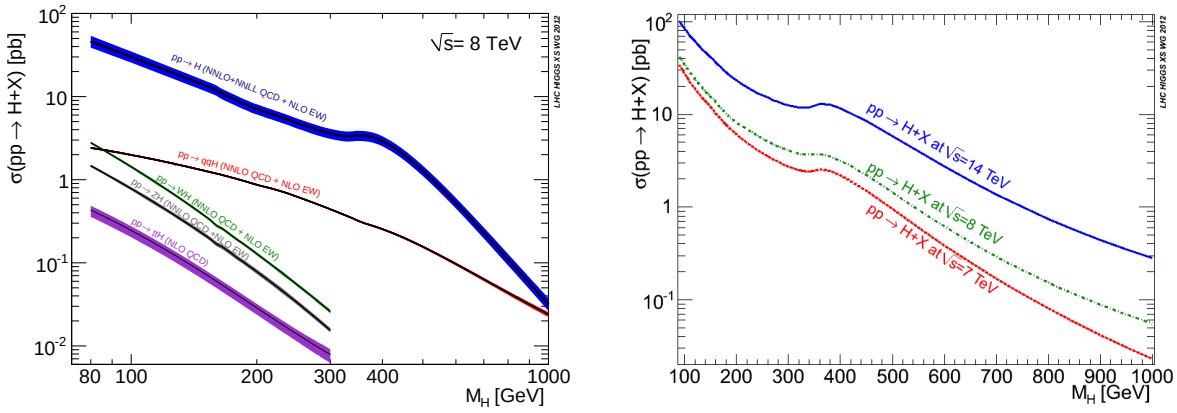

Figure 1.2: Left: Scalar boson production cross sections in proton-proton collisions at a center-of-mass energy of 8 TeV for the ggH, VBF, VH and $t\bar{t}H$ production mechanisms. Right: Total production cross sections of the scalar boson in proton-proton collisions at 7, 8 and 14 TeV center-of-mass energies. [17]

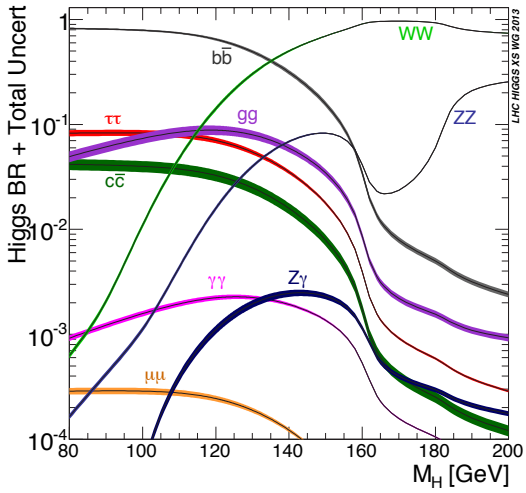

Figure 1.3: Branching fractions of the SM scalar boson for m_H between 80 and 200 GeV. [17]

1.3.3 SM H decay modes

Assuming a mass for the scalar boson, it is possible to compute its partial decay width to any combination of SM particles. The branching fraction is obtained by dividing the partial decay width by the sum of the partial decay widths of all possible decay channels:

$$\mathcal{B}(H \to XX) = \frac{\Gamma(H \to XX)}{\sum_{Y \in SM} \Gamma(H \to YY)}. \tag{1.41}$$

The partial decay widths can be computed following the prescriptions in [6, 18], and are shown in Fig. 1.3 for scalar boson masses between 80 and 200 GeV.

Decay to fermions

In the SM, scalar couplings to fermions are directly proportional to fermion masses. The Born approximation gives the partial decay width of the scalar boson to fermion pairs. If m_f is the fermion mass, and N_C the color factor [5], it can be written as:

$$\Gamma_{Born}(H \to f\bar{f}) = \frac{G_F N_C}{4\sqrt{2}\pi} m_H m_f^2 \beta_f^3, \tag{1.42}$$

where β is the velocity of the fermions in the final state and can be expressed as:

$$\beta = \sqrt{1 - \frac{4m_f^2}{m_H^2}}, \tag{1.43}$$

5. Equal to one for leptons and to three for quarks.

and G_F is the Fermi coupling constant [6]:

$$\frac{G_F}{\sqrt{2}} = \frac{\pi g'}{2m_W^2(1 - m_W^2/m_Z^2)}. \tag{1.44}$$

As the partial decay width is proportional to the square of the fermion mass, the branching fraction of the H boson to tau leptons is approximately a two hundred times larger than its branching fraction to muons, while the branching fraction to electrons is negligible.

In the case of H boson decays to quarks, QCD corrections cannot be neglected. For H boson masses much larger than the quark mass, the NLO decay width, including Feynman diagrams with gluon exchange and the emission of a gluon in the final state, can be expressed as:

$$\Gamma_{NLO}(H \to q\bar{q}) \simeq \frac{3G_F}{4\sqrt{2}\pi} m_H m_q^2 \left[1 + \frac{4}{3}\frac{g_s}{\pi}\left(\frac{9}{4} + \frac{3}{2}\ln\frac{m_q^2}{m_H^2}\right)\right]. \tag{1.45}$$

Decay to bosons

For masses above the WW and ZZ kinematical thresholds, the H boson decays essentially to electroweak boson pairs. The partial decay widths to a pair of electroweak bosons V (W or Z boson) is given by:

$$\Gamma(H \to VV) = \frac{G_F m_H^3}{16\sqrt{2}\pi}\delta_V\sqrt{1-4x}(1 - 4x + 12x^3), \tag{1.46}$$

with $x = m_V^2/m_H^2$, $\delta_W = 2$ and $\delta_Z = 1$.

However, below the WW and ZZ kinematical thresholds, the two-body decay as described above is forbidden. The scalar boson can still decay to a pair of electroweak gauge bosons, with one or two of them being off-shell (three-body and four-body decays respectively). For $m_H = 125$ GeV, the three-body decay dominates, and its partial decay width can be expressed, assuming massless fermions f, as:

$$\Gamma(H \to VV^*) = \frac{3G_F^2 m_V^4}{16\pi^3} m_H \delta_V' R_T(x), \tag{1.47}$$

with $\delta_W' = 1$, $\delta_Z' = \frac{7}{12} - \frac{10}{9}\sin^2\theta_W + \frac{40}{9}\sin^4\theta_W$, and

$$R_T(x) = \frac{3(1 - 8x + 20x^2)}{(4x-1)^{1/2}}\arccos\left(\frac{3x-1}{2x^{3/2}}\right) - \frac{1-x}{2x}(2 - 13x + 47x^2) - \frac{3}{2}(1 - 6x + 4x^2)\ln x. \tag{1.48}$$

Even if massless particles do not couple to the H boson, H boson decays to gg, $Z\gamma$ and $\gamma\gamma$ are allowed through massive particle loops. The $H\gamma\gamma$ and $HZ\gamma$ couplings are mediated by W boson and charged fermion loops, and the Hgg couplings by quark loops.

6. $G_F \simeq 1.17 \times 10^{-5}$ GeV^{-2}. [9]

1.3.4 The SM scalar boson at the LHC

The discovery by the CMS and ATLAS experiments of a new particle, H, compatible with the scalar boson of the SM was announced in July 2012 at CERN [19, 20]; this constituted a triumph for the theory but also for the thousands of experimentalists who had designed and worked on the experiments at the LHC. With a mass of 125 GeV, a large variety of decays are accessible experimentally and can be used to test the compatibility of the new particle with the SM scalar hypothesis. The status of H boson studies after the first run of the LHC is detailed in Chapter 14.

1.4 Chapter summary

The standard model of particle physics

The SM successfully describes the elementary particles, and three of the four fundamental interactions. The recently discovered particle is, given the measurements performed in the first run of the LHC, compatible with the scalar boson of the SM, and all the constituents of the SM have now been observed. With a measured mass of approximately 125 GeV, this boson is supposed to decay to a rich variety of final states, which should be studied to assess the compatibility of the new particle with the SM hypothesis.

Chapter 2

Physics beyond the standard model

The SM has been demonstrated as successful by many measurements performed at high-energy experiments. In particular, the discovery of a new particle compatible with the SM scalar boson, considered as the cornerstone of the SM, has consecrated the theory. However there are strong indications that the SM is only a low-energy expression of a more global theory. If new physics shows up beyond the SM, it could be related to the scalar sector. Some motivations for the existence of BSM physics are detailed in Section 2.1, while two-Higgs-doublet models, supersymmetry including the minimal supersymmetric extension of the SM, and two-Higgs-doublet models extended with a scalar singlet, are presented in Sections 2.2, 2.3 and 2.4 respectively. Section 2.5 discusses how to uncover a possibly extended scalar sector at the LHC, while the chapter ends, in Section 2.6, with a comparison between the reach of precision measurements and direct discovery of new scalars, in a simple benchmark scenario.

2.1 Motivations for new physics

The existence of new physics beyond the SM [7, 21] is strongly motivated. Some motivations are based on direct evidence from observation, such as the existence of neutrino masses, the existence of dark matter and dark energy, or the matter-antimatter asymmetry, while others come from conceptual problems in the SM, such as the large number of free parameters, the "hierarchy problem" or the coupling unification. Each of these issues is shortly described in the next sections.

2.1.1 Neutrino masses

It is well-established by experiments with solar, atmospheric, reactor and accelerator neutrinos, that neutrinos can oscillate and change their flavor in flight [22, 23]. Such oscillations are possible if neutrinos have masses. Flavor neutrinos $(\nu_e, \nu_\mu, \nu_\tau)$ are then linear combinations of the fields of at least three mass eigenstate neutrinos ν_1, ν_2, ν_3. Only upper limits on the neutrino masses have been set as of now ($m_\nu < 2$ eV), but the

differences between the neutrino squared masses have been measured: $\Delta m^2_{12} = (7.53 \pm 0.18) \times 10^{-5}$ eV^2 and $\Delta m^2_{32} = (2.44 \pm 0.06) \times 10^{-3}$ eV^2 [9].

2.1.2 Dark matter and dark energy

In 1933, Zwicky carried measurements of the velocities of galaxies in the Coma cluster, using the Doppler shift of their spectra [24]. With the virial theorem, he could relate these results to the total mass of the Coma cluster. Zwicky also measured the total light output of the cluster, and compared the ratio of the luminosity to the mass for the Coma cluster and for the nearby Kapteyn stellar system. The two orders of magnitude difference between both of them made him conclude that the Coma cluster contains some massive matter that does not radiate: dark matter. The ordinary matter that surrounds us and is described by the SM, only represents 5% of the mass/energy content of the universe. Astrophysical evidence indicates that dark matter contributes approximately to 27%, and dark energy to 68% of this content. Measurements of the temperature and polarization anisotropies of the cosmic microwave background (CMB) by the Planck experiment could determine a density of cold non-baryonic matter [25].
Nowadays little is also known about dark energy, which is responsible for the accelerated expansion of the universe.

2.1.3 Asymmetry between matter and antimatter

It is believed that matter and antimatter were produced in exactly the same quantities at the time of the Big Bang. It is clear however that we are surrounded by matter, and a legitimate question is "How is it possible to explain this preponderance of matter over antimatter?". It is very unlikely that our matter-dominated corner of the universe is balanced by another corner of the universe dominated by antimatter, as this would have been seen as perturbations in the CMB. Sakharov, in 1967, identified the three mechanisms necessary to obtain a global matter/antimatter asymmetry [26]:

- Baryon and lepton number violation;
- Interactions in the universe out of thermal equilibrium at a given moment of the universe history;
- C- and CP-violation (the rate of a process $i \to f$ can be different from the CP-conjugate process $\tilde{i} \to \tilde{f}$).

The SM includes sources of CP-violation, through the residual phase in the CKM matrix, but they are in no way sufficient to explain the magnitude of the matter-antimatter asymmetry observed.

2.1.4 Free parameters in the SM

The SM contains no less than nineteen free parameters, which can be taken as:

- 9 fermion masses (m_e, m_μ, m_τ, m_u, m_d, m_c, m_s, m_t, m_b);
- 3 CKM [1] mixing angles and 1 CP-violating phase;

1. The Cabibbo-Kobayashi-Maskawa (CKM) matrix contains information about the likelihood of weak decays with flavor changing in charged currents.

– 1 electromagnetic coupling constant (g');
– 1 weak coupling constant (g);
– 1 strong coupling constant (g_S);
– 1 QCD vacuum angle;
– 1 vacuum expectation value (v);
– 1 mass for the scalar boson (m_H).

This large number of free parameters, especially in the scalar sector, could be an indication for the existence of a more general and elegant theory than the SM.

2.1.5 Hierarchy problem

The so-called gauge hierarchy problem [27] is related to the huge energy difference between the weak scale and the Planck scale. The weak scale is given by the vev of the Brout-Englert-Higgs field, which is equal to approximately 246 GeV. Radiative corrections to the scalar boson squared mass, coming from its couplings to fermions and gauge bosons, and from its self-couplings, are quadratically proportional to the ultraviolet momentum cutoff Λ_{UV}, which is at least equal to the energy to which the SM is valid without any addition of new physics. If one considers that the SM is valid up to the Planck mass M_P, the quantum correction to m_H^2 is about thirty orders of magnitude larger than m_H^2, which implies that some extraordinary cancellation of terms should happen. Even if these corrections are absorbed in the renormalization process, some may find uncomfortable with this sensitivity to the details of high scales. This is also known as the naturalness problem of the H boson mass.

In particular, the correction to the squared mass of the scalar boson coming from a fermion f that couples directly to the scalar field ϕ with a coupling λ_f is:

$$\Delta m_H^2 = -\frac{|\lambda_f|^2}{8\pi^2}\Lambda_{UV}^2. \tag{2.1}$$

Similarly, some corrections to the mass of the SM scalar boson also arise from scalars. In the case of a scalar particle S with a mass m_S and that couples to the Brout-Englert-Higgs field with a Lagrangian term $-\lambda_S|\phi|^2|S|^2$, the correction to the squared scalar boson mass is:

$$\Delta m_H^2 = \frac{\lambda_S}{16\pi^2}\left[\Lambda_{UV}^2 - 2m_S^2\ln(\Lambda_{UV}/m_S) + ...\right]. \tag{2.2}$$

Again, the correction term to the squared mass is much larger than the squared mass itself. BSM models that avoid this fine-tuning introduce new scalar particles at the TeV scale that couple to the scalar boson, in such a way as to cancel the Λ_{UV}^2 divergence.

Additionally, the large mass differences between fermions, related to Yukawa couplings that can differ by up to six orders of magnitude in the case of the electron and the top quark, constitute the fermion mass hierarchy problem.

2.1.6 Coupling unification

One of the fundamental questions raised by the SM concerns the particular choice of the $SU(3) \times SU(2) \times U(1)$ symmetry group. Additionally, the three forces included in the SM, the weak, the electromagnetic and the strong forces, are treated separately. The intensity of the forces shows an apparent large disparity around the electroweak scale, but at higher energies their coupling constants tend to have comparable strengths. The electromagnetic and weak forces can be unified in a so-called electroweak interaction, but in the SM, the strong coupling constant does not meet the two other coupling constants at high energies. The running of the coupling constants can be modified by the addition of new particles, such as to reach a grand unification.

2.2 Two-Higgs-doublet models

Two-Higgs-doublet models (2HDM) [28] are simple extensions of the SM. They introduce two doublets of scalar fields, which, after symmetry breaking lead to five physical states: two charged scalars $H^{\pm}$, one CP-odd pseudoscalar A and two neutral scalars h and H. Similarly to all models that have extra scalar singlets or doublets relative to the SM, 2HDM satisfy the condition $\rho = m_W/(m_Z \cos\theta_W) = 1$. 2HDM include the minimal supersymmetric extension of the SM (MSSM), which addresses the hierarchy problem and the coupling unification (see Section 2.3). Moreover 2HDM allow for the existence of additional CP-violation sources with respect to the SM, which could explain the baryon asymmetry in the universe. Finally, 2HDM are a simple extension of the SM in the scalar sector, and there is no strong motivation against adding an additional scalar doublet to the SM.

2.2.1 Formalism

The most general gauge invariant form of the scalar potential V in 2HDM can be written as [6, 28]:

$$\begin{aligned} V = {} & m_{11}^2 \phi_1^\dagger \phi_1 + m_{22}^2 \phi_2^\dagger \phi_2 - m_{12}^2 \left(\phi_1^\dagger \phi_2 + \phi_2^\dagger \phi_1 \right) + \frac{\lambda_1}{2} \left(\phi_1^\dagger \phi_1 \right)^2 \\ & + \frac{\lambda_2}{2} \left(\phi_2^\dagger \phi_2 \right)^2 + \lambda_3 \phi_1^\dagger \phi_1 \phi_2^\dagger \phi_2 + \lambda_4 \phi_1^\dagger \phi_2 \phi_2^\dagger \phi_1 \\ & + \left\{ \frac{\lambda_5}{2} \left(\phi_1^\dagger \phi_2 \right)^2 + \left[\lambda_6 \left(\phi_1^\dagger \phi_1 \right) + \lambda_7 \left(\phi_2^\dagger \phi_2 \right) \right] \phi_1^\dagger \phi_2 + h.c. \right\}. \end{aligned} \tag{2.3}$$

Under the widely-used assumptions that CP is conserved in the scalar sector and not spontaneously broken, and that all quartic terms odd in either of the doublets are eliminated by discrete symmetries, the expression can be simplified as:

$$\begin{aligned} V = {} & m_{11}^2 \phi_1^\dagger \phi_1 + m_{22}^2 \phi_2^\dagger \phi_2 - m_{12}^2 \left(\phi_1^\dagger \phi_2 + \phi_2^\dagger \phi_1 \right) + \frac{\lambda_1}{2} \left(\phi_1^\dagger \phi_1 \right)^2 + \frac{\lambda_2}{2} \left(\phi_2^\dagger \phi_2 \right)^2 \\ & + \lambda_3 \phi_1^\dagger \phi_1 \phi_2^\dagger \phi_2 + \lambda_4 \phi_1^\dagger \phi_2 \phi_2^\dagger \phi_1 + \frac{\lambda_5}{2} \left[\left(\phi_1^\dagger \phi_2 \right)^2 + \left(\phi_2^\dagger \phi_1 \right)^2 \right], \end{aligned} \tag{2.4}$$

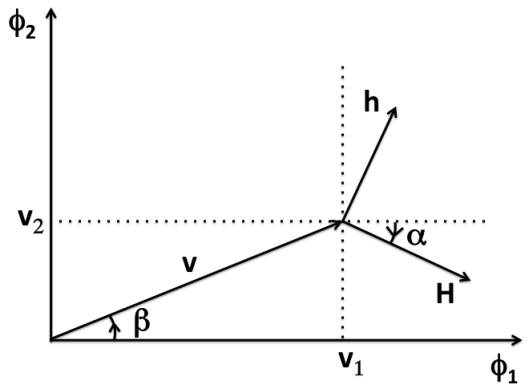

Figure 2.1: Schematic view of the two angle parameters of 2HDM. The parameter $\tan\beta$ is the ratio between the vacuum expectation values of the two doublets ϕ_1 and ϕ_2, whereas α is the mixing angle between the neutral scalars. The vacuum expectation value $v = 246$ GeV can be decomposed in two components v_1 and v_2 along the doublets ϕ_1 and ϕ_2 respectively. Adapted from [30].

where all the parameters are real.

The minima of the ϕ_1 and ϕ_2 doublets are respectively $\begin{pmatrix} 0 \\ v_1/\sqrt{2} \end{pmatrix}$ and $\begin{pmatrix} 0 \\ v_2/\sqrt{2} \end{pmatrix}$. The ratio of the vacuum expectation values of the two doublets is written as:

$$\tan\beta = \frac{v_2}{v_1}. \tag{2.5}$$

The squared mass matrix of the neutral scalars can be diagonalized to obtain the physical states h and H; the rotation angle performing the diagonalization is called α. The angle β defined in equation (2.5) can also be seen as the angle diagonalizing the squared mass matrices of the charged scalars and of the pseudoscalars (one massive pseudoscalar A and one massless Goldstone boson). Without loss of generality, β can be chosen in the first quadrant, whereas α is either in the first or in the fourth quadrant [29]. The meaning of the angles α and β is illustrated in Fig. 2.1.

The scalar couplings to gauge bosons and fermions in 2HDM can be expressed as a function of the two parameters α and $\tan\beta$. There are four types of 2DHM that do not violate flavor conservation in neutral current interactions; the condition for avoiding flavor changing neutral currents being that all fermions with the same quantum numbers couple to a same scalar multiplet [31]. A Z_2 symmetry ($\phi_1 \to +\phi_1$, $\phi_2 \to -\phi_2$) can be found to ensure that only these interactions exist. The Z_2 symmetry is softly broken if the term m_{12}^2 is non-zero [32]. As shown in Tab. 2.1, the difference between the four types lies in the doublets to which the charged leptons, up-type quarks and down-type quarks couple. Type-1 is the easiest of them and is the most SM-like: leptons, up-type quarks and down-type quarks all couple to the same doublet, ϕ_1. In type-2, the leptons and

down-type quarks couple to ϕ_2, whereas up-type quarks couple to ϕ_1. In the so-called "lepton-specific" type-3, all quarks couple to ϕ_1 and leptons to ϕ_2. Finally in the flipped type-4 model, leptons and up-type quarks couple to ϕ_1 while down-type quarks couple to ϕ_2. In a general way, the intensity of the couplings in the different scenarios are functions of both α and β as presented in Tab. 2.2.

	Type-1	Type-2	Type-3 (lepton specific)	Type-4 (flipped)
ℓ	ϕ_2	ϕ_1	ϕ_1	ϕ_2
u	ϕ_2	ϕ_2	ϕ_2	ϕ_2
d	ϕ_2	ϕ_1	ϕ_2	ϕ_1

Table 2.1: Scalar doublet to which the leptons ℓ, up-type quarks u and down-type quarks d couple in the different types of 2HDM.

Particle	Coupling	Type-1	Type-2	Type-3 (lepton specific)	Type-4 (flipped)
h	g_{hVV}	$\sin(\beta-\alpha)$	$\sin(\beta-\alpha)$	$\sin(\beta-\alpha)$	$\sin(\beta-\alpha)$
	$g_{hu\bar{u}}$	$\cos\alpha/\sin\beta$	$\cos\alpha/\sin\beta$	$\cos\alpha/\sin\beta$	$\cos\alpha/\sin\beta$
	$g_{hd\bar{d}}$	$\cos\alpha/\sin\beta$	$-\sin\alpha/\cos\beta$	$\cos\alpha/\sin\beta$	$-\sin\alpha/\cos\beta$
	$g_{h\ell\bar{\ell}}$	$\cos\alpha/\sin\beta$	$-\sin\alpha/\cos\beta$	$-\sin\alpha/\cos\beta$	$\cos\alpha/\sin\beta$
H	g_{HVV}	$\cos(\beta-\alpha)$	$\cos(\beta-\alpha)$	$\cos(\beta-\alpha)$	$\cos(\beta-\alpha)$
	$g_{Hu\bar{u}}$	$\sin\alpha/\sin\beta$	$\sin\alpha/\sin\beta$	$\sin\alpha/\sin\beta$	$\sin\alpha/\sin\beta$
	$g_{Hd\bar{d}}$	$\sin\alpha/\sin\beta$	$\cos\alpha/\cos\beta$	$\sin\alpha/\sin\beta$	$\cos\alpha/\cos\beta$
	$g_{H\ell\bar{\ell}}$	$\sin\alpha/\sin\beta$	$\cos\alpha/\cos\beta$	$\cos\alpha/\cos\beta$	$\sin\alpha/\sin\beta$
A	g_{AVV}	0	0	0	0
	$g_{Au\bar{u}}$	$\cot\beta$	$\cot\beta$	$\cot\beta$	$\cot\beta$
	$g_{Ad\bar{d}}$	$-\cot\beta$	$\tan\beta$	$-\cot\beta$	$\tan\beta$
	$g_{A\ell\bar{\ell}}$	$-\cot\beta$	$\tan\beta$	$\tan\beta$	$-\cot\beta$

Table 2.2: Yukawa couplings of vector bosons V, up-type quarks u, down-type quarks d and leptons ℓ to the neutral scalars and pseudoscalar in the four types of 2HDM without flavor changing neutral currents. The Yukawa couplings to the charged scalars can be determined from the couplings of to the neutral pseudoscalar. [28]

2.2.2 Decoupling and alignment limits

In the SM, there is one neutral scalar boson, while there are two (h and H) in 2HDM. The lightest neutral scalar of 2HDM is in all generality not identical to the one of the SM, which points to the possibility of determining with property measurements whether the new observed particle belongs to the SM or to 2HDM. As of now, the measured properties of the 125 GeV-state are all compatible with the SM hypothesis within experimental uncertainties. However the 2HDM hypothesis is not ruled out, as there are two important scenarios where the neutral h of 2HDM tends to be SM-like: the decoupling and the alignment limits [33, 34]:

– In the decoupling limit, the mass of the H, A and $H^{\pm}$ all are much larger than the h mass, which causes h to have SM-like couplings. Indeed, if there are two very different mass scales $m_L \ll m_S$ such that $m_h \simeq m_L$ and $m_H, m_{H^{\pm}}, m_A \simeq m_S$, a low mass effective theory can be derived and corresponds to the SM because the m_S-related effects have been integrated out. The decoupling limit implies $\cos(\beta-\alpha) \simeq 0$.

– In the alignment limit, the whole vacuum expectation value (246 GeV) lies in the neutral component of only one of the scalar doublets, and the mixing between the h and H states disappears, which causes one of the neutral mass eigenstates to align with the direction of the scalar field vacuum expectation value and to become SM-like. In this case, the H, A and $H^{\pm}$ particles are not necessarily heavy. The alignment limit corresponds to $\cos(\beta-\alpha) \simeq 0$, and is more general than the decoupling limit.

In Fig. 2.1, the equality $\cos(\beta-\alpha) = 0$, which is satisfied both in the decoupling and the alignment limits, corresponds to the alignment of the state h along the vacuum expectation value v.

2.2.3 Light scalars in 2HDM

In 2HDM, in the alignment limit, one of the neutral scalars (h) can be SM-like, while the pseudoscalar A can be lighter than 125/2 GeV. In the case where the branching fraction of the SM-like scalar to two light pseudoscalars is limited ($\mathcal{B}(h \to AA)$ less than about 0.3), such a topology is still allowed by the limited precision measurements made on the 125-GeV state at the LHC. The branching fraction $\mathcal{B}(h \to AA)$ can be small in the alignment limit when the mass mixing parameter m_{12} has a modest value. Another case where $\mathcal{B}(h \to AA)$ is allowed to take small values with larger m_{12} is when $\sin(\beta+\alpha) \simeq 1$; this relation is compatible with the measured $h \to VV$ signal strength when $\tan\beta$ is large (> 5). When $\sin(\beta+\alpha) \simeq 1$, $\sin\alpha$ has to be positive, which, in the type-2 of 2HDM, leads to a so-called "wrong sign" Yukawa coupling of the SM-like h boson to down-type quarks and leptons (see Tab. 2.2).

The production cross section of light pseudoscalars at the LHC can be large [35]. Fig. 2.2 illustrates the viable production cross sections for the gluon-gluon fusion production (ggA) and the production in association with b quarks (bbA) of the pseudoscalar boson A, in type-1 and type-2 of 2HDM. The two scenarios that give small $\mathcal{B}(h \to AA)$ are shown. It can be seen that the largest cross section times branching ratio for A decays to tau leptons is achieved in 2HDM type-2 in the wrong-sign Yukawa coupling scenario.

2.3 Supersymmetry

Supersymmetry (SUSY) [36–38] is a symmetry that relates bosons and fermions. The SUSY operator Q, an anticommuting spinor, transforms a fermionic field F into a bosonic field B and vice-versa:

$$Q|B\rangle = F \text{ and } Q|F\rangle = B. \tag{2.6}$$

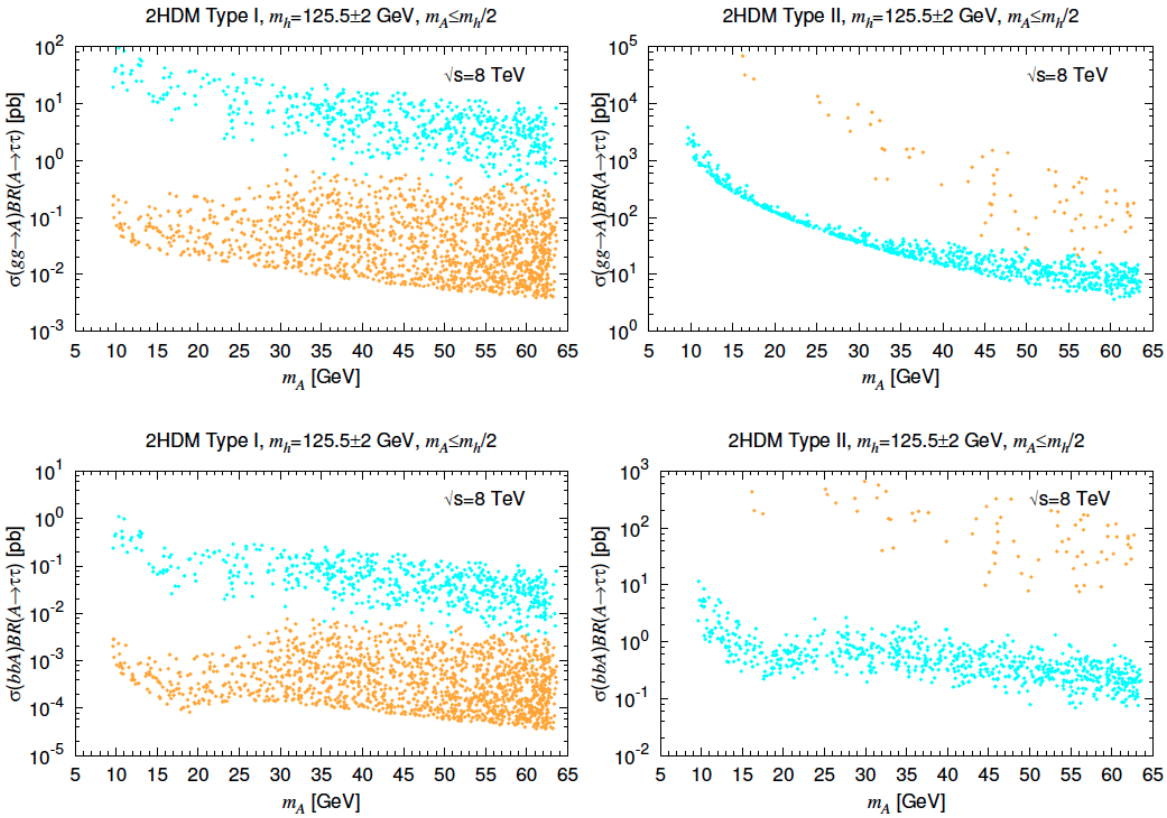

Figure 2.2: Viable production cross sections for the ggA (top) and bbA (bottom) productions at a center-of-mass energy of 8 TeV, times the branching fraction for A decay to a pair of tau leptons in type-1 (left) and type-2 (right) 2HDM. The cyan points have $\sin(\beta-\alpha) \simeq 1$, $\cos(\beta-\alpha) > 0$ and modest m_{12}, whereas orange points have $\sin(\beta+\alpha) \simeq 1$ and $\tan\beta > 5$, and correspond to the wrong-sign Yukawa coupling scenario. The largest production cross sections times branching fraction are obtained in 2HDM type-2 with wrong-sign Yukawa couplings. [35]

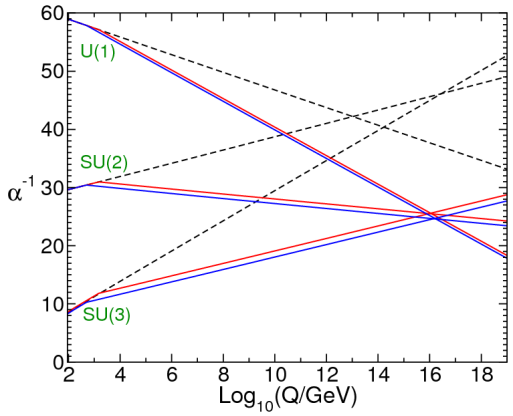

Figure 2.3: Evolution of the $U(1)_Y$, $SU(2)_L$ and $SU(3)_C$ couplings in the SM (dashed lines), and in two MSSM scenarios (solid lines). Unlike the SM case, the three couplings can be unified at a high energy scale in the MSSM. [36]

A new quantum number R can be introduced to enforce baryon number and lepton number conservation:

$$R = (-1)^{2S+3(B-L)}, \tag{2.7}$$

where S, B and L are respectively the spin, lepton and baryon numbers. With this definition, all SM particles have $R = +1$ and all their superpartners have $R = -1$. R is usually assumed to be conserved in such a way as to forbid fast rates of proton decays. The R-parity conservation implies that supersymmetric particles can only be produced in pairs and that the lightest supersymmetric particle (LSP) is stable. This LSP is an excellent dark matter candidate.

One of the main motivations for the existence of SUSY is the solution to the hierarchy problem. Because fermion loops and boson loops have opposite signs, and SUSY associates a new boson to each fermion and vice-versa, the Λ_{UV}^2 terms in equations (2.1) and (2.2) can exactly cancel for each fermion-scalar pair. Additionally, SUSY can unify the electromagnetic, weak and strong forces below the Planck scale, as illustrated in the case of the minimal supersymmetric extension of the SM (see Section 2.3.1) in Fig. 2.3.

Individual particles are grouped in supermultiplets. As the supersymmetric operators Q and $Q^\dagger$ commute with the generators of gauge transformations, particles sharing a same supermultiplet have the same electric charge, weak isospin and color degrees of freedom. In addition, because the same operators also commute with the squared-mass operator $-P^2$, the fermions and bosons in a same supermultiplet should have the same mass. The last point is however known not to be true in reality, because superpartners at the electroweak scale would already have been observed at colliders. If superparticles are heavier than SM particles, which would explain why they have not been discovered yet,

SUSY must be broken. For radiative corrections not to exceed typical scalar masses, the SUSY breaking scale should be limited to a few TeV.

2.3.1 Minimal supersymmetric extension of the SM (MSSM)

In the minimal supersymmetric extension of the SM (MSSM) [39–41], there exist two types of supermultiplets: vector supermultiplets, where a spin-1 vector boson is associated to a spin-1/2 Weyl fermion, and chiral supermultiplets, where a single Weyl fermion is associated to a complex scalar field. The particle content of the MSSM is shown in Tab. 2.3 and 2.4. The superpartners of quarks are called squarks, while the superpartners of leptons are called sleptons. The bino, the neutral wino and the higgsinos mix to form four neutralinos ($\tilde{\chi}_1^0$, $\tilde{\chi}_2^0$, $\tilde{\chi}_3^0$ and $\tilde{\chi}_4^0$), while the winos and charged higgsinos mix to form four charginos ($\tilde{\chi}_1^\pm$ and $\tilde{\chi}_2^\pm$). Two chiral superfields, (H_1^+, H_1^0) and (H_2^0, H_2^-), with hypercharges +1/2 and -1/2 as seen in Tab. 2.3, are necessary to cancel chiral anomalies.

Particles	Spin-0	Spin-1/2	$(SU(3)_C, SU(2)_L, U(1)_Y)$
quark, squark	$(\tilde{u}_{iL}, \tilde{d}_{iL})$	(u_{iL}, d_{iL})	(3,2,+1/6)
	$\tilde{u}_{iR}^*$	$u_{iR}^\dagger$	(3*,1,-2/3)
	$\tilde{d}_{iR}^*$	$d_{iR}^\dagger$	(3*,1,+1/3)
lepton, slepton	$(\tilde{e}_{iL}, \tilde{\nu}_{iL})$	(e_{iL}, ν_{iL})	(1,2,-1/2)
	$\tilde{e}_{iR}^*$	$e_{iR}^\dagger$	(1,1,+1)
H, higgsino	(H_1^+, H_1^0)	$(\tilde{H}_1^+, \tilde{H}_1^-)$	(1,2,+1/2)
	(H_2^0, H_2^-)	$(\tilde{H}_2^0, \tilde{H}_2^-)$	(1,2,-1/2)

Table 2.3: MSSM chiral supermultiplets.

Particles	Spin-1/2	Spin-1	$(SU(3)_C, SU(2)_L, U(1)_Y)$
gluino, gluon	$\tilde{g}$	g	(8,1,0)
wino, W boson	$\tilde{W}^\pm, \tilde{W}^0$	$W^\pm, W^0$	(1,3,0)
bino, B boson	$\tilde{B}^0$	B^0	(1,1,0)

Table 2.4: MSSM vector supermultiplets.

The MSSM is a particular case of 2HDM type-2. The main specificities in the scalar sector are that, in the MSSM, the mass of the lightest scalar is constrained by some upper bounds, the scalar self-couplings are specified, α and β are not independent from each other, and the decay of the charged scalars $H^\pm$ to a pseudoscalar A and a W boson is kinematically forbidden because $m_{H^\pm} \simeq m_A$ [28].

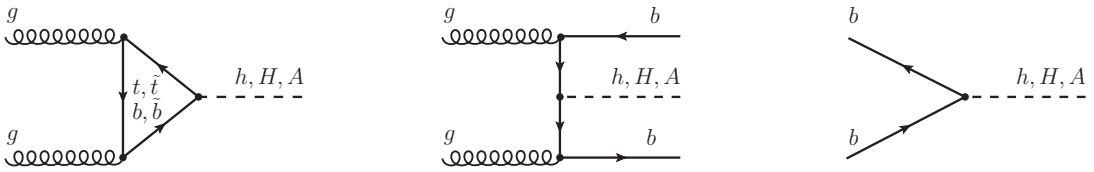

Figure 2.4: Feynman diagrams for the production of neutral scalars in the MSSM, in gluon-gluon fusion (left), and production with b quarks (center and right). [42]

2.3.2 Scalar sector in the MSSM

In the MSSM, neutral scalars $\Phi = H/A/h$ can be produced by two mechanisms: gluon-gluon fusion ($gg\Phi$) and production with b quarks ($bb\Phi$). Characteristic Feynman diagrams for such processes are shown in Fig 2.4, where the $bb\Phi$ mechanism is shown in two different schemes of proton parton distribution functions. The $bb\Phi$ production cross section is increased at large $\tan\beta$ because of the enhanced Yukawa couplings to down-type fermions.

At tree level in the MSSM, the only two free parameters can be taken as the mass of the pseudoscalar, m_A, and $\tan\beta$. The masses of the neutral scalars and of the charged scalars, as well as the angle α can be expressed as [43]:

$$m^2_{h/H} = \frac{1}{2}\left(m^2_A + m^2_Z \mp \sqrt{(m^2_A + m^2_Z)^2 - 4m^2_A m^2_Z \cos^2 2\beta}\right), \tag{2.8}$$

$$m^2_{H^\pm} = m^2_A + m^2_W, \text{ and} \tag{2.9}$$

$$\tan 2\alpha = \tan 2\beta \left(\frac{m^2_A + m^2_Z}{m^2_A - m^2_Z}\right) \text{ with } -\frac{\pi}{2} \leq \alpha \leq 0. \tag{2.10}$$

This leads to:

$$m_h \leq \min(m_A, m_Z) \times |\cos 2\beta| \leq m_Z. \tag{2.11}$$

The mass of the lightest neutral scalar is thus inferior to the Z boson mass, which is excluded by LEP bounds and does not correspond to the observation of the 125-GeV scalar at the LHC. Fortunately, radiative corrections above tree level, essentially loop corrections due to top and stop quarks, enable the h scalar to be as heavy as approximately 135 GeV. In the case where m_A is much larger than the Z boson mass, the relations above give:

$$m_H \simeq m_{H^\pm} \simeq m_A \text{ and } \alpha \simeq \beta - \frac{\pi}{2}, \tag{2.12}$$

which is the decoupling limit as seen in Section 2.2.2.

The phenomenology of the scalar sector of the MSSM can be described by two parameters: the mass of the pseudoscalar m_A, and $\tan\beta$. It is generally assumed that $\tan\beta$ lies approximately between 1 and 60, where 60 is the ratio between the top quark mass and the bottom quark mass. Above tree level, more parameters appear and some benchmark

scenarios fixing these parameters can be studied. It has been shown however that, taking into account the mass measured for the h boson, the MSSM can be approximately reparameterized as a function of m_A and $\tan\beta$, in the so-called hMSSM [44]. One can distinguish three regions of the parameter space, where the search strategies will differ: the low m_A, the high $\tan\beta$ and the low $\tan\beta$ regions. It has been shown in [44] that the full parameter space of the MSSM could be almost entirely covered in the search for additional scalars at the LHC at 14 TeV with a luminosity of 300 fb^{-1}, while a good part of the parameter space has already been explored in LHC searches at 7 and 8 TeV, as shown in Fig. 2.5.

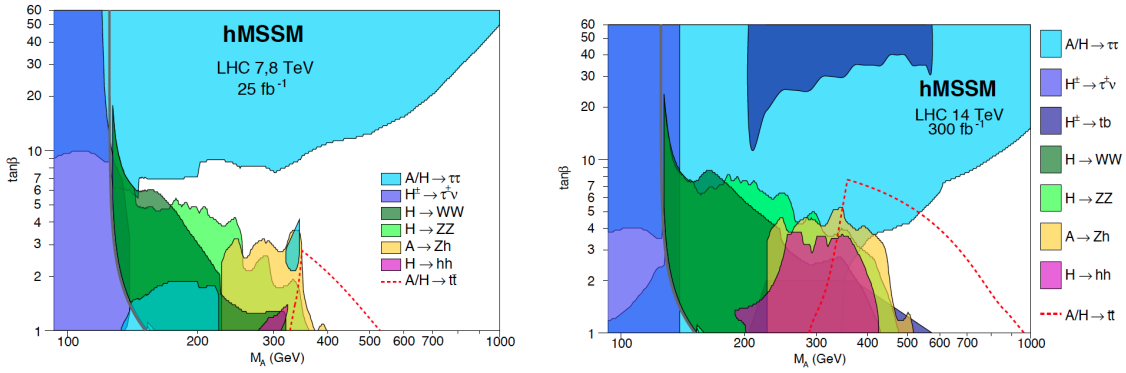

Figure 2.5: Sensitivity of MSSM scalar searches at the LHC at 7 and 8 TeV in LHC Run-1 (left) and projection with 300 fb^{-1} of 14 TeV data collected at the LHC (right), in the context of the hMSSM parameterization. The $A \to t\bar{t}$ search (dashed red line) has not yet been performed at the LHC, and the sensitivity is predicted. The exclusion limit of the $A \to \tau\tau$ analysis around $m_A = 350$ GeV and $2 < \tan\beta < 4$ is due to the strong increase of the $gg \to A$ cross section at the $t\bar{t}$ threshold, coupled to the suppression of $A \to Zh$ decays and enhanced couplings to down-type quarks and leptons because $\tan\beta > 1$. The hMSSM scenario takes into account the mass measured for the new SM-like scalar. [44]

Low m_A region

At low m_A, the most powerful channel to search for an MSSM scalar sector is clearly $H^+ \to \tau^+\nu_\tau$ (and its charge conjugate decay). The limits shown in Fig. 2.5 correspond to the $t \to H^+b$ production, for charged scalar masses below the difference of the top quark and bottom quark masses.

High $\tan\beta$ region

In the region of the parameter space where $\tan\beta$ is large, say $\tan\beta > 5$, the most sensitive final state to search for new heavy resonances Φ is by far $\Phi = A/H/h \to \tau\tau$. The reason for this is that the couplings to leptons and down-type quarks are enhanced with increased $\tan\beta$, because these particles couple to the second scalar doublet (see Tab. 2.1). In addition, for the same reason, the production cross section for the Φ resonance in association with bottom quarks is also enhanced at large $\tan\beta$. Even if the

decay branching fraction of the resonance to bottom quarks remains larger (approximately nine times higher), the experimental difficulties, such as the distinction between b jets and other flavor jets, make the channel $\Phi \to bb$ less sensitive. Finally, the channel $\Phi \to \mu\mu$ also has some potential, but is hurt by its low decay branching fraction: $\mathcal{B}(\Phi \to \mu\mu) \simeq \mathcal{B}(\Phi \to \tau\tau) \times m_\mu^2/m_\tau^2$.

Low $\tan\beta$ region

The phenomenology in the low $\tan\beta$ region is much richer than in the high $\tan\beta$ region. Experimentally, one interesting decay of the A pseudoscalar to study is $A \to Zh$, in the intermediate mass range $m_Z + m_h < m_A < 2m_t$, as seen in Fig. 2.6. If the Z boson decays leptonically, it is possible to achieve a good background reduction, and the most favorable h decays in terms of branching fractions, $h \to bb$ and $h \to \tau\tau$, can be targeted. At higher m_A, the $A \to t\bar{t}$ channel opens, but, due to interference effects with the SM backgrounds, it is experimentally a difficult channel. The dominant H decay channel in the intermediate mass range $2m_h < m_H < 2m_t$ is $H \to hh$, whereas there are also non negligible contributions from $H \to WW$ and $H \to ZZ$. Outside of the low m_A region described previously, for $m_{H^\pm} > m_t + m_b$, the charged scalars $H^\pm$ almost exclusively decay to a top and a b quarks.

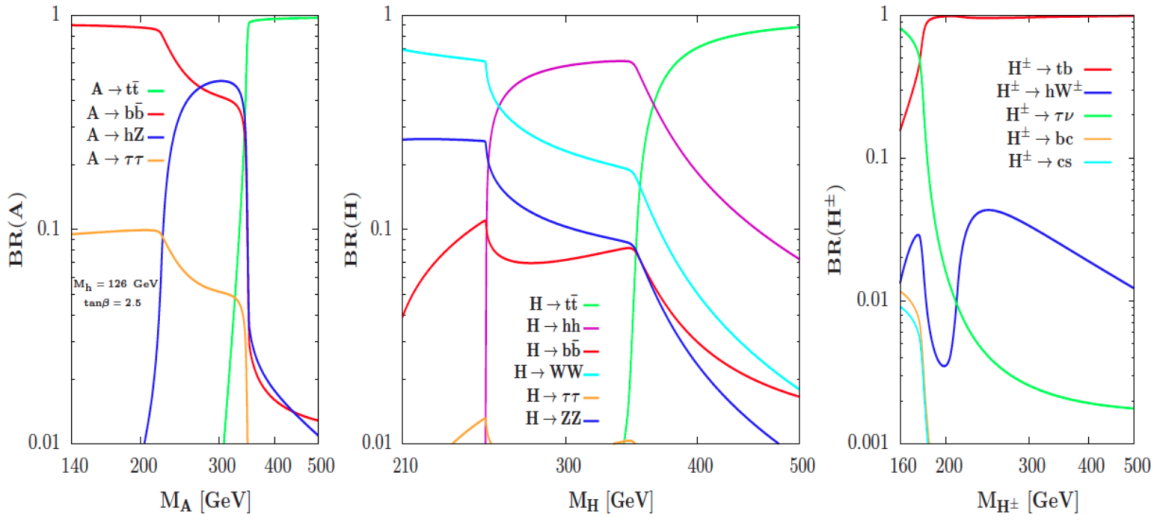

Figure 2.6: Branching fractions of the A, H and $H^\pm$ scalars in the MSSM as a function of their masses, for $\tan\beta = 2.5$ and $m_h = 126$ GeV. [45]

2.4 Two-Higgs-doublet models + a singlet

2.4.1 Introduction to 2HDM+S

The extensions of 2HDM where a complex scalar singlet is added to the already present scalar doublets, are called 2HDM+S. Because of the additional singlet, two new bosons are

introduced. The next–to-minimal supersymmetric extension of the SM (NMSSM) [46, 47] (for a review, see [48]) is a case of 2HDM+S type-2 and is the easiest extension of the MSSM. The supersymmetric potential in the MSSM contains a mass parameter μ in the expression $\mu\phi_1\phi_2$, which has to be at the SUSY breaking scale (m_{SUSY}). The fact that μ is at a scale well below the Planck scale without any theoretical reason, constitutes the so-called μ problem [49]. This problem disappears in the NMSSM, where an effective mass is generated via a coupling to the complex scalar field associated to the new singlet; this is a strong motivation for the existence of the NMSSM over the MSSM. Another motivation comes from the fact that new scalar particles contribute to the mass of the scalar boson h in the NMSSM, which removes the tensions in the MSSM originating from the large measured mass of the new particle.

2.4.2 Exotic decays of the 125-GeV particle

In 2HDM+S, the h boson, identified as the 125-GeV particle discovered in 2012, can decay exotically to non-SM particles. Even though decays of the h boson of 2HDM to non-SM particles are theoretically allowed, the 2HDM parameter space is by now extremely constrained by LHC searches. However, in 2HDM+S, a wide range of exotic decays of the 125-GeV boson is still allowed after the Run-1 of the LHC. The singlet added to 2HDM does not have Yukawa couplings of its own, and only couples to ϕ_1 and ϕ_2 in the potential, from which it inherits its couplings to SM fermions. To keep the scalar h SM-like, the mixing with the singlet S needs to be small. The imaginary part of the singlet gives rise to a pseudoscalar a (after a small mixing with the pseudoscalar A), and the real part to a scalar s (after mixing with H and h). Exotic decays of the type $h \to aa$, $h \to ss$ or $h \to Za$ are then possible.

In the pseudoscalar case, the light pseudoscalar a, mostly singlet-like, inherits its couplings to fermions from the heavy pseudoscalar A. As in the case of general 2HDM, the four types of 2HDM+S lead to different scenarios and give rise to many exploitable signatures for exotic h decays at the LHC:

- Type-1: All fermions couple to ϕ_1, and therefore the branching fractions of the pseudoscalar are proportional to those in the SM, without any dependence on $\tan\beta$.
- Type-2: Leptons and down-type quarks couple to the same doublet, as in the MSSM. For values of $\tan\beta$ larger than unity, the branching fractions of the pseudoscalar to leptons and down-type quarks are enhanced, which makes $h \to aa \to bbbb$, $h \to aa \to \mu\mu bb$ and $h \to aa \to \tau\tau bb$ interesting channels to search for exotic h decays.
- Type-3 (lepton-specific): Leptons couple to the ϕ_2 doublet contrarily to quarks, which means that the branching fractions for pseudoscalar decays to leptons increase for large values of $\tan\beta$. In this scenario with large $\tan\beta$, $h \to aa \to \mu\mu\tau\tau$ and $h \to aa \to \tau\tau\tau\tau$ are favoured channels when kinematically allowed.
- Type-4 (flipped): Pseudoscalar decays to leptons and up-type quarks are enhanced with respect to down-type quarks when $\tan\beta > 1$. In this case, $h \to aa \to \tau\tau cc$ and $h \to aa \to \tau\tau bb$ can be interesting channels.

2.5 Search for BSM physics in the scalar sector

The scalar sector is a favored place to look for new physics, because it is described much less elegantly than the other parts of the SM as most free parameters of the theory are related to the scalar interaction. The existence of a Higgs-portal [50], where the scalar sector is the only one to interact with BSM physics, is strongly motivated. Complementary ways exist to point to the existence of BSM physics in the scalar sector:

1. Precision measurements of the properties of the 125-GeV scalar boson, that would reveal deviations from the SM;
2. Direct discovery of new scalar particles;
3. Discovery of BSM decays of the 125-GeV scalar boson;
4. Observation of BSM physics in signatures involving scalar bosons.

A review about the complementarity between precision measurements and direct searches in the MSSM can be found in [51]. The four points are detailed below:

– **Precision measurements:** The properties of the lightest scalar h of 2HDM can deviate from the properties of the SM scalar boson; precision measurements of the 125-GeV state therefore should make the distinction between 2HDM and SM possible. However, as seen in Section 2.2.2, many extended sector scalar models have a decoupling or an alignment limit, which makes the properties of the h boson of 2HDM very close to those of the SM scalar boson. Fig. 2.7 illustrates the dependence of the production cross section of the MSSM h boson as a function of the mass of the pseudoscalar A for a given $\tan\beta$, as well as the ratio between the decay branching fractions of the MSSM h and the SM scalar boson. As expected according to the decoupling limit, the branching fractions tend to be very similar in the two scenarios when the mass of the pseudoscalar increases, and a great precision is needed to highlight deviation from the SM. The measurement of the properties of the discovered 125 GeV-boson in the decay channel to tau leptons is presented in Chapter 7.

– **Direct discovery of new scalar particles:** Discovering new scalar particles would be a direct evidence of BSM physics. Many searches for extra scalars, in the context of general 2HDM or MSSM for example, are performed at the LHC. The search for a heavy neutral scalar decaying to a pair of tau-leptons is described in Chapter 13, while the search for the heavy pseudoscalar A of the MSSM, decaying to a Z and a SM-like h bosons is described in Chapter 10. Light bosons with a mass lighter than the Z boson could also be discovered at the LHC; Chapter 12 details the search for such a particle in its decays to tau leptons. Many other searches exist at the LHC but are not described in this thesis, such as the search for charged scalars.

– **Discovery of BSM decays of the 125-GeV scalar boson**: Motivations for the existence of exotic decays of the 125-GeV boson to non-SM particles are various [52, 53]. First, the SM scalar boson has an extremely narrow width ($\Gamma \simeq 4.07$

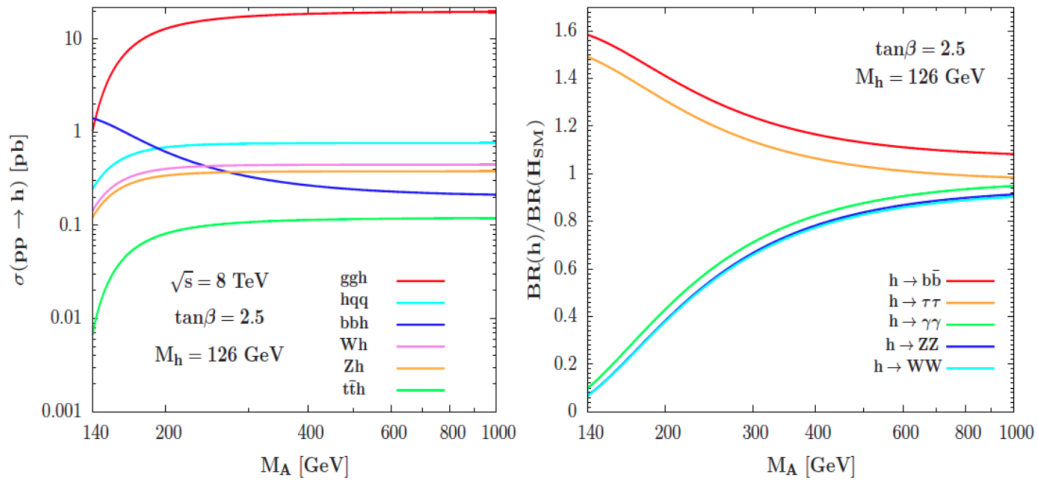

Figure 2.7: Left: Production cross sections of the MSSM h boson at 8 TeV, for $\tan\beta = 2.5$. Right: Evolution of the decay branching ratios of the h scalars in the MSSM and SM as a function of the pseudoscalar mass m_A, for $\tan\beta = 2.5$. [45]

MeV) compared to its mass, because of the suppression of tree-level Yukawa couplings. Given that the coupling to two b quarks has the small value of approximately 0.02, the coupling, even small, to another light state could open non negligible decay modes. Second, the scalar sector could be a portal to new physics, which allows SM matter to interact with a hidden-sector matter. If there exists a Higgs portal, the hidden-sector matter does not have to be charged under SM forces. And finally, exotic scalar decays are a relatively simple extension of the SM, and are still allowed after all the measurements made during LHC Run-1. Indeed an upper limit on the branching fraction of the 125-GeV boson to BSM particles can be set experimentally and, as of today, this upper limit leaves a large room for exotic decays. In particular, CMS measured $\mathcal{B}(H \to \text{BSM}) < 30\%$ at 95% CL, using all data collected during LHC Run-1 [54]. Projections for future LHC runs give a final precision on $\mathcal{B}(H \to \text{BSM})$ of the order of 10%, which still allows for non negligible decays of the 125-GeV particle. The variety of possible BSM decays is extremely large. A group of searches among others explores the possibility for the h boson to decay to invisible particles, resulting in missing transverse energy in the detector. A search for exotic decays with SM particles in the final state is presented in Chapter 11.

– **Observation of BSM physics in signatures involving scalar bosons:** Scalar bosons could be produced in some BSM physics processes. An example of such a process is a squark-gluino production with subsequent cascade decays via neutralinos into the h_1 boson of the NMSSM; the corresponding Feynman diagram is shown in Fig. 2.8. This method to look for an extended scalar sector is not explored in this thesis.

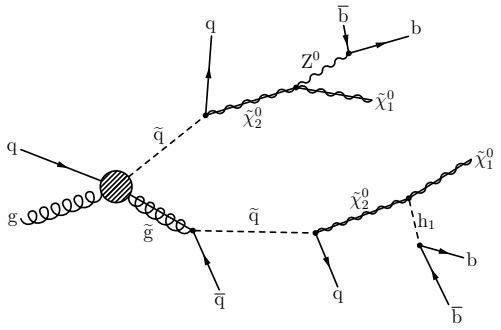

Figure 2.8: Feynman diagram of quark-gluino production with subsequent cascade decays via neutralinos into the h_1 boson of the NMSSM. [55]

2.6 Precision measurements vs. direct discovery in the case of the SM+S

To compare the reach of precision measurements and direct discovery of new scalars, one can take the simple case where a real scalar singlet S is added to the usual scalar doublet ϕ of the SM [56]. After symmetry breaking, the singlet mixes with the doublet with a mixing angle α, resulting in two neutral mass eigenstates H_1 and H_2:

$$H_1 = \phi \cos\alpha + S \sin\alpha, \tag{2.13}$$

$$H_2 = -\phi \sin\alpha + S \cos\alpha, \tag{2.14}$$

where H_1 has a mass $m_1 = 125$ GeV and H_2 a mass m_2 lower or greater than 125 GeV. The H_1 and H_2 states interact only via their ϕ component. The case where the new particle interacts only through mixing is studied here. While the decay modes and branching fractions of the new states are the same as predicted for the scalar boson in the SM at their respective masses m_1 and m_2, their production rates are however scaled by factors $\cos^2\alpha$ in the case of H_1 and $\sin^2\alpha$ in the case of H_2. The decay $H_2 \to H_1 H_1$ should be taken into account when kinematically allowed.

The SM+S benchmark model can be represented by the equality $\cos^2\alpha + \sin^2\alpha = 1$, as shown in Fig. 2.9 (left) with the continuous blue line. Precision measurements of the signal strength of the 125-GeV state give some constraints on the parameter $\cos^2\alpha$, which scales the H_1 production cross section; the measured signal strength, when lower than one, is equivalent to the measured $\cos^2\alpha$. The best-fit signal strength was measured to be $\hat{\mu} = 0.80 \pm 0.14$ (where the uncertainties correspond to one standard deviation) in 2013 [57]; this value is represented together with its uncertainty by the horizontal pink lines in Fig. 2.9 (left). In a first approximation, the uncertainty band can be doubled to correspond to uncertainties at the level of two standard deviations. On the other hand, searches for extra scalars with masses different from 125 GeV can set constraints on $\sin^2\alpha$;

the upper limit on the signal strength at a given mass, if lower than one, is equivalent to an upper limit on $\sin^2\alpha$ at that same mass. Limits from searches for additional scalars with masses between 100 and 800 GeV [57–60] are shown in Fig. 2.9 (left) with the vertical dashed lines. This makes it possible to compare the reach of the two approaches, using the CMS data collected during Run-1 and presented at the HCP12 conference. It can be seen in the figure that in this particular benchmark model, in most part of the accessible mass range, namely between 125 and 600 GeV, the direct detection is a more powerful approach than precision measurements.

The limit on $\cos^2\alpha$ obtained by the precision measurements on the signal strength of the 125-GeV state can be converted to a limit on $\sin^2\alpha$ for all m_2. In the right part of Fig. 2.9, the upper limits on $\sin^2\alpha$ are superimposed to the constraint from the precision measurement (uncertainty at two standard deviations level), for all masses m_2 probed at the LHC. Also superimposed is the limit set by tree level unitarity constraints in SM+S, which play a role at large m_2.

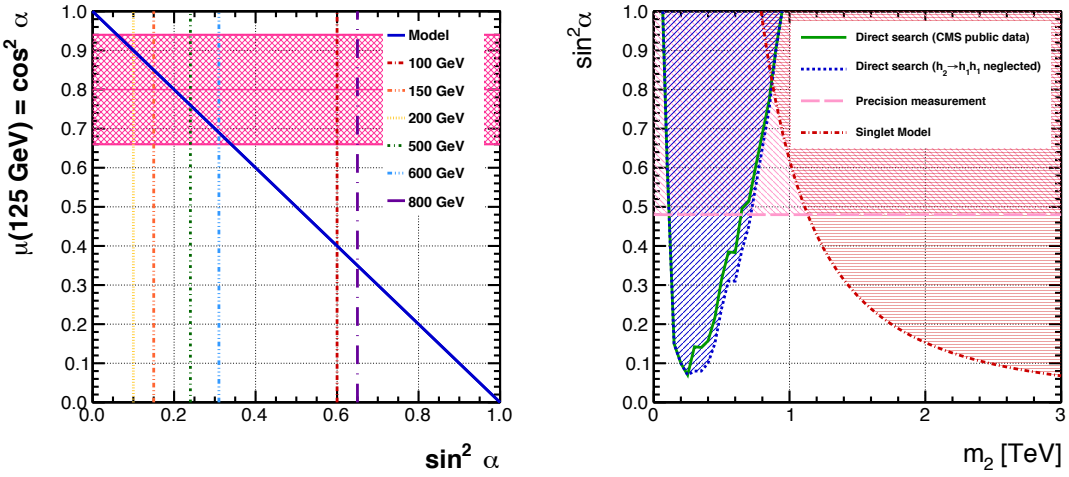

Figure 2.9: Left: Comparison of the reach of the precision measurement of the signal strength of the 125 GeV state at 1σ and of the search for extra scalars at 2σ for different masses (100, 150, 200, 500, 600 and 800 GeV). The blue line corresponds to the SM+S benchmark: $\cos^2\alpha + \sin^2\alpha = 1$. Right: Comparisons of the constraints on the parameter $\sin^2\alpha$ set by direct searches for extra scalar states (blue curve if the decay $H_2 \to H_1H_1$ is neglected, green curve otherwise), by indirect constraints on the measurement of the strength parameter of the 125 GeV state with a partial set of data collected by CMS during LHC Run-1, and by perturbative unitarity conditions, in the case of the SM+S model. Uncertainties are given at 2σ level. [56]

2.7 Chapter summary and personal contributions

Physics beyond the standard model

The SM is known not to answer a series of fundamental questions, such as the hierarchy problem or the existence of dark matter. Many BSM models that address some of the SM issues predict the existence of more than one scalar particle. This is the case of the minimal supersymmetric extension of the SM (MSSM): it brings a solution to the hierarchy problem and the coupling unification, proposes a dark matter candidate, and introduces in total five scalar bosons. The MSSM is part of a more generic class of models, two-Higgs-doublet models (2HDM), which have five scalar particles and give rise to a large variety of phenomenological signatures. Three complementary manners to uncover an eventually exotic scalar sector are explored in this thesis:
– Precision measurements of the properties of the discovered boson, which may highlight deviations from the SM;
– Direct search for new scalar particles in specific models;
– Search for exotic decays of the discovered boson.

Summary of notations

In the next chapters, the following notations are used for the (pseudo)scalar bosons:

– H: scalar boson of the SM, or heavy scalar of 2HDM (including MSSM) and 2HDM+S.
– h: light scalar of 2HDM and 2HDM+S, generally considered to be the 125-GeV particle.
– A: pseudoscalar in 2HDM, with a mass lower or higher than 125 GeV.
– Φ: scalar neutral resonance in the MSSM, equivalent to H, A or h.
– a: lightest pseudoscalar in 2HDM+S.

My contributions

Figure: 2.9.

I have actively participated in the results presented in Section 2.6 and published in [56]. I have cross-checked the theory calculations, and made Fig. 2.9, which compares the reach of the direct searches and precision measurements in the case of the SM+S model.

Chapter 3

Statistics

The physics searches presented in the next chapters heavily rely on statistical tools and interpretation. In Section 3.1, the notion of likelihood is introduced, and the way to include systematic uncertainties is detailed. Maximum likelihood fits, described in Section 3.2, are used to find the values of the parameters that give the best match between predicted processes and data. They can be used to extract the value of a parameter of interest, such as the signal strength, or to check the validity of a model from the pulls of the nuisance parameters. To set upper limits on a signal process, the CL_s method, in Section 3.3, uses ratios of likelihoods. In case an excess of events is observed on top of the predicted backgrounds, the significance of the excess can be calculated (Section 3.4) as the probability that a background fluctuation can cause such a large deviation. Another tool to check the background modeling consists in goodness-of-fit tests (Section 3.5), which are a kind of generalized chi-square test that measures the agreement between data and predictions. The last two sections of the chapter concern multivariate analysis methods to classify events.

3.1 Likelihood

3.1.1 Basics

In a counting experiment, data events follow a Poisson law, which is a discrete probability law describing the repartition of the number of events observed in a given time interval if their average rate, λ, is known and if they do not depend on each other. The Poisson probability function of parameter λ is:

$$f(n) = \frac{e^{-\lambda}\lambda^n}{n!}. \tag{3.1}$$

It can be shown that the best estimation of the parameter λ is the expected number of events in the time interval.

For a simple counting experiment, where n events are observed while b events are expected, the likelihood, which quantifies the agreement between some expectation and the observation, is simply:

$$\mathcal{L}(n|b) = \frac{e^{-b}b^n}{n!}. \tag{3.2}$$

If data are binned in a histogram, the N bins can be considered as independent of each other and the likelihood is given by the product of the likelihoods of every bin of the distribution:

$$\mathcal{L}(\vec{n}|\vec{b}) = \prod_{i=1}^{N} \frac{e^{-b_i}b_i^{n_i}}{n_i!}, \tag{3.3}$$

considering $\vec{n}$ as the vector of the observed data in the different bins, and $\vec{b}$ its equivalent for expected processes. If, on the contrary, data are not binned in a histogram but are described by a probability distribution function (pdf) $f_b(x)$ of some observable x, if k events are observed and if b events are expected in the full x range, the likelihood is then [61]:

$$\mathcal{L}(\vec{x}|b, f_b(x)) = k^{-1} \prod_{i=1}^{k} b f_b(x_i) e^{-b}. \tag{3.4}$$

3.1.2 Introducing systematic uncertainties

Systematic uncertainties are nuisance parameters that influence the model but are not of direct interest in the decision. In the analyses presented later, they come from three different sources:

1. Theoretical uncertainties, such as cross section or parton distribution function uncertainties;
2. Statistical uncertainties, coming for example from the limited number of events in the MC simulations or from the limited number of observed events in a control region used to estimate some background processes;
3. Experimental uncertainties, for example from luminosity or trigger efficiency measurements.

They can be embedded in the likelihood [61]. The nuisance parameters $\vec{\theta}$ impact the number of expected events, which can therefore be expressed as $b(\vec{\theta})$. Introducing the probability density function $p(\tilde{\theta}|\theta)$, where $\tilde{\theta}$ is the inferred default value of the nuisance and reflects our degree of belief on what the real value of the parameter θ is, the likelihood becomes for L nuisance parameters in the case of a binned histogram:

$$\mathcal{L}(\vec{n}|\vec{b}) = \prod_{i=1}^{N} \frac{e^{-b_i}b^{n_i}}{n_i!} \prod_{j=1}^{L} p(\tilde{\theta}_j|\theta_j). \tag{3.5}$$

According to Bayes' theorem, the Bayesian probability $p(\tilde{\theta}|\theta)$ can be expressed as a function of the frequentist probability $\rho(\theta|\tilde{\theta})$.

Most systematic uncertainties, corresponding to multiplicative factors on the signal or background yields, could be described by a Gaussian pdf of the type:

$$\rho(\theta|\tilde{\theta}) = \frac{1}{\sqrt{2\pi}\sigma}\exp\left(-\frac{(\theta-\tilde{\theta})^2}{2\sigma^2}\right), \tag{3.6}$$

but this has the inconvenient side-effect to cause problems for positively defined observables. Instead, log-normal pdfs of parameter κ, which have longer tails than Gaussian distributions for comparable uncertainties, and go to zero at $\theta = 0$, are preferred to avoid negative values of these observables:

$$\rho(\theta|\tilde{\theta}) = \frac{1}{\sqrt{2\pi}\ln(\kappa)}\exp\left(-\frac{(\ln(\theta/\tilde{\theta}))^2}{2(\ln\kappa)^2}\right)\frac{1}{\theta}. \tag{3.7}$$

While, for small uncertainties, a Gaussian distribution with relative uncertainty ϵ is asymptotically identical to a log-normal distribution with parameter $\kappa = 1 + \epsilon$, it clearly behaves less appropriately for large uncertainties, as illustrated in Fig. 3.1 (left).

In the case of uncertainties coming from statistically limited numbers of events, gamma distributions are used. If the event rate n in the signal region is directly proportional to the small number N of events in the control region or in MC samples, with a proportionality factor α, the gamma distribution reads:

$$\rho(n) = \frac{1}{\alpha}\frac{(n/\alpha)^N}{N!}\exp(-n/\alpha). \tag{3.8}$$

The log-normal and gamma distributions are illustrated in Fig. 3.1 for a given set of parameters.

Additionally, shape uncertainties affect the distribution of the parameter of interest [62], and are modeled with a linear extrapolation method [63]. Practically, they are implemented in CMS by providing two alternative shapes, corresponding to the variation by $\pm$ 1 standard deviation of the nuisance parameter. In the likelihood, a parameter θ is added to interpolate smoothly between the alternative shapes with a "vertical template morphing" technique. If there are N shape nuisance parameters, modeled with the parameters $\vec{\theta} = (\theta_1, \theta_2, ..., \theta_N)$, and if h_0, h_j^+ and h_j^- correspond respectively to the nominal histogram distribution, the histogram for a variation by +1 standard deviation of the jth nuisance parameter and the histogram for a variation by -1 standard deviation of the jth nuisance parameter, then the histogram distribution as a function of the shape nuisance parameters $\vec{\theta}$ is given by:

$$h(\vec{\theta}) = h_0 + \sum_{j=1}^{N}\left(a(\theta_j)h_j^+ + b(\theta_j)h_0 + c(\theta_j)h_j^-\right), \tag{3.9}$$

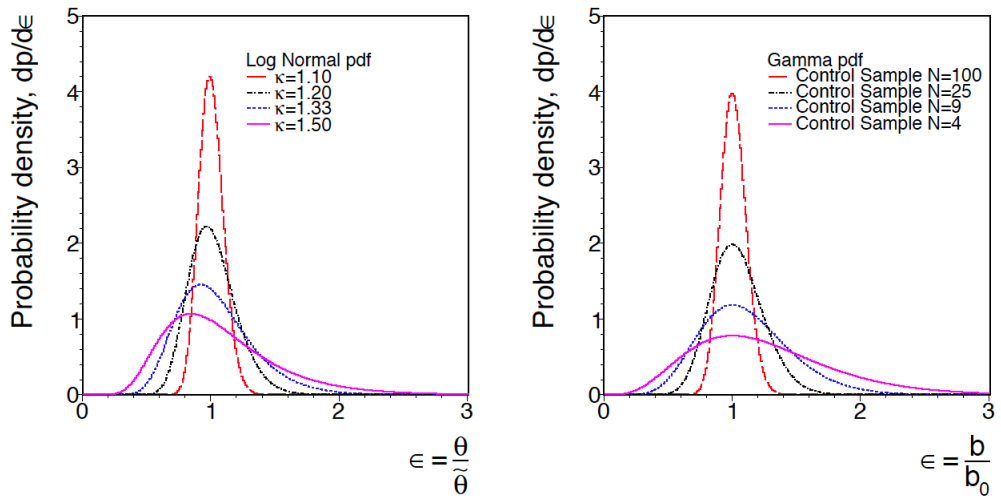

Figure 3.1: Log-normal (left) and gamma (right) distributions for different parameter values. Log-normal distributions are positively defined; they are similar to Gaussian distributions for small uncertainties (e.g. $\kappa = 1.10$), but extend to higher tails for large uncertainties (e.g. $\kappa = 1.50$). [61]

with

$$a(\theta) = \begin{cases} \theta(\theta+1)/2 & \text{if} \quad |\theta| \leq 1 \\ 0 & \text{if} \quad \theta < -1 \\ \theta & \text{if} \quad \theta > +1 \end{cases}, \tag{3.10}$$

$$b(\theta) = \begin{cases} -\theta^2 & \text{if} \quad |\theta| \leq 1 \\ -(|\theta|-1) & \text{if} \quad |\theta| > 1 \end{cases}, \tag{3.11}$$

and

$$c(\theta) = \begin{cases} \theta(\theta-1)/2 & \text{if} \quad |\theta| \leq 1 \\ 0 & \text{if} \quad \theta > +1 \\ |\theta| & \text{if} \quad \theta < -1 \end{cases}. \tag{3.12}$$

It can be noticed that the effect of different shape uncertainties is additive.

A special kind of shape uncertainty is associated to the uncertainty on the number of MC events or on the number of events from a control region used to estimate the background in every bin of the distribution. This has an impact on the shape of the distribution, but the behavior of each bin is independent from the behavior of the others for a single process. Barlow and Beeston proposed a method to treat such cases [64]: a separate nuisance parameter is introduced for every bin of every process, and multiplies the number of expected events in this particular bin for this given process. A large number of nuisance parameters is added to the likelihood model, but it is possible to prune some of them depending on their effects on the results. These uncertainties are later called bin-by-bin (bbb) uncertainties.

3.2 Maximum likelihood fit

A maximum likelihood fit can be performed to find the parameters of interest that provide the best agreement between expectation and observation. Two common scenarios are possible:

- Background-only fit: the nuisance parameters, acting on the expected background distribution $\vec{b}$, are varied to the values $\hat{\vec{\theta}}$ that maximize the likelihood $\mathcal{L}(\vec{n}|\vec{b},\vec{\theta})$;
- Signal-plus-background fit: the nuisance parameters as well as the freely floating signal strength μ of the expected signal distribution $\vec{s}$ are varied to their optimal values $\hat{\vec{\theta}}$ and $\hat{\mu}$ to maximize the likelihood $\mathcal{L}(\vec{n}|\mu\vec{s}+\vec{b},\vec{\theta})$.

The variations of the nuisance parameters after a maximum likelihood fit are called pulls; abnormally large values indicate an incoherence in the signal or background modeling. In a more general way, maximum likelihood fits can be performed for any freely floating parameter, called parameter of interest (POI), and any set of constrained nuisance parameters.

3.3 Exclusion limits

In the case where no significant excess of data is observed on top of the expected backgrounds, upper limits can be set on the production cross section of a hypothetical signal. The CL_s method [61, 65–67], is used to do so in CMS physics analyses. The test statistic q_μ used to analyze LHC results is based on a profile likelihood ratio:

$$q_\mu = -2\ln\frac{\mathcal{L}(\vec{n}|\mu\vec{s}+\vec{b},\hat{\vec{\theta}}_\mu)}{\mathcal{L}(\vec{n}|\hat{\mu}\vec{s}+\vec{b},\hat{\vec{\theta}})},\ \text{with } 0\leq\hat{\mu}\leq\mu. \tag{3.13}$$

The signal strength $\hat{\mu}$ that optimizes the likelihood is constrained to lie between zero and the signal strength μ, for which the test statistic is computed, in order to have a positive signal rate and one-sided confidence intervals. In the numerator, the signal strength is fixed while the nuisance parameters are allowed to float to the values that maximize the likelihood, whereas in the denominator, the signal strength and the nuisance parameters may both float to maximize the likelihood [1].

The observed value of the test statistic assuming a value of the signal strength μ, q_μ^{obs}, can easily be computed from Equation (3.13). The nuisance parameters $\hat{\vec{\theta}}_0^{obs}$ and $\hat{\vec{\theta}}_\mu^{obs}$ that maximize the likelihood in the background-only ($\mu = 0$) and background-plus-signal ($\mu > 0$) hypotheses respectively can also be determined.

The probability density functions of the test statistics $f(q_\mu|\vec{b},\hat{\vec{\theta}}_0^{obs})$ and $f(q_\mu|\mu\vec{s}+\vec{b},\hat{\vec{\theta}}_\mu^{obs})$, which describe the test statistic distribution in the background-only and signal-plus-

1. $\hat{\vec{\theta}}_\mu$ therefore represents the nuisance parameters that maximize the likelihood under a given signal strength μ, whereas $\hat{\vec{\theta}}$ represents the nuisance parameters that maximize the likelihood when the signal strength is allowed to float to its best-fit value.

background hypotheses respectively, are estimated from toy MC pseudo-data, using the optimal value of the nuisance parameters, $\hat{\vec{\theta}}_0^{obs}$ and $\hat{\vec{\theta}}_\mu^{obs}$, computed in the previous step. It is now possible to evaluate the probabilities to obtain the observation under both hypotheses. This leads to:

$$p_{\mu s+b} = P(q_\mu \geq q_\mu^{obs}|\text{signal-plus-background}) = \int_{q_\mu^{obs}}^{\infty} f(q_\mu|\mu\vec{s}+\vec{b},\hat{\vec{\theta}}_\mu^{obs})dq_\mu, \tag{3.14}$$

and

$$1-p_b = P(q_\mu \geq q_\mu^{obs}|\text{background-only}) = \int_{q_b^{obs}}^{\infty} f(q_\mu|\vec{b},\hat{\vec{\theta}}_0^{obs})dq_\mu. \tag{3.15}$$

The CL_s value, for a given signal strength μ, is given by the ratio of both probabilities:

$$CL_s(\mu) = \frac{p_{\mu s+b}}{1-p_b}. \tag{3.16}$$

Figure 3.2 illustrates an example of test statistic distributions for the background-only and signal-plus-background scenarios. The 95% confidence level upper limit is obtained for the parameter μ such that $CL_s(\mu) = 0.05$.

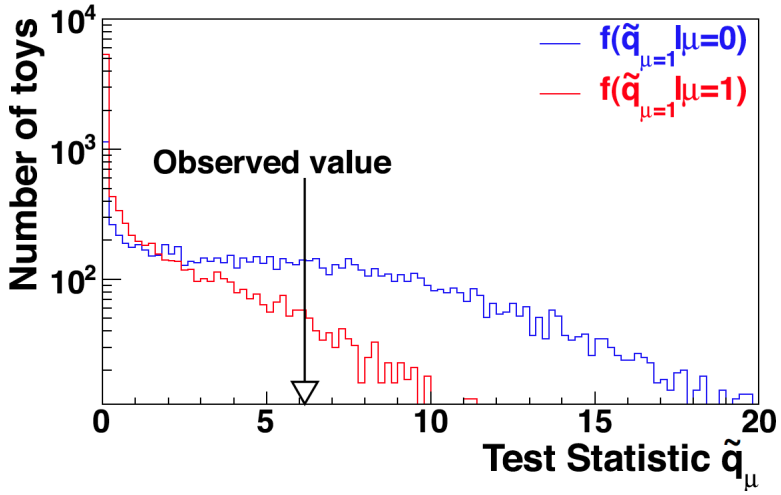

Figure 3.2: Test statistic distributions in the background-only (blue) and signal-plus-background (red) hypotheses. The signal-plus-background test statistic distribution is shown in the particular case where the signal strength is equal to one. The observed value, shown with an arrow, permits to compute the p_b and $p_{\mu s+b}$ probabilities by integration, which are then used to compute $CL_s(\mu)$. [61]

The non-conventional definition of the probability CL_s as a ratio of probabilities, as given in Equation (3.16), makes it possible to treat cases where the signal is so small that both hypotheses are compatible with the observation, or where a deficit in data would lead to a negative signal strength with large significance if only $p_{\mu s+b}$ was considered. The definition of CL_s leads to rather conservative limits. In order to facilitate comparisons

between both experiments, ATLAS also works with the CL_s method and uses the same test statistic as CMS.

The procedure to obtain the median expected limit, as well as the ± 1 and ± 2 standard deviation bands, is easy. A large number of pseudo-datasets based on the background-only expectation (including nuisance parameters) is generated, and the signal strength that gives $CL_s = 0.05$ is computed for each of them. A cumulative distribution function is then built with these results, from which the median (50% quantile), $\pm 1\sigma$ (16% and 84% quantiles) bands, and $\pm 2\sigma$ (2.5% and 97.5% quantiles) bands can be extracted, as illustrated in Fig 3.3.

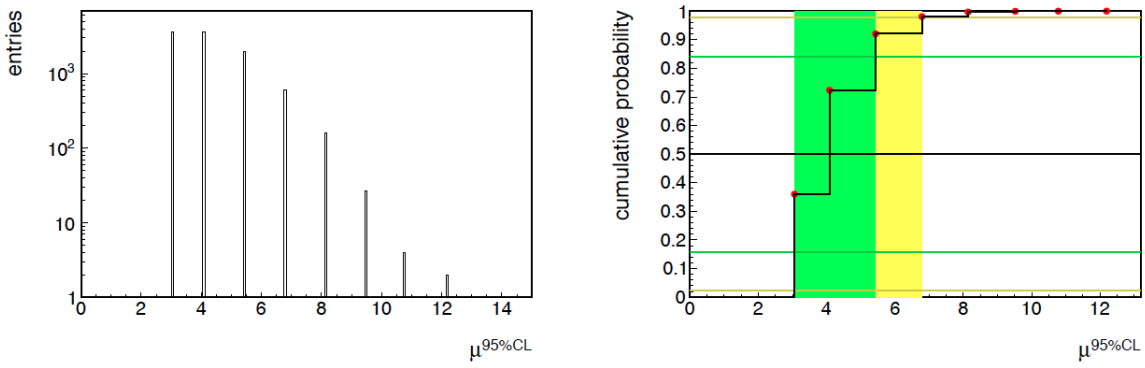

Figure 3.3: Left: Signal strengths that give $CL_s = 0.05$ for a set of pseudo-experiments generated in the background-only scenario. Right: Cumulative distribution of the signal strengths, and extraction of the median and uncertainty bands based on the quantiles. [61]

Generating hundreds of toys for every signal strength hypothesis can quickly become time- and CPU-consuming. When the expected number of events is large enough, asymptotic limits, which do not require the use of toy MC samples, can be used as an excellent approximation of "full" CL_s limits [68]. The set of simulated pseudo-data can be replaced by a single dataset with specific properties, called an Asimov dataset in honor of the writer's novel "Franchise" where a single voter represents the entire population. From the Asimov dataset, in which the observed rate corresponds to the expected rate, can be extracted the parameters of a (non-central) chi-square distribution, that mimic very well the test statistic distribution from toy MC, already for a small number of expected events, as illustrated in Fig. 3.4. Using the properties of the Asimov dataset permits to compute not only the median expected limit, but also the uncertainty bands.

3.4 Significance

If an excess of data is observed on top of the predicted backgrounds, a p-value for the background-only hypothesis is determined; it corresponds to the probability that the backgrounds fluctuate to create an excess as large or larger than the one observed. The

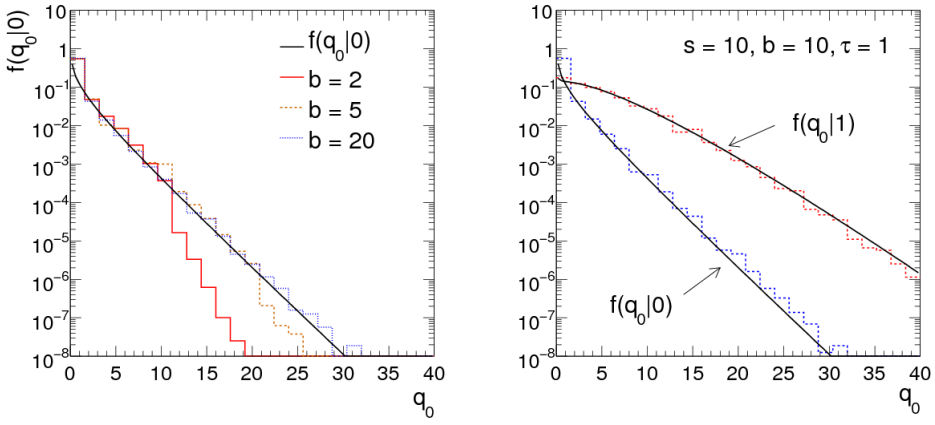

Figure 3.4: Left: Test statistic distributions for a background-only hypothesis, in a simple counting experiment with expected background events between 2 and 20. Histograms correspond to toy MC, while the curve is obtained with the asymptotic method. The agreement between asymptotic curve and toy MC is good already for five expected background events. Right: Histograms from toy MC and curves from the asymptotic method for the test statistic distributions in the case of background-only (blue) and signal-plus-background (red) hypotheses. In this example, ten signal events and ten background events are considered, and the agreement between both methods is excellent. The parameter τ is a scale factor for the number of background events, and is taken as equal to one in this example. [68]

same test statistic as defined in equation (3.13) is used, where the signal strength μ is set to 0:

$$q_0 = -2 \ln \frac{\mathcal{L}(\vec{n}|\vec{b}, \hat{\vec{\theta}}_0)}{\mathcal{L}(\vec{n}|\hat{\mu}\vec{s} + \vec{b}, \hat{\vec{\theta}})}, \text{ with } \hat{\mu} \geq 0. \tag{3.17}$$

The optimized value of the signal strength, $\hat{\mu} \geq 0$, is chosen to be positive as significance calculations only interpret excesses of events. The distribution $f(q_0|\vec{b}, \hat{\vec{\theta}}_0^{obs})$ is built by generating toy pseudo-datasets, and the p-value of an observation with a test statistic q_0^{obs} is given by:

$$p_0 = P(q_0 \geq q_0^{obs}) = \int_{q_0^{obs}}^{\infty} f(q_0|\vec{b}, \hat{\vec{\theta}}_0^{obs}) dq_0. \tag{3.18}$$

An equivalent way to quantify an excess is to use the notion of significance. The p-value p_0 is related to the significance Z_0 with:

$$p_0 = \int_{Z_0}^{\infty} \frac{1}{\sqrt{2\pi}} \exp(-x^2/2) dx = \frac{1}{2} P(\chi_1^2 \geq Z_0^2). \tag{3.19}$$

This corresponds to the higher tail of a Gaussian distribution. Asymptotically, there exists a much faster way to estimate to p-value without generating toy pseudo-datasets:

$$p_0 \simeq \frac{1}{2} \left[1 - \text{erf} \left(\sqrt{q_0^{obs}/2} \right) \right]. \tag{3.20}$$

If a signal is searched for over a large mass range, the probability of observing excesses is larger; this is called the look-elsewhere effect [69]. Practically, the local significance measured as previously described needs to be corrected into a global significance. The magnitude of the look-elsewhere effect depends not only on the probed mass range, but also on the mass resolution since an excess of data at a given mass in an analysis with a poor mass resolution will lead to large p-values for mass hypotheses in a broad range. The relatively poor di-tau mass resolution causes the $H \to \tau\tau$ searches not to be extremely sensitive to the look-elsewhere effect. The effect can be estimated by counting the number of times $N_{Z_{up}}$ the observed significance distribution up-crosses a certain level of significance Z_{up}, low enough that the statistical uncertainty is not too large. The number of up-crossings N_{Z_0} for a significance Z_0 as large as the local significance (e.g. five standard deviations) can be computed from the value $N_{Z_{up}}$, with the following relation:

$$N_{Z_0} = N_{Z_{up}} \exp\left(-\frac{Z_0^2 - Z_{up}^2}{2}\right). \tag{3.21}$$

The notion of up-crossing is illustrated in Fig. 3.5. The global p-value is then given, considering Z_0 as the local significance of the excess, by:

$$p_0^{global} \leq p_0^{local} + N_{Z_0}. \tag{3.22}$$

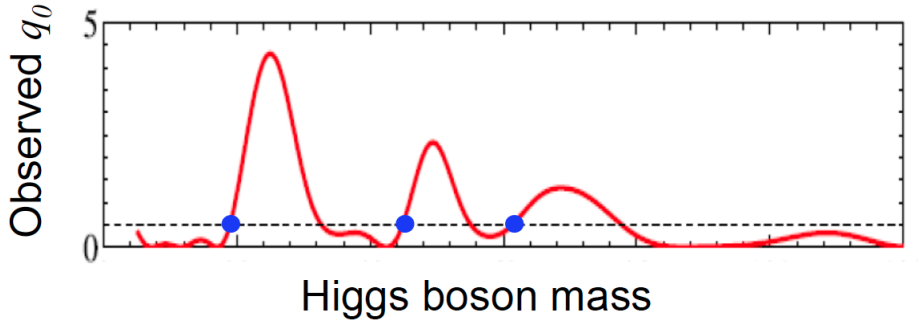

Figure 3.5: Example of scan of the test statistic as a function of the mass of the scalar boson. The three up-crossings at a certain level Z_{up} are shown with blue points ($N_{Z_{up}} = 3$). [61]

3.5 Goodness-of-fit test

Goodness-of-fit (GOF) tests [70] are used to quantify the agreement between the expected processes and the observation. They consist in the test of the null hypothesis [2] when the alternative hypothesis is not specified, and permit to notice departures from the

2. In this case the null hypothesis can be either background-only or signal-plus-background.

null hypothesis that would point to the existence of a mismodeling of expected processes. A likelihood ratio can be built without dependence on the metric in which the parameters are described. In so-called saturated models, the alternative hypothesis is taken as matching exactly the observed data in each bin of the distribution, and corresponds to a likelihood $\mathcal{L}_{sat}(\vec{n}|\vec{n})$. The test statistic in a saturated GOF test is:

$$q_\mu = -2 \ln \frac{\mathcal{L}(\vec{n}|\mu\vec{s} + \vec{b}, \vec{\theta})}{\mathcal{L}_{sat}(\vec{n}|\vec{n})}. \tag{3.23}$$

Using Poisson pdfs, and after simplification, one is left with:

$$q_\mu = -2 \ln \left[\prod_{i=1}^{N} \left(\frac{\mu s_i(\vec{\theta}) + b_i(\vec{\theta})}{n_i} \right)^{n_i} \exp(-(\mu s_i(\vec{\theta}) + b_i(\vec{\theta})) + n_i) \right]. \tag{3.24}$$

The observed value of the test statistic q_{obs} is obtained by minimizing q_μ.

To test if the observed test statistic is compatible with what could be expected given the background (or signal-plus-background) predictions, toy MC pseudo-datasets are generated according to the likelihood for the background (or signal-plus-background) hypothesis. A minimal q_μ is obtained for each pseudo-dataset, q_{toy}, and the observed q_{obs} is compared to the distribution of all the q_{toy}: if q_{obs} lies in the bulk of the distribution, it means that the agreement between data and expectation is good, while if it lies in the tails, careful checks are needed to determine if the expected processes are mismodeled. An example of goodness-of-fit test where expectation agrees well with observation is shown in Fig. 3.6.

3.6 Boosted decision trees

Multivariate analysis (MVA) methods are based on machine learning techniques, and permit, from a sample of training signal and background events, to determine a mapping function that helps classifying events according to their similarity with background and signal events. Boosted decision trees (BDT) [71, 72] are the most widely used MVA method in CMS. They are used to classify events considering a large number of variables and their correlations. They proceed from samples of background and signal events, for which discriminating variables are specified.

A single decision tree discriminating between background and signal events, is built as follows:

1. Signal and background samples are divided into two parts: the first halves are used to train the discriminator, while the second halves are used to test it.
2. The variable and the cut threshold that give the best separation between background and signal are determined [3], and the tree trunk is divided into two branches with different signal purities.

3. The variables can be decorrelated in a first stage to enhance the sensitivity of the MVA method.

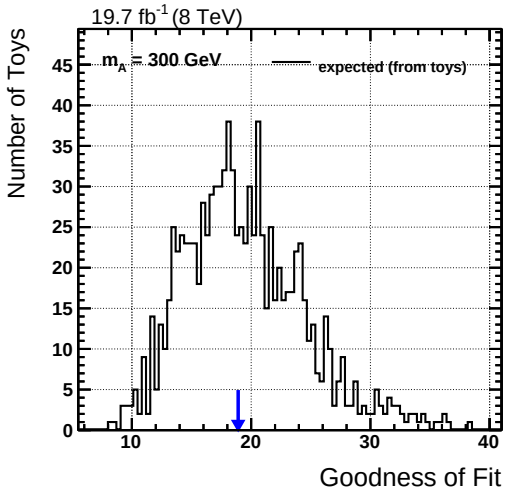

Figure 3.6: Example of goodness-of-fit test. The blue arrow represents the observed value of the test statistic, while the black distribution is obtained from toy MC pseudo-datasets. The observed value lies in the bulk of the distribution, indicating a good agreement between the expected processes and the observed data.

3. The leaves of the tree are further divided using the variables and thresholds giving the best separation, until a certain number of leaves has been created or until all leaves have reached a given purity.

The procedure is schematically summarized in Fig. 3.7. There are different metrics to evaluate the purity; the most commonly used is called "Gini". If an event i in a branch of n events has a weight w_i, the branch purity is defined as:

$$p = \frac{\sum_{signal} w_i}{\sum_{signal} w_i + \sum_{bkg} w_i}. \tag{3.25}$$

This is used to define the Gini weight:

$$\text{Gini} = \left(\sum_{i=1}^{n} w_i \right) p(1-p). \tag{3.26}$$

The variable and the threshold chosen to divide a branch are those that minimize the sum of the Gini weights of the two daughter branches. If the purity of the leaf is greater than 0.5, it is considered as a signal leaf, while if it is less than 0.5, it is a background leaf.

A way to enhance the performance of decision trees and to make them less sensitive to fluctuations in the training samples, is to combine a set of several decision trees into a boosted decision tree. The principle consists in boosting misclassified events by giving them a larger weight for the training of the next tree. Typically several thousands of decision trees are combined in a single boosted decision tree. The boosting algorithm is

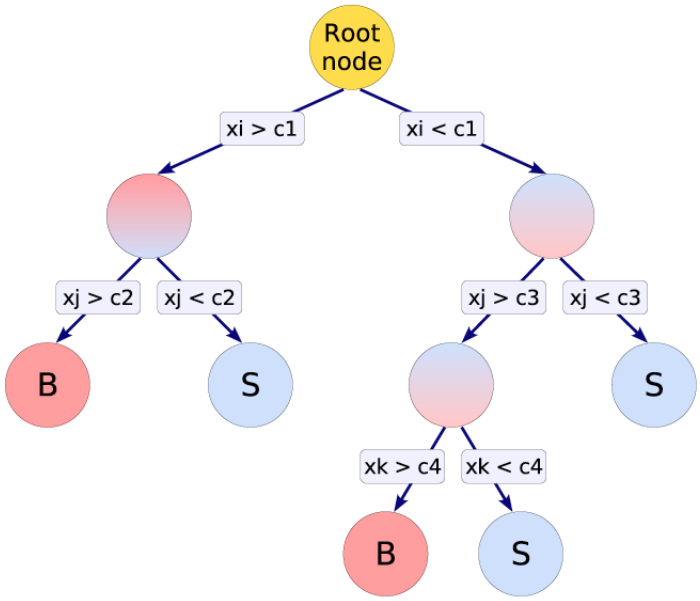

Figure 3.7: Schematic overview of a decision tree. Starting from a root node, branches are created by cutting on the $x_{i,j,k}$ variables with thresholds $c_{1,2,3,4}$, in such a way as to obtain the highest signal (blue) and background (red) purities as possible. [71]

often chosen to be AdaBoost. The AdaBoost weight, α, that multiplies the weight w_i of all misclassified events of a tree is:

$$\alpha = \frac{1}{2} \ln \frac{1-\epsilon}{\epsilon}, \tag{3.27}$$

where

$$\epsilon = \frac{\sum_{misclassified} w_i}{\sum_{all} w_i}. \tag{3.28}$$

The final BDT score of an event is computed as the fraction of trees where the event ended up in a signal leaf. It can be checked that there is no overtraining by observing a good agreement in BDT scores obtained with the training and testing samples. The BDT weights computed with such a technique are afterwards applied to observed data, as well as to MC simulation events not used in the training phase.

3.7 k-Nearest Neighbor classifier

The k-Nearest Neighbor (kNN) classifier [71] is another MVA method. For every test event, the algorithm searches for the k closest events of the background and signal training samples. The distance d between test and training events is determined with a Euclidian

metric:

$$d = \left(\sum_{i=1}^{n} |x_i - y_i|^2 \right)^{\frac{1}{2}}, \tag{3.29}$$

where x_i and y_i are the values of the i variable for the test and training events respectively. In order to account for variables with different units or different widths, the width w_i of the variable i is introduced to compute the distance:

$$d = \left(\sum_{i=1}^{n} \frac{1}{w_i^2} |x_i - y_i|^2 \right)^{\frac{1}{2}}. \tag{3.30}$$

A probability P is assigned to every test event depending on the number of signal (k_S) and background (k_B) events among its k nearest neighbors:

$$P = \frac{k_S}{k_S + k_B}. \tag{3.31}$$

The choice of the number k of neighbors is a compromise between the local description of the probability function (better with less neighbors) and the stability of the probability density estimate (less fluctuations with more neighbors). Fig. 3.8 illustrates the principle of the kNN algorithm.

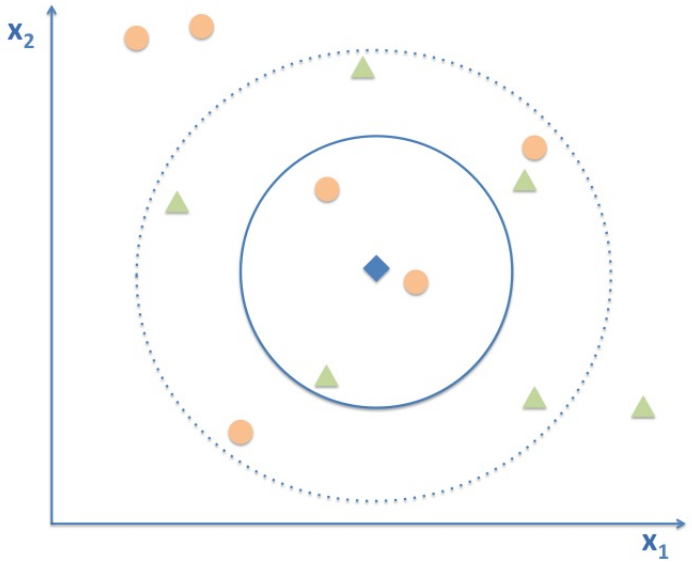

Figure 3.8: Schematic overview of a kNN classifier in two dimensions. The blue square represents the test event, while green triangles are signal training events, and orange disks are background training events. If the number of neighbors is chosen to be equal to three, the test event is considered as background-like, while if the number of neighbors is nine, the event is signal-like. The smaller number of events reflects the local density better, but is subject to larger statistical fluctuations.

3.8 Chapter summary

Statistics

Statistical methods are used to extract results from data analyses in high-energy experiments. Maximum likelihood functions can be associated to data and predicted background distributions, using a specific test statistic defined for LHC experiments. They permit to perform maximum likelihood fits to extract some parameter of interest, such as the signal strength, to control the good agreement between data and predicted processes with goodness-of-fit tests for example, to set upper exclusion limits in case no excess of data is observed, or to measure the significance of an excess if applicable. The last sections of the chapter describe how Boosted Decision Trees and k-Nearest Neighbor classifiers rank events according to their similitude with background or signal events after a dedicated training. These tools are used in the analyses described in Chapters 6-13.

Part II

Experimental bases

Chapter 4

Experimental setup

One of the main objectives that motivated the design and the construction of the LHC and of its general-purpose detectors, is the search for the SM scalar boson. Before the LHC operation, it was known from LEP and Tevatron results that the scalar boson mass had to be larger than about 114 GeV [73, 74], while unitarity and perturbativity constraints limited it to about 1 TeV [18]. The physics motivations for building the LHC were obviously wider, and also covered among others the search for supersymmetry or dark matter. The first part of this chapter describes the LHC and the acceleration process for protons to reach the design energy, while the second part presents the CMS detector.

4.1 Large Hadron Collider

The Large Hadron Collider (LHC) [75] is the largest circular particle collider ever built. It is situated about 100 m underground close to Geneva, and has a circumference of 26.7 km. It was built in the tunnel previously used by the LEP, and the first collisions happened in 2009. While the LHC can also support lead-lead or lead-proton collisions, the following sections will describe only the proton-proton collisions as they correspond to the data used in the physics results exposed in the next chapters.

4.1.1 Proton production and acceleration

Protons are produced in a duoplasmatron, where electrons from a heated cathode ionize a hydrogen gas. A magnetic field coupled to an electric field creates an intense ionization and the confinement of a plasma. An electrode extracts the protons from the plasma. Protons are first accelerated in a linear accelerator, the LINAC2, until they reach an energy of about 50 MeV. They are then injected in a circular accelerator, the PS booster, where they reach an energy of 1.4 GeV, before entering the Proton Synchrotron (PS). In the Super Proton Synchrotron (SPS), the proton energy increases from 26 to 450 GeV, and the protons are then injected in the LHC, where they are finally accelerated to their final energy (3.5 TeV in 2011, 4 TeV in 2012, 6.5 TeV in 2015). The acceleration chain is

illustrated in Fig. 4.1. Three to four cycles of the PS synchrotron are needed to fill the SPS, whereas twelve cycles of the SPS are required to fill the LHC. The total injection time is about twenty minutes, and about twenty additional minutes are needed to increase the beam energy from 450 GeV to 6.5 TeV. When completely filled, the LHC nominally contains 2808 bunches of approximately 10^{11} protons.

Inside the LHC, protons are accelerated by sixteen radiofrequency cavities, while 1232 niobium-titanium superconducting dipole magnets ensure the deflection of the beams, and quadrupole magnets their collimation. The two proton beams circulate in opposite directions in the LHC, which requires the existence of two rings with opposite magnetic dipole fields and separate vacuum chambers. Because of the limited size of the tunnel inherited from the LEP era, the LHC uses twin bore magnets instead of two separate rings of magnets. The superconducting magnets operate at a temperature below 2 K, obtained with a pressurized bath of superfluid helium at about 0.13 MPa. Three vacuum systems are part of the LHC architecture: the beam vacuum (10^{-10} to 10^{-11} mbar at room temperature), the insulation vacuum for helium distribution (about 10^{-6} mbar) and the insulation vacuum for cryomagnets (about 10^{-6} mbar).

The interaction rate, $\frac{dN}{dt}$, depends on the process cross section σ, and on the luminosity $\mathcal{L}$ with the relation:

$$\frac{dN}{dt} = \mathcal{L}\sigma. \tag{4.1}$$

The nominal design luminosity of the LHC is 10^{34} cm^{-2}s^{-1}. The number of interactions per unit of time can also be expressed as a function of the beam characteristics. Given q the charge of the beam particles, I the beam intensity, l the collision distance of the beams, and s the beam section, the number n of particles that cross each beam per unit of time and per unit of surface is $n = \frac{I}{qs}$. As the two beams interact during a time laps of $\frac{l}{c}$, one obtains:

$$\frac{dN}{dt} = \frac{I^2 l \sigma}{q^2 c s}. \tag{4.2}$$

Therefore, combining equations (4.1) and (4.2), the instantaneous luminosity is:

$$\mathcal{L} = \frac{I^2 l}{q^2 c s}. \tag{4.3}$$

Another way to express the luminosity, with beam characteristic properties is:

$$\mathcal{L} = \frac{N_b^2 n_b f_{rev} \gamma}{4\pi \epsilon_n \beta^*} F, \tag{4.4}$$

where N_b is the number of protons in each bunch, n_b the number of bunches, f_{rev} the revolution frequency, γ the Lorentz factor, ϵ_n the normalized emittance, β^* the beta function at the collision point and F a reduction factor coming from the crossing angle of the two beams. The integrated luminosity L, later called simply luminosity, is the integral of the instantaneous luminosity $\mathcal{L}$ over a given range of time.

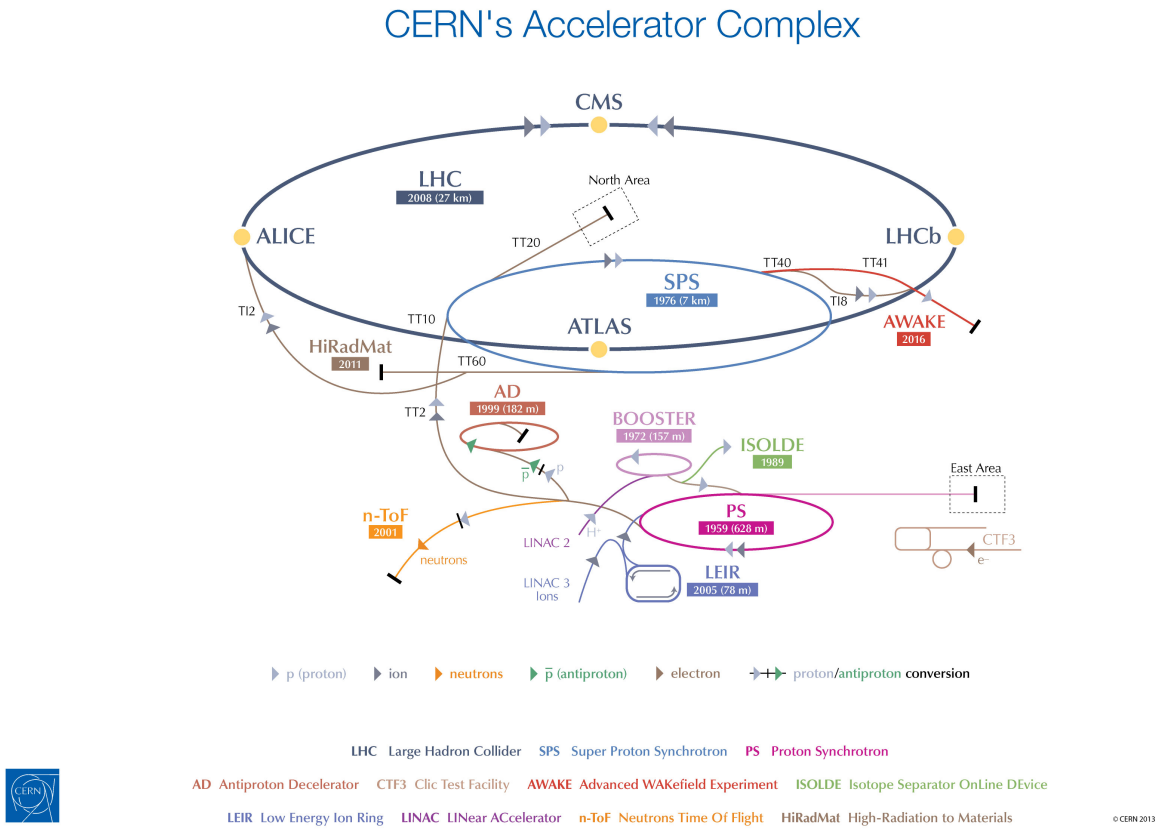

Figure 4.1: Overview of the CERN accelerator complex. To reach their final energy, protons successively pass through the LINAC2, the PS booster, the PS, the SPS and finally the LHC. [76]

4.1.2 Experiments

Four detectors are located at collision points in the LHC:
- CMS (Compact Muon Solenoid) [77], which will be described in greater details in Section 4.2, is a multi-purpose detector with wide physics objectives, such as the search of the SM scalar boson, of dark matter candidates or of supersymmetric particles;
- ATLAS (A Toroidal LHC ApparatuS) [78] covers the same physics objectives as CMS and exploits different technical solutions, including a large toroidal magnet;
- LHCb (Large Hadron Collider beauty) [79] studies matter-antimatter asymmetry via CP violation, through studies involving b quarks;
- ALICE (A Large Ion Collider Experiment) [80] is designed to address the physics of strongly interacting matter and the quark-gluon plasma at extreme values of energy density and temperature in nucleus-nucleus collisions.

ATLAS and CMS analyze completely independent datasets; their respective results can cross-check each other, or be combined to increase the precision of the measurements.

4.1.3 Data taking and LHC schedule

While the first beams could circulate in the LHC in 2008, a mechanical damage, which caused severe leaks of liquid helium, delayed the first proton-proton collisions at the injection energy of 450 GeV to the end of 2009. In March 2010 were recorded the first collisions at a center-of-mass energy of 7 TeV. The LHC delivered an integrated luminosity of 6.14 fb^{-1} in 7 TeV center-of-mass collisions in 2010 and 2011, of 23.30 fb^{-1} at 8 TeV in 2012 and, after the first long shut down (LS1), of 4.22 fb^{-1} at 13 TeV in 2015. The evolution with the time of the integrated luminosity in 2011 and 2012 is presented in Fig. 4.2. A bit more than 90% of the luminosity delivered by the LHC was recorded by the CMS detector. On average several collisions occur per bunch crossing, which constitutes the so-called pileup phenomenon. The mean number of interactions per bunch crossing was around twenty in 2012.

The LHC should operate at 13 or 14 TeV center-of-mass energy between 2016 and 2018. A second long shutdown (LS) is planned in 2019 and 2020, while Run-3 will extend until 2023. After Phase-1, which includes Run-1, Run-2 and Run-3, Phase-2 should extend up to approximately 2037. The integrated luminosity collected in Phase-1 is expected to reach 300 fb^{-1}, while 3000 fb^{-1} should be collected by the end of Phase-2. An overview of the LHC schedule is presented in Fig. 4.3.

4.2 Compact Muon Solenoid

The CMS detector is a multi-purpose apparatus, designed to cover a wide physics program, from the discovery of the SM scalar boson to the search for BSM physics. Its main specifications to meet these goals consisted in achieving a good muon identification and momentum resolution, a good charged-particle reconstruction efficiency and momentum resolution, a good electromagnetic energy resolution and a good missing transverse energy

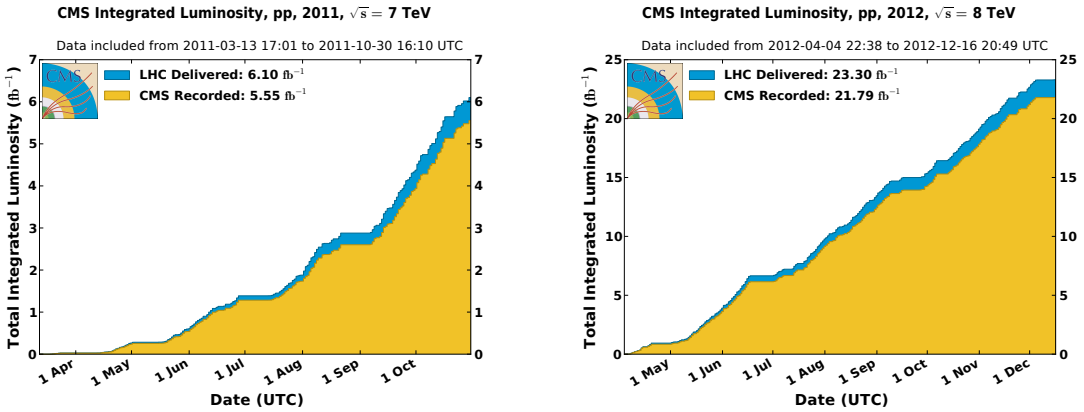

Figure 4.2: Integrated luminosity delivered by the LHC (blue) and collected by CMS (yellow) at a center-of-mass energy of 7 TeV in 2011 (left) and 8 TeV in 2012 (right). [81]

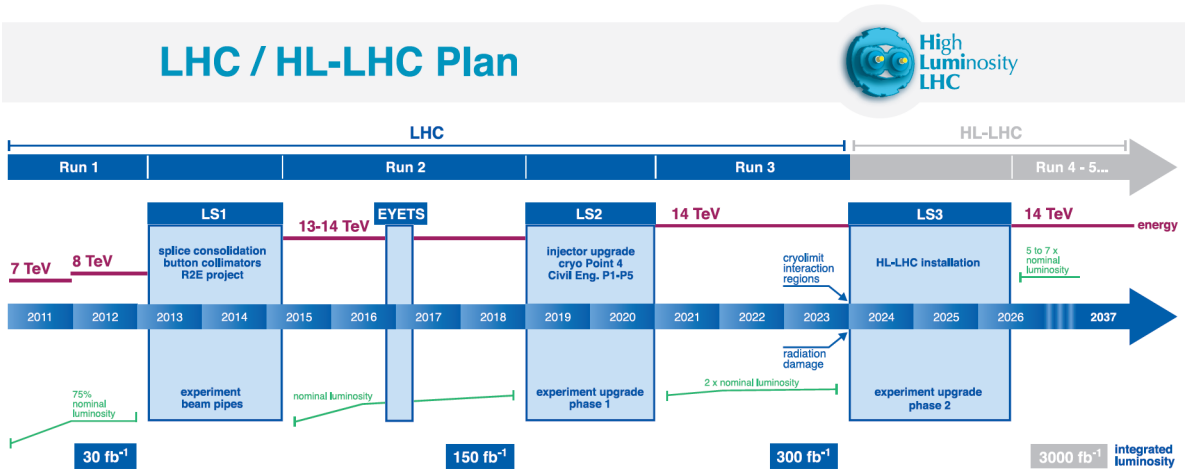

Figure 4.3: Overview of LHC schedule until 2037. The integrated luminosity collected in Phase-1 is expected to reach 300 fb^{-1}, while 3000 fb^{-1} should be collected by the end of Phase-2. [82].

and di-jet mass resolution [77]. The detector gets its name from its limited size considering its complexity, its sophisticated muon system, and its solenoidal superconducting magnet.

4.2.1 Overview of the CMS detector

The CMS detector is 28.7 m long, has a diameter of 15.0 m and weighs 14 000 t. It is composed of different subdetector layers, arranged in a central cylinder, the barrel, and closed by two endcaps. The origin of the right-handed coordinate system adopted by CMS is at the nominal collision point, while the x-axis points radially towards the center of the LHC and the y-axis points vertically. The z-axis is orthogonal to the other axes and is directed along the beam direction, towards the Jura mountains from LHC Point 5. The azimuthal angle ϕ is measured in the plane defined by the x- and y-axes, from the x-axis. The polar angle θ is measured from the z-axis, in a plane orthogonal to the xy-plane and containing the z-axis, and is used to define the more widely-used pseudorapidity η:

$$\eta = -\ln\tan(\theta/2). \tag{4.5}$$

The pseudorapidity is a good approximation for particles with $E \gg m$ of the rapidity y:

$$y = \frac{1}{2}\ln\left(\frac{E+p_z}{E-p_z}\right). \tag{4.6}$$

The difference of the rapidities of two particles is invariant under a Lorentz boost in the z-direction.

The key elements of the CMS detector, described in the next sections and illustrated in Fig. 4.4, are, from the innermost to the outermost part:

- An inner tracking system, which measures the trajectory of charged particles and reconstructs secondary vertices;
- An electromagnetic calorimeter, which measures and absorbs the energy of electrons and photons;
- A hadronic calorimeter, which measures and absorbs the energy of hadrons;
- A superconducting magnet, which provides a 3.8 T magnetic field parallel to the beam axis to bend the tracks of charged particles;
- A muon system, which measures the energy of muons and reconstructs their tracks.

In addition, because of the high collision rate at the LHC, a trigger system has been designed to only record data interesting for physics analyses.

4.2.2 Tracker

The subdetector layer closest to the beams is the tracker. Its function consists in recording the tracks of charged particles, which can be used to estimate the momentum of these particles with a great precision, or to reconstruct secondary vertices from long-lived particle decays. The tracking takes place in a 5.8 m length and 2.5 m diameter cylinder, around the interaction point. Because of the high number of particles produced in overlapping proton-proton collisions, it is of primary importance that the tracker has a high

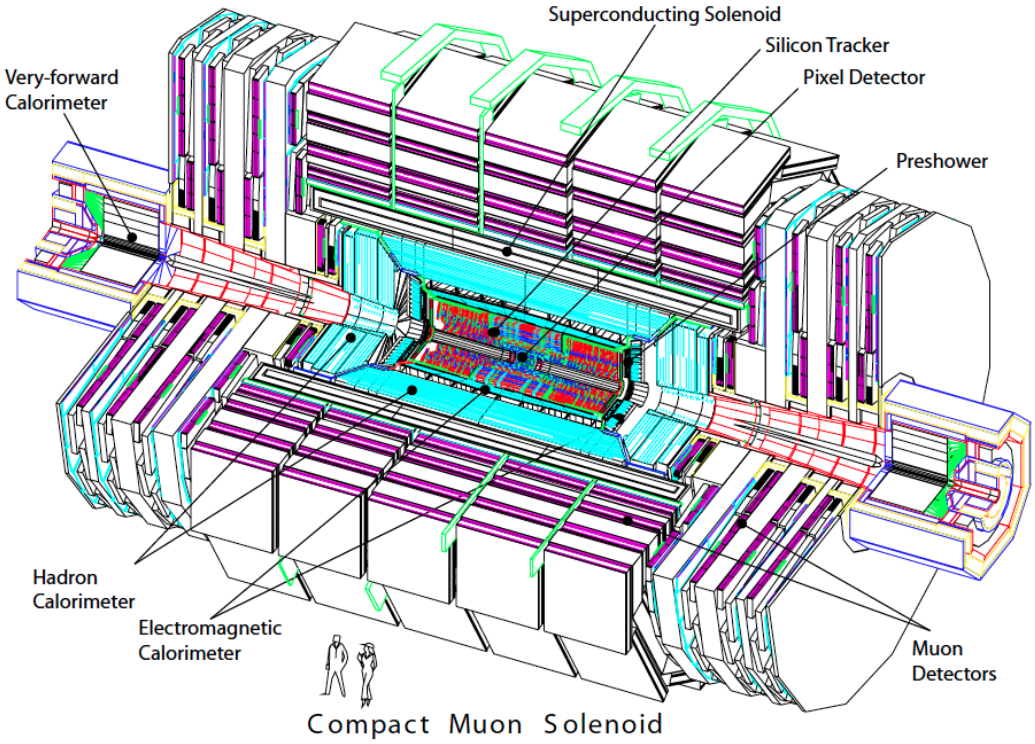

Figure 4.4: Overview layout of the CMS detector. The CMS detector is composed, from the innermost to the outermost part, of an inner tracking system, an electromagnetic calorimeter, a hadronic calorimeter, a superconducting magnet, and a muon system. [77]

granularity. While the quantity of material had to be kept low to limit photon conversion, multiple scattering, bremsstrahlung and nuclear interactions, the tracker had to have a high power density of electronics and to be radiation resistant.

In the barrel region, the tracker is composed of ten layers of silicon microstrip detectors, and of three layers of silicon pixel detectors. The system is completed in the endcaps by two disks in the pixel detector and three plus nine disks in the strip tracker, for pseudorapidities up to $|\eta| < 2.5$. A sectional view of the tracker is shown in Fig. 4.5. In total, the inner tracker consists of 1440 silicon pixel and 15 148 silicon strip detector modules. The resolution on the transverse momentum for a 100-GeV charged particle is about 2.0%, while the impact parameter resolution achieved by the inner tracker is about 15 μm.

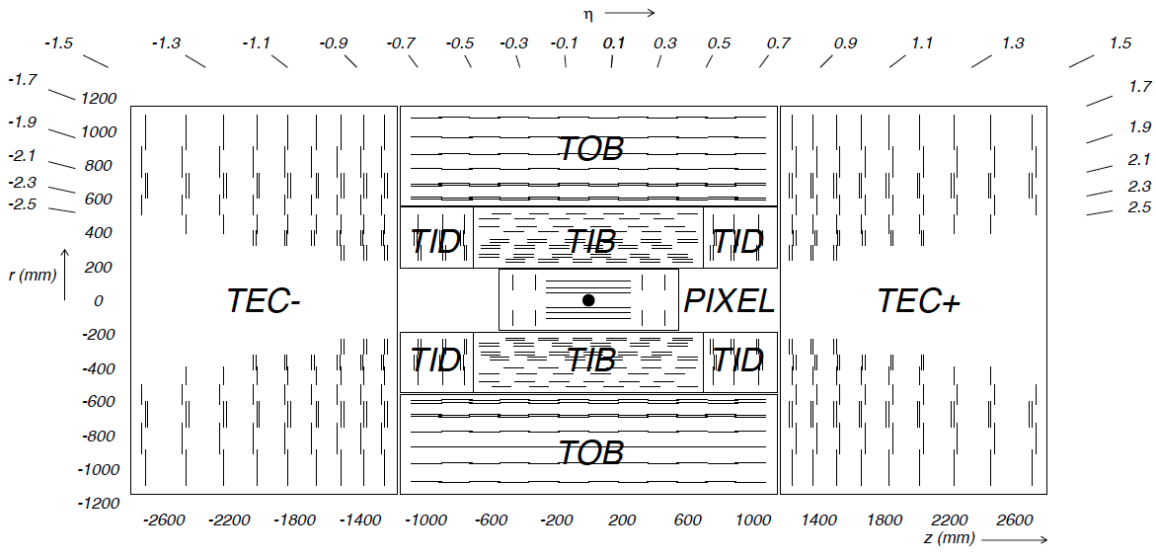

Figure 4.5: Sectional view of the tracker. [77]

4.2.3 Electromagnetic calorimeter

The electromagnetic calorimeter (ECAL) measures the energy of electrons and photons, and covers pseudorapidity regions between -3.0 and 3.0. Electromagnetic showers produced by electrons or photons entering crystals, ionize the crystal atoms, which emit a scintillation light that is collected by photodetectors when they de-excite. It uses 75 848 lead tungstate (PbWO4) crystals, which produce a blue-green scintillation light, with a broad maximum at 420 nm, detected by silicon avalanche photodiodes (APDs) in the barrel region ($|\eta| < 1.479$) and vacuum phototriodes (VPTs) in the endcap region ($1.479 < |\eta| < 3.0$). A preshower detector consisting of two planes of silicon sensors interleaved with a total of $3X_0$ of lead is located in front of the endcap ECAL. A sectional view of the ECAL illustrates its geometry in Fig. 4.6.

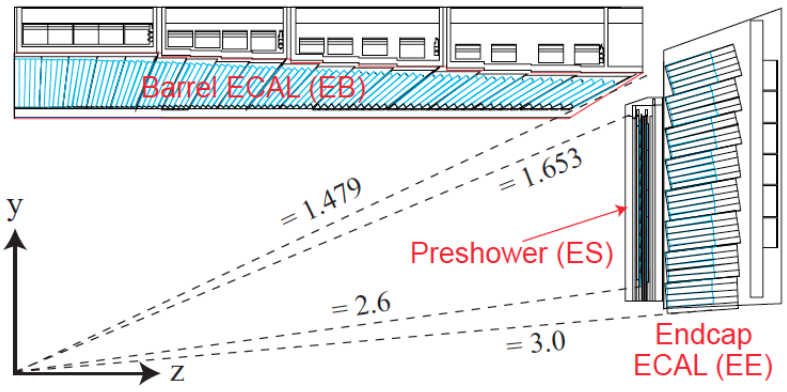

Figure 4.6: Sectional view of the ECAL. The barrel ECAL and the endcap ECAL are composed of lead tungstate crystals, and of silicon avalanche photodiodes or vacuum phototriodes respectively. A preshower is located in front of the endcap ECAL. [83]

Lead tungstate crystals demonstrate a short radiation length (0.89 cm), a high density (8.3 g/cm^3) and a small Molière radius [1] (2.2 cm); this allows the calorimeter to be compact despite its fine granularity. In addition, the scintillation decay time is such that 80% of the light is emitted in 25 ns, the design bunch crossing time. As the scintillation light output depends on the temperature of the crystals, with approximately -1.9% per °C at 18 °C, special care is taken to maintain the temperature stable within ± 0.05 °C. The length of the crystals (23 cm, equivalent to more than 25 times the radiation length) can contain the full electromagnetic showers.

The barrel photodetectors, the APDs, have an active area of 5×5 mm^2. Two of them are glued to every lead tungstate crystal, with a mean gain of 50. In the endcaps, where the radiation rate is higher, one vacuum phototriode, VPT, with a 25 mm diameter, is glued to the back of every crystal, and has a mean gain of 10.2. The signal collected by the photodetectors is converted with an Analog To Digital Converter (ADC). Crystals in the barrel are inclined by 3° in the η- and ϕ-directions to prevent particles from passing through the intersection of two crystals. In the endcaps, crystals are organized in rows and lines in the x- and y-directions.

The preshower detector is used to identify neutral pions, decaying to photon pairs, in a high-pseudorapidity region with $1.653 < |\eta| < 2.6$. The first layer of the preshower consists of lead radiators that initiate electromagnetic showers from incoming photons and electrons, while the second layer is composed of silicon strip sensors, with an active area of 61×61 mm^2 and a nominal thickness of 320 μm, that measure the deposited energy and the transverse shower profiles. Its thickness corresponds to approximately three radiation lengths.

1. Radius of a cylinder containing on average 90% of the shower energy deposition.

The energy resolution of the ECAL, obtained from Gaussian fits to the reconstructed energy, can be parameterized as a function of the energy as:

$$\left(\frac{\sigma}{E}\right)^2 = \left(\frac{S}{\sqrt{E}}\right)^2 + \left(\frac{N}{E}\right)^2 + C^2, \tag{4.7}$$

where the stochastic term S represents statistical fluctuations on the number of secondary particles produced, N is the noise coming from the electronics and digitization, and C is a constant that accounts for calibration errors and for the leak of part of the shower outside of the calorimeter. Without magnetic field and without material in front of the ECAL, the parameters measured in an electron test beam are: $S = 0.028\ \sqrt{\text{GeV}}$, $N = 0.12$ GeV and $C = 0.003$ [84]. For unconverted photons with a transverse energy greater than 100 GeV, the energy resolution provided by the ECAL is better than 0.5%.

4.2.4 Hadronic calorimeter

The hadronic calorimeter (HCAL) is crucial for physics analyses with hadron jets or missing transverse energy. Located around the ECAL, the HCAL extends between $1.77 < r < 2.95$ m up to the magnet coil, where r is the radius in the transverse plane with respect to the beams. Because of the limited space between the ECAL and the magnet, the HCAL needs to be compact and made from materials with short interaction lengths. In addition, to provide a good measurement of the transverse missing energy in the event, it should be as hermetic as possible and extend to large absolute pseudorapidity values. The HCAL is a sampling calorimeter, composed of layers of absorbers and scintillators, that measures destructively the energy of hadron jets.

The architecture of the HCAL is illustrated in Fig. 4.7. The hadron barrel calorimeter (HB), located inside the magnet coil, covers pseudorapidities such that $|\eta| < 1.3$. It is divided in $\eta \times \phi$ towers of dimension 0.087×0.087. The HB is made of sixteen absorber plates, most of them being built with brass while the others are made of stainless steel. Because the thickness of the HB corresponds only to five to ten interaction lengths depending on the pseudorapidity, an outer calorimeter (HO) is added around the magnet to complement the HB, and the total thickness of the combination of the HB and the HO increases to twelve interaction lengths. The hadron endcap calorimeter (HE) covers a pseudorapidity range $1.3 < |\eta| < 3.0$, and is composed of brass absorber plates. Its thickness corresponds to approximately ten interaction lengths. Forward hadron calorimeters (HF) cover the high pseudorapidity regions ($3.0 < |\eta| < 5.2$), which undergo high particle fluxes. They are Cherenkov light detectors made of radiation-hard quartz fibers. The ECAL and the HCAL combined can measure the energy of hadrons with a resolution $\Delta E/E \simeq 100\%\sqrt{E\ [\text{GeV}]} + 5\%$.

4.2.5 Magnet

A superconducting solenoid magnet, with a length of 12.9 m and an inner diameter of 5.9 m, is used to curve the tracks of charged particles. It provides a 3.8 T magnetic

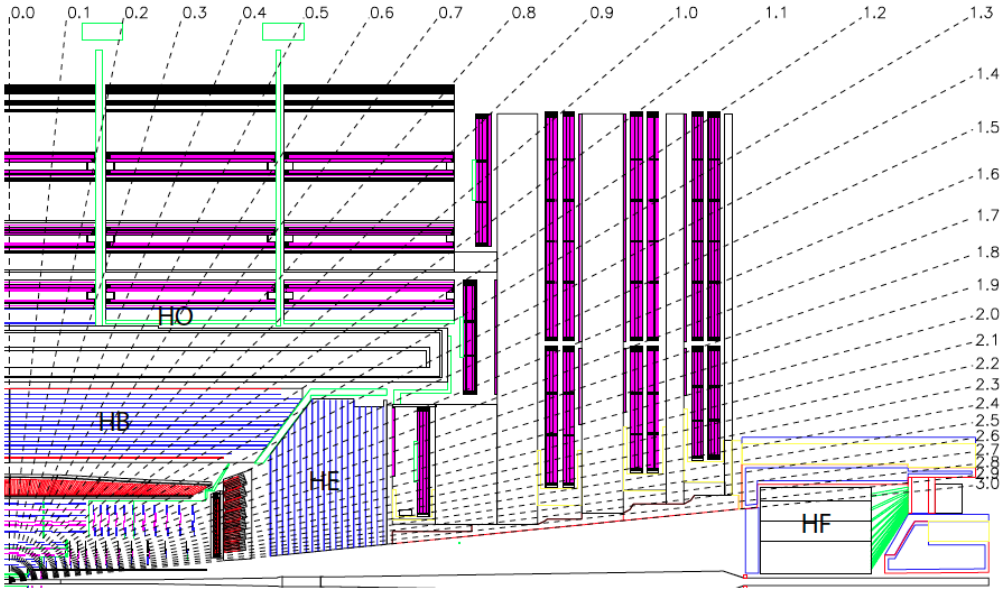

Figure 4.7: Longitudinal view of the CMS detector. The locations of the hadron barrel (HB), endcap (HE), outer (HO) and forward (HF) calorimeters are indicated. [77]

field, with a large bending power. The magnet is made of 2168 turns carrying a 19.5 kA current. It is cooled down with liquid helium.

4.2.6 Muon system

The muon system has to identify muons, to measure their momenta, and to contribute to the event triggering. It relies on three types of gaseous detectors, located outside the magnet solenoid. The gas is composed of a mixture of 40% Ar, 50% CO_2 and 10% CF_4, and gets ionized by the muons. Ions created via this mechanism are accelerated in an electric field and form avalanches in dedicated materials. The barrel part extends to $|\eta| < 1.2$, whereas the endcaps, consisting each of four disks, cover pseudorapidities up to $|\eta| < 2.4$. Each muon station consists of several layers of aluminum drift tubes (DT) in the barrel region and cathode strip chambers (CSC) in the endcap region, complemented by resistive plate chambers (RPC).

In the barrel there are four concentric muon stations consisting of 250 chambers inside the magnet return yoke. The barrel muon system is further divided into five wheels around the beam axis, which are themselves divided in twelve sectors. The exact composition of the muon stations in terms of the number of DTs and their orientation, depends on the position of the station, and is chosen in such a way as to provide a good efficiency for reconstructing muon tracks from muon hits in different stations. The resolution of a single station is close to 100 μm in position and 1 mrad in direction. The muon endcap system regroups 468 CSCs, divided in four stations per endcap. The CSCs, which consist

in multiwire proportional chambers, have a trapezoidal shape and count six gas gaps. Unlike DT, they can support the high rate of neutron-induced background and cope with a large and non-uniform magnetic field.

For low-momenta muons, the momentum resolution is by far dominated by the tracker measurements, while for particles with high momenta (around 1 TeV), the tracker and the muon system both provide a momentum resolution of about 5%. Combining the inner tracker and the muon system, the transverse momentum resolution for particles up to 1 TeV lies between 1 and 5%. Although DTs and CSCs can be used to trigger events based on the p_T of the muons with a good efficiency, their time response is comparable to the design bunch crossing space. Therefore, RPCs, which are double-gap chambers operated in avalanche mode, composed of parallel anode and cathode plates with a gas gap in between, have been introduced in the barrel and endcaps as a dedicated trigger system with a fast response and good time resolution. The position resolution of RPCs is however coarser than that of DTs and CSCs. Six layers of RPC are embedded in the barrel, whereas three layers of RPCs are part of each endcap muon system.

Without complementary information form the tracker, the muon system provides a resolution of about 10% for muons with $|\eta| < 2.4$ and $p_T < 200$ GeV.

4.2.7 Trigger

For a bunch spacing of 25 ns, the beam crossing frequency is 40 MHz. Given the high crossing rate, the large size of an event (about 1 MB), and the fact that typically tens of collisions happen for a same bunch crossing, storing and processing every single event is simply not feasible. The trigger system reduces the rate by selecting events that have a physical interest, based on the characteristics of these events such as the transverse momentum of the particles. The rate reduction by at least a factor of 10^6 is done in two steps: Level-1 (L1) Trigger and High-Level Trigger (HLT). Prescaled triggers, which have loose selection conditions and thus do not permit to keep all events passing these conditions, can be used to study more frequent collisions.

The L1 Trigger, which has a design output rate of 100 kHz and a response time of 3.2 μs, relies on coarse information from the calorimeters and the muon system. Field-Programmable Gate Array (FPGA) technology is mainly exploited for the L1 Trigger hardware, while application-specific integrated circuits (ASICs) and programmable memory lookup tables (LUT) are also used in special cases where speed, density and radiation resistance are of high importance. The first step of the Calorimeter Trigger is local, and consists in measuring the transverse energies in ECAL crystals and HCAL read-out towers, grouped in so-called trigger towers. The Regional Calorimeter Trigger then determines regional candidate electrons or photons (up to $|\eta| = 2.5$), tau veto bits (up to $|\eta| = 3.0$), transverse energy sums, and other information of interest for muons. Finally the highest-rank calorimeter trigger objects in the whole detector are determined by the Global Calorimeter Trigger. The Muon Trigger uses information from the three muon sys-

tems, and covers pseudorapidities $|\eta| < 2.1$. Locally, DT chambers in the barrel provide track segments in the ϕ-projection and hit patterns in the η-projection, while CSCs in the endcaps provide information as three-dimensional track segments. Regionally, complete tracks are made from joining the tracks and hits reported by the DTs and CSCs, and physical parameters are associated to them. RPCs, which have a better timing resolution, contribute also regionally by producing their own track candidates based on regional hit patterns. Globally, the Muon Trigger combines all pieces of regional information from the three subdetectors.

Events passing the L1 Trigger are then processed by the HLT, which performs more complex calculations, based on a combination of information from the different subdetectors. It reduces the rate to about 400 Hz. The HLT is based on software techniques, and is flexible. The full read out information can be accessed at this stage, and processed by a filter farm of about a thousand processors. The events passing the HLT are kept for storage.

4.3 Chapter summary

Experimental setup

The excellent performance of the LHC permitted to collect during its first run about 5, 20 and 3 fb^{-1} of proton-proton data in 2011, 2012 and 2015, at 7, 8 and 13 TeV center-of-mass energies respectively. This thesis is based on the collision data collected by the CMS detector in 2012 essentially, but also includes some analyses of 2011 and 2015 data. CMS is composed of several subdetectors: a tracker, an electromagnetic calorimeter, a hadronic calorimeter and muon chambers. Tau leptons, which are the common point between all analyses presented in this thesis, are reconstructed from information from all subdetectors.

Chapter 5

Event generation, simulation and reconstruction

To search for new physics, observed collision data should be compared to the expectation from SM processes. SM processes, as well as hypothetical signals, can be modeled with Monte Carlo (MC) event simulations. The generated events are then passed through a full simulation of the CMS detector, to model the interactions events undergo before being detected, as well as the detector response. The first part of this chapter concerns generation and simulation. The signatures left inside the detector (or its simulation) by the data (or generated) events need to be reconstructed into physical objects, such as electrons, muons, taus or jets. The reconstruction of the different types of physical objects is described in the second part of the chapter, with an emphasis on the objects used in the physics analyses presented in this thesis.

5.1 Event generation and simulation

Monte Carlo sample generation proceeds through the following steps [85]:

1. **Hard-scattering process.** At the LHC, the central part of the interaction consists in the hard-scattering of the two incoming protons. As the collision actors are rather constituents of the protons, called partons, it is required to extract the momenta of these incoming partons. This is done thanks to parton distribution functions (PDFs), which give the probability that a parton carries a certain fraction of the proton momentum, at a given scale Q^2. The most commonly used PDFs are provided by the CTEQ group. Given the large energy scale, the hard-scattering process itself is computed with the matrix element (ME) formalism in perturbative QCD, at leading order (LO) or next-to-LO (NLO) depending on the generator.
2. **Parton showering.** Parton showering techniques are used to describe the hadronization and radiation of quarks and gluons in the initial and final states. While parton showering can be encapsulated in the matrix element computation, this is however

often not feasible for a large number of final state particles.

3. **Underlying events.** Underlying events, coming from the interactions of the remaining parts of the protons that did not take part in the hard scattering process, are then modeled. They typically consist in soft QCD interactions, and can be modeled from phenomenological inputs.
4. **Hadronization.** When quarks and gluons have low energies, below typically 1 GeV, they cannot be treated as free anymore and the perturbative QCD formalism fails. The hadronization stage models their recombination into hadrons without any color charge.
5. **Hadron and tau decays.** The decay of short-lived particles is then simulated. In particular, tau decays are simulated with Tauola [86], interfaced to a generator that takes care of the previous steps.
6. **Pileup.** To describe the observed data more exactly, pileup interactions, consisting in an additional set of soft inelastic collisions, are added to the main hard scattering process. As it is difficult to predict the distribution of the number of pileup interactions in data, MC datasets are usually generated for a scenario with a higher number of vertices and afterwards reweighted to match the observed distribution of pileup interactions.

Many MC generators have been developed. The ones used in the analyses presented in the next chapters are Madgraph [87], Pythia [88], Powheg [89] and aMC@NLO [90]. Powheg and aMC@NLO can compute NLO matrix elements. The events are then passed through Geant4 [91], which simulates the response of the CMS detector.

5.2 Object reconstruction and identification

The detector response is analyzed to identify physical objects. The particle-flow algorithm used in CMS is described in Section 5.2.1, and is followed by the strictly speaking object reconstruction, with tracks and vertices in Section 5.2.2, jets and b-tagged jets in Section 5.2.3, electrons in Section 5.2.4, muons in Section 5.2.5, taus in Section 5.2.6, and finally missing transverse energy in Section 5.2.7.

5.2.1 Particle-flow

Stable particles are reconstructed in CMS with a particle-flow (PF) algorithm [92, 93], which combines information from all subdetectors under the form of muon tracks, calorimeter clusters and tracks from other charged particles. This is made possible by the high granularity of the detector. The individual PF particles – electrons, photons, muons, charged and neutral hadrons – are then combined to form more complex objects such as hadronically decaying taus, jets, or transverse missing energy.

The track reconstruction algorithm is performed with an iterative tracking strategy, which achieves a high efficiency and a low misidentification rate, and is described more in details in Section 5.2.2. In the calorimeters, a clustering algorithm is performed to

reconstruct neutral particles and to complement the tracking to measure the energy of charged particles among others. The first step of the calorimeter clustering algorithm consists in identifying cells from calorimeter cluster seeds with an energy above a given threshold, while in a second time, topological clusters are built by joining adjacent cells with a minimum energy threshold. PF clusters are then formed from topological clusters; their energies and sizes are determined iteratively based on their distance from each cell. As a single physical particle can create multiple PF elements, such as a track and several calorimeter clusters, a link algorithm has been designed to fully reconstruct particles and to limit double counting. It computes a distance between objects based on characteristics extracted from the iterative tracking and calorimeter clustering algorithms, and determines whether they correspond to different physical objects.

5.2.2 Tracks and vertices

Track reconstruction [94] is based on the collection of hits from the pixel and strip trackers. The Combinatorial Track Finder (CTF) software, which is an adaptation and extension of the Kalman filter, fits tracks from the hits. All tracks are reconstructed after several iterations of the CTF, in an iterative tracking process. In the first iteration, tracks are seeded and reconstructed with very tight criteria; this ensures a low fake rate at the price of a moderate efficiency. In the next iterations, the seeding criteria are loosened to increase the efficiency, while hits unambiguously assigned to the track in the previous steps are removed to keep the fake rate low as a consequence of the reduced combinatorics. A typical iteration proceeds in four steps. First, tracks are seeded from a small number of hits, which determine the five parameters needed to describe the helical path of charged particles in the quasi-uniform magnetic field of the tracker. Second, the track finding step extrapolates the few hits from the seeding stage, adding more hits layer after layer to the track candidate with a Kalman filter. Third, track candidates are fitted with a Kalman filter to provide an estimate of the track trajectory parameters. And finally, some quality cuts are applied to the reconstructed tracks, in order to remove fake tracks not associated with charged particles. The track reconstruction efficiency for single isolated muons is illustrated in the left-hand side part of Fig. 5.1.

Prompt tracks originating from the interaction region are used to reconstruct interaction vertices [95]. They need to satisfy some quality criteria, based for example on their chi-square or on the number of pixel and strip hits. Tracks that are close enough to each other in the interaction region in the z-direction are clustered to form a vertex. If several tracks are assembled, an adaptative vertex fit is performed to determine the vertex characteristics, such as its exact position. The primary vertex reconstruction efficiency distribution, close to 1, is illustrated in the right-hand side part of Fig. 5.1. Weights w between 0 and 1, representing the compatibility of a track with the common vertex, are assigned to each track, and the number of degrees of freedom of the vertex is computed as follows:

$$n_{dof} = 2 \sum_{i=1}^{N_{tracks}} w_i - 3. \tag{5.1}$$

This variable can be used to identify real proton-proton interactions, and to reduce the vertex misidentification rate. The primary vertex is usually considered as the one with the largest scalar sum of track transverse momenta.

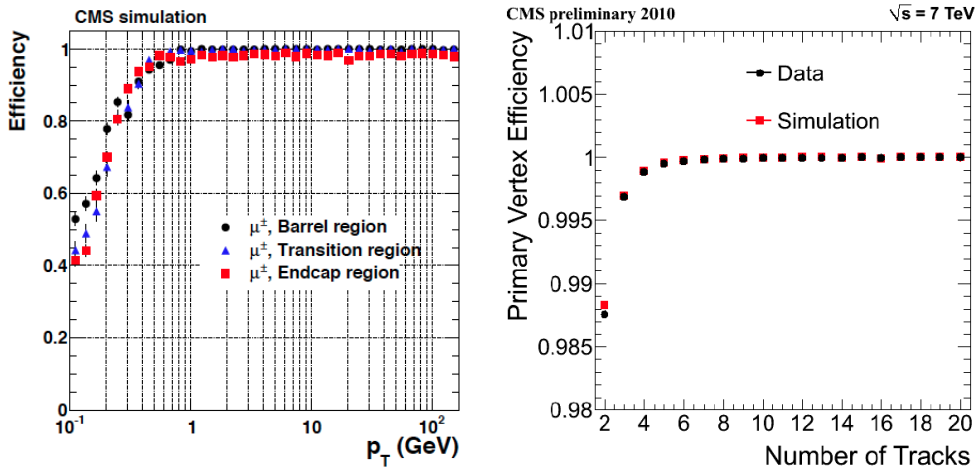

Figure 5.1: Left: Track reconstruction efficiency for single isolated muons in the barrel ($|\eta| < 0.9$), transition ($0.9 < |\eta| < 1.4$) and endcap ($1.4 < |\eta| < 2.5$) regions of the tracker. The efficiency reaches a plateau close to 1 for muons with p_T larger than about 1 GeV. [94] Right: Primary vertex reconstruction efficiency in simulation and 7 TeV data. A plateau is reached for a number of tracks larger than about six. [95]

5.2.3 Jets

Quark and gluon jets are built from PF objects. The anti-k$_T$ algorithm [96] is used to cluster individual objects into jets. It proceeds by defining distances d_{ij} between two entities (particles, pseudojets) i and j, and distances d_{iB} between an entity i and the beam:

$$d_{ij} = \min(k_{ti}^{-2}, k_{tj}^{-2}) \frac{\Delta_{ij}^2}{R^2}, \text{ and} \tag{5.2}$$

$$d_{iB} = k_{ti}^{-2}, \tag{5.3}$$

where k_{ti} and k_{tj} are the transverse momenta of the i and j entities respectively, $\Delta_{ij}^2 = (\phi_i - \phi_j)^2 + (\eta_i - \eta_j)^2$, and R is a cone parameter chosen to be 0.5 in CMS in Run-1 and 0.4 in Run-2. If the smallest distance is of d_{ij}-type, the entities i and j are combined into a new single entity, while if it is of d_{iB}-type, the i entity is considered as a jet and removed from the list of entities. The procedure continues until the entity list is empty. Unlike other jet clustering algorithms, the anti-k$_T$ algorithm produces jets with a conical shape, clustered around the hardest particles and with boundaries resilient with respect to soft radiation.

The jet energies are corrected to ensure a uniform response in η and an absolute calibration in p_T. The objective of the calibration is that the reconstructed jet energy

matches the energy of the generated jet. The correction to the raw p_T of the jet can be decomposed in four multiplicative terms [97]:

- An offset correction, to remove the energy due to particles not involved in the hard-scattering process (pileup particles, detector noise);
- An MC calibration factor, which corrects the reconstructed energy to match the generated MC particle jet energy, based on simulations;
- A residual calibration for the relative energy scale, to correct the energy response as a function of the pseudorapidity, in order for the response to be flat with respect to the pseudorapidity;
- A residual calibration for the absolute energy scale, to make the energy response uniform with the transverse momentum.

B jets, originating from b quark hadronization, can be distinguished from other jets coming from gluons, light-flavor quarks (u, d, s) and c-quark fragmentation using track, vertex and identified lepton information. Different algorithms to tag b jets exist; only the Combined Secondary Vertex (CSV) algorithm is described here as it is used in the physics analyses presented in the next chapters. Because b hadrons typically have a lifetime of $c\tau \simeq 450$ μm, a powerful handle to discriminate between b jets and non-b jets is the existence of a secondary vertex. A secondary vertex is defined as a vertex sharing less than 65% of its tracks with the primary vertex and separated radially from the primary vertex with a significance at least 3σ. In addition, if the radial distance exceeds 2.5 cm and if the mass is compatible with a K^0 or larger than 6.5 GeV, the secondary vertex is rejected. The last condition for secondary vertices is that the flight direction of each candidate is in a cone with $\Delta R = 0.5$ around the jet direction. When no secondary vertex is found, in about 35% of cases for real b jets, the CSV algorithm can use so-called "pseudo-vertices", from tracks with a significance of the impact parameter (IP) larger than 2. If no pseudo-vertex is found, the CSV algorithm proceeds from simple track variables. The list of variables used to identify b jets are, when available in the event [98]:

- If the event has a secondary vertex, a pseudo-vertex or none of them;
- The flight distance significance between the primary and the secondary (or pseudo-) vertex in the transverse plane;
- The number of tracks at the secondary or pseudo-vertex;
- The ratio of the energy carried by tracks at the vertex with respect to all tracks in the jet;
- The pseudorapidities of the tracks at the vertex with respect to the jet axis;
- The 2D IP significance of the first track that raises the invariant mass above the c quark mass;
- The number of tracks in the jet;
- The 3D IP significances for each track in the jet.

A likelihood ratio to reject c jets and another one to reject light-parton jets are combined to form the final CSV discriminator. The efficiency of the CSV algorithm in data and simulations is shown in Fig. 5.2; for the medium working point the efficiency is close to 70% for a mistagging rate of about 1.5%.

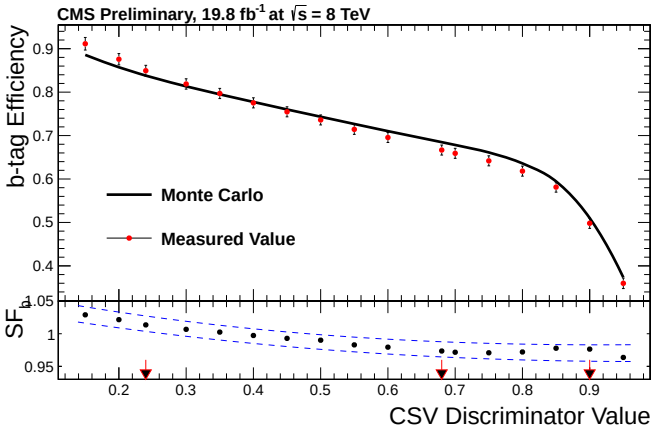

Figure 5.2: B-tagging efficiency as a function of the CSV discriminator threshold, in 8 TeV simulations and data. The arrows indicate the three working points in Run-1. For information, the misidentification probabilities for jets with p_T between 80 and 120 GeV are, for the loose, medium and tight working points respectively, 0.0990±0.0004, 0.0142±0.0002 and 0.0016±0.0001, where the quoted uncertainties are statistical only. [99]

5.2.4 Electrons

Electrons are reconstructed from energy deposits in the ECAL and tracks in the tracker [100]. Special emphasis has to be given to the spread, mostly in the ϕ-direction, of the electron energy in the ECAL caused by photon radiation. Indeed, on average 33% of the electron energy is lost before reaching the ECAL at $\eta = 0$, while up to 86% can be lost when the budget material in front of the ECAL is large (e.g. at $|\eta| = 1.4$).

The clustering of the electron energy in the ECAL proceeds with different algorithms in the barrel and in the endcaps, because the subdetector geometries are different. In the barrel, the hybrid algorithm starts from the seed crystal that contains the largest energy deposit above 1 GeV. Strips of 5×1 crystals in the $\eta \times \phi$ plane are delimited around the seed crystal, and are merged to adjacent strips if their energy exceeds 0.1 GeV. A supercluster is then formed from all the strip clusters that have a seed strip with an energy of at least 0.35 GeV. In the endcaps, the multi 5×5 algorithm starts from a seed crystal with an energy deposit larger than 0.18 GeV. A primary cluster of 5×5 crystals is built around the seed, while secondary clusters of 5×5 crystals are centered around crystals that are not further than 0.3 in the ϕ-direction and 0.07 in the η-direction from the seed crystal. The supercluster is finally built from the primary cluster and all secondary clusters that have an energy deposit larger than 1 GeV, and the energy collected in the preshower is added to it. The position of the supercluster is computed as the energy-weighted mean of the cluster positions, whereas its energy is simply taken as the sum of the energy of all its constituent clusters.

Although electron tracks can be, as any charged particle track, reconstructed from tracker information with the standard Kalman filter (KF) track reconstruction, large energy losses caused by radiation in the tracker material hurt the reconstruction efficiency of such a method. The electron track reconstruction in CMS proceeds in two steps: the seeding and the tracking. The seeding stage uses two complementary algorithms, the results of which are combined. The tracker-based seeding is based on tracks, reconstructed with general tools for charged particles, that are matched to a supercluster after extrapolation towards the ECAL, whereas the ECAL-based seeding starts from a supercluster and selects electron seeds to extrapolate the trajectory towards the collision vertex. The tracking phase is composed of the track building and the track fitting. The energy loss of electrons in the tracker material does not follow a Gaussian distribution, as assumed by the KF algorithm, but a Bethe-Heitler distribution, which has a larger tail. The Gaussian Sum Filter (GSF) algorithm is used to estimate the track parameters from a hit collection obtained with a KF algorithm, by approximating the Bethe-Heitler distribution with a sum of Gaussian distributions.

Tracks and superclusters are matched to each other in GSF electron candidates. ECAL-driven tracks are compatible with a supercluster if their extrapolated tracks in the supercluster from the innermost track position is compatible with the supercluster position within $\Delta\eta \times \Delta\phi = 0.02 \times 0.15$. The compatibility of tracker-driven tracks with superclusters is estimated with a multivariate technique that combines track and supercluster information.

While the electron charge can be easily evaluated from the sign of the GSF track curvature, this leads to a charge misidentification of up to 10% for electrons at large pseudorapidity, because of bremsstrahlung followed by photon conversions. To reduce the charge misidentification rate, two other charge estimates are computed; the final electron charge is then the one given by at least two of the methods. The first alternative method is based on the KF track associated to a GSF track if they share at least one innermost hit, whereas the second one defines the charge sign as the sign of the ϕ differences between the vector joining the beam spot to the supercluster position, and the vector joining the beam spot and the first hit of the electron GSF tracks. The combination of the three charge estimates reduces the charge misidentification rate to 1.5% for reconstructed electrons from Z boson decays.

The electron momentum is evaluated from a weighted combination of the measurements from track parameters – dominant for low energy candidates –, and from supercluster parameters – dominant for high energy candidates.

Several variables may help to discriminate real electrons from hadronic jets. They are classified into three categories: the observables that measure the agreement between ECAL and tracker measurements (such as $\Delta\eta_{in}$ and $\Delta\phi_{in}$, respectively the distances in η and ϕ between the superscluster and the track direction extrapolated from the primary

Working point	Electron p_T	$\|\eta\| < 0.8$	$0.8 \leq \|\eta\| < 1.479$	$1.479 \leq \|\eta\|$
Very loose	-	0.500	0.120	0.600
Loose	$p_T \leq 20$ GeV	0.925	0.915	0.965
	$p_T > 20$ GeV	0.905	0.955	0.975
Tight	$p_T \leq 20$ GeV	0.925	0.915	0.965
	$p_T > 20$ GeV	0.925	0.975	0.985

Table 5.1: Thresholds on the BDT output used to define the very loose, loose and tight electron identification.

vertex position to the ECAL), the observables based on calorimeter information only (such as the ratio between hadronic and electromagnetic energy around the seed cluster, H/E) and the observables based on tracking measurements (such as the compatibility between the KF- and GSF-fitted tracks). Two identification methods exist: the cut-based electron identification directly cuts on the variables presented before, while the MVA identification combines them in a BDT to obtain a final discriminator on which a cut is applied. The MVA identification typically has a better performance as shown in Fig. 5.3. The thresholds on the BDT output used to define the very loose, loose and tight MVA electron identifications are indicated in Tab. 5.1; they depend on the electron transverse momentum and pseudorapidity.

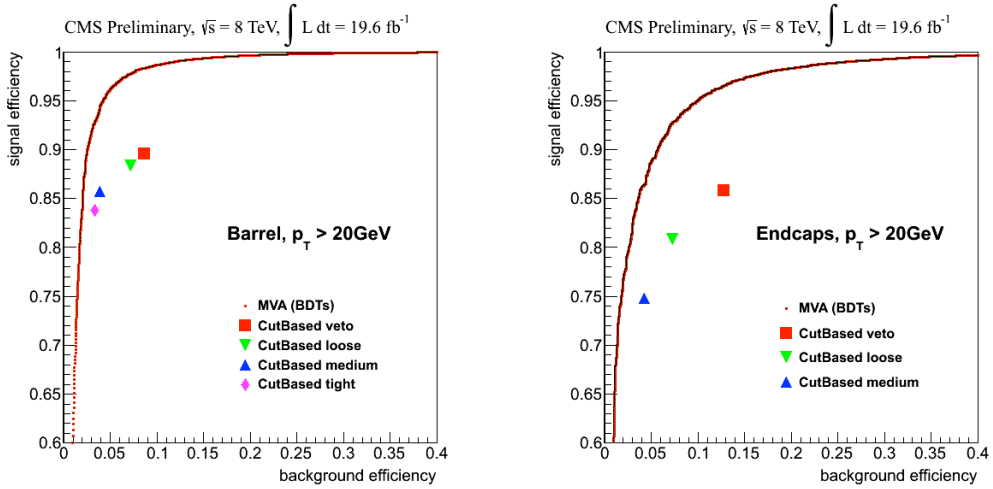

Figure 5.3: Electron identification performance for the MVA-based (continuous line) and cut-based (one symbol for every working point) identification in terms of signal and background efficiencies, in the barrel (left) and endcaps (right). The performance is computed for electrons with p_T greater than 20 GeV. The signal efficiency is measured for electrons in simulated $Z \to ee$ events, whereas the background efficiency is measured for jets reconstructed in data. The background efficiency is lower for the MVA-based identification relative to the cut-based identification, for a same signal efficiency. [100]

The electron absolute isolation, used to reject non-prompt or misidentified leptons, is defined as follows:

$$I = \sum_{charged} p_T + \max\left(0, \sum_{neutral} p_T + \sum_{\gamma} p_T - \frac{1}{2} \sum_{charged,PU} p_T\right), \tag{5.4}$$

where $\sum_{charged} p_T$ is the scalar sum of the transverse momenta of all charged particles originating from the primary vertex and located in a cone with $\Delta R = 0.4$ around the electron direction. The sums $\sum_{neutral}$ and $\sum_{\gamma}$ are the equivalent for neutral hadrons and photons respectively. The last term represents so-called $\delta\beta$ corrections, which remove the contribution from pileup vertices from the neutral isolation: neutral contributions from pileup vertices are estimated to amount to half of the scalar p_T sum of charged particles from pileup vertices inside the isolation cone [1]. The relative isolation of an electron is simply the ratio between its absolute isolation and its transverse momentum.

5.2.5 Muons

Muons are reconstructed from tracks in the inner tracker (tracker tracks), and from tracks in the muon system (standalone-muon tracks) [101]. The global muon reconstruction associates tracker tracks to stand-alone muon tracks to form global-muon tracks by combining with a KF filter the hits from both types of tracks. The tracker muon reconstruction starts from tracker tracks and extrapolate them to the muon system, where a muon segment should be found. While the global muon reconstruction is especially efficient for muons leaving hits in several muon stations, the tracker muon reconstruction is more efficient for low p_T muon candidates. The efficiency for reconstructing a muon as global or tracker muon is as high as 99%.

Different identification working points can be used in physics analyses. To be identified as "loose", a muon candidate should be reconstructed as a PF muon, and to be either a global or a tracker muon. "Medium" muons, used in Run-2 analyses, should be loose muons, and have a segment compatibility probability between the tracker and muon tracks larger than 0.451 or pass the following set of requirements:

- To be global muons;
- The normalized chi-square of their global tracks is less than 3;
- χ^2 of the compatibility between the position of the standalone and trackers tracks less than 12;
- χ^2 from the kink finder on the inner track less than 20 (used to remove muons from decays in flight);
- Segment compatibility probability between the tracker and muon tracks larger than 0.303.

Finally, tight muons are global and PF muons that satisfy the following requirements:

- $\chi 2$/number of degrees of freedom of the global muon track fit, using tracker and muon chamber hits, less than 10;

1. The ratio of neutral to charged isolation from pileup vertices is estimated from MC simulations.

– Muon segments present in at least two muon stations;
– Transverse impact parameter d_{xy} of the tracker track with respect to the primary vertex less than 2 mm;
– Longitudinal distance d_z of the tracker track with respect to the primary vertex less than 5 mm;
– Non zero number of pixel hits;
– At least five tracking layers with hits.

The efficiency of the tight muon identification is shown in Fig 5.4. In practice, the choice of the identification working point depends on the analysis.

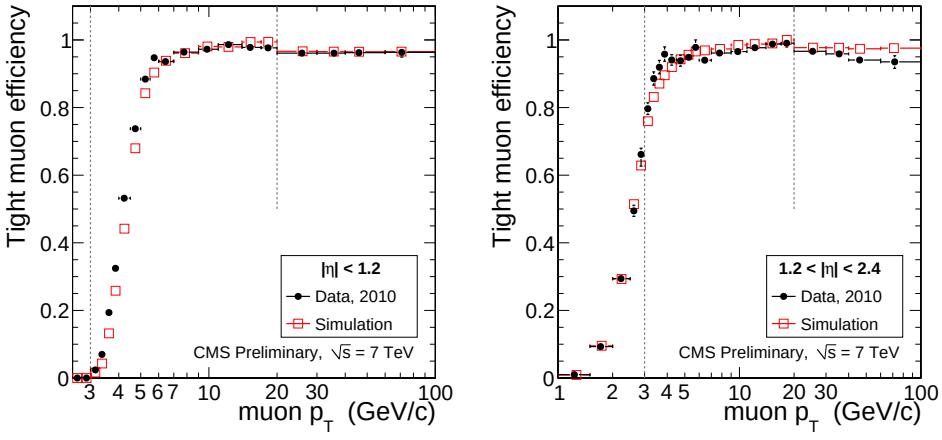

Figure 5.4: Efficiency of the tight muon identification in 2010 data (black) and simulation (red), in the barrel (left) and endcaps (right). [101]

The absolute and relative $\delta\beta$-corrected isolations for muons are computed exactly as for electrons in equation (5.4).

5.2.6 Taus

Muons and electrons originating from tau decays are reconstructed with the standard tools for electron and muon reconstruction described in Sections 5.2.4 and 5.2.5 respectively. In about two thirds of cases, taus decay hadronically; they are in this case reconstructed with the Hadrons plus Strips (HPS) algorithm [102, 103]. The HPS algorithm builds taus from tracks, and energy deposits in ECAL strips. The main handles to discriminate hadronically decaying taus from quark and gluon jets are the track multiplicity – taus have only one or three tracks –, and the isolation – taus are on average more collimated and isolated than quark and gluon jets. The efficiency in identifying hadronically decaying taus is typically between 45 and 70%, for misidentification rates of a jet as a tau of the order of 1%. The HPS algorithm is described in more details in Chapter 6.

5.2.7 Transverse missing energy

Neutrinos and other hypothetical neutral weakly interacting particles cannot be detected by CMS. However, some information about their presence can be gathered from the detection of a momentum imbalance in the transverse plan to the beam axis. The missing transverse energy is noted $\vec{\not{E}}_T$, while its magnitude is referred to as $\not{E}_T$. The $\vec{\not{E}}_T$ measurement [104] strongly relies on the reconstruction of all other physics objects, and is sensitive to a wide range of effects: mismeasurement or misidentification of physics objects, detector noise or malfunctions, pileup interactions, ...

The most widely used type of $\vec{\not{E}}_T$ in CMS is the particle-flow (PF) $\vec{\not{E}}_T$, which is the negative vectorial sum over the transverse momenta of all PF particles. A bias in the $\not{E}_T$ measurement can be introduced for several reasons, such as the nonlinearity of the response of the calorimeter for hadronic particles, or the minimum energy thresholds in the calorimeters. This bias is found to be greatly reduced by correcting the p_T of jets with an electromagnetic energy fraction less than 0.9 and a corrected p_T greater than 10 GeV, to the particle-level p_T. In addition, another bias comes from the pileup interactions. This can be corrected by subtracting from the $\vec{\not{E}}_T$ a certain fraction $f(\vec{v})$ of $\vec{v}$, the vectorial p_T sum of charged particles associated to each pileup vertex:

$$\vec{\not{E}}_T^{corr} = \vec{\not{E}}_T - \sum_{PU} f(\vec{v})\vec{v}. \tag{5.5}$$

Finally, an asymmetry in the ϕ variable is observed for data and simulated events, and is found to be related to the number of reconstructed vertices N_{vtx}. The $\vec{\not{E}}_T$ projection in the x- and y-directions are independently corrected by some functions of N_{vtx}.

Another type of $\not{E}_T$, used in the physics results presented in the next chapters, is based on an MVA method. It is designed to reduce the influence of pileup interactions, which do not have significant $\not{E}_T$ but degrade the $\not{E}_T$ measurement resolution by 3.3-3.6 GeV on average for each single pileup vertex. The MVA $\vec{\not{E}}_T$ relies on the identification of jets originating from pileup interactions with a MVA discriminator that takes as input jet shape variables and vertex information. In Z boson decay events, the transverse energy can be decomposed in three components, as illustrated in Fig. 5.5: a well-measured momentum scale $\vec{q_T} = \vec{p_T}(l^+) + \vec{p_T}(l^-)$, an error-prone hadronic recoil $\vec{u_T}$, which is the vectorial sum of all reconstructed PF particles except the leptons originating from the Z boson decay, and the missing transverse energy $\vec{\not{E}}_T$:

$$\vec{q}_T + \vec{u}_T + \vec{\not{E}}_T = \vec{0}. \tag{5.6}$$

The hadronic recoil can be decomposed in two components parallel or perpendicular to $\vec{q}_T$ direction: $\vec{u}_T = \vec{u}_\perp + \vec{u}_\parallel$. The MVA $\not{E}_T$ is computed as a correction to the hadronic recoil $\vec{u_T}$. A first BDT is trained to correct the direction of $\vec{u_T}$ to correspond to the generated direction in simulated Z+jets events, while a second BDT estimates the magnitude after direction corrections. The corrected hadronic recoil is added to $\vec{q}_T$ to give the negative

MVA $\not\!\!E_T$. In comparison with the PF $\vec{\not\!\!E}_T$, the MVA $\vec{\not\!\!E}_T$ resolution is much less sensitive to the number of interaction vertices, as shown in Fig. 5.6, which may lead to an improvement of the sensitivity of physics analyses such as $H \to \tau\tau$ by as much as 20%.

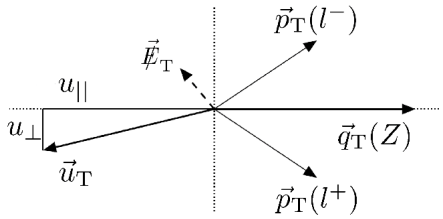

Figure 5.5: Schematic view of the Z boson transverse momentum $\vec{q}_T$, the hadronic recoil $\vec{u}_T$ with its parallel and perpendicular projections along $\vec{q}_T$, and the $\vec{\not\!\!E}_T$. [104]

Artificially large $\not\!\!E_T$ can be measured because of spurious detector signals. Sources of fake $\not\!\!E_T$ are:

- Dead cells in the ECAL;
- Beam-halo particles;
- Particles striking sensors in the ECAL barrel detector;
- Noise from HCAL hybrid photodiode and readout box electronics;
- Direct particle interactions with light guides and photomultipliers tubes in the forward calorimeter;
- High-amplitude anomalous pulses in the ECAL endcaps;
- A misfire of the HCAL laser calibration system;
- A defective track reconstruction, from coherent noise in the silicon strip tracker.

Dedicated algorithms are used to identify and remove these events with fake $\not\!\!E_T$.

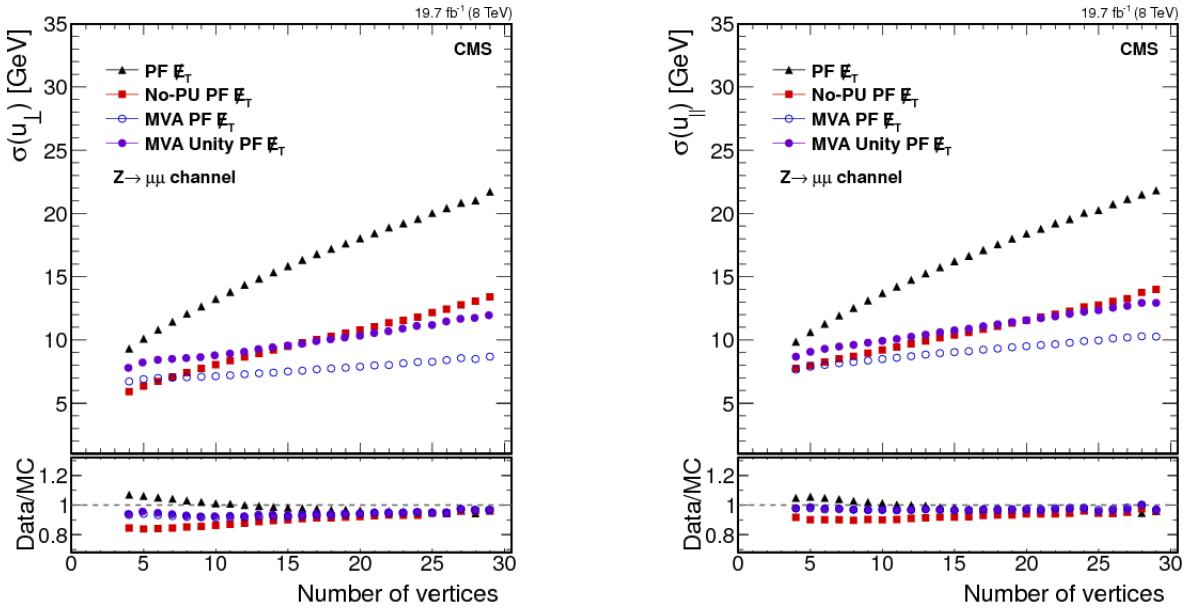

Figure 5.6: Hadronic recoil resolution as a function of the number of interaction vertices, in the perpendicular (left) and parallel (right) directions to the transverse momentum of the Z boson, in $Z \to \mu\mu$ events, for the PF $\vec{\not{E}}_T$, the MVA $\vec{\not{E}}_T$, and two other $\vec{\not{E}}_T$ types not described in the text: no-PU PF $\vec{\not{E}}_T$ and MVA unity PF $\vec{\not{E}}_T$. [104]

5.3 Chapter summary

Event generation simulation and reconstruction

This chapter describes how events are generated and simulated, and how the physics objects (electrons, muons, taus, jets, $\not{E}_T$) used in the analyses presented in the next chapters, are reconstructed and identified.

Chapter 6

Tau lepton reconstruction and identification

Tau leptons play an important role in physics analyses in the scalar sector. In the SM, $H \to \tau\tau$ is the most sensitive fermionic decay channel of the scalar boson, and provides the most precise test of its Yukawa couplings. Additionally, in some models with an extended scalar sector, such as the MSSM, the couplings of high mass scalars to tau leptons can be enhanced for some choices of the model parameters. Experimentally, identifying and reconstructing tau leptons is however challenging, as they are, unlike other leptons, heavy enough to decay hadronically. Table 6 shows the tau decay modes and their corresponding branching fractions. In about one third of cases, tau leptons decay leptonically, to an electron, an electronic neutrino and a tauic neutrino, or to a muon, a muonic neutrino and a tauic neutrino. The other decay modes are hadronic, with, in the dominant modes, one or three charged hadrons (pions or kaons), zero to two π^0 and one tauic neutrino. Some decay modes involve intermediary resonances, such as $\rho(770)$ and $a_1(1260)$. Taus decaying hadronically will be denoted by τ_h. Leptonically decaying taus are identified through standard electron and muon identification algorithms, while hadronic taus are reconstructed in CMS with the Hadrons Plus Strips (HPS) algorithm. The next sections present the HPS algorithm, as well as the measurement of its performance with data collected in Run-1 and Run-2.

6.1 HPS algorithm description

The HPS algorithm [102, 103] is designed to identify hadronically decaying taus. The main challenge lies in the similarity between hadronic taus and jets from QCD multijet processes, which have a production cross section five orders of magnitude larger than the Drell-Yan process at the LHC. The first step of the HPS algorithm is the reconstruction, where it is checked that the tau candidate topology is compatible with one of the hadronic tau decay modes. The next step, the identification, rejects quark or gluon jets, electrons, or muons that might have been wrongly identified as hadronic taus.

Decay mode	Resonance	$\mathcal{B}$ [%]
$\tau^- \to e^- \bar{\nu}_e \nu_\tau$		17.8
$\tau^- \to \mu^- \bar{\nu}_\mu \nu_\tau$		17.4
$\tau^- \to h^- \nu_\tau$		11.5
$\tau^- \to h^- \pi^0 \nu_\tau$	$\rho(770)$	26.0
$\tau^- \to h^- \pi^0 \pi^0 \nu_\tau$	$a_1(260)$	10.9
$\tau^- \to h^- h^+ h^- \nu_\tau$	$a_1(260)$	9.8
$\tau^- \to h^- h^+ h^- \pi^0 \nu_\tau$		4.8
Other hadronic modes		1.8

Table 6.1: Tau decay modes, their approximate branching fractions, and the eventual intermediary resonances. The symbol h stands for kaons or pions. Charge conjugation is implied. [9]

6.1.1 Reconstruction

Tau candidates are reconstructed from a combination of tracks identifying charged hadrons $h^\pm$, and ECAL energy deposits identifying π^0. The charged tracks are required to have a p_T greater than 0.5 GeV and to be compatible with the hypothetical production vertex of the τ_h candidate ($|d_z| < 0.4$ cm and $d_{xy} < 0.03$ cm with respect to the vertex closest to the leading charged particle within the jet). The dimensions of the ECAL strips in the $\eta \times \phi$ plan are 0.05×0.20; the widening in the ϕ direction accounts for the bending in the magnetic field of the electrons/positrons produced by the conversion of photons from $\pi^0 \to \gamma\gamma$ decays. The electrons and photons used to build the ECAL strips are required to have transverse momenta greater than 0.5 GeV, and the total transverse momentum of a strip needs to be larger than 2.5 GeV to be considered in the HPS algorithm. Hadronic taus are reconstructed in one of these four topologies:

- **Three prongs** - $h^-h^+h^-$: Three charged tracks, compatible with originating from the same event vertex, are required. The charges of the three tracks should not be all identical, and their invariant mass should lie between 0.8 and 1.5 GeV. This topology aims at reconstructing both $\tau^- \to h^-h^+h^-\nu_\tau$ and $\tau^- \to h^-h^+h^-\pi^0\nu_\tau$ decays. In the latter case however, the algorithm efficiency is low because the neutral pion energy is considered as part of the isolation, which often leads the tau candidate to fail the second step of the HPS algorithm (see Section 6.1.2).
- **One prong plus two strips** - $h^-\pi^0\pi^0$: The mass of the tau candidate formed by the track and the strips should satisfy: $0.4 < m_\tau < 1.2\sqrt{p_T(\text{GeV})/100}$ GeV. The p_T dependence in the upper limit accounts for resolution effects. If the transverse momentum is less than 100 GeV or greater than 1111 GeV, the upper limit is fixed to 1.2 or 4.0 GeV respectively.
- **One prong plus one strip** - $h^-\pi^0$: The tau candidate built from the track and the ECAL strip should have a mass such that $0.3 < m_\tau < 1.3\sqrt{p_T(\text{GeV})/100}$ GeV. If the transverse momentum is less than 100 GeV or greater than 1044 GeV, the upper limit is fixed to 1.3 or 4.2 GeV respectively.
- **One prong** - h^-: The reconstructed visible tau mass, m_τ is set to the mass of a charged pion.

All charged hadrons and ECAL strips are required to lie within a signal cone with $\Delta R = 3.0/p_T(\text{GeV})$ around the momentum vector of the tau candidate [1]. This so-called "shrinking cone algorithm" takes into account the fact that the decay products of taus with higher p_T are more collimated. If a tau candidate can be reconstructed in more than one topology and pass all selection criteria described above, the topology that gives the highest p_T for the tau candidate is kept. Hadronic taus that are reconstructed as described above are said to pass the decay mode finding discriminator.

6.1.2 Identification

Jet rejection - Isolation

Genuine hadronically decaying taus are typically more collimated and isolated than quark and gluon jets that have passed the reconstruction step; this is the main handle to differentiate these physics objects. Two types of isolations have been designed: cut-based and MVA-based.

The cut-based isolation is measured as the scalar sum of the transverse momenta of charged particles with $p_T > 0.5$ GeV and photons with $E_T > 0.5$ GeV within a cone centered around the tau candidate and with a radius $\Delta R = 0.5$. The charged particles are further required to be compatible with originating from the tau candidate production vertex ($|d_z| < 0.2$ cm along the beamline, $d_{xy} < 0.03$ cm in the transverse plan), in order to reduce the contribution from pileup jets. So-called $\Delta\beta$ corrections are applied to remove the contribution of pileup from the photon isolation; they are computed as the scalar sum of the transverse momenta of charged particles in a cone with $\Delta R < 0.8$ around the tau candidate and with a distance larger than 0.2 cm in the beamline direction from the tau candidate production vertex, and are scaled by a factor 0.46 to make the tau identification efficiency independent from pileup. The tau candidate isolation, I_τ, reads:

$$I_\tau = \sum p_T^{charged}(|d_z| < 0.2 \text{ cm}) + \max(p_T^\gamma - \Delta\beta, 0), \tag{6.1}$$

with $\Delta\beta$ corrections computed as follows:

$$\Delta\beta = 0.46 \times \sum p_T^{charged}(|d_z| > \ 0.2 \text{ cm}). \tag{6.2}$$

The loose, medium and tight isolation working points correspond respectively to I_τ less than 0.8, 1.0 and 2.0 GeV.

The MVA-based discriminator, in addition to isolation criteria, also takes benefit from the fact that taus have a non negligible lifetime compared to the secondary vertex resolution in the CMS detector: $c\tau$=87 μm. A BDT discriminator is built to distinguish genuine hadronic taus from quark and gluon jets. The input variables, illustrated in Fig. 6.1, are:

– The charged particle energy in the isolation cone $p_T^{charged}$;
– The neutral particle energy p_T^γ in the isolation cone;

1. The lowest and highest ΔR considered are 0.05 and 0.10.

- The reconstructed tau decay mode (h^-, $h^-\pi^0$, $h^-\pi^0\pi^0$ or $h^-h^+h^-$);
- The transverse impact parameter d_0 of the leading track of the tau candidate and its significance d_0/σ_{d_0};
- The distance between the tau production and the tau decay vertices, $|\vec{r}_{SV} - \vec{r}_{PV}|$, and its significance, in the case of three-prong tau candidates;
- A boolean indicating if a tau decay vertex has been reconstructed;
- The tau candidate pseudorapidity;
- The tau candidate transverse momentum;
- The $\Delta\beta$ corrections.

The BDT is trained on MC samples: signal events come from $Z \to \tau\tau$, $Z' \to \tau\tau$ and $W' \to \tau\nu_\tau$ and the background events from W+jets and QCD multijet simulations. The Z' and W' samples in addition to the SM Drell-Yan process permit to cover a large p_T range for the tau candidate, between 20 and 2000 GeV. The BDT output is shown in Fig. 6.2, and illustrates that a good discrimination between hadronic taus, and quark and gluon jets can be achieved. Different working points are defined based on the BDT output.

Muon rejection

Muons have a high probability to be misidentified as hadronic taus in the h^- decay mode. A cut-based and an MVA-based discriminators are designed to separate muons from hadronic taus. Two cut-based working points are defined:

- **Loose**: The tau candidate does not pass this working point if the ECAL and HCAL energy deposits associated to its leading track is less than 0.2 times the momentum of this track, or if there are track segments in more than one muon station within a cone with $\Delta R = 0.5$ around the tau direction;
- **Tight**: The tau candidate does not pass this working point if it fails the loose working point, or if hits within a cone with $\Delta R = 0.5$ around the tau direction are found in the CSC, DT or RPC chambers of the two outermost muon stations.

Meanwhile, the BDT takes as input the following variables:

- ECAL and HCAL energy deposits of the leading charged particle of the tau candidate;
- ECAL and HCAL energy deposits of any charged particle or photon of the tau candidate;
- The fraction of the tau energy carried by the leading charged particle;
- The number of track segments in the muon system in a cone with $\Delta R = 0.5$ around the tau direction;
- The number of muon stations in the DT, CSC or RPC, that have a least one hit detected within a cone with $\Delta R = 0.5$ around the tau direction;
- The pseudorapidity of the tau candidate.

The BDT is trained on $Z/\gamma^* \to \tau\tau$, $Z/\gamma^* \to \mu\mu$, $Z' \to \mu\mu$, $W \to \tau\nu$, $W \to \mu\nu$, $t\bar{t}$, $H \to \tau\tau$, $Z' \to \tau\tau$, $W' \to \tau\nu$ and $W' \to \mu\nu$ events.

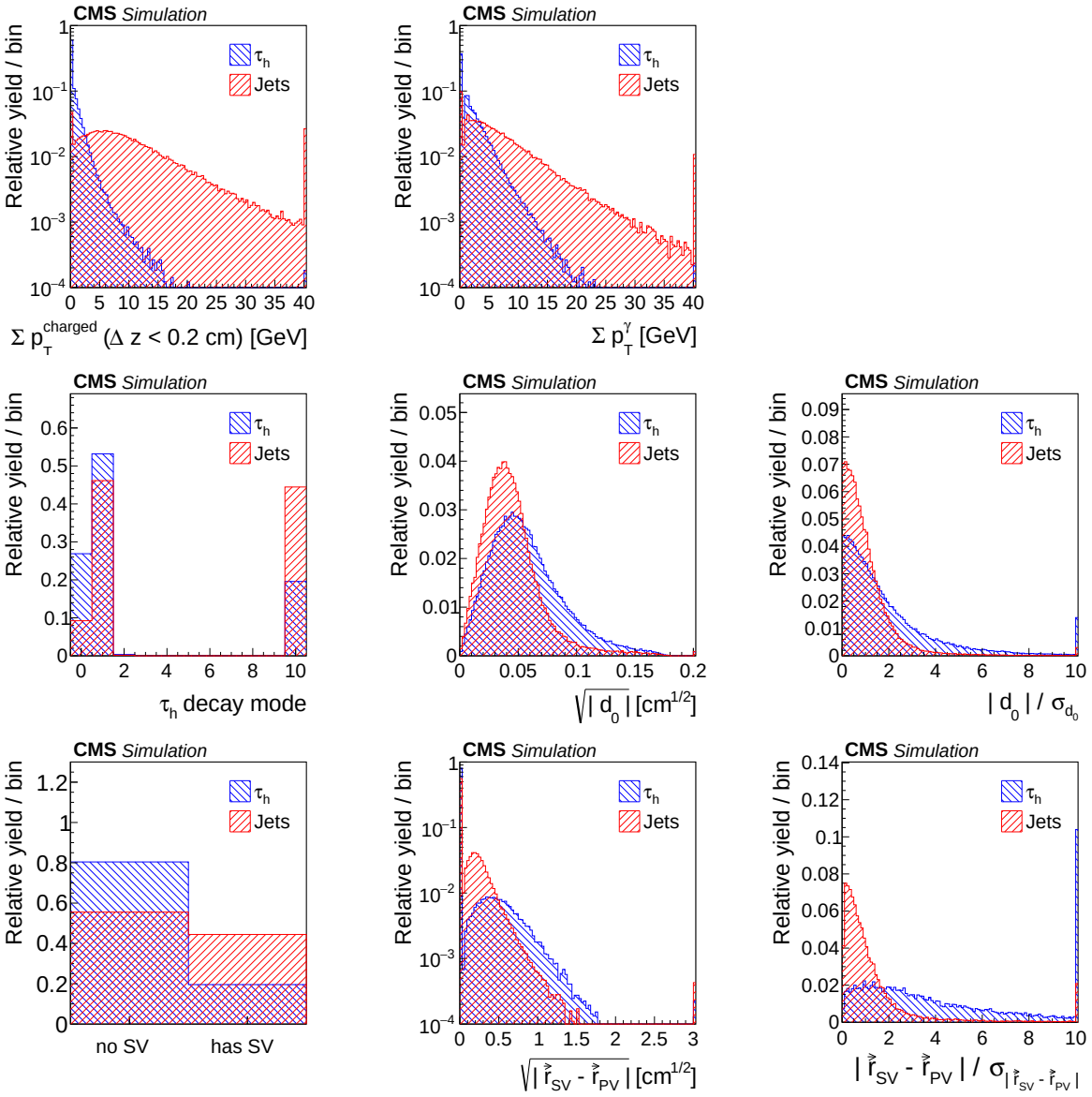

Figure 6.1: Input variables distributions, normalized to unity, for the MVA-based isolation discriminator for simulated $Z/\gamma^* \to \tau\tau$ (blue) with real hadronic taus and W+jets (red) events with jets. In the τ decay mode plot the entry 0 represents the decay mode "one prong", 1 and 2 represent the decay modes "one prong plus one strip " and "one prong plus two strips" respectively and the entry 10 represents the "three prongs" decay mode. [103]

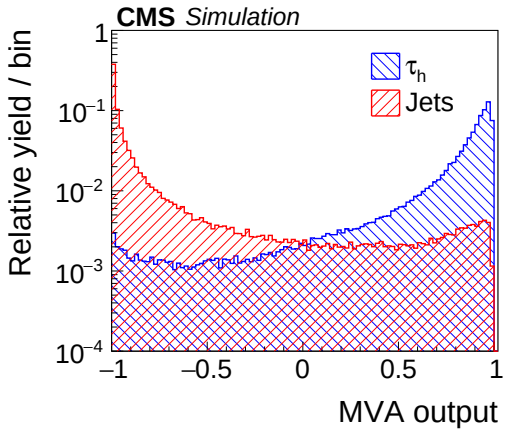

Figure 6.2: BDT output of the MVA-based isolation including tau lifetime information, for simulated $Z/\gamma^* \to \tau\tau$ (blue) with real hadronic taus and W+jets (red) events with quark and gluon jets. [103]

Electron rejection

Electrons also have a high probability to be misidentified as hadronic taus in the h^- decay mode, or in the $h^-\pi^0$ if they radiate a bremsstrahlung photon that converts. A BDT is trained to discriminate between electrons and hadronic taus, with $Z/\gamma^* \to \tau\tau$, $Z/\gamma^* \to ee$, $Z' \to ee$, $W \to \tau\nu$, $W \to e\nu$, $t\bar{t}$, $H \to \tau\tau$, $Z' \to \tau\tau$, $W' \to \tau\nu$ and $W' \to e\nu$ event samples. It takes as input the following variables:

- The electromagnetic energy fraction $E/(E+H)$, defined as the ratio of the energy deposits associated to the tau candidate in the ECAL, and ECAL plus HCAL together;
- E/P and H/P, where E and H are respectively the energy in the ECAL and HCAL of the leading track of the tau candidate, and P is the transverse momentum of this track;
- E^γ/E_τ, the fraction of the tau candidate energy carried by photons;
- $F_{brem} = (P_{in} - P_{out})/P_{in}$, where P_{in} and P_{out} are the GSF track momentum measured by the curvature of the track at the innermost and outermost position;
- $\sum E_\gamma/(P_{in} - P_{out})$, the ratio between the bremsstrahlung photon energy measured in the ECAL and in the tracker;
- $(N_{hits}^{GSF} - N_{hits}^{KF})/(N_{hits}^{GSF} + N_{hits}^{KF})$, where N_{hits}^{GSF} is the number of hits in silicon pixel plus strip tracking detector associated to the track reconstructed by the GSF algorithm, and N_{hits}^{KF} is its equivalent for the Kalman filter algorithm;
- The mass of the tau candidate;
- $\chi^2/ndof$ of the GSF track;
- The pseudorapidity and the transverse momentum of the tau candidate;
- The transverse momentum, its significance and the pseudorapidity of the GSF track;
- The distances in the η and ϕ directions between the GSF track and the nearest boundary between ECAL modules.

These variables characterize the compactness and the shape of energy deposits in the ECAL, the particle multiplicity, and the level of bremsstrahlung emitted. Any tau candidate in the non-instrumented region between the ECAL barrel and endcaps ($1.446 < |\eta| < 1.558$) does not pass the electron rejection.

6.2 HPS algorithm performance in Run-1

The expected performance of the HPS algorithm is measured in MC samples, as described in Section 6.2.1. The results of the performance measurements with data collected in 2012 with the CMS detector are presented in the following sections.

6.2.1 Expected performance

The expected performance of the HPS algorithm in terms of efficiency and misidentification rates, averaged over the p_T and η of taus, is detailed in Tab. 6.2. The isolation efficiency depends on the working point, and is typically of the order of 50%, for $j \to \tau_h$ misidentification rates at the percent or permille level, as shown in Fig. 6.3. The efficiency for taus to pass the discrimination against electrons varies between 60 and 95% depending on the working point, and the corresponding $e \to \tau_h$ misidentification rates range from about 3×10^{-4} to 2×10^{-2}. Finally an efficiency of almost 100% is obtained for taus to pass the discrimination against muons, while the $\mu \to \tau_h$ misidentification rates are below the permille level. The working points to be used in the physics analyses are a case-by-case choice that depends on the expected level of backgrounds. In about 90% of cases, taus are reconstructed in their true decay mode, with no dependence on the number of reconstructed vertices.

6.2.2 Tau identification efficiency in data

Measuring the tau identification efficiency in data is necessary for all physics analyses that study final states with taus, as scale factors have to be applied to simulations to correct for potential differences between data and MC simulations. In addition, the uncertainty on the scale factor has to be considered as a nuisance parameter when extracting the results.

The tau identification efficiency is measured in $Z/\gamma^* \to \tau_h\tau_\mu$ and in $t\bar{t} \to bb\mu\tau_h$ events. Even though the $Z/\gamma^* \to \tau_h\tau_\mu$ process has a larger cross section than $t\bar{t} \to bb\mu\tau_h$ and less backgrounds contributing to the final state, allowing for a more precise result, the measurement in $t\bar{t} \to bb\mu\tau_h$ events is strongly motivated. First, hadronic taus in $t\bar{t}$ events have typically larger transverse momenta than hadronic taus originating from the Drell-Yan process, as illustrated in Fig. 6.4, which makes the measurement in $t\bar{t}$ events sensitive to larger tau transverse momenta. Second, the jet activity, which may spoil the tau isolation, is larger in $t\bar{t}$ than in Drell-Yan events; both measurements thus probe different topologies. Finally, the measurement in $t\bar{t}$ events is a precious cross-check of the measurement in $Z/\gamma^* \to \tau_h\tau_\mu$ events. This is particularly interesting because the tau identification measurements are mainly used in $H \to \tau\tau$ analyses, which have a selection

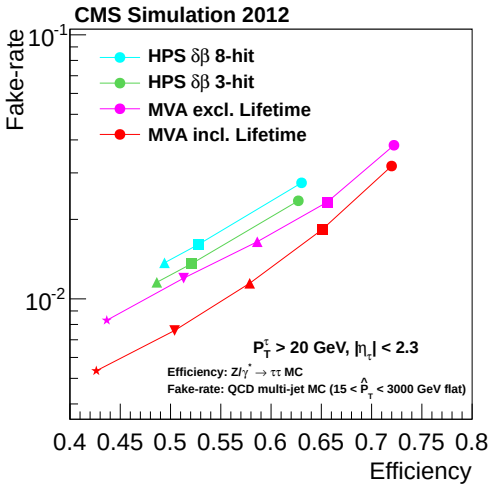

Figure 6.3: Expected performance of the HPS algorithm in terms of efficiency (measured in $Z/\gamma^* \to \tau\tau$ MC simulations) and $j \to \tau_h$ misidentification rate (measured in QCD multijet MC samples). The cut-based isolation described in the text corresponds to the green line and the MVA-based isolation including lifetime information to the red line. [105]

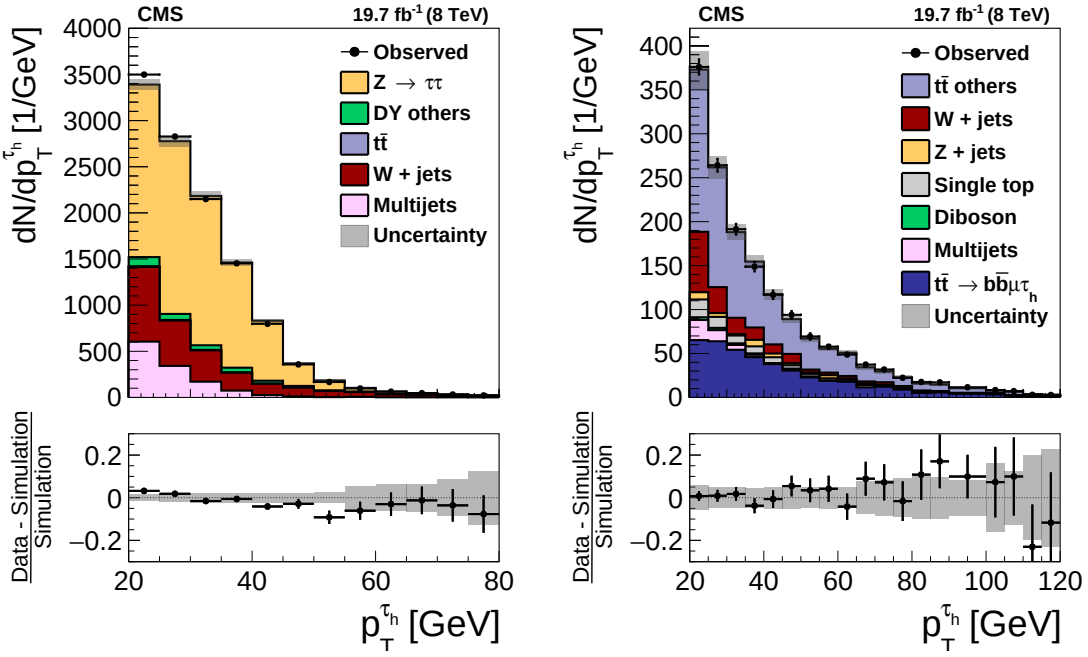

Figure 6.4: Distribution of the transverse momentum of τ_h candidates in $Z/\gamma^* \to \tau\tau$ and $t\bar{t}$ (right) events in data and in simulations. The $Z/\gamma^* \to \ell\ell$ and $t\bar{t}$ events in which either the reconstructed muon or the reconstructed τ_h candidate is misidentified, are denoted in the MC simulation by "DY others" and "tt others", respectively. [103]

Tau isolation discriminators				
	Efficiency		Jet $\to \tau_h$ misidentification rate	
	$Z/\gamma^* \to \tau\tau$	$Z'(2.5\text{ TeV}) \to \tau\tau$	W+jets	QCD multijet
Cut-based				
Loose	49.0%	58.9%	$9.09 \cdot 10^{-3}$	$3.86 \cdot 10^{-3}$
Medium	40.8%	50.8%	$5.13 \cdot 10^{-3}$	$2.06 \cdot 10^{-3}$
Tight	38.1%	48.1%	$4.38 \cdot 10^{-3}$	$1.75 \cdot 10^{-3}$
MVA-based				
Very loose	55.9%	71.2%	$1.29 \cdot 10^{-2}$	$6.21 \cdot 10^{-3}$
Loose	50.7%	64.3%	$7.38 \cdot 10^{-3}$	$3.21 \cdot 10^{-3}$
Medium	39.6%	50.7%	$3.32 \cdot 10^{-3}$	$1.30 \cdot 10^{-3}$
Tight	27.3%	36.4%	$1.56 \cdot 10^{-3}$	$4.43 \cdot 10^{-4}$

Discriminator against electrons			
	Efficiency		$e \to \tau_h$ misidentification rate
	$Z/\gamma^* \to \tau\tau$	$Z'(2.5\text{ TeV}) \to \tau\tau$	$Z \to ee$
Very loose	94.3%	89.6%	$2.38 \cdot 10^{-2}$
Loose	90.6%	81.5%	$4.43 \cdot 10^{-3}$
Medium	84.8%	73.2%	$1.38 \cdot 10^{-3}$
Tight	78.3%	65.1%	$6.21 \cdot 10^{-4}$
Very tight	72.1%	60.0%	$3.54 \cdot 10^{-4}$

Discriminators against muons			
	Efficiency		$\mu \to \tau_h$ misidentification rate
	$Z/\gamma^* \to \tau\tau$	$Z'(2.5\text{ TeV}) \to \tau\tau$	$Z \to \mu\mu$
Cut-based			
Loose	99.3%	96.4%	$1.77 \cdot 10^{-3}$
Tight	99.1%	95.0%	$7.74 \cdot 10^{-4}$
MVA-based			
Loose	99.5%	99.4%	$5.20 \cdot 10^{-4}$
Medium	99.0%	98.8%	$3.67 \cdot 10^{-4}$
Tight	98.0%	97.7%	$3.18 \cdot 10^{-4}$

Table 6.2: Expected efficiencies and misidentification rates of various tau identification discriminators, measured in 8 TeV MC simulations.

close to the one used to measure the efficiency in $Z/\gamma^* \to \tau_h\tau_\mu$ events. Both measurements are performed with a "tag and probe" method [106], where the "tag" is the muon and the "probe" the hadronic tau.

Measurement in $Z/\gamma^* \to \tau_h\tau_\mu$ events

The events are triggered with the lowest unprescaled single muon trigger, which requires a muon with $p_T > 24$ GeV at HLT, so that the tau candidate is not affected by any trigger requirement [2]. Loose tau candidates, which constitute the probes in the measurement, are preselected with the following criteria:

- Transverse momentum of the jet associated to the tau candidate larger than 20 GeV;
- Absolute value of the pseudorapidity of the jet associated to the tau candidate less than 2.3;
- Passing the tight working point of the cut-based muon rejection discriminator;
- Passing the loose working point of the MVA-based electron rejection discriminator;
- At least one track with transverse momentum larger than 5 GeV.

Muons, which constitute the tags in the measurement, are selected with a transverse momentum larger than 25 GeV, an absolute value of the pseudorapidity less than 2.1, passing the tight working point of the PF muon identification and with a relative $\delta\beta$ isolation less than 0.1. The muon and the tau candidate are required to have an opposite electric charge and to be separated by at least $\Delta R = 0.5$.

The $t\bar{t}$ background is reduced by vetoing events that have a jet with $p_T > 20$ GeV and $|\eta| < 2.4$ that passes the medium CSV working point. Additionally, the events that have an identified and isolated electron and muon on top of the tag are discarded to reduce the contribution from other $Z/\gamma^* \to \ell\ell$ events or from diboson production.

In order to reduce the contribution from the W+jets background, with one jet misidentified as a hadronic tau, a selection criterion on the transverse mass between the muon and the $\not\!\!E_T$ is applied:

$$m_T(\mu, \vec{\not\!\!E}_T) = \sqrt{2p_T^\mu \not\!\!E_T (1 - \cos\Delta\phi)} < 30 \text{ GeV}, \tag{6.3}$$

where $\Delta\phi$ is the difference in azimuthal angle between the muon momentum and $\vec{\not\!\!E}_T$. The motivation of such a cut lies in the fact that, in W+jets, the lepton and the neutrino typically fly in opposite directions, which gives rise to large $m_T(\mu, \vec{\not\!\!E}_T)$ values. Typical distributions of the m_T variable in the $\mu\tau_h$ final state are illustrated for the W+jets, Drell-Yan and $t\bar{t}$ processes in Fig. 6.5 (left).

In addition, another variable, P_ζ, is introduced to take benefit from the fact that in $Z/\gamma^* \to \tau\tau$ events, the missing energy from the tau decay neutrinos typically forms a small angle with the visible tau decay products. P_ζ is defined as a linear combination of

2. A precise list of the trigger paths, MC samples and collected datasets, used in this chapter can be found in Appendix A

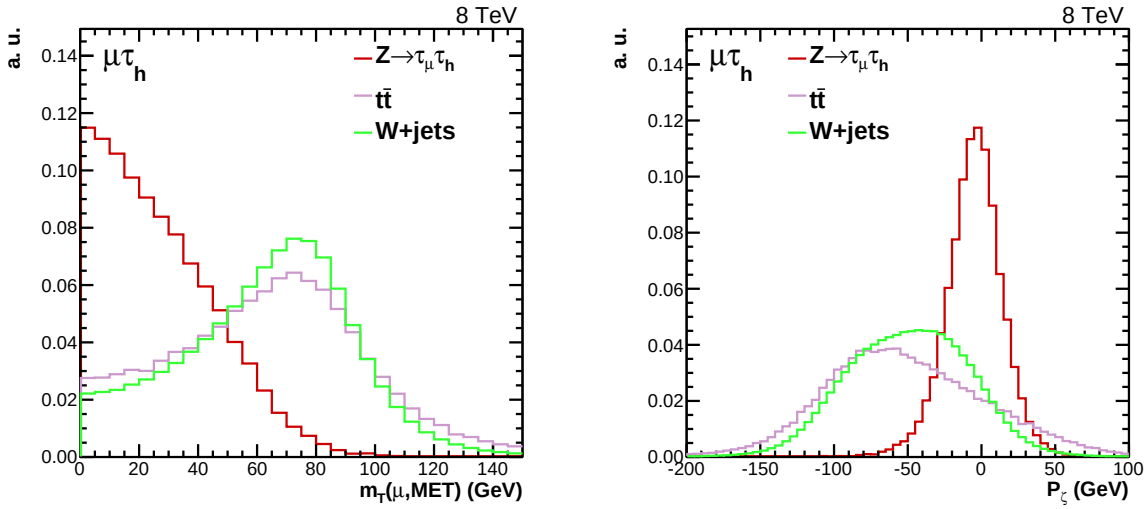

Figure 6.5: Typical normalized distributions in the $\mu\tau_h$ final state of the $m_T(\mu,\not\!\!E_T)$ (left) and P_ζ (right) variables, for the W+jets, Drell-Yan and $t\bar{t}$ processes.

the quantities P_ζ^{all} and P_ζ^{vis} [107]:

$$P_\zeta^{all} = (\vec{p_T^{\mu}} + \vec{p_T^{\tau}} + \vec{\not\!\!E}_T).\frac{\vec{\zeta}}{|\zeta|}, \tag{6.4}$$

$$P_\zeta^{vis} = (\vec{p_T^{\mu}} + \vec{p_T^{\tau}}).\frac{\vec{\zeta}}{|\zeta|}, \tag{6.5}$$

$$P_\zeta = P_\zeta^{all} - 0.85P_\zeta^{vis}. \tag{6.6}$$

The axis $\vec{\zeta}$ is the bisector of the momenta in the transverse plane of the visible decay products of the two taus; this is illustrated in Fig. 6.6. The factor 0.85 has been optimized in the context of the CMS MSSM $\Phi \to \tau\tau$ analysis (see Chapter 13), and is checked to perform well in this case too. The variable P_ζ is required to be larger than -15 GeV in this measurement. Typical distributions of the P_ζ variable in the $\mu\tau_h$ final state are illustrated for the W+jets, Drell-Yan and $t\bar{t}$ processes in Fig. 6.5 (right). The selection thresholds on the variables $m_T(\mu,\not\!\!E_T)$ and P_ζ are determined in such a way as to maximize the $Z \to \tau\tau$ significance in events where the tau candidates passes the tau isolation criteria.

The signal, consisting of $Z/\gamma^* \to \tau\tau$ events with a tau decaying to a muon and a muonic neutrino, and a hadronic tau matched at generated level, is estimated from MC simulations. Other Drell-Yan events, corresponding to other Z or tau decay modes, or to $Z/\gamma^* \to \tau_\mu\tau_h$ where the reconstructed hadronic tau does not match the generated hadronic tau, are taken from MC simulations too and are considered as background events. The

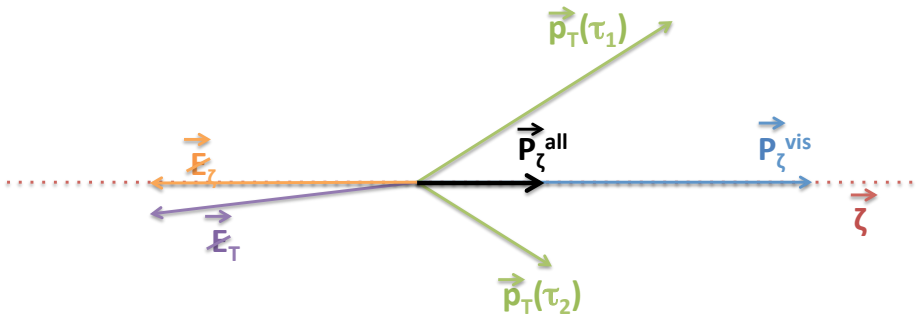

Figure 6.6: Schematic representation of the quantities used to compute P_ζ.

contribution from the $t\bar{t}$ production is limited by to the b-jet veto; its contribution is also estimated from MC simulations, and it is scaled to the most precise cross section measurement at CMS [108].

The most important backgrounds, W+jets and QCD multijet processes, are fully or partially estimated with data-driven methods. The shape of the W+jets background is estimated from MC simulations. To increase the number of W+jets events from MC samples passing the full selection, a so-called "stitching" method is applied. Five MC samples are generated with different numbers of jets: inclusive, W+1 jet, W+2 jets, W+3 jets and W+ 4jets. The cross sections of these samples are known, but the weight to apply to the selected events depends on the number of generated events, which, except for events with no generated jet, depends on two MC samples (the inclusive and one of the exclusive samples). The weight to apply to events with n generated jets ($0 < n < 5$) is computed as follows. The number of generated events n_{gen} with a number of jets n is:

$$n_{gen} = n_{gen}^{incl} \frac{\sigma_n}{\sigma_{incl}} + n_{gen}^{excl,n}, \tag{6.7}$$

where n_{gen}^{incl} is the number of generated events in the inclusive samples, $n_{gen}^{excl,n}$ is the number of generated events in the exclusive sample with n jets, σ_{incl} is the inclusive cross section of W+jets events and $\sigma_{excl,n}$ is the exclusive production cross section of W+n jets events. Therefore, events with n jets in the inclusive and in the exclusive samples should be weighted by a weight w_n, computed as follows:

$$w_n = \frac{\sigma_n}{n_{gen}} = \left(\frac{n_{gen}^{incl}}{\sigma_{incl}} + \frac{n_{gen}^{excl,n}}{\sigma_{excl,n}} \right)^{-1}. \tag{6.8}$$

While the shape of the W+jets background is taken from MC simulations with the stitching technique, its normalization is estimated from a control region in data enriched in W+jets events. The region enriched in W+jets events is defined in the same way as the signal region, except that the transverse mass between the muon and $\not{E}_T$ is required to

be larger than 70 GeV. The small contribution from other processes is subtracted from data to obtain the W+jets normalization in this control region. The yield in the signal region is extrapolated from this value with a scale factor measured in MC simulation as the ratio between the number of events satisfying $m_T(\mu, \vec{\not{E}}_T) < 30$ GeV to the number of events with $m_T(\mu, \vec{\not{E}}_T) > 70$ GeV.

The QCD multijet background is fully estimated with data-driven methods. Its shape is taken from a region in data where the selection is the same as in the signal region, except that the muon relative isolation is required to be greater than 0.3. This region is highly dominated by QCD multijet events, and the small contribution from other processes is estimated from MC simulations and subtracted from the data. Meanwhile, the normalization comes from a region similar as the signal region except that the muon and tau candidates are required to carry the same electric charge (so-called "SS" region). In this region, the $Z/\gamma^* \to \tau_\mu \tau_h$ signal is strongly suppressed, and the main contributions come from QCD multijet and W+jets processes. The contributions from the processes other than QCD are estimated from MC simulations and subtracted from the observed data. The normalization obtained in such a way is multiplied by 1.06 to reflect the yield difference between regions where the tau and muon candidates do or do not carry a same electric charge. This scale factor, which reflects a charge asymmetry mostly due to gluon splitting and low mass QCD resonances, is measured as the ratio between opposite-sign and same-sign events in a region where the muon and the tau have inverted isolations.

The events selected as described here above are divided into two categories, "*pass*" and "*fail*", depending on whether the loosely selected tau passes or fails the working point of the isolation under study. The *pass* category has a high $Z/\gamma^* \to \tau\tau$ purity, while large background contributions from W+jets and QCD multijet, with jets misidentified as hadronic taus, enter the *fail* category. The efficiency ϵ for hadronic taus to pass the isolation under study is defined as :

$$\epsilon = \frac{N^{pass}_{Z/\gamma^* \to \tau\tau}}{N^{pass}_{Z/\gamma^* \to \tau\tau} + N^{fail}_{Z/\gamma^* \to \tau\tau}}. \tag{6.9}$$

The numbers of signal events in the *pass* and in the *fail* regions are determined from a maximum likelihood fit of the predicted processes to the observed data.

The simultaneous fit in the *pass* and *fail* categories is performed for two different observables. The most obvious choice of fit variable is the invariant mass between the muon and the hadronic tau. This variable is computed from the visible decay products of both taus, and is therefore denoted m_{vis}. For signal events – $Z/\gamma^* \to \tau\tau$ with a muon from a tau decay and a hadronic tau matched at generated level –, the m_{vis} distribution peaks around 70 GeV and has a shape distinguishable from other processes, the distributions of which are flatter and extend to higher m_{vis} values. The other observable chosen to perform the simultaneous fit is N_{tracks}, which is defined as the multiplicity of tracks within a cone of size $\Delta R = 0.5$, centered on the tau candidate direction. Genuine hadronic

taus typically have a smaller track multiplicity than quark or gluon jets, which makes of N_{tracks} a powerful variable to discriminate the signal from backgrounds with jets misidentified as hadronic taus. The reason to measure the tau identification efficiency with two observables is two-fold. First, as the results from both measurements are expected to be compatible with each other, this constitutes a useful cross-check of the fit technique. Second, because it does not depend on the tau transverse momentum, N_{tracks} can be used to perform a measurement of the tau identification efficiency in given ranges of hadronic tau transverse momentum.

The parameter of interest (POI) in the fit is the data-to-MC scale factor for the tau identification efficiency. The signal yield in the *pass* region is directly proportional to the POI, while the signal yield in the *fail* region is related to the POI in a more complex way. Indeed the total number of signal events in both regions remains constant, but migrations can happen between the regions. If one considers a constant total number of signal events c, and a data-to-MC scale factor x, the multiplicative factor to the signal yield in the *fail* region, y, is obtained as follows:

$$N^{pass}_{Z/\gamma^* \to \tau\tau} + N^{fail}_{Z/\gamma^* \to \tau\tau} = c, \tag{6.10}$$

$$x \times N^{pass}_{Z/\gamma^* \to \tau\tau} + y \times N^{fail}_{Z/\gamma^* \to \tau\tau} = c, \tag{6.11}$$

thus:

$$y = \frac{c - x \times N^{pass}_{Z/\gamma^* \to \tau\tau}}{N^{fail}_{Z/\gamma^* \to \tau\tau}}. \tag{6.12}$$

A closure test has been performed by running the maximum likelihood fit with pseudo-data equal to the sum of the expected processes, where the $Z/\gamma^* \to \tau_\mu \tau_h$ is scaled with different values of the tau identification scale factor. The procedure returns the input scale factor without any bias.

Nuisance parameters, affecting the shape and the normalization of the different processes, are considered in the simultaneous fit. The luminosity uncertainty, amounting to 2.6% in 2012 [109], is taken into account for processes with yields estimated from MC simulations. Drell-Yan events are attributed a 3% uncertainty related to their cross section, and the normalization of the $t\bar{t}$ process is known with an uncertainty of 15%. To obtain the uncertainty on the W+jets normalization, the yield in the high-m_T region is recomputed when subtracting processes for which the missing transverse energy has been modified within its uncertainties. The maximum yield variation amounts to 3% and is taken as a nuisance parameter on the W+jets background. The uncertainty on the tau energy scale amounts to 3%; as it affects the shapes of the distributions – mostly when the observable is m_{vis}–, alternative distributions are provided to the maximum likelihood fit for variations of the tau energy scale by ±3%. Bin-by-bin uncertainties take into account the statistical uncertainty related to the limited number of events in every bin of every distribution.

	Signal: $Z \to \tau\tau$	Other DY	$t\bar{t}$	W+jets	QCD multijet
Tau ID efficiency (POI)	(a)	-	-	-	-
Luminosity	2.6% (f)	2.6% (f)	2.6% (f)	-	-
Muon ID efficiency	2% (f)	2% (f)	2% (f)	-	-
Drell-Yan cross section	3% (f)	3% (f)	-	-	-
$t\bar{t}$ cross section	-	-	15% (f)	-	-
W+jets normalization	-	-	-	3% (u)	-
Tau energy scale	Shape (f)	Shape (f)	Shape (f)	Shape (f)	Shape (f)
$j \to \tau_h$ misidentification	-	Shape (a)	Shape (a)	-	-
QCD multijet estimation	-	-	-	-	Shape (u)
Hadronization	-	Shape (f)	Shape (f)	Shape (f)	Shape (f)
Tracking	Shape (f)	Shape (f)	Shape (f)	Shape (f)	-
Bin-by-bin	Shape (u)	Shape (u)	Shape (u)	Shape (u)	Shape (u)

Table 6.3: Parameter of interest and systematic uncertainties taken into account in the simultaneous fit to determine the tau identification efficiency in $Z/\gamma^* \to \tau\tau$ events. The uncertainties may be fully correlated (f), anticorrelated (a) or uncorrelated (u) between the *pass* and *fail* regions.

In the case of the fit with N_{tracks} as observable, two additional shape uncertainties are taken into account. First, the track reconstruction efficiency is known with a 3.9% uncertainty [94]. Second, the uncertainty on the multiplicity of charged hadrons produced in the hadronization of quark and gluon jets is known with 10% precision. Therefore, additional shape templates are provided to the fit, and correspond to the variations by 3.9% or 10% of the N_{tracks} distribution means for hadronically decaying taus and $j \to \tau_h$ fakes respectively. In practice, the downward variations are created by removing tracks from tau candidates with a probability of 3.9 or 10%, and the upward variations by adding a track with a probability of 3.9 or 10% for every single track of the tau candidate. The set of systematic uncertainties is summarized in Tab. 6.3.

The m_{vis} distributions after the maximum likelihood fit are shown in Fig 6.7 for the loose working point of the cut-based and MVA-based discriminators, while the corresponding N_{tracks} distributions are shown in Fig. 6.8. A good agreement between expected processes and observed data is observed in both the *pass* and *fail* regions. The tau identification efficiency scale factors extracted from the fits are presented in Tab. 6.4: they are generally compatible with 1.0, with a 5% uncertainty. A 3.9% uncertainty has been added in quadrature to the uncertainty returned by the fit to account for the uncertainty to pass the loose tau preselection criteria, and especially the requirement that all tau candidates have a track with $p_T > 5$ GeV. The results obtained with the two observables are also compatible with each other.

The efficiency can also be measured in different $|\eta|$ and p_T ranges, or for a different number of reconstructed vertices. This is important because some differences in the performance of the algorithm could arise respectively from different detector geometries (the efficiency is less when there is a large budget material for taus to cross), different

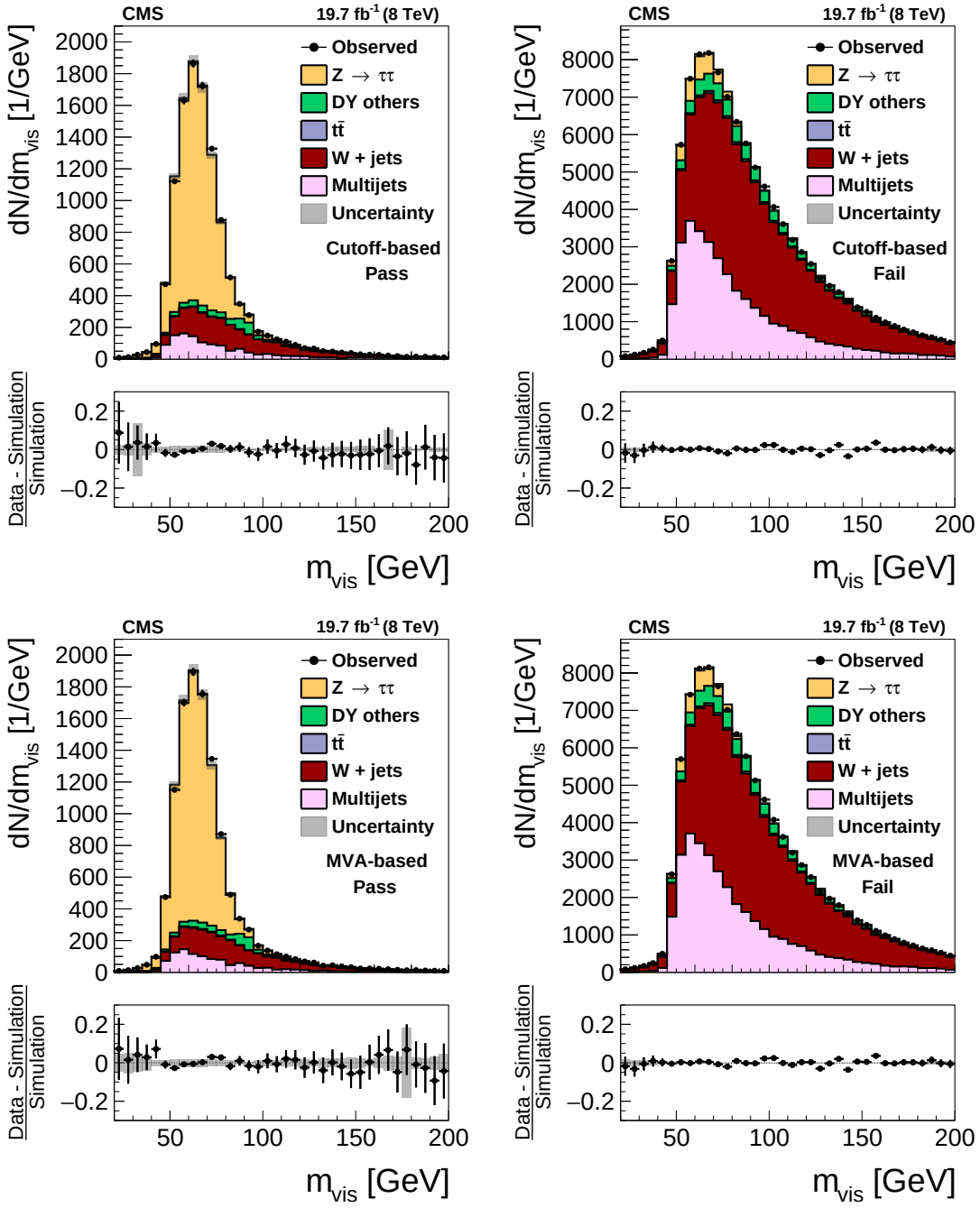

Figure 6.7: Distributions of the visible invariant mass between the muon and the tau candidates, in the *pass* (left) and *fail* (right) regions, for the loose working point of the cut-based (top) and MVA-based (bottom) isolation discriminators. The various processes are shown after the simultaneous maximum likelihood fit. [103]

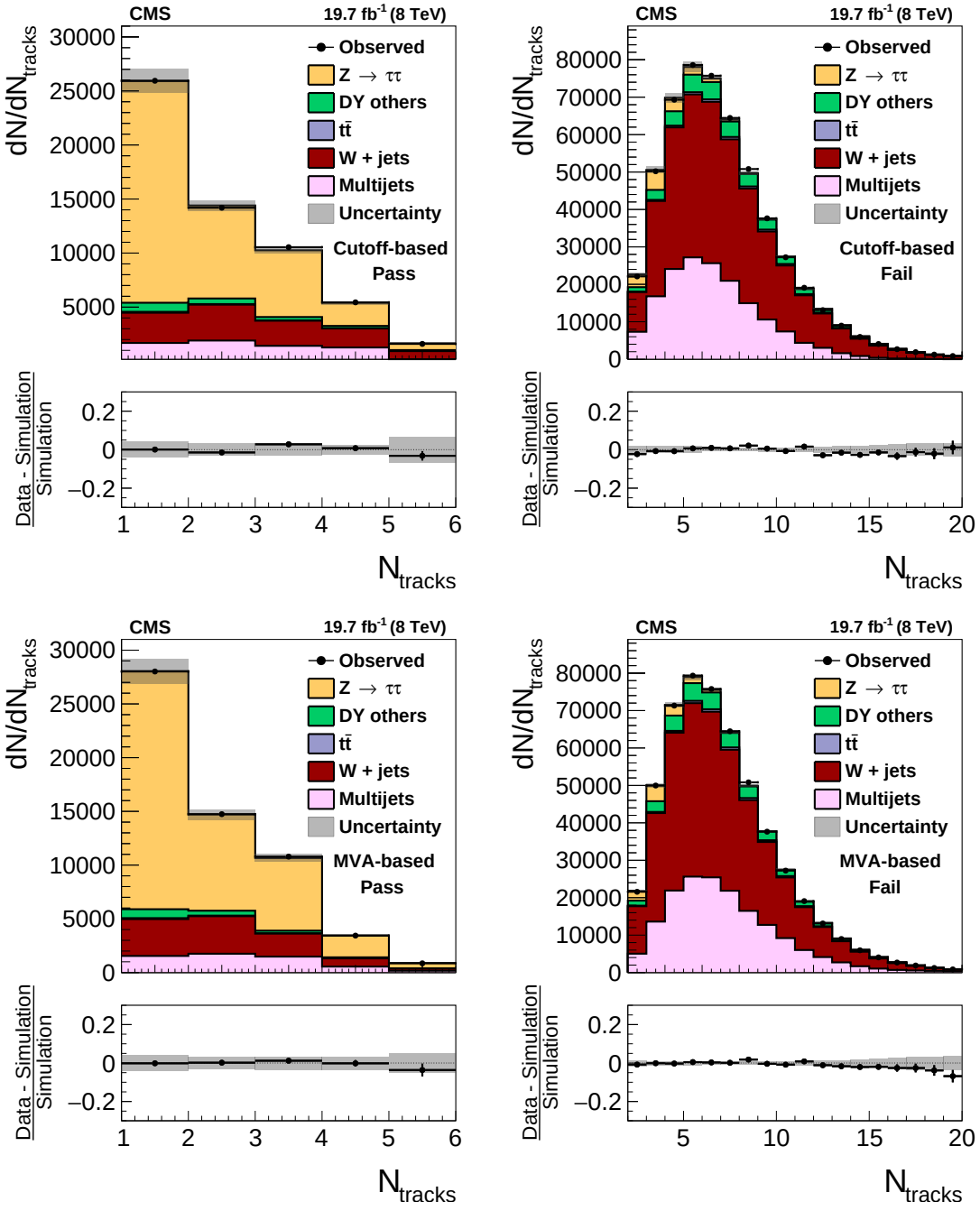

Figure 6.8: Distributions of the number of tracks inside the signal and isolation cones of the tau candidate, N_{tracks}, in the *pass* (left) and *fail* (right) regions, for the loose working point of the cut-based (top) and MVA-based (bottom) isolation discriminators. The various processes are shown after the simultaneous maximum likelihood fit. [103]

	Data/Simulation	
	N_{tracks}	m_{vis}
Cut-based		
Loose	0.963 ± 0.051	1.006 ± 0.044
Medium	0.982 ± 0.048	0.984 ± 0.044
Tight	0.997 ± 0.052	0.982 ± 0.044
MVA-based		
Very loose	0.940 ± 0.086	1.034 ± 0.044
Loose	1.026 ± 0.054	1.017 ± 0.044
Medium	0.992 ± 0.057	1.014 ± 0.044
Tight	0.975 ± 0.052	1.015 ± 0.045

Table 6.4: Data-to-simulation scale factors for the efficiency for hadronic tau decays to pass different tau identification discriminators, measured in $Z/\gamma^* \to \tau\tau$ events. The columns labeled data/simulation give the ratio of efficiencies measured in data relative to the MC expectation, separately for the two cases that the observable N_{tracks} respectively m_{vis} is used in the template fit. The efficiency to pass the tau decay mode reconstruction and to satisfy the p_T >20 GeV and $|\eta| < 2.3$ cuts are included in the data/simulation ratios given in the table.

tau decay product shapes (harder taus are more collimated) or different number of pileup vertices (pileup vertices contribute to spoiling the tau isolation). The maximum likelihood fits are performed with N_{tracks} as observable because this variable is not directly impacted by the choice of $|\eta|$, p_T or the number of vertices. The results are shown in Fig. 6.9, 6.10 and 6.11. All scale factors are seen to be compatible with 1.0 within the uncertainties.

Measurement in $t\bar{t} \to bb\mu\tau_h$ events

As stated previously, the measurement in $t\bar{t} \to bb\mu\tau_h$ events permits to probe taus with higher transverse momentum, and in a topology with higher jet activity. The events are selected in the fully leptonic decay of top quarks, with one prompt muon and one tau decaying hadronically. The main backgrounds are other $t\bar{t}$ decays (fully hadronic decays, semi-leptonic decays, or fully-leptonic decays where the reconstructed objects are not matched to a muon and a hadronically decaying tau at generated level), W+jets and QCD multijet events.

The events are again required to pass the lowest unprescaled single muon trigger, and a muon with $p_T > 25$ GeV and $|\eta| < 2.1$ is selected. The muon is further required to pass the tight PF identification and to have a relative isolation less than 0.1. The hadronic tau candidate is selected with $p_T > 20$ GeV, $|\eta| < 2.3$, and an opposite sign charge compared to the muon. The muon and the tau candidate should be separated by at least $\Delta R = 0.5$. The events are required to have at least two jets with $p_T > 30$ GeV and $|\eta| < 2.5$, and separated from the muon and the tau candidate by at least $\Delta R = 0.5$. At least one of these should pass the medium working point of the b-tagging CSV algorithm. To reject background events from Drell-Yan process, the $\not{E}_T$ should be larger than 40 GeV. Finally, events that contain an additional electron ($p_T > 15$ GeV, $|\eta| < 2.3$) or muon ($p_T > 10$ GeV, $|\eta| < 2.4$) passing the loose identification and isolation criteria, are vetoed.

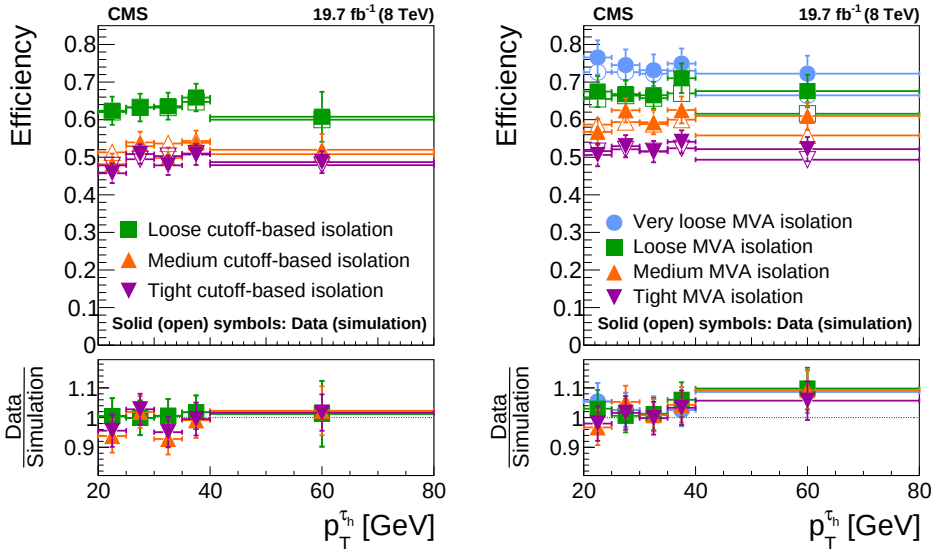

Figure 6.9: Efficiency in data (plain symbols) and MC simulations (open symbols) for the tau identification as a function of the visible p_T of the tau candidate, for the cut-based (left) and MVA-based (right) discriminators. [103]

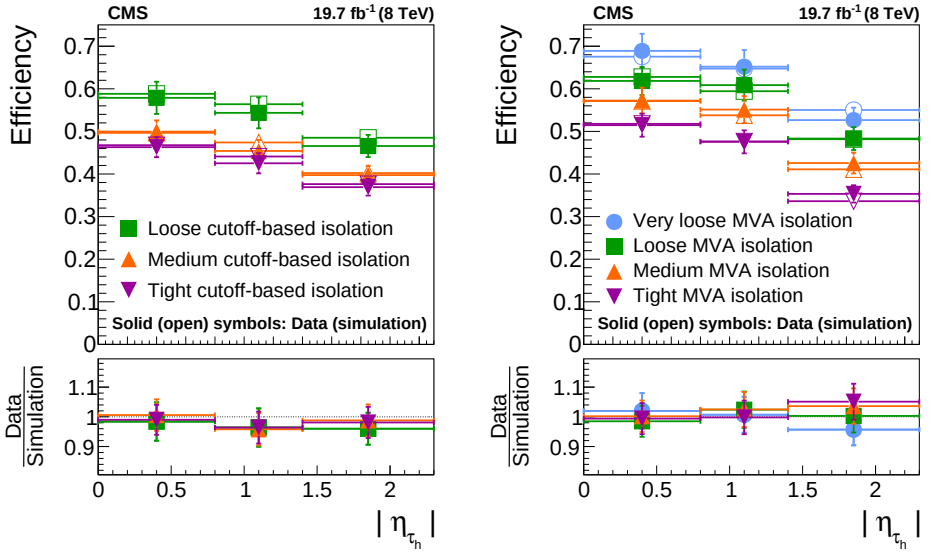

Figure 6.10: Efficiency in data (plain symbols) and MC simulations (open symbols) for the tau identification as a function of the visible $|\eta|$ of the tau candidate, for the cut-based (left) and MVA-based (right) discriminators. [103]

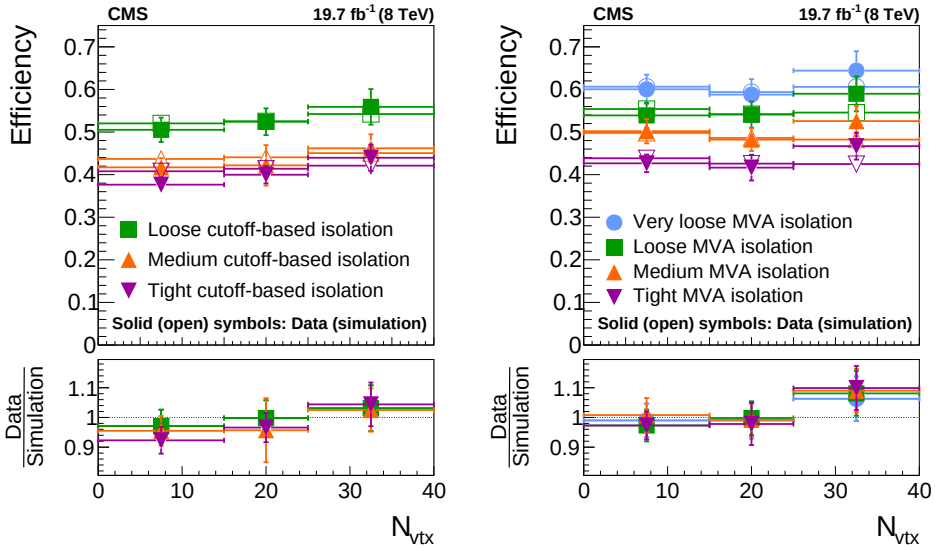

Figure 6.11: Efficiency in data (plain symbols) and MC simulations (open symbols) for the tau identification as a function of the number of reconstructed vertices, for the cut-based (left) and MVA-based (right) discriminators. [103]

The exact same method as the measurement in $Z/\gamma^* \to \tau\tau$ events cannot be applied because of the overwhelming background in the *fail* region. Therefore, another category with two muons in the final state is considered; it is used to constrain the processes in the *pass* region. The *di-muon* region aims at selecting $t\bar{t} \to bb\mu\mu$ events, with a selection very close to the $t\bar{t} \to bb\mu\tau_h$ selection in order to have the same effect of systematic uncertainties.

The selection of the *di-muon* region is chosen to be as close as possible to the *pass* region, in such a way as their nuisance parameters are correlated. Events are required to contain two muons with $p_T > 20$ GeV (25 GeV for the leading muon), $|\eta| < 2.4$ ($|\eta| < 2.1$ for the leading muon), passing the tight PF isolation and with a relative isolation less than 0.1. To remove contributions from Drell-Yan events, the invariant mass of these muons is required to be above 50 GeV, and not to be within 10 GeV of the Z boson mass: $m_{\mu\mu} > 50$ GeV and $|m_{\mu\mu} - m_Z| > 10$ GeV. The same criteria about the jets, $\not\!\!E_T$ and additional leptons as in the *pass* region, are applied.

Because of the b jet requirement, the region with high m_T is not hugely dominated by W+jets events as it was the case in the measurement in $Z/\gamma^* \to \tau\tau$ events; therefore the W+jets background is fully estimated from MC simulations and a 30% uncertainty is attributed to its normalization. All other processes – $t\bar{t}$ production, Drell-Yan, single top quark production, diboson production– but QCD multijet are also taken from MC simulations. The normalization and the distribution of the QCD multijet background are

estimated from data-driven techniques. The distribution of the QCD multijet background is taken from a control region, identical to the signal region except that the muons isolation requirement is inverted. This control region is highly dominated by QCD multijet events, and the small contribution from other processes is estimated from MC simulations and subtracted. The normalization of the QCD multijet background is determined in another control region, where all cuts from the signal region are applied, except that the muon and the tau candidate are required to have the same charge (SS region). The contribution of the QCD multijet background to the signal region with opposite-sign charge (OS region) is expected to be approximately the same as in the SS region; a scale factor of 1.06, measured for SM $H \to \tau\tau$ analysis, is applied to extrapolated from the SS region to the OS region. The normalization in the SS region is estimated from a template maximum likelihood fit. The distribution of the QCD multijet process used to perform the fit is estimated in a QCD-enriched region obtained by inverting the muon isolation requirement and requiring the muon and the tau to carry the same electric charge.

The variable found to discriminate in the most efficient way the signal from the backgrounds is the transverse mass between the muon and the missing transverse energy. Typical signal distributions indeed extend to higher m_T values than backgrounds. In the case of the di-muon region, the transverse mass is computed with respect to one of the two muons, chosen randomly.

Systematic uncertainties considered in the maximum likelihood fit are partly identical to those used in the fit in $Z/\gamma^* \to \tau\tau$ events, among them the luminosity, the muon identification efficiency, or the $t\bar{t}$ production cross section for example. Other uncertainties are related to the b jet requirement: the b-tagging efficiency uncertainty (typically between 2 and 7%), and the b mis-tag rate uncertainty for light jets misidentified as coming from b-quarks (typically between 10 and 20%) [98], are considered as shape systematics. The jet energy resolution and the jet energy scale also affect the distribution of the m_T distributions [97], since the transverse missing energy is recomputed for variations of the jet kinematics within the uncertainties to keep the transverse momentum conservation. An uncertainty on the OS/SS scale factor for the QCD multijet of 5% is considered as affecting the yield of this background, as in the measurement in $Z/\gamma^* \to \tau\tau$ events. A summary of the systematics considered in the analysis is shown in Tab. 6.5.

A simultaneous fit of the two regions is performed for every isolation discriminator, as illustrated in Fig. 6.12 for the loose working point of the cut-based and MVA based isolations. The results obtained for the data-to-simulation scale factors of the different working points of the cut-based and MVA-based algorithms are presented in Tab. 6.6. The uncertainty on the measurement amounts to approximately 10%, which is more than the uncertainty of the measurement in $Z/\gamma^* \to \tau\tau$ events due to the larger background fraction and the smaller discrimination efficiency of the m_T variable. The scale factors are well compatible between each measurement, and in agreement with 1.0 within the uncertainties.

	$t\bar{t} \to bb\mu\tau_h$	Other $t\bar{t}$	Drell-Yan	Single top	W+jets	QCD multijet
Tau ID efficiency SF	yes	-	-	-	-	-
Luminosity	2.6% (f)	2.6% (f)	2.6% (f)	2.6%	2.6%	-
Muon ID efficiency	2% (f)	2% (f)	2% (f)	2%	2%	2%
Drell-Yan cross section	-	-	10% (f)	-	-	-
$t\bar{t}$ production cross section	15%	15%	-	-	-	Shape
Single-t cross section	-	-	-	30% (f)	-	-
W+jets normalization	-	-	-	-	22% (u)	-
OS-to-SS scale factor	-	-	-	-	-	5%
Tau energy scale	Shape (f)	Shape (f)	Shape (f)	Shape (f)	Shape (f)	Shape (f)
$j \to \tau_h$ misidentification	-	Shape (a)	Shape (a)	Shape (f)	Shape (f)	Shape (f)
Jet resolution	Shape (f)	Shape (f)	Shape (f)	Shape (f)	Shape (f)	Shape (f)
Jet energy scale	Shape (f)	Shape (f)	Shape (f)	Shape (f)	Shape (f)	Shape (f)
b-Tagging efficiency	Shape (f)	Shape (f)	Shape (f)	Shape (f)	Shape (f)	Shape (f)
Mis-b-tagging rate	Shape (f)	Shape (f)	Shape (f)	Shape (f)	Shape (f)	Shape (f)
$\not\!\!E_T$ modeling	Shape (f)	Shape (f)	Shape (f)	Shape (f)	Shape (f)	Shape (f)
Bin-by-bin	Shape (u)	Shape (u)	Shape (u)	Shape (u)	Shape (u)	Shape (u)

Table 6.5: Parameter of interest and systematic uncertainties taken into account in the simultaneous fit to determine the tau identification efficiency in $t\bar{t} \to bb\mu\tau_h$. The uncertainties may be fully correlated (f), anticorrelated (a) or uncorrelated (u) between the *pass* and *fail* regions.

	Data/Simulation
Cut-based	
Loose	1.037 ± 0.097
Medium	1.050 ± 0.107
Tight	1.047 ± 0.108
MVA-based	
Very loose	0.927 ± 0.097
Loose	1.009 ± 0.097
Medium	0.956 ± 0.118
Tight	1.080 ± 0.117

Table 6.6: Data-to-simulation scale factors for the efficiency for τ_h decays in $t\bar{t} \to bb\mu\tau_h$ events to pass different tau identification discriminators. The column labelled data/simulation gives the ratio of efficiencies measured in data relative to the MC expectation.

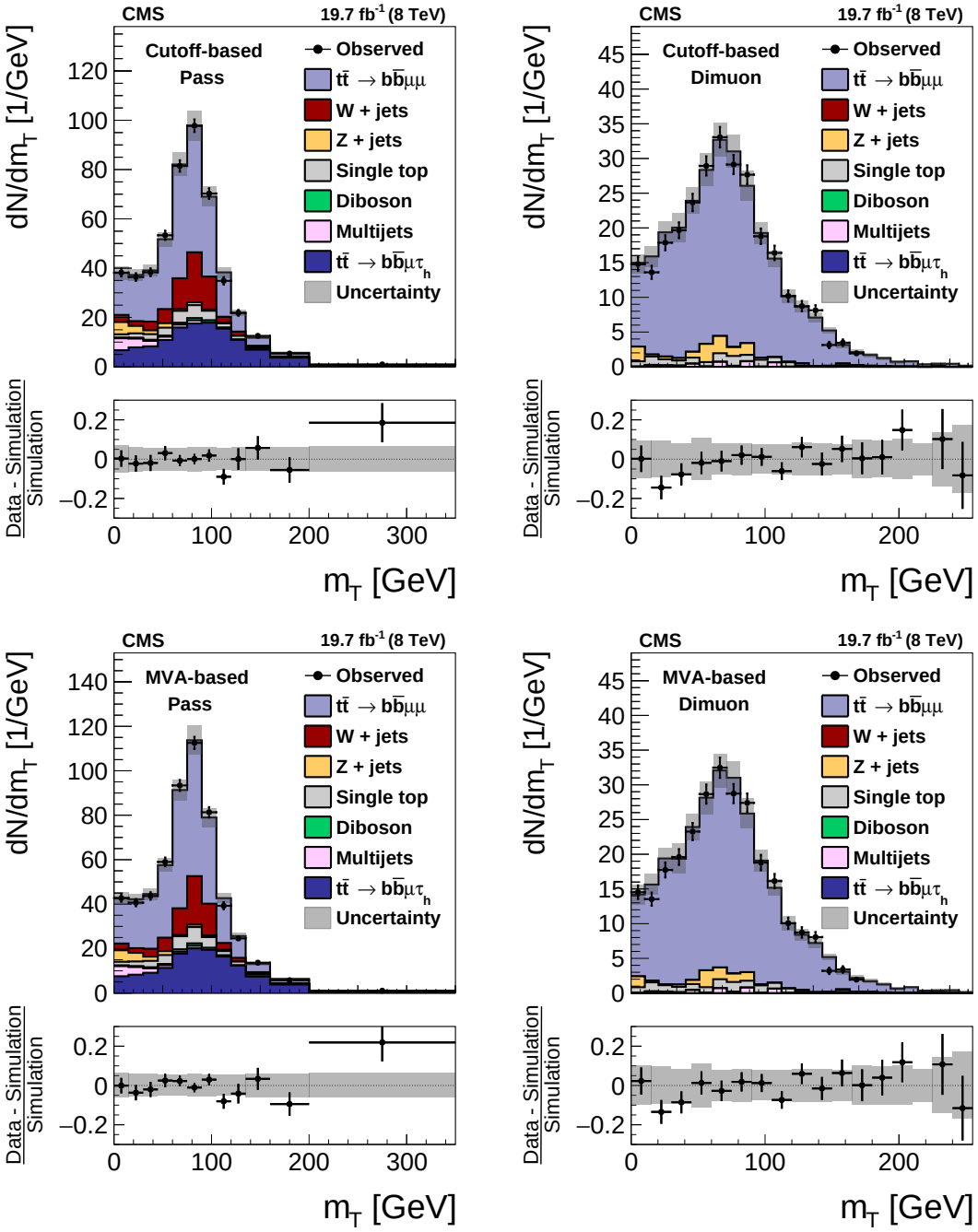

Figure 6.12: Distributions of the transverse mass between the muon and the $\not\!\!E_T$, in events with one (left) or two (right) muons, for the loose working point of the cut-based (top) and MVA-based (bottom) isolation discriminators. The results are shown after a simultaneous maximum likelihood fit in the two regions. [103]

6.2.3 Anti-lepton discriminator efficiency

The efficiency for hadronic tau decays in $Z/\gamma^* \to \tau\tau$ events to pass the discriminators against electrons and muons has also been measured in data and MC simulations. The measurement is pretty similar to the measurement of the isolation efficiency in $Z/\gamma^* \to \tau\tau$ events, except that the tau candidates in the *pass* and *fail* categories now all pass the reconstruction and isolation conditions, but pass or fail respectively the rejection against light lepton. The results are given in Tab. 6.7. The efficiencies measured in data are in agreement with the MC predictions within the uncertainty of the measurement, amounting to less than 1%. Control plots of the m_{vis} distributions in the *pass* and *fail* regions are presented in Fig. 6.13 for two different light lepton rejection discriminators.

Discriminators against electrons	
Working point	SF
MVA very loose	0.996 ± 0.004
MVA loose	0.995 ± 0.004
MVA medium	0.994 ± 0.005
MVA tight	0.997 ± 0.006
MVA very tight	1.003 ± 0.007

Discriminators against muons	
Working point	SF
Cut-based loose	0.990 ± 0.003
Cut-based tight	0.990 ± 0.003
MVA loose	0.990 ± 0.003
MVA medium	0.989 ± 0.003
MVA Ttght	0.985 ± 0.004

Table 6.7: Data-to-MC scale factors for hadronic tau decays in $Z/\gamma^* \to \tau\tau \to \mu\tau_h$ events to pass the discriminators against electrons and muons.

6.2.4 $\mu \to \tau_h$ and $e \to \tau_h$ misidentification rates

The measurement of the $\mu \to \tau_h$ and $e \to \tau_h$ misidentification rates in data is a challenging task, considering their low values (in general below the permille level). This requires a large quantity of collected data, and a precise description of all background processes.

The technique used to measure the $\mu \to \tau_h$ and $e \to \tau_h$ misidentification rates in data is close to the one used for the measurement of the tau identification efficiency in $Z/\gamma^* \to \tau\tau$ events. The signal is now $Z/\gamma^* \to \mu\mu$ or $Z/\gamma^* \to ee$ events, and the parameter of interest acting on it is the misidentification rate scale factor. The events are divided into two categories, *pass* and *fail*, whether the tau candidate (which is actually a light lepton for signal events) passes or fails some working point of the discriminator that rejects electrons or muons.

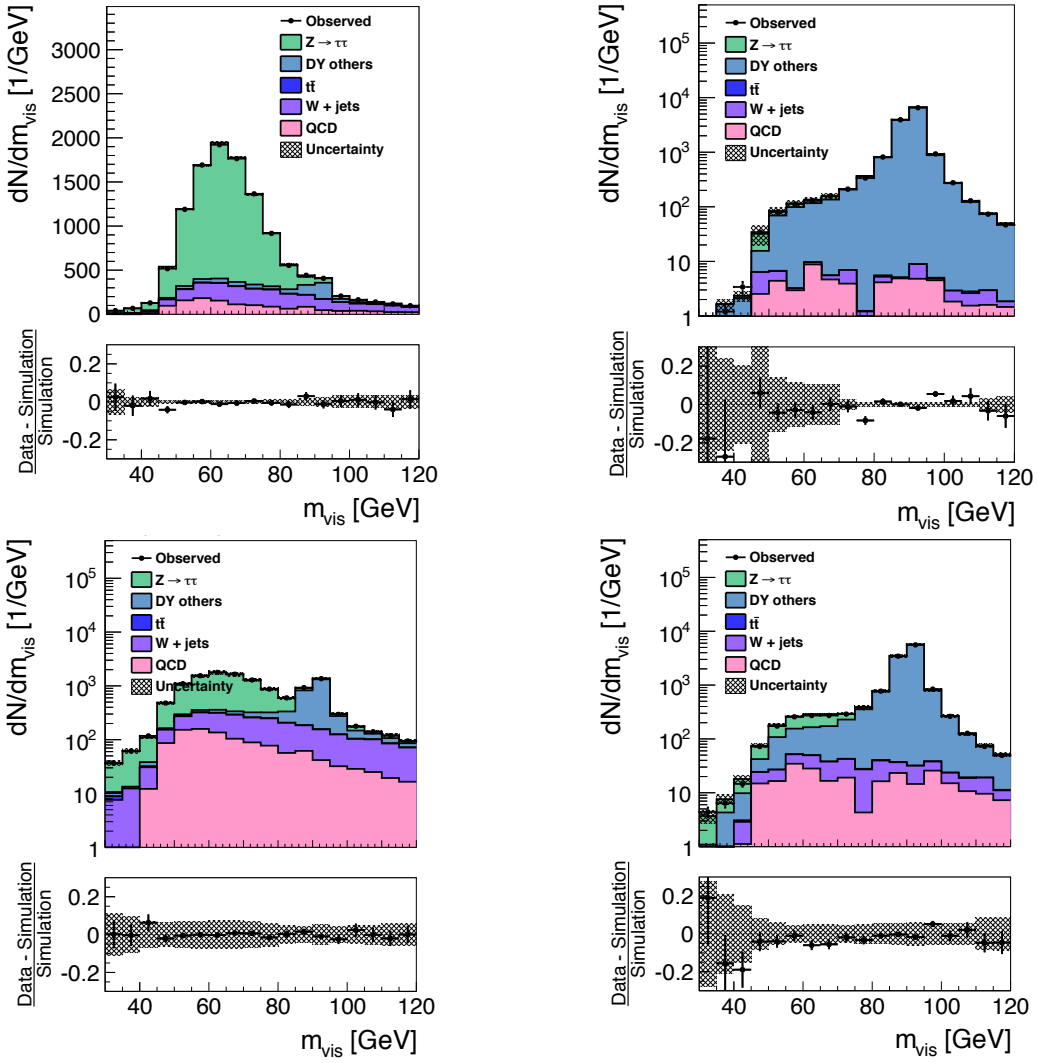

Figure 6.13: Distribution of m_{vis} observed in the *pass* (left) and *fail* (right) regions compared to the MC expectation, for the loose working point of the cut-based rejection against muons (top) and MVA-based rejection against electrons (bottom). The expected m_{vis} distribution is shown for the postfit value of the nuisance parameters.

The selection is designed to ensure a large $Z/\gamma^* \to \mu\mu/ee$ purity. The events should contain a well-identified light lepton (the tag), and one loosely preselected hadronic tau (the probe). Tag muons are selected identically as in Section 6.2.2, with $p_T > 25$ GeV, $|\eta| < 2.1$, tight PF identification and relative isolation less than 0.1. Similarly, tag electrons are required to satisfy $p_T > 30$ GeV, $|\eta| < 2.1$ (and η outside of the transition region between ECAL barrel and endcaps), tight identification and to have a relative isolation less than 0.1. The probe is a loose τ_h candidate with $p_T > 20$ GeV and $|\eta| < 2.3$, that passes the decay mode finding discriminator and the loose cut-based HPS isolation. The tag and the probe should carry an opposite sign electric charge and be separated by at least $\Delta R = 0.5$. The W+jets and $t\bar{t}$ backgrounds are reduced by requiring the $\not\!\!E_T$ to be less than 25 GeV (applied only for the $e \to \tau_h$ misidentification rate measurement), and the transverse mass between the tag and the $\not\!\!E_T$ to be less than 40 GeV (or 25 GeV for the $e \to \tau_h$ misidentification rate measurement).

The backgrounds are estimated with the methods described in Section 6.2.2. Namely, all processes are taken from MC simulations, except the QCD multijet background, estimated from a SS region, and the W+jets, the normalization of which is derived from a high-m_T sideband. Because some probes are not real electrons or muons, but rather come from $j \to e/\mu$ misidentifications, such events are removed from the signal templates, based on MC estimations. Uncertainties include, apart from those already described in Section 6.2.2, the uncertainties on the energy scale of tag electrons (2%), tag muons (1%), probe electrons (5%) and probe muons (3%).

Simultaneous fits are performed in the pass and fail regions for different working points of the discriminators, and a set of these results is shown in Fig. 6.14 and Fig. 6.15 for the $\mu \to \tau_h$ and $e \to \tau_h$ measurements respectively. The observable is the visible invariant mass between the tag and the probe.

The muon misidentification rates are measured in three η regions: $|\eta| < 1.2$, $1.2 < |\eta| < 1.7$ and $|\eta| > 1.7$, for different working points of the cut-based and MVA-based discriminators against muons. The data-to-MC scale factors obtained after the fits are given in Tab. 6.8 and summarized in Fig. 6.16. The correction factors to apply to simulations are in general greater than 1.0, and larger for tighter working points and in the forward regions of the detector.

The $e \to \tau_h$ misidentification rates are measured separately in the barrel ($|\eta| < 1.460$) and endcap ($|\eta| > 1.558$) regions of the ECAL. The results obtained after the fits are given in Tab. 6.9 and summarized in Fig. 6.17. The simulation correction factor amounts to up to 1.7. The difference between the rates in data and simulation is larger in the barrel and for tighter discriminator working points.

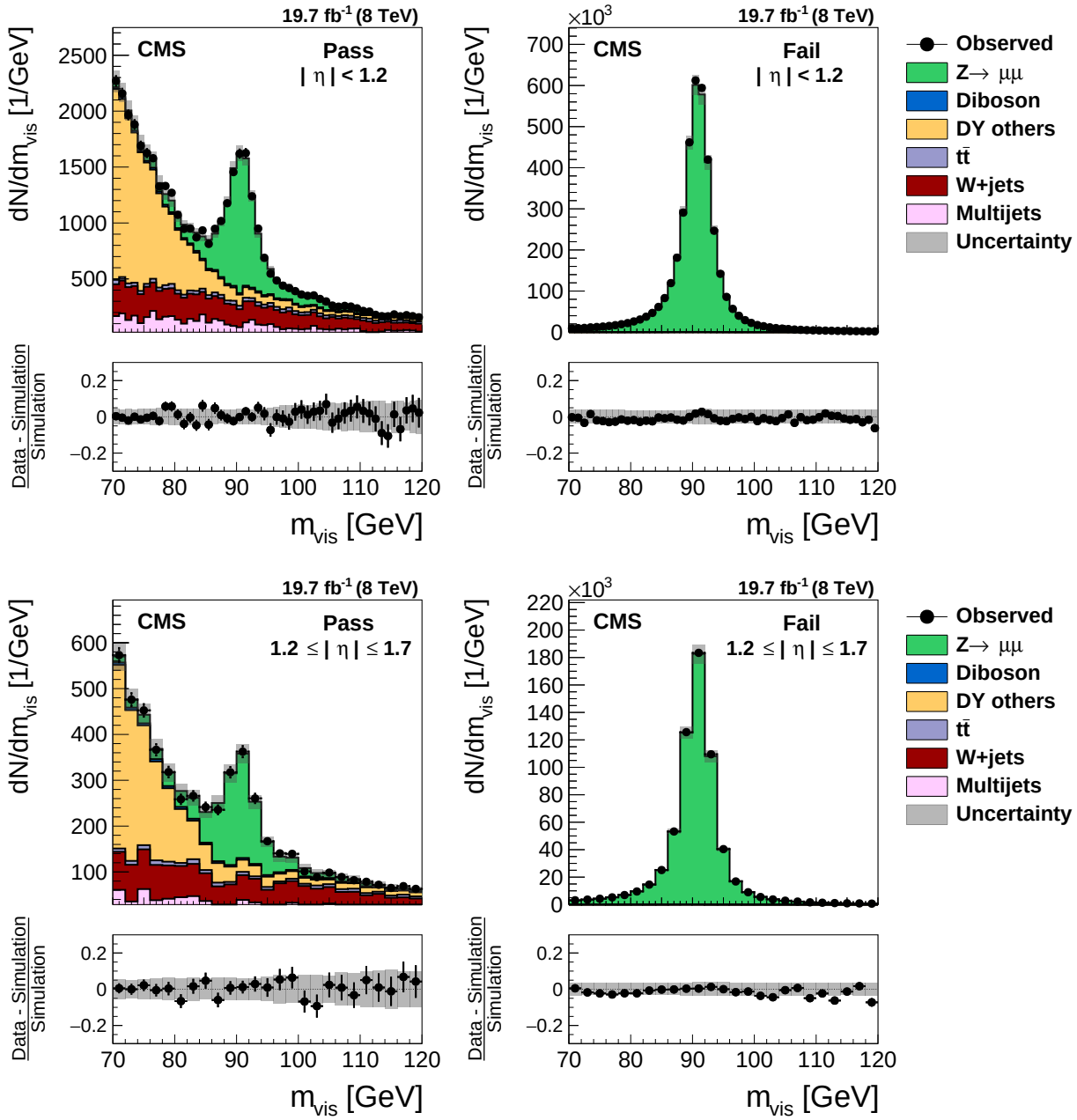

Figure 6.14: Distribution of tag plus probe mass observed in the *pass* (left) and *fail* (right) region, for the loose working point of the cut-based discriminator against muons in the regions $|\eta| < 1.2$ (top) and $1.2 < |\eta| < 1.7$ (bottom). The distributions observed in $Z/\gamma^* \to \mu\mu$ candidate event selected in data are compared to the MC expectation, shown for the values of nuisance parameters obtained from the likelihood fit to the data. $Z/\gamma^* \to \ell\ell$ ($\ell = e, \mu, \tau$) events in which either the tag or the probe muon are due to a fake are denoted by "DY others". [103]

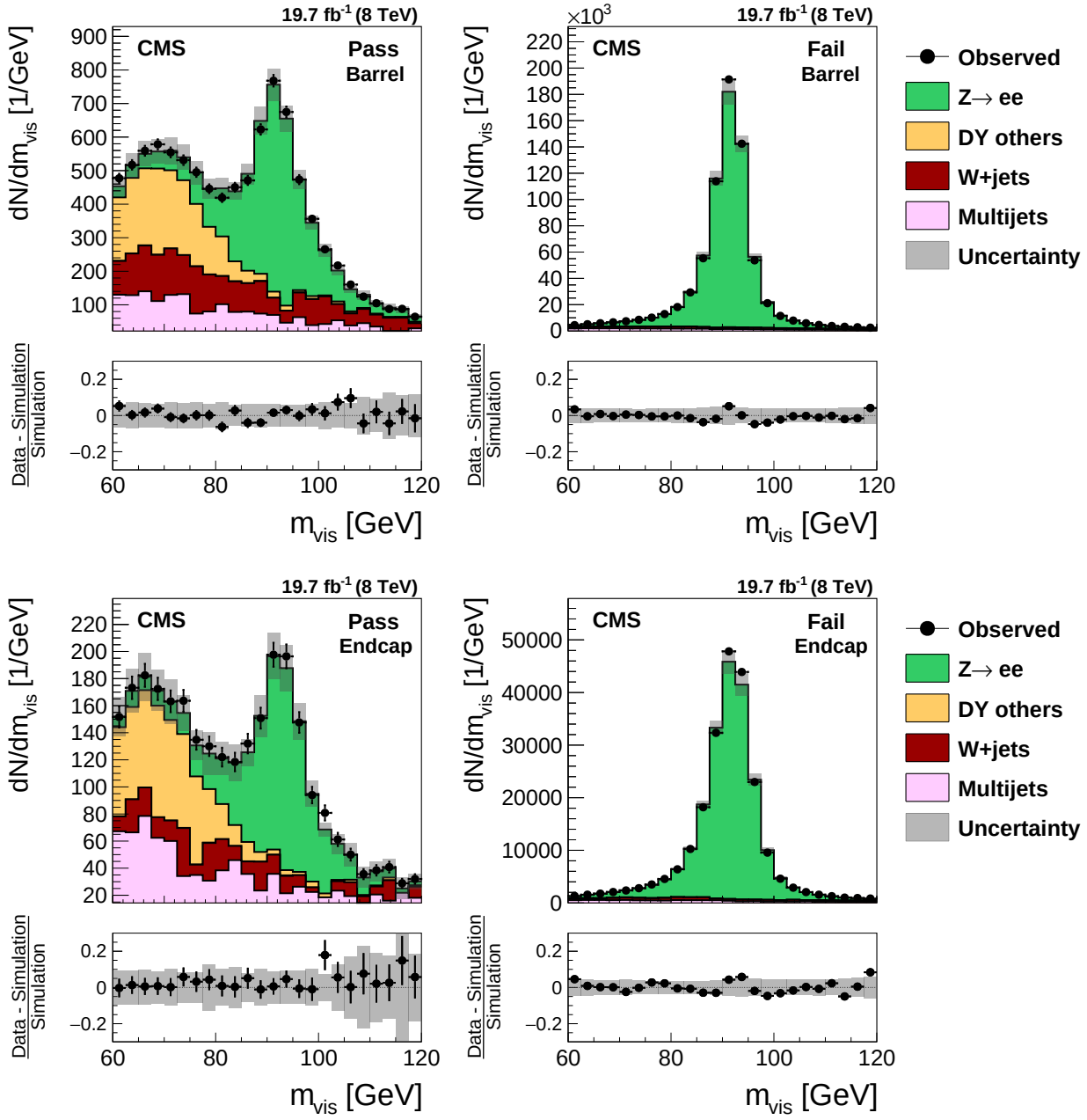

Figure 6.15: Distribution of tag plus probe visible mass, m_{vis}, observed in the *pass* (left) and *fail* (right) regions compared to the MC expectation, for the loose working point of the anti–e discriminator in the barrel (top) and endcap (bottom) regions. The expected m_{vis} distributions are shown for the postfit value of nuisance parameters. [103]

$\|\eta\| < 1.2$			
	Simulation	Data	Data/Simulation
Cut-based loose	$(2.48 \pm 0.02) \cdot 10^{-3}$	$(2.65 \pm 0.06) \cdot 10^{-3}$	1.068 ± 0.025
Cut-based tight	$(9.94 \pm 0.10) \cdot 10^{-4}$	$(1.05 \pm 0.05) \cdot 10^{-3}$	1.053 ± 0.053
MVA loose	$(4.28 \pm 0.09) \cdot 10^{-4}$	$(4.63 \pm 0.49) \cdot 10^{-4}$	1.082 ± 0.116
MVA medium	$(2.91 \pm 0.07) \cdot 10^{-4}$	$(3.08 \pm 0.50) \cdot 10^{-4}$	1.058 ± 0.172
MVA tight	$(2.56 \pm 0.07) \cdot 10^{-4}$	$(2.66 \pm 0.50) \cdot 10^{-4}$	1.039 ± 0.197
$1.2 < \|\eta\| < 1.7$			
Cut-based loose	$(1.64 \pm 0.03) \cdot 10^{-3}$	$(1.92 \pm 0.10) \cdot 10^{-3}$	1.169 ± 0.066
Cut-based tight	$(6.54 \pm 0.19) \cdot 10^{-4}$	$(8.33 \pm 0.81) \cdot 10^{-4}$	1.274 ± 0.129
MVA loose	$(5.61 \pm 0.18) \cdot 10^{-4}$	$(7.28 \pm 0.94) \cdot 10^{-4}$	1.297 ± 0.172
MVA medium	$(3.28 \pm 0.14) \cdot 10^{-4}$	$(5.05 \pm 0.97) \cdot 10^{-4}$	1.540 ± 0.303
MVA tight	$(2.63 \pm 0.12) \cdot 10^{-4}$	$(4.06 \pm 0.95) \cdot 10^{-4}$	1.543 ± 0.368
$\|\eta\| > 1.7$			
Cut-based loose	$(9.85 \pm 0.30) \cdot 10^{-4}$	$(1.42 \pm 0.11) \cdot 10^{-3}$	1.445 ± 0.118
Cut-based tight	$(4.99 \pm 0.18) \cdot 10^{-4}$	$(7.42 \pm 1.09) \cdot 10^{-4}$	1.488 ± 0.224
MVA loose	$(4.66 \pm 0.17) \cdot 10^{-4}$	$(6.99 \pm 1.20) \cdot 10^{-4}$	1.501 ± 0.264
MVA medium	$(2.46 \pm 0.12) \cdot 10^{-4}$	$(4.57 \pm 0.92) \cdot 10^{-4}$	1.856 ± 0.384
MVA tight	$(1.95 \pm 0.11) \cdot 10^{-4}$	$(2.77 \pm 1.25) \cdot 10^{-4}$	1.423 ± 0.644

Table 6.8: Probability for muons to pass the loose working point of the cut-based tau isolation discriminator plus different working points of the cut-based and MVA-based discriminators against muons. The $\mu \to \tau_h$ misidentification rates measured in $Z/\gamma^* \to \mu\mu$ events are compared to the MC predictions in three regions of η: $|\eta| < 1.2$, $1.2 < |\eta| < 1.7$ and $|\eta| > 1.7$.

ECAL barrel ($\|\eta\| < 1.46$)			
	Simulation	Data	Data/Simulation
Very loose	$(2.06 \pm 0.01) \times 10^{-2}$	$(2.37 \pm 0.06) \times 10^{-2}$	1.15 ± 0.03
Loose	$(4.48 \pm 0.05) \times 10^{-3}$	$(5.61 \pm 0.17) \times 10^{-3}$	1.25 ± 0.04
Medium	$(1.73 \pm 0.03) \times 10^{-3}$	$(2.30 \pm 0.18) \times 10^{-3}$	1.33 ± 0.10
Tight	$(9.70 \pm 0.02) \times 10^{-4}$	$(1.28 \pm 0.21) \times 10^{-3}$	1.32 ± 0.21
Very tight	$(6.83 \pm 0.02) \times 10^{-4}$	$(1.13 \pm 0.20) \times 10^{-3}$	1.66 ± 0.30
ECAL endcap ($\|\eta\| > 1.56$)			
Very loose	$(2.93 \pm 0.02) \times 10^{-2}$	$(3.11 \pm 0.09) \times 10^{-2}$	1.06 ± 0.03
Loose	$(4.46 \pm 0.09) \times 10^{-3}$	$(4.67 \pm 0.22) \times 10^{-3}$	1.05 ± 0.05
Medium	$(1.54 \pm 0.05) \times 10^{-3}$	$(1.83 \pm 0.22) \times 10^{-3}$	1.19 ± 0.15
Tight	$(8.83 \pm 0.38) \times 10^{-4}$	$(1.16 \pm 0.26) \times 10^{-3}$	1.32 ± 0.31
Very tight	$(6.50 \pm 0.33) \times 10^{-4}$	$(1.04 \pm 0.26) \times 10^{-3}$	1.60 ± 0.40

Table 6.9: Probability for electrons to pass different working points of the discriminant against electrons. The $e \to \tau_h$ misidentification rates measured in $Z/\gamma^* \to ee$ events are compared to the MC expectation, separately for electrons in the ECAL barrel and endcap regions.

6.2.5 Other performance measurements

The last two performance measurements performed with 2012 data concern the tau energy scale and the $j \to \tau_h$ misidentification rate. They are only briefly covered in the

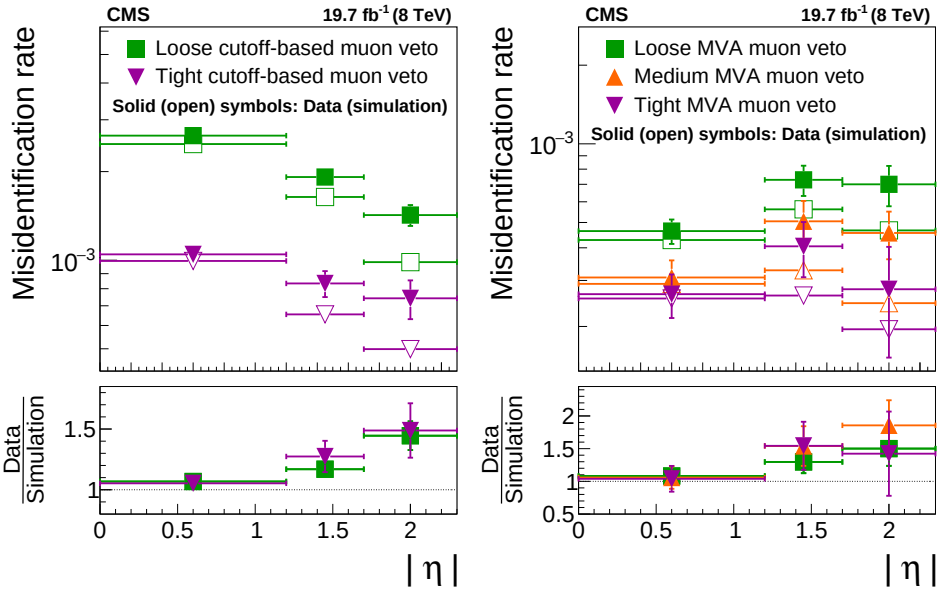

Figure 6.16: Probability for muons in $Z/\gamma^* \to \mu\mu$ events to pass the loose working point of the cut-based tau isolation discriminator plus different working points of the cut-based (left) MVA-based (right) discriminators against muons. The $\mu \to \tau_h$ misidentification rates measured in data are compared to the MC simulation in three regions of η: $|\eta| < 1.2$, $1.2 < |\eta| < 1.7$ and $|\eta| > 1.7$. [103]

next paragraphs, and more details can be found in [103].

Tau energy scale

The tau energy scale has a large impact on physics analyses with taus, and is therefore important to be measured in data. The measurement is performed in $Z/\gamma^* \to \tau_\mu\tau_h$ events, by creating different signal templates for variations of the tau energy scale and choosing the variation that gives the best agreement between data and predicted processes after a maximum likelihood fit to the observed data. The measurement is performed separately for the different tau decay modes, and with two observables: the invariant mass of the two tau candidates, m_{vis}, and the reconstructed hadronic tau mass, m_τ. It is found that the tau energy scale is about 1% lower in data than in simulation for the $h^\pm\pi^0 s$ decay mode, and the uncertainty associated to the measurements in all topologies is 3%.

Jet$\to \tau_h$ misidentification rate

The $j \to \tau_h$ misidentification rate is measured in W+jets events and in QCD multijet events. Because W+jets events contain a higher fraction of quark jets (as opposed to gluon jets) than QCD multijet events, the misidentification rate measured in such events is higher. Indeed, quark jets are typically more collimated and have a lower track multiplicity than gluon jets. The rates measured in data usually agree with the predictions from MC simulations, but some disagreements are observed at high $|\eta|$ because of an imprecise

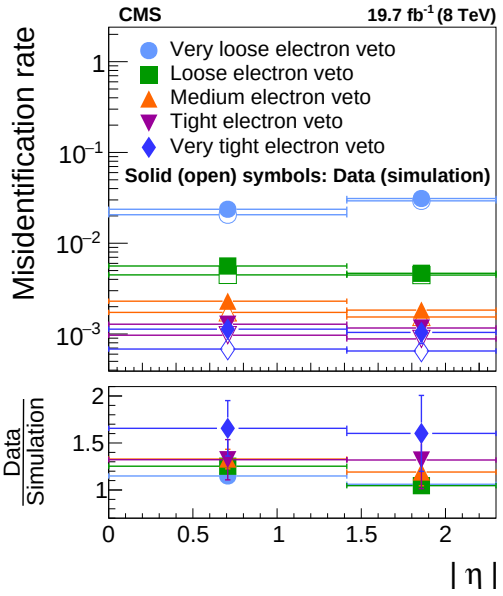

Figure 6.17: Probability for electrons in $Z/\gamma^* \to ee$ events to pass different working–points of the MVA-based discriminator against electrons. The $e \to \tau_h$ misidentification rates measured in data are compared to the MC simulation, separately for electrons in the barrel ($|\eta| < 1.460$) and in the endcap ($|\eta| > 1.558$) region of the ECAL. [103]

modeling of the isolation in MC simulations, and a trend with respect to the transverse momentum is observed, with a deviation magnitude of the order of 20%. In practice, most processes with jets misidentified as hadronic taus are not estimated from MC simulations, but from data-driven methods.

6.3 HPS algorithm in Run-2

In Run-2 some improvements have been made to the HPS algorithm to recover efficiency losses [110]. The main changes concern the τ_h decay modes covered by the algorithm, the strip reconstruction, and the definition of the isolation discriminators.

6.3.1 Modifications with respect to Run-1

A higher τ_h identification efficiency can be achieved by including decay modes with relaxed requirements in the reconstruction step, at the price of a larger $j \to \tau_h$ misidentification rate. The following decay modes are covered for the first time in Run-2:

- **Two prongs plus one strip**: This category is used to reconstruct τ_h decays with three charged hadrons, where one of the tracks escapes detection or is merged with another one. It especially helps recovering efficiency losses for high-p_T taus.
- **Two prongs plus two strips**: Similarly, this category is targeted at τ_h decays with three tracks, where one is not detected.

Tau candidates that are reconstructed in any of the above-mentioned categories or in one of those used in Run-1, are said to pass the "new decay mode finding". The new decay mode finding is mostly useful for analyses with high-p_T taus, for which the efficiency recovery is the largest, and with low backgrounds, as the additional decay modes suffer from a larger $j \to \tau_h$ misidentification rate than the old decay modes. The charge of the two-prong candidates is taken as the charge of the leading track; the charge is correctly determined in about 75% of cases.

Whereas the size of the strips was fixed to 0.20×0.05 in the $\phi \times \eta$ plan in Run-1, the strips are reconstructed dynamically with variable dimensions in Run-2. The strips are supposed to cover the ECAL energy deposits of photons and electrons originating from neutral pion decays. It happens that, because of the bending of their trajectory in the magnetic field, low-p_T electrons or positrons from photon conversions are outside of the fixed-size strip, and contribute to the τ_h candidate isolation. This fake contribution to the isolation of a τ_h constituent may cause the τ_h candidate to fail the isolation discriminator. In Run-2, the size of the strip is adjusted dynamically according to the transverse momentum of electrons and photons that are added to the strips. It is a function of the p_T of the strip and the electron/photon to be merged:

$$\Delta\eta = f(p_T^{e/\gamma}) + f(p_T^{\text{strip}}), \tag{6.13}$$

$$\Delta\phi = g(p_T^{e/\gamma}) + g(p_T^{\text{strip}}), \tag{6.14}$$

where

$$f(p_T) = 0.20 \times p_T^{-0.66}, \tag{6.15}$$

$$g(p_T) = 0.35 \times p_T^{-0.71}. \tag{6.16}$$

The functions are chosen from MC studies in such a way as 95% of electrons and photons from tau decays are contained within the strip.

The isolation discriminators have been slightly modified with respect to Run-1. The $\delta\beta$ correction factor used in Run-1 to compute the cut-based isolation was seen to overcorrect the pileup effects; it is chosen in Run-2 to be equal to 0.20 instead of 0.46. In addition, the p_T-sum of electrons and photons included in the strips but outside the isolation cone is required not to exceed 10% of the τ_h candidate transverse momentum:

$$p_T^{strip,outer} = \sum p_T^{e/\gamma}(\Delta R > R_{sig}) < 0.10 \times p_T^{\tau}. \tag{6.17}$$

As shown in Fig. 6.19 (left), the latter requirement reduces the fake rate by about 5% for a same efficiency, whereas the modified $\Delta\beta$ correction factor and the dynamic strip reconstruction itself both bring an additional 5% improvement. The loose, medium, and tight cut-based isolation working points are defined in Run-2 in such a way as the points are equidistant in terms of τ_h identification efficiency: the isolation is required to be less than 2.5, 1.5 and 0.8 GeV respectively. Some new variables with respect to Run-1 have been included in the MVA-based isolation in Run-2 to improve the discrimination between τ_h and, quark and gluon jets:

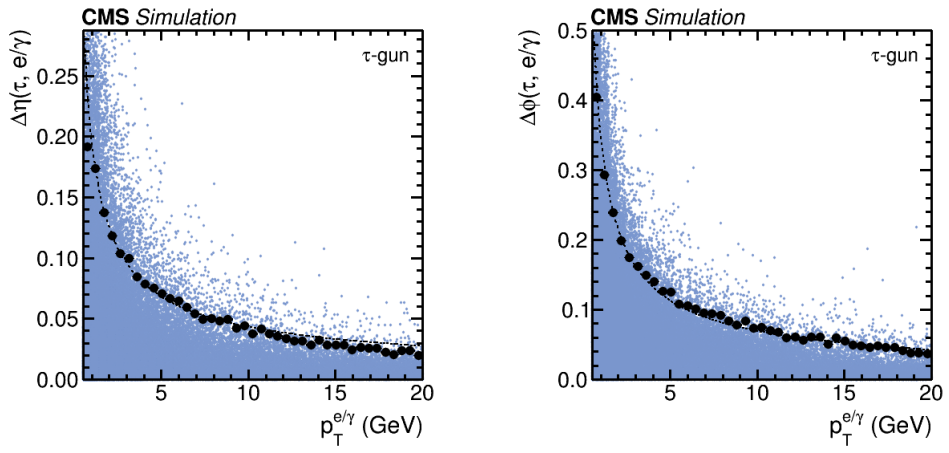

Figure 6.18: Distance in η (left) and in ϕ (right) between the τ_h direction and e/γ that are due to tau decay products in simulated events, as a function of the transverse momentum of the electron or photon. The size of the window is larger in the ϕ-direction to account for the bending of the trajectory of charged particles in the magnetic field. The black dots indicate the strip sizes that contain 95% of electrons and photons from tau decays, whereas the dashed lines represent the analytical functions $f(p_T)$ and $g(p_T)$. [110]

- $p_T^{strip,outer}$;
- The sign of the transverse impact parameter of the leading track;
- The signed 3-dimensional impact parameter and its significance;
- The chi-square of the fit for the leading track of the τ_h candidate;
- The ratio of the electromagnetic energy to the total energy within the τ_h signal cone;
- The total number of signal and isolation photons with $p_T > 0.5$ GeV;
- The p_T-weighted ΔR of photons within signal cone and the isolation annulus;
- The p_T-weighted $\Delta\eta$ and $\Delta\phi$ of photons in strips outside of signal cone.

A comparison between the performance of the cut-based and MVA-based isolations is shown in Fig. 6.19 (right). Different BDT are trained for the old and new decay modes.

6.3.2 Performance in 2015 data

The performance of the algorithm is measured with the data collected at a center-of-mass energy of 13 TeV in 2015.

Identification efficiency

The identification efficiency is measured in $Z/\gamma^* \to \tau_\mu\tau_h$, with a tag-and probe method similar as in Run-1. The events are again divided into a *pass* and *fail* regions depending on whether the τ_h candidates pass or fail the isolation discriminator under study. The events are selected with the lowest unprescaled single muon trigger available in 2015 data; offline the muon candidate should have a transverse momentum larger than 19 GeV and $|\eta| < 2.1$, and correspond to the object that fired the trigger. The muon should addi-

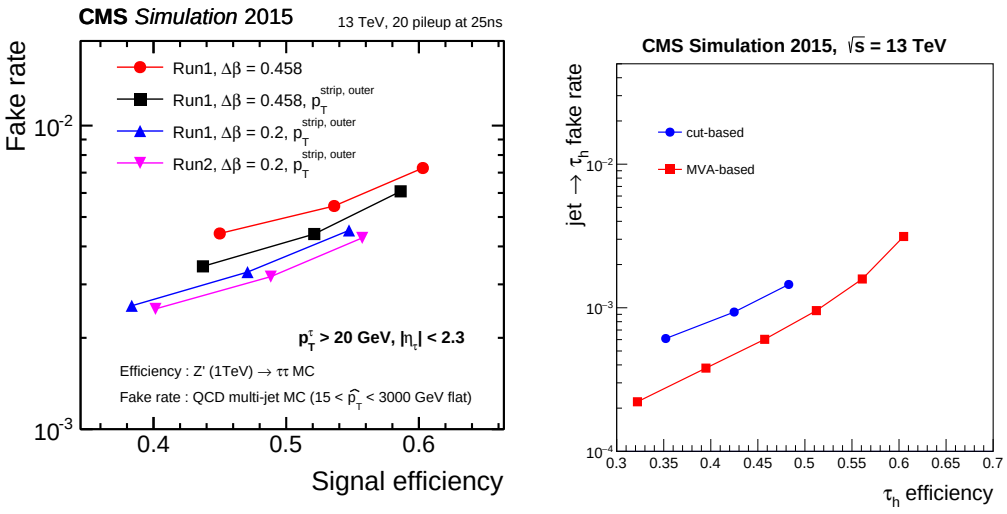

Figure 6.19: Left: Comparison of the τ_h identification performance between Run-1 and Run-2 HPS algorithm for the cut-based isolation. The tree points correspond to, from left to right, tight, medium and loose working point. Z' ($m_{Z'}$ = 1TeV) and QCD samples are used for the signal efficiency and the misidentification rate calculations, respectively. Right: Comparison of the τ_h identification performance between cut-based and MVA-based isolations. The points correspond to working points of the discriminators. [110]

tionally have a relative isolation less than 0.1, pass the medium identification, and have $|d_z| < 0.2$ cm and $d_{xy} < 0.045$ cm. The tau candidate is required to satisfy: $p_T > 20$ GeV, $|\eta| < 2.3$, leading track $p_T > 5$ GeV, old decay mode finding, no overlap with any global muon with $p_T > 5$ GeV. The muon and tau candidates should be separated by at least $\Delta R = 0.5$, and carry an opposite-sign charge. Finally, in order to reduce the W+jets background, the transverse mass between the muon and the $\not\!\!E_T$ is required to be less than 40 GeV, and P_ζ to be greater than -25 GeV.

The Drell-Yan, $t\bar{t}$, diboson and single top processes are fully estimated from MC simulations. The W+jets distribution is also taken from MC simulations, while its normalization is taken from a region where the transverse mass is greater than 80 GeV. The QCD multi-jet is estimated from a region where the tau and muon candidates have the same charge, from the subtraction of other processes estimated from MC samples to the observed data. The normalization in the signal region is obtained by applying a scale factor equal to 1.06. The systematic uncertainties considered in the extraction of the final results are the same as those used in Run-1. Simultaneous fits in the *pass* and *fail* regions are performed with m_{vis} or N_{tracks} as observable, for the different isolation discriminators, as illustrated in Fig. 6.20 for the loose working point of the MVA-based isolation with old decay modes. The data-to-simulations scale factors measured in 2015 data with both observables are given in Tab. 6.10 for different isolation working points: they are all compatible with unity, with an uncertainty close to 6%.

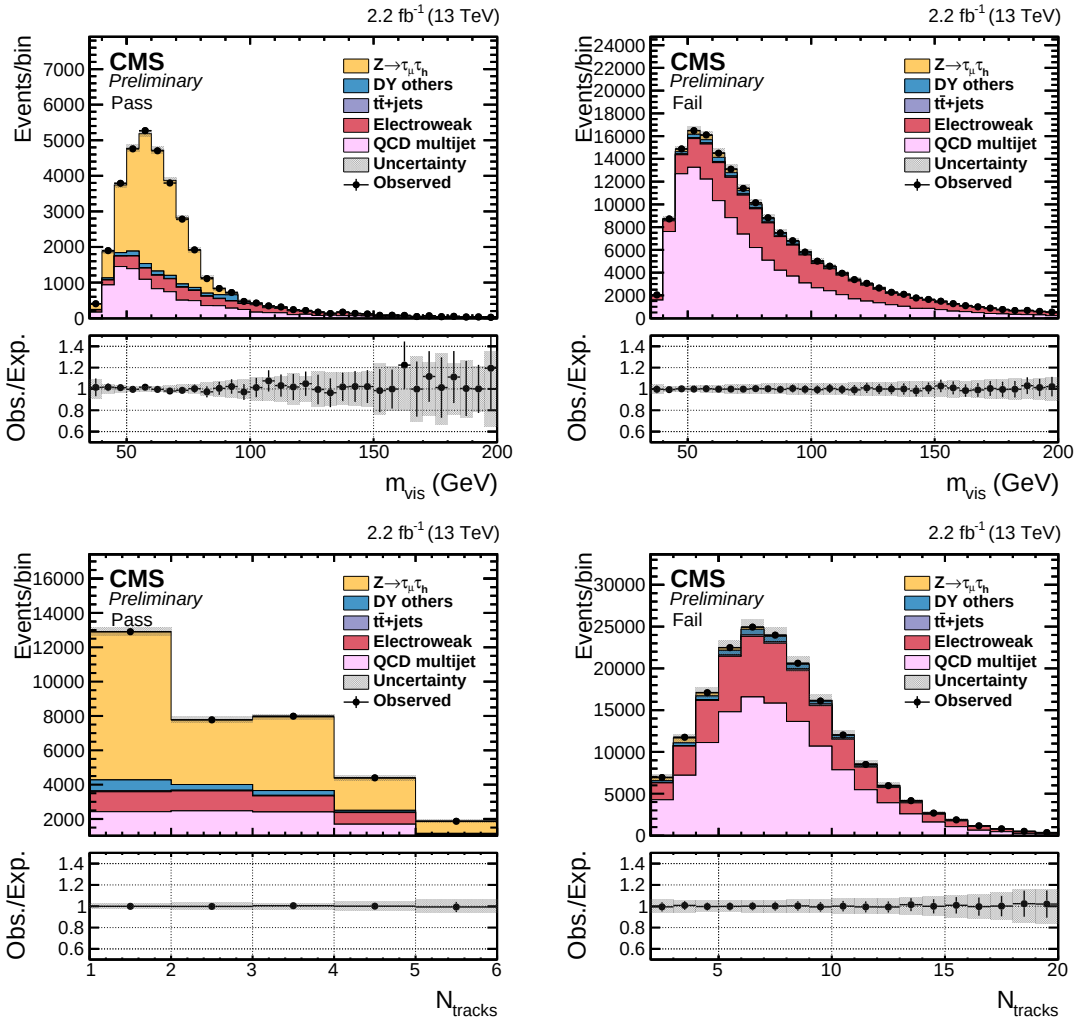

Figure 6.20: Distributions of the visible invariant mass between the muon and the tau candidates (top) or of the number of tracks inside the signal and isolation cones of the τ_h candidate (bottom), in the *pass* (left) and *fail* (right) regions, for the loose working point of the MVA-based isolation discriminator with old decay modes. The various processes are shown after the simultaneous maximum likelihood fit. [110]

	Data/Simulation	
	N_{tracks}	m_{vis}
Cut-based		
Old decay modes, loose	0.981 ± 0.055	1.016 ± 0.056
Old decay modes, medium	0.967 ± 0.054	1.006 ± 0.056
Old decay modes, tight	0.962 ± 0.051	0.999 ± 0.057
New decay modes, loose	0.982 ± 0.057	0.992 ± 0.057
New decay modes, medium	0.989 ± 0.060	0.990 ± 0.058
New decay modes, tight	0.985 ± 0.057	0.986 ± 0.059
MVA-based		
Old decay modes, loose	1.027 ± 0.055	1.037 ± 0.054
Old decay modes, medium	1.007 ± 0.054	1.018 ± 0.056
Old decay modes, tight	1.000 ± 0.052	1.027 ± 0.056
Old decay modes, very tight	0.998 ± 0.052	1.015 ± 0.055
New decay modes, loose	1.080 ± 0.090	1.026 ± 0.059
New decay modes, medium	1.055 ± 0.064	1.024 ± 0.057
New decay modes, tight	1.035 ± 0.064	1.002 ± 0.057
New decay modes, very tight	1.054 ± 0.067	1.005 ± 0.057

Table 6.10: Data-to-simulation scale factors for the efficiency for hadronic tau decays to pass different tau identification discriminators, measured in $Z/\gamma^* \to \tau\tau$ events in data collected in 2015. The columns labeled data/simulation give the ratio of efficiencies measured in data relative to the MC expectation, separately for the two cases that the observable N_{tracks} respectively m_{vis} is used in the maximum likelihood fit. Old decay modes are a subset of new decay modes.

Charge misidentification rate

The tau charge misidentification rate is measured in 2015 data for the first time at CMS. A tag-and-probe method is also used, and the events are this time divided into a "same-sign (SS)" and on "opposite-sign (OS)" regions. The parameter of interest is the data-to-MC scale factor for the tau charge misidentification rate; it directly multiplies the $Z/\gamma^* \to \tau_\mu\tau_h$ signal in the SS region and is anticorrelated to the signal yield in the OS region. The muon charge is supposed to be correctly reconstructed in all cases, which is justified from MC studies. The selection is the same as for the identification efficiency measurement, except that the τ_h candidate is required to pass the tight combined isolation working point, and that the visible invariant mass between the muon and the tau candidates is required to be less than 100 GeV.

The background estimation methods are also the same as those used for the identification efficiency measurement, except that the QCD background cannot be estimated in the SS region anymore as it is now a region used to extract the results. Instead, the QCD background distribution is taken from a signal-free region where the muon and tau candidates have a same sign charge, and the muon relative isolation is required to lie between 0.1 and 0.5. The QCD multijet distribution is taken as the difference between the observed data and the other backgrounds estimated from MC samples. The number of events in the control region is about the same as in the signal region. To cover for a bias

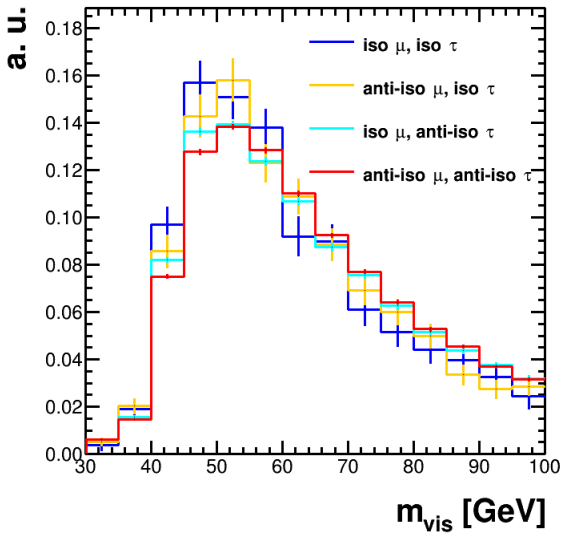

Figure 6.21: QCD multijet distributions obtained by subtracting other SM processes, estimated from MC simulations, from observed data in four regions with different muon and τ_h isolations. The QCD multijet distribution is taken from a region with an anti-isolated muon (relative isolation between 0.1 and 0.5, yellow line), and additional uncertainties are considered for masses between 40 and 50 GeV to account for the difference observed between the distributions obtained in regions where the τ_h isolation is inverted (cyan and red lines).

that may be introduced by relaxing the muon isolation, an uncertainty is added in the bins between 40 and 50 GeV. The size of this uncertainty is related to the shape difference observed between the high-statistic distributions of events selected with an anti-isolated tau candidate and an isolated or anti-isolated muon. The QCD multijet distributions obtained in the four above-mentioned SS selections are illustrated in Fig. 6.21. The QCD normalization is taken from a signal-free region where the selection is the same as in the SS signal region, except that the visible invariant mass between the muon and tau candidates is required to be larger than 100 GeV. A 10% uncertainty related to the limited statistics in the high-m_{vis} region and to the extrapolation to the low-m_{vis} region is associated to the normalization estimation. A scale factor equal to 1.06 ± 0.05, measured in a region where the muon isolation is inverted, is applied to determine the normalization in the OS region. The visible mass distributions obtained after a simultaneous maximum likelihood of the same-sign and opposite-sign regions are shown in Fig 6.22. The expected charge misidentification rate for two-prong taus is about 23%, and a data-to-simulation scale factor equal to 1.2 ± 0.3 is measured, leading to a misidentification rate in data of approximately 28 ± 7%. Taus reconstructed with the old decay mode finding are expected to have a mis-measured charge in about 0.25% of cases only; a data-to simulation scale factor equal to $3.8^{+4.6}_{-3.8}$ is measured, which indicates that the rate measured in data is compatible with the rate predicted in MC simulations, and that it is less than 1.1% at 68% CL.

The charge misidentification rate is measured separately for the old decay modes and for the two-prong decays; it is expected to be higher for the two-prong taus, for which the charge is chosen as the charge of the leading track. A simultaneous fit is performed in the SS and OS categories, considering the same nuisance parameters as for the efficiency measurement, except the following differences:

– The tau identification efficiency uncertainty is set to 5% and affects the signal in both regions;
– The QCD normalization has a 10% uncertainty correlated between the OS and SS regions, and an additional 5% in the OS region only, associated to the OS/SS scale factor.

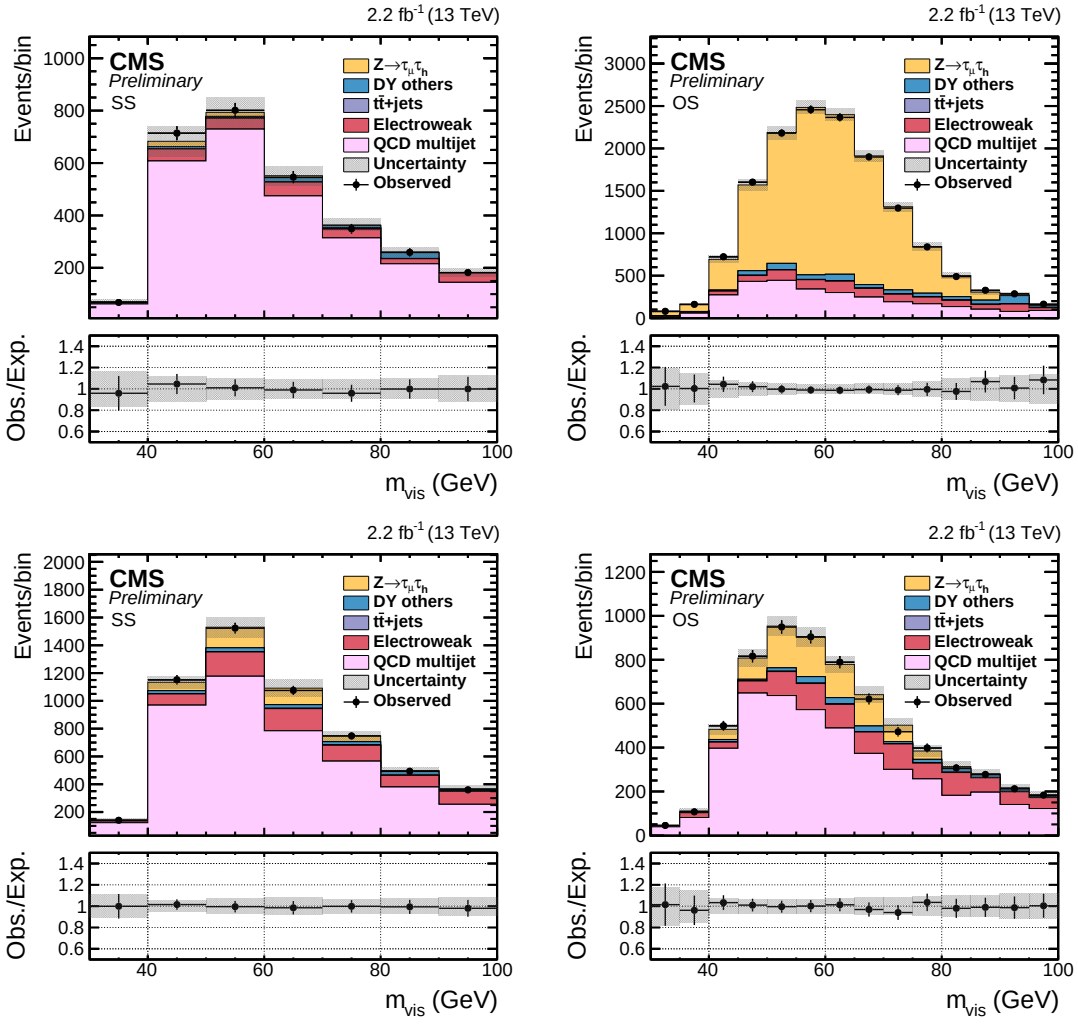

Figure 6.22: Visible mass distributions for the muon and τ_h candidates, in regions where they have the same (left) or a different (right) electric charge, obtained after a simultaneous maximum likelihood fit in both regions. The τ_h candidates considered in the top row figures pass the old decay mode finding, while in the row below they are reconstructed in one of the two-prong decay modes exclusively. [110]

6.4 Chapter summary and personal contributions

Tau lepton reconstruction and identification in CMS

Tau leptons are an important ingredient in physics analyses, especially in the scalar sector where their high mass compared to other leptons and to most quarks make them a favored decay channel for scalars. Due to their short lifetime, taus decay within the CMS detector: in about one third of cases they decay to an electron or a muon plus neutrinos, while they otherwise decay hadronically. This chapter describes first how hadronically decaying taus are identified in CMS. The first step of the HPS algorithm is to reconstruct tau candidates in one of the possible decay modes by counting the number of tracks and ECAL energy deposits. The second step prevents jets, electrons and muons from being misidentified as hadronically decaying taus, by applying among others isolation conditions. Typically, the algorithm efficiency is 60% for a $j \to \tau_h$ misidentification rate at the percent level, $e \to \tau_h$ rate at the permille level and $\mu \to \tau_h$ rate below the permille level. The performance of the algorithm is also measured in data collected by the CMS detector in 2012 and 2015. In particular, the efficiency in data is seen to be compatible with the efficiency predicted by MC simulations, with about 6% uncertainty.

My contributions

Figures: 6.4-6.17, 6.20-6.22.

I have been responsible for the tau identification efficiency measurement in $Z \to \tau_\mu \tau_h$ and in $t\bar{t} \to bb\mu\tau_h$ events, for the anti-lepton discriminator efficiency performance in Drell-Yan events, for the tau charge misidentification rate measurement, as well as for the maximum likelihood fits for the $e \to \tau_h$ and $\mu \to \tau_h$ misidentification rate measurements.

Part III

SM physics analyses

The next chapters detail searches for the SM scalar boson decaying to tau leptons. Chapter 7 is devoted to the associated production with a Z boson, Chapter 8 to the associated production with a W boson in the $e\mu\tau_h$ final state, and Chapter 9 to the combination of the searches for the SM scalar boson decaying to taus produced in gluon-gluon fusion, vector boson fusion or in association with a vector boson.

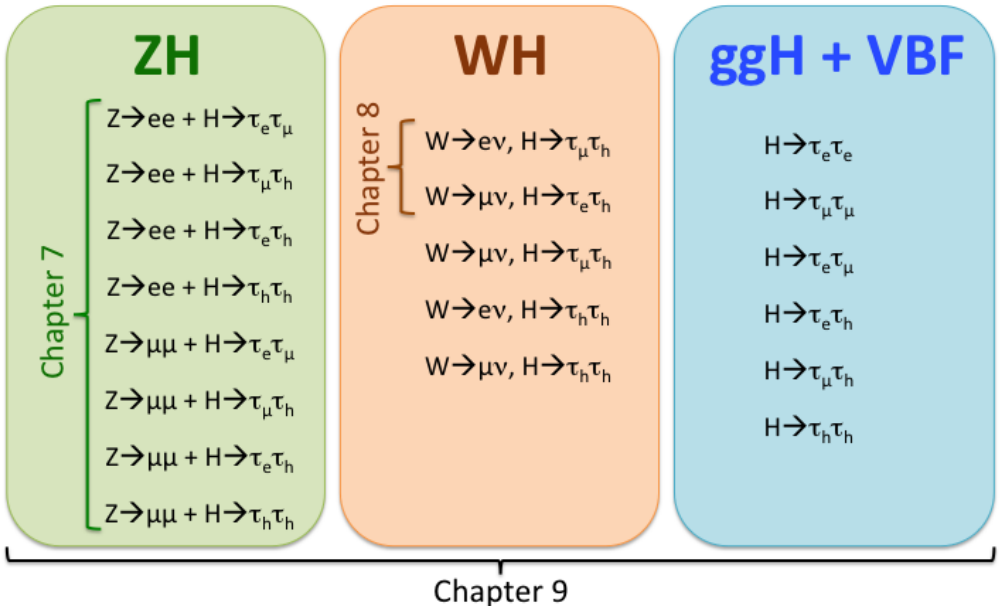

Chapter 7

Search for the SM scalar in the $ZH \to \ell\ell\tau\tau$ channel

In the SM, the scalar boson decays approximately 6% of the time to taus if it has a mass around 125 GeV. This decay mode, despite its relatively large branching fraction, is challenging experimentally due to the similarity between hadronically decaying taus, and quark and gluon jets. This chapter focuses on the production of the SM scalar boson in association with a Z boson that decays to a pair of light leptons ($\mu\mu$ or ee) [16]. Even if the ZH associated production has a low cross section (about 2% of the total H boson production cross section at the LHC), the two light leptons that originate from the Z boson can be identified more efficiently than hadronic taus and contribute to a great background reduction.

7.1 Analysis overview

The analysis covers eight different final states. The Z boson can decay to a di-muon pair or to a di-electron pair, while the di-tau final states from the H boson decay considered in this analysis are $\tau_e\tau_\mu$, $\tau_e\tau_h$, $\tau_\mu\tau_h$ and $\tau_h\tau_h$. Two di-tau final states, $\tau_e\tau_e$ and $\tau_\mu\tau_\mu$ are not studied because they overlap with the $H \to ZZ^*$ search [60] and have anyway a very low branching fraction. The dominant irreducible background comes from the ZZ diboson production, while tiny irreducible contributions are also due to the $t\bar{t}Z$ process. The rest of the background consists in reducible processes, for which at least one jet is misidentified as one of the four final state leptons. Reducible processes include essentially Z+jets and WZ+jets processes, but also small fractions of $t\bar{t}$ or QCD multijet processes among others. Irreducible processes are estimated directly from MC samples, while reducible processes are estimated with data-driven methods based on the misidentification rates of jets as leptons. Data samples correspond to 5.0 and 19.7 fb^{-1} of parked datasets collected at 7 and 8 TeV respectively with a di-muon trigger path. The complete list of MC samples, collected datasets and trigger paths, used in this analysis, can be found in Appendix A. The selected data and the expected processes are binned in distributions using the full

invariant mass of the taus (see Section 7.4) as an observable, and results are obtained from a fit of the expected processes to the observed data.

7.2 Selection

The event selection proceeds in three successive steps:
– Z boson candidate selection, from two same-flavor light leptons;
– H boson candidate selection, from two leptonic or hadronic taus;
– Other selection criteria common to all final states.

7.2.1 Z boson candidate selection

The Z boson candidate is reconstructed from two opposite-sign same-flavor light leptons. The dilepton invariant mass is required to be compatible with the Z boson mass: $|m_{\ell\ell} - m_Z| < 30$ GeV. This selection criterion is loose because most backgrounds also have a real Z boson. The events are triggered based on the two light leptons, and are required to fire trigger paths with either two muons with $p_T(\mu_1) > 17$ GeV and $p_T(\mu_2) > 8$ GeV at HLT, or two electrons with $p_T(e_1) > 17$ GeV and $p_T(e_2) > 8$ GeV at HLT. This involves that, to safely select events in the trigger efficiency plateau, the offline p_T for the light leptons are required to be larger than 20 GeV for the leading lepton, and 10 GeV for the subleading one.

The electrons in the case of $Z \to ee$ decays are required to pass the very loose PF identification (see Section 5.2.4) and to have a relative $\delta\beta$-corrected isolation less than 0.3. In addition, their pseudorapidity is such that $|\eta| < 2.5$. The muons in the case of $Z \to \mu\mu$ decays are global or tracker muons, and have an absolute pseudorapidity less than 2.4. They are required to pass the loose PF identification, and to have a relative $\delta\beta$-corrected isolation less than 0.3.

7.2.2 H boson candidate selection

After a good Z boson candidate has been found, the four di-tau final states are selected with different criteria. In every case, the two tau candidates are required to carry an opposite-sign charge and to have a transverse impact parameter with respect to the beam, $|d_z|$, less than 0.1.

To select $H \to \tau_h\tau_h$ decays, two hadronic taus with visible p_T greater than 15 GeV and $|\eta|$ less than 2.3 are required. The taus need to pass the decay mode finding discriminator, and the medium cut-based isolation is chosen because it gives the best compromise between signal efficiency and background (essentially Z+jets) rejection, and brings the highest signal sensitivity. In order to reject electrons or muons misidentified as hadronic taus, the loose working points of the discriminator against electrons (MVA-based) and muons (cut-based) are applied to the tau candidates.

Final state	τ isolation	e/μ relative isolation	L_T (GeV)
$\ell\ell\tau_h\tau_h$	medium cut-based	-	70
$\ell\ell\tau_e\tau_h$	loose cut-based	0.2	30
$\ell\ell\tau_\mu\tau_h$	loose cut-based	0.3	45
$\ell\ell\tau_e\tau_\mu$	-	0.3	25

Table 7.1: Optimal thresholds on the lepton isolation and on L_T for the different di-tau final states.

The selection of the $H \to \tau_e\tau_h$ channel requires the presence of an electron with p_T greater than 10 GeV and $|\eta|$ less than 2.5, and of a hadronic tau with p_T greater than 15 GeV and $|\eta|$ less than 2.3. The electron is required to pass the loose MVA ID and to have a relative isolation less than 0.2. The hadronic tau is required to pass the decay mode finding discriminator, as well as the loose cut-based isolation, the loose cut-based discriminator against muons and the tight working point of the MVA-based discriminator against electrons to reduce the probability of selecting a Z boson decaying to a di-electron pair.

The $H \to \tau_\mu\tau_h$ decay is reconstructed from a muon with p_T greater than 10 GeV and $|\eta| < 2.4$, and from a hadronic tau with p_T greater than 15 GeV and $|\eta| < 2.3$. The muon is required to pass the tight PF identification and to have a relative $\delta\beta$-corrected isolation less than 0.3. The hadronic tau needs to pass the decay mode finding discriminator, the loose cut-based isolation, the tight working point of the cut-based discriminator against muons and the loose working point of the cut-based discriminator against electrons.

In the $H \to \tau_e\tau_\mu$ case, an electron with p_T greater than 10 GeV and $|\eta| < 2.5$, as well as a muon with p_T greater than 10 GeV and $|\eta| < 2.4$, are selected. The muon is required to pass the tight PF identification and to have a relative $\delta\beta$-corrected isolation less than 0.3, while the electron passes the loose MVA identification and has a relative $\delta\beta$-corrected isolation less than 0.3.

The identification and isolation conditions on the leptons have been chosen in such a way as to optimize the analysis sensitivity to the hypothetical presence of a signal. Additionally, upper exclusion limits are found to improve if the events are selected with a minimal threshold on the L_T variable, defined as the scalar sum of the visible transverse momenta of the two tau candidates. Indeed, backgrounds, and especially reducible processes, typically produce leptons with lower transverse momenta than the signal. The light lepton isolation and L_T thresholds in each final state are chosen to optimize simultaneously the expected upper limits on the signal strength for a scalar boson with a mass of 125 GeV, as shown in Fig. 7.1. The optimized isolation values have been quoted in the previous paragraphs, and the L_T thresholds are 70, 30, 45 and 25 GeV in the $\tau_h\tau_h$, $\tau_e\tau_h$, $\tau_\mu\tau_h$ and $\tau_e\tau_\mu$ di-tau final states respectively. A summary of the optimized isolations and L_T thresholds for the different di-tau final states are given in Tab. 7.1.

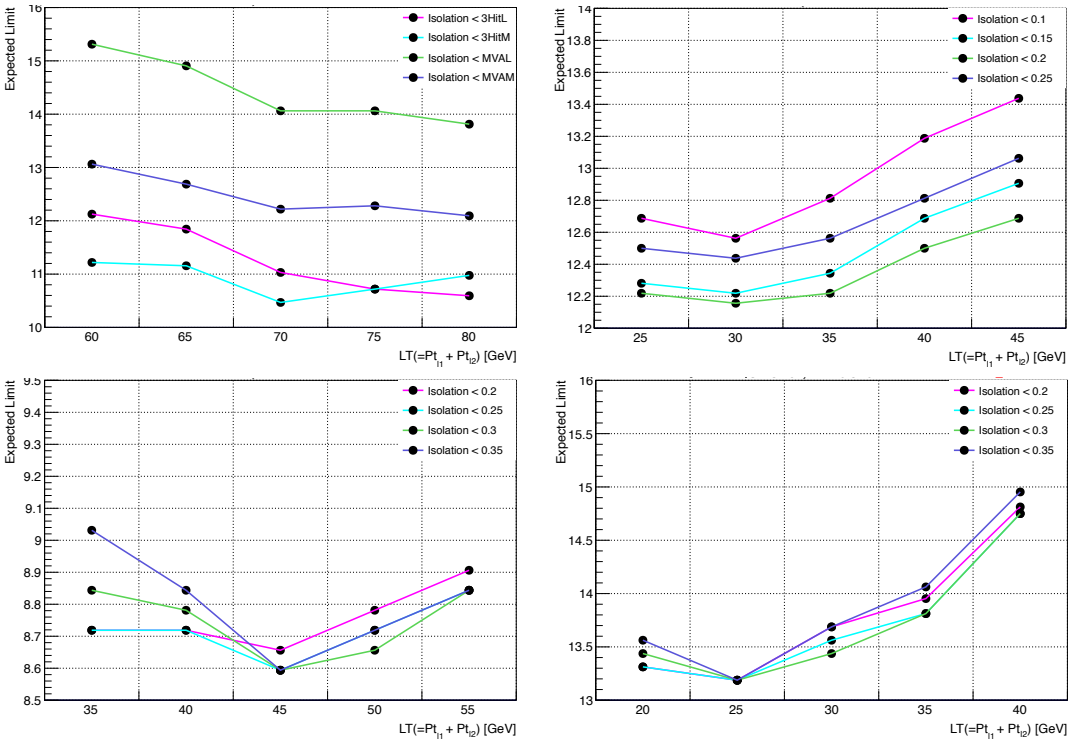

Figure 7.1: Expected upper limit on the signal strength for a scalar boson with a mass of 125 GeV produced in association with a Z boson, for different lepton isolations and L_T thresholds, in the $\ell\ell\tau_h\tau_h$ (top left), $\ell\ell\tau_e\tau_h$ (top right), $\ell\ell\tau_\mu\tau_h$ (bottom left) and $\ell\ell\tau_e\tau_\mu$ (bottom right) final states, using data collected at 8 TeV center-of-mass energy. In the $\ell\ell\tau_h\tau_h$ final state, the minimal limit is obtained with the medium working point of the cut-based isolation and $L_T > 70$ GeV, while $L_T > 30$ GeV and relative electron isolation less than 0.2 are found to optimize the limits in the $\ell\ell\tau_e\tau_h$ final state. In the $\ell\ell\tau_\mu\tau_h$ final state, $L_T > 45$ GeV and muon relative isolation between 0.25 and 0.35 minimize the expected limit, and in the $\ell\ell\tau_e\tau_\mu$ final state the best L_T threshold is 25 GeV.

7.2.3 Other common selection criteria

In order to reduce backgrounds with b jets, such as $t\bar{t}$ (reducible) or $t\bar{t}Z$ (irreducible), events that have a jet with p_T greater than 20 GeV, $|\eta| < 2.4$, and passing the medium working point of the CSV discriminator are discarded. In addition, the four selected leptons need to be separated from each other by at least $\Delta R = 0.5$, and to come from the same primary vertex ($|d_z| < 0.1$). To prevent a single event from passing the selection of different final states, a veto on extra muons and electrons is imposed: if a muon or an electron with relative isolation less than 0.3 and p_T greater than 10 GeV is found on top of the four selected leptons, the event does not pass the selection for this final state.

7.3 Background estimation

7.3.1 Irreducible process estimation

The irreducible processes, $ZZ \to 4\ell$ in its $q\bar{q}$ and gg production modes, as well as the tiny $t\bar{t}Z$ and $ZH \to ZWW$ contributions, are estimated from MC samples and normalized to their (N)NLO cross sections. The H boson decays to a pair of W bosons contribute mainly to the di-tau final state with one electron and one muon, and are considered as a background because the search targets H boson decays to taus only.

7.3.2 Reducible process estimation

All backgrounds that possess at least one jet misidentified as one of the four final state leptons, are estimated together with data-driven methods. The normalization and the distribution of the reducible processes are estimated separately. The dominant contributions come from Z+jets where two jets are misidentified as tau candidates, and WZ+jets where one jet is misidentified as a tau candidate.

Reducible background distribution

The distribution of the reducible background is obtained by selecting tau candidates with a same-sign charge (SS region). This effectively removes the contributions from $ZZ \to 4\ell$ and from the signal, and only leaves reducible processes. However, applying the full selection described in Section 7.2 except that the charge requirement on the tau candidates is inverted, leads to a statistically limited control region. In order to obtain smoother templates populated with more data events, some selection criteria that do not bias the distributions need to be relaxed. The isolation on the light leptons is relaxed to 2.0 instead of 0.2 or 0.3 in the signal region; this can be shown not to bias the distributions (see Fig. 7.2). The hadronic taus are not required to pass the loose or medium working points of the cut-based isolation, but to have a BDT output of the MVA-based isolation without lifetime information greater than 0. Relaxing the L_T thresholds is seen to shift the $m_{\tau\tau}$ distributions to lower values, as shown in Fig. 7.3. Therefore, all L_T thresholds are kept the same as in the signal region.

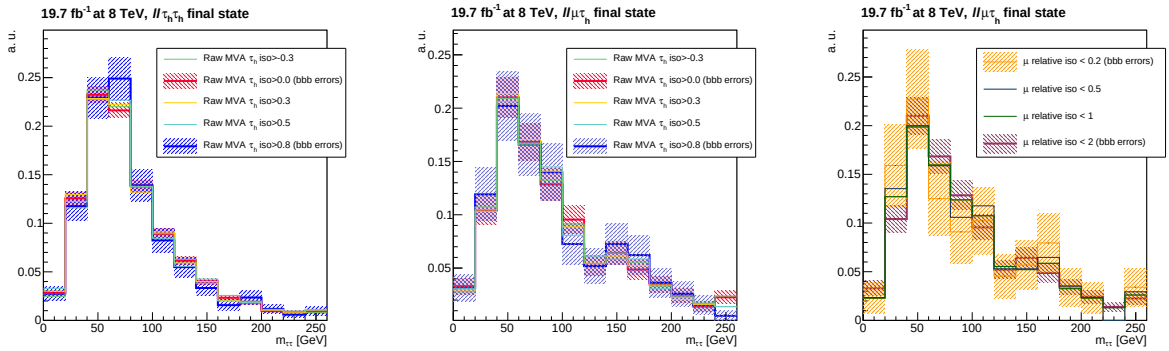

Figure 7.2: Reducible background distributions in the $\ell\ell\tau_h\tau_h$ (left) and $\ell\ell\tau_\mu\tau_h$ (center and right) final states, obtained from a region where the two tau candidates have a same-sign charge, and no L_T selection criteria are applied. The distributions are shown for different MVA output thresholds for hadronic tau isolations (left and center), or for different relative muon isolation (right). Within the statistical errors, the distributions are compatible with each other, which indicates that the isolation thresholds can be relaxed to obtain smoother non-biased templates.

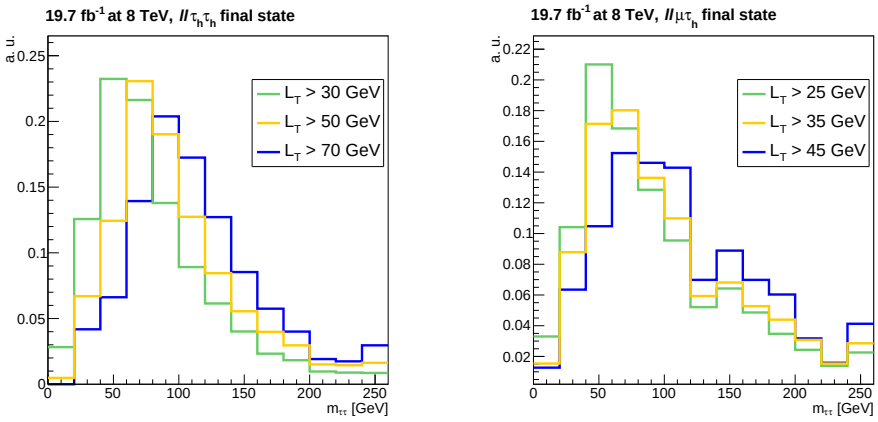

Figure 7.3: Reducible background distributions in the $\ell\ell\tau_h\tau_h$ (left) and $\ell\ell\tau_\mu\tau_h$ (right) final states, obtained from a region where the two tau candidates have a same-sign charge, and pass the relaxed isolation values described in the text. The distributions are shown for different L_T thresholds. As the L_T selection criteria bias the reducible background mass distributions, they are not relaxed to model the distribution in the signal region.

Reducible background normalization

The normalization of the reducible background is estimated with the so-called "misidentification rate method". The reducible background is essentially composed of Z+jets events, with two jets misidentified as leptons, and of WZ+jets with one jet misidentified as a lepton. One can note f_i the probability that the jet i is misidentified as a lepton and x_i the probability that the lepton i is correctly identified as a lepton, and divide the events into four different categories depending on whether the tau candidates pass the isolation and identification criteria (N_{pp}: both tau candidates pass the isolation and identification criteria, N_{pf}: the first tau candidate passes and the second one fails the isolation and/or identification criteria, N_{fp}: the first tau candidate fails and the second one passes the isolation and/or identification criteria, N_{ff}: both tau candidates fail the isolation or identification criteria). For a total number N_Z of Z+jets events, where the two tau candidates are jets, the contributions in the four regions are:

$$N_Z \rightarrow \begin{cases} N_{pp} = N_Z f_1 f_2 \\ N_{pf} = N_Z f_1 (1 - f_2) \\ N_{fp} = N_Z (1 - f_1) f_2 \\ N_{ff} = N_Z (1 - f_1)(1 - f_2) \end{cases} . \tag{7.1}$$

For a total number N_{WZ1} of WZ+jets events, where the first tau candidate is a lepton and the second one a jet, the contributions in the four regions are:

$$N_{WZ1} \rightarrow \begin{cases} N_{pp} = N_{WZ1} x_1 f_2 \\ N_{pf} = N_{WZ1} x_1 (1 - f_2) \\ N_{fp} = N_{WZ1} (1 - x_1) f_2 \\ N_{ff} = N_{WZ1} (1 - x_1)(1 - f_2) \end{cases} . \tag{7.2}$$

For a total number N_{WZ2} of WZ+jets events, where the first tau candidate is a jet and the second one a lepton, the contributions in the four regions are:

$$N_{WZ2} \rightarrow \begin{cases} N_{pp} = N_{WZ2} f_1 x_2 \\ N_{pf} = N_{WZ2} f_1 (1 - x_2) \\ N_{fp} = N_{WZ2} (1 - f_1) x_2 \\ N_{ff} = N_{WZ2} (1 - f_1)(1 - x_2) \end{cases} . \tag{7.3}$$

Therefore the total number of events in the four regions are:

$$\begin{cases} N_{pp} = N_Z f_1 f_2 + N_{WZ1} x_1 f_2 + N_{WZ2} f_1 x_2 \\ N_{pf} = N_Z f_1 (1 - f_2) + N_{WZ1} x_1 (1 - f_2) + N_{WZ2} f_1 (1 - x_2) \\ N_{fp} = N_Z (1 - f_1) f_2 + N_{WZ1} (1 - x_1) f_2 + N_{WZ2} (1 - f_1) x_2 \\ N_{ff} = N_Z (1 - f_1)(1 - f_2) + N_{WZ1} (1 - x_1)(1 - f_2) + N_{WZ2} (1 - f_1)(1 - x_2) \end{cases} . \tag{7.4}$$

One can see that the contribution of events in the signal region, N_{pp}, is given by a weighted combination of the events in the three other regions:

$$N_{pp} = N_{pf}\frac{f_2}{1-f_2} + N_{fp}\frac{f_1}{1-f_1} - N_{ff}\frac{f_1 f_2}{(1-f_1)(1-f_2)}. \quad (7.5)$$

The first term of the equation counts the WZ+jets events with the first tau candidate being a lepton and the Z+jets events, whereas the second term counts the WZ+jets events with the second tau candidate being a lepton and the Z+jets events. The subtraction of the third term removes the Z+jets contribution because it has been counted twice. If N_{pp} ends up to be negative, the reducible background contribution is estimated to be equal to the positive third term. The different terms of the equation are given for every final state studied in this analysis in Tab. 7.2, together with the estimated reducible background yield obtained by combining them.

Channel	N_{ff}		N_{pf}		N_{fp}		Estimated N_{pp}
	Weighted	Raw	Weighted	Raw	Weighted	Raw	
$\mu\mu\tau_h\tau_h$ (7 TeV)	0.17	4545	0.15	24	0.16	55	0.14±0.05
$\mu\mu\tau_e\tau_h$ (7 TeV)	0.42	2943	0.65	37	0.80	132	1.03±0.18
$\mu\mu\tau_\mu\tau_h$ (7 TeV)	0.07	544	0.72	33	0.23	16	0.88±0.18
$\mu\mu\tau_e\tau_\mu$ (7 TeV)	0.03	162	0.13	4	0.03	3	0.13±0.09
$ee\tau_h\tau_h$ (7 TeV)	0.15	4187	0.55	23	0.15	48	0.56±0.14
$ee\tau_\mu\tau_h$ (7 TeV)	0.09	555	0.33	27	0.07	8	0.31±0.09
$ee\tau_e\tau_h$ (7 TeV)	0.42	2969	1.00	54	0.46	87	1.04±0.19
$ee\tau_e\tau_\mu$ (7 TeV)	0.04	148	0.09	7	0.09	6	0.15±0.08
$\mu\mu\tau_h\tau_h$ (8 TeV)	0.86	18849	3.04	157	0.91	270	3.09±0.30
$\mu\mu\tau_e\tau_h$ (8 TeV)	1.88	14107	6.53	187	2.74	502	7.38±0.62
$\mu\mu\mu\tau_h$ (8 TeV)	0.39	2853	3.97	156	0.98	67	4.55±0.44
$\mu\mu\tau_e\tau_\mu$ (8 TeV)	0.27	879	0.90	52	0.92	46	1.55±0.27
$ee\tau_h\tau_h$ (8 TeV)	0.81	17560	2.23	149	0.87	277	2.30±0.24
$ee\tau_\mu\tau_h$ (8 TeV)	0.36	2506	2.58	138	0.59	54	2.81±0.31
$ee\tau_e\tau_h$ (8 TeV)	1.75	12655	4.82	198	2.60	430	5.67±0.48
$ee\tau_e\tau_\mu$ (8 TeV)	0.20	691	0.23	33	0.77	37	0.80±0.17

Table 7.2: Weighted and raw contributions in the N_{ff}, N_{pf} and N_{fp} regions, and their combination to obtain an estimate of the yield of the reducible background in the N_{pp} region. The last column is the sum of the weighted N_{fp} and N_{pf}, minus the weighted N_{ff}, and the quoted uncertainty is statistical only.

In order to apply the misidentification rate method, and to estimate the yields presented in Tab. 7.2, the rates with which jets are identified as electrons, muons or hadronic taus need to be computed. They are evaluated from signal- and ZZ-free regions, obtained with the signal selection except that the tau candidates are required to carry a same-sign charge and that there is no requirement on their isolation and identification (such candidates are called "relaxed" in the rest of the section).

The rate with which jets j are misidentified as τ_h ($j \to \tau_h$ misidentification rate) is computed for events with two relaxed τ_h candidates that have a same sign charge,

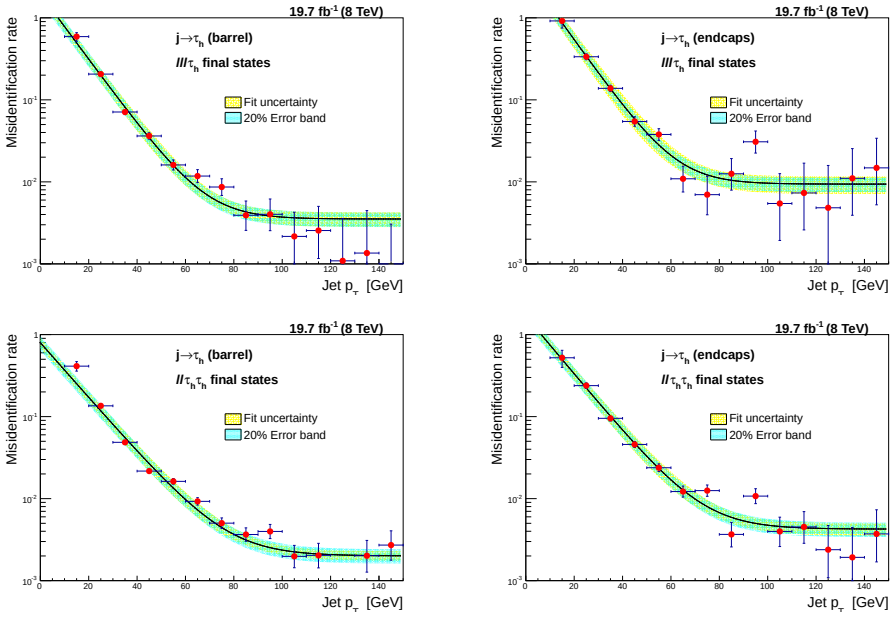

Figure 7.4: Rates with which jets are misidentified as hadronic taus, in the barrel (left) and endcap (right) regions, for the isolation working points used in the $\ell\ell\ell\tau_h$ (top) and $\ell\ell\tau_h\tau_h$ (bottom) final states. The fit uncertainties are shown with yellow bands, while 20% uncertainty bands are shown in blue.

following the $\ell\ell\tau_h\tau_h$ selection criteria except that the L_T threshold is lowered from 70 to 50 GeV. It corresponds to the ratio between the number of relaxed taus passing the isolation over the total number of relaxed taus. There is a strong dependence of the misidentification rate on the transverse momentum of the taus, because high p_T hadronic taus tend to get more collimated, which ensures a better distinction from quark and gluon jets. However the transverse momentum of tau candidates that do not pass the decay mode finding discriminator is not a well defined quantity, and a better variable is the transverse momentum of the jet closest to the tau candidate. Therefore, the $j \to \tau_h$ misidentification rates are computed as a function of the transverse momentum of the closest jet, and can be parameterized by decreasing exponentials with three constants c_1, c_2, and c_3 as:

$$f(p_T) = c_1 + c_2 e^{c_3 p_T}. \tag{7.6}$$

The $j \to \tau_h$ misidentification rates are measured separately for the loose and medium working points of the cut-based isolation, in the barrel and endcap regions, and the four corresponding curves are shown in Fig. 7.4 .

The $j \to e$ and $j \to \mu$ misidentification rates are measured in events with a good Z boson candidate, a hadronic tau and a light lepton, following the $\ell\ell\tau_e\tau_h$ and $\ell\ell\tau_\mu\tau_h$ selections. Again the tau candidates are required to carry the same charge, and the electron or muon isolation and identification criteria are relaxed. In order to increase the number of selected events, the τ_h is required to have a p_T larger than 5 GeV instead of 15

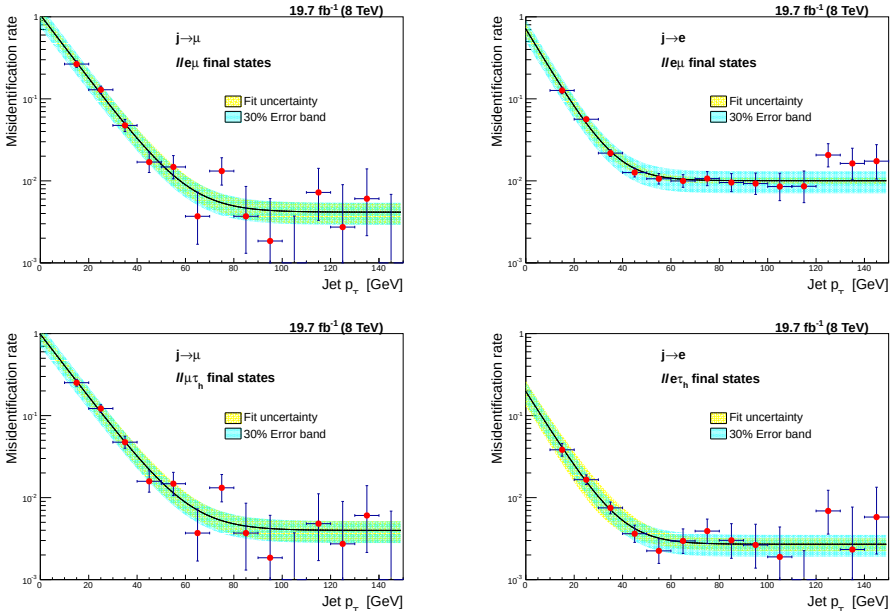

Figure 7.5: Rates with which jets are misidentified as muons (left) or electrons (right), in the $\ell\ell e\mu$ (top) or $\ell\ell\ell\tau_h$ (bottom) final states, for the isolation and identification working points used in the respective final states. The fit uncertainties (shown with yellow bands) are fully covered by 30% uncertainty bands (shown in blue).

GeV in the signal region. The presence of events with real electrons and muons, such as WZ+jets events, is reduced by requiring the transverse mass between the light lepton and the transverse missing energy to be less than 30 GeV. To be consistent with the $j \to \tau_h$ case, the misidentification rates are also parameterized as a function of the closest jet to the electron/muon [1] with a decreasing exponential. They are measured for the different isolation and identification criteria chosen to select the di-tau candidates in the different final states. Because of the limited number of events selected, the misidentification rates are measured for the barrel and endcap regions together. The misidentification rate functions are illustrated in Fig. 7.5.

To validate the background estimation method, the results from the reducible background estimation in the $\ell\ell\tau_h\tau_h$ are compared to the observed data, in a signal- and ZZ-free region where the two tau candidates have the same sign. Better statistical precision is achieved by relaxing the L_T selection criterion and the hadronic tau isolation. As shown in Fig. 7.6, both are in good agreement, in terms of distribution and normalization.

1. If no jet is found within a cone of $\Delta R = 0.5$ around the light lepton, then the transverse momentum of the light lepton itself is considered.

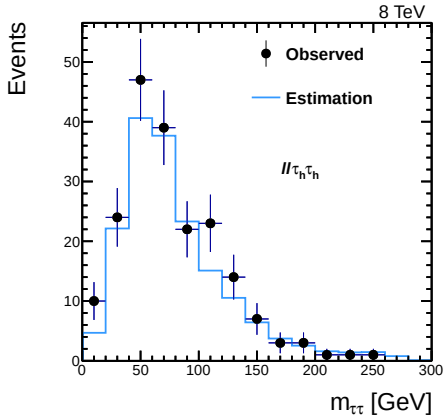

Figure 7.6: Comparison between the reducible background estimation and the observed data in the $\ell\ell\tau_h\tau_h$ final state, in a control region where the tau candidates have the same charge. Compared to the final signal selection, the isolation and L_T conditions have been relaxed to increase the number of selected events.

7.4 Di-tau mass reconstruction

As neutrinos are always present in tau decays, computing the invariant mass of two taus from their visible decay products underestimates the real mass of the resonance and leads to a poor mass resolution. The SVfit algorithm [111] can reconstruct the full di-tau mass with a likelihood technique. The kinematics of a tau decay is described by two or three parameters, in the case of hadronic or leptonic tau decays respectively:

- X, the fraction of tau energy carried by the visible decay products;
- ϕ, the angle between the visible decay product system and the full tau lepton momentum vector;
- $m_{\nu\nu}$, the invariant mass of the two neutrinos in case of a leptonic tau decay.

This leads to between four and six unknowns for a di-tau system. However, only two measured parameters can constrain the momenta of the neutrinos: the transverse missing energy magnitude and its orientation.

A probability $P(m_{\tau\tau})$ can be measured for any hypothetical di-tau mass $m_{\tau\tau}$; the best estimate of the di-tau mass corresponds to the mass that maximizes this probability. The probability is computed as follows:

$$P(m_{\tau\tau}) = \int \delta(m_{\tau\tau} - m_{\tau\tau}(\vec{y}, \vec{a}))p(\vec{x}|\vec{y}, \vec{a})d\vec{a}, \tag{7.7}$$

where the tau decay pair kinematics is described by $\vec{a} = (X_1, \phi_1, m^1_{\nu\nu}, X_2, \phi_2, m^2_{\nu\nu})$, the visible decay product momenta are given by $\vec{y} = (p_1^{vis}, p_2^{vis})$ and the missing transverse energy vector is $\vec{x}$. The expression $p(\vec{x}|\vec{y}, \vec{a})$ represents the probability that a given missing transverse energy is measured knowing the values of the visible decay products momenta

and the tau decay kinematics.

The likelihood $p(\vec{x}|\vec{y},\vec{a})$ is the product of the likelihood functions for both tau decays and of the likelihood function describing the compatibility of a di-tau pair decay with the measured $\vec{\not{E}}_T$. The individual likelihood functions are the following ones:

– Leptonic tau decays are modeled with matrix elements, and, assuming unpolarized taus, their likelihood functions read:

$$\mathcal{L}_{\tau_\ell} = \frac{d\Gamma}{dX\, dm_{\nu\nu} d\phi} \propto \frac{m_{\nu\nu}}{4m_\tau^2}(m_\tau^2 + 2m_{\nu\nu}^2)(m_\tau^2 - m_{\nu\nu}^2). \tag{7.8}$$

– For hadronic tau decays, the likelihood function is:

$$\mathcal{L}_{\tau_h} = \frac{d\Gamma}{dX\, d\phi} = \frac{1}{2\pi}\left(\frac{1}{1-\frac{m_{vis}^2}{m_\tau^2}}\right), \tag{7.9}$$

where the visible decay products are considered as a single particle with mass m_{vis}.

– If neutrinos are the only source of missing transverse energy, the measured $\vec{\not{E}}_T$ should be equal to the vectorial sum of the transverse momenta of all neutrinos. However some differences between the two quantities can occur because of experimental resolution effects. The latter are taken into account when building the $\not{E}_T$ likelihood, assuming a Gaussian resolution:

$$\mathcal{L}_\nu = \frac{1}{2\pi\sqrt{|V|}} \exp\left(-\frac{1}{2}\begin{pmatrix}\not{E}_x - \Sigma p_x^\nu \\ \not{E}_y - \Sigma p_y^\nu\end{pmatrix}^T V^{-1}\begin{pmatrix}\not{E}_x - \Sigma p_x^\nu & \not{E}_y - \Sigma p_y^\nu\end{pmatrix}\right). \tag{7.10}$$

In this expression V is the missing transverse energy covariance matrix of the event.

With respect to the so-called visible mass, the SVfit mass, later simply denoted $m_{\tau\tau}$, improves significantly the mass resolution and ensures a better discrimination between the scalar boson signal and the Z boson background, as illustrated in Fig. 7.7. In the context of the analysis presented in this chapter, the improvement on the expected upper limit brought by using the SVfit algorithm, ranges from about 10 to 40% depending on the probed H mass, as illustrated in Fig. 7.8.

7.5 Systematic uncertainties and simulation corrections

The simulations are reweighted so that they reproduce the number of true vertices measured in data.

Theoretical uncertainties on the signal cross section arise from variations of the renormalization and factorization scales (2.9% and 3.1% at 7 and 8 TeV respectively), and from

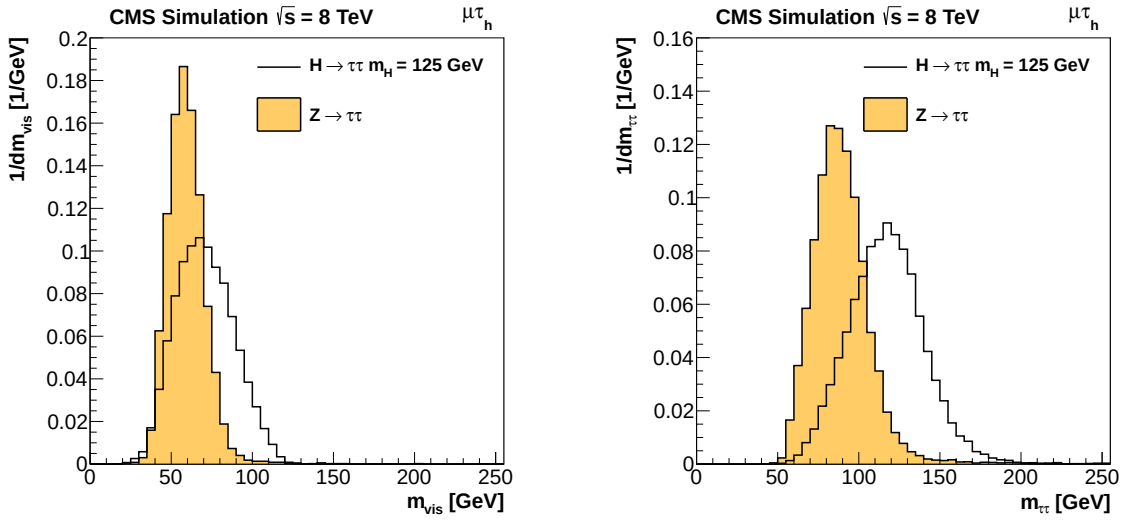

Figure 7.7: Invariant mass of two taus, using only visible decay products (left) or with the SVfit algorithm (right). One tau is chosen to decay hadronically, while the second one decays leptonically to a muon plus neutrinos. The $Z \to \tau\tau$ background is represented by the filled yellow area, whereas the black distribution represents a SM scalar boson signal with a mass of 125 GeV. The SVfit mass enhances the separation between the two processes with respect to the visible mass, and brings a better mass resolution for the signal. [16]

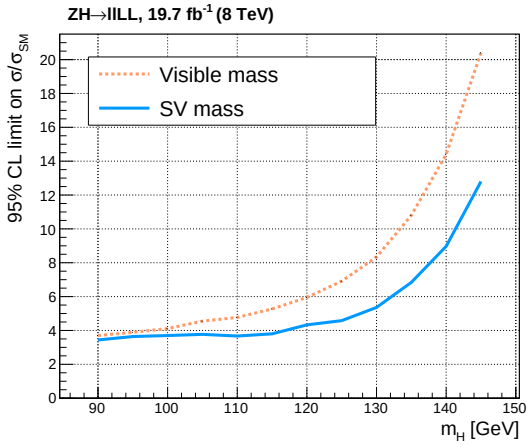

Figure 7.8: Expected upper limits at 95% CL on the signal strength of the H boson, in the $ZH \to \ell\ell\tau\tau$ channel, with 8 TeV data. The orange dashed line indicates the limit obtained when using the visible invariant mass of the taus as observable, and the plain blue line shows the corresponding limit when the SVfit-reconstructed mass, $m_{\tau\tau}$, is the observable.

uncertainties on the parton distribution functions (2.7% and 2.5% at 7 and 8 TeV respectively) [112]. The ZZ production cross section also suffers from theoretical uncertainties from parton distribution functions and QCD scale. The uncertainty on the cross section of the $t\bar{t}Z$ process is 50% [113, 114], while 44% uncertainty is assigned to the $gg \to ZZ$ background to account for theoretical uncertainties from QCD scale.

Because the lepton identification and isolation efficiencies differ in data and simulations, the MC events are reweighted with some scale factors, determined via tag and probe methods. The scale factors and their uncertainties are usually measured for different p_T and $|\eta|$ values of the leptons. The uncertainties amount to 2% per single muon, 2% per single electron and 6% per single hadronic tau. Conservatively, they are multiplied by the number of leptons. The simulations are also corrected for the differences in trigger efficiency observed in data. The muon and electron trigger efficiency uncertainties amount to 1% and are also measured from tag and probe methods. An uncertainty of 1%, introduced by the b-tag veto, is associated to the yield of all processes estimated from MC simulations. The effect on the yield is relatively small because the mis-tagging rate is low. The luminosity uncertainty amounts to 2.2% in 2011 [115] and 2.6% in 2012 [109]. It is fully correlated between all processes estimated from MC samples, namely the irreducible backgrounds ($ZZ \to 4\ell$, $t\bar{t}Z$ and $ZH \to ZWW$) and the signal samples.

An uncertainty of 3% is related to the tau energy scale, as explained in Chapter 6. This does not only impact the normalization of the distributions taken from MC simulations (if a tau has a larger energy, it is more likely to pass the p_T threshold requirements), but also their distributions ($m_{\tau\tau}$ strongly depends on the visible four-momenta of the two taus). Therefore the tau energy scale is considered as a shape uncertainty, and two additional distributions for every MC-estimated process, corresponding to the variations by ± 1 standard deviation of the tau energy scale, are provided to compute the limits. The nominal and alternative distribution for the signal and irreducible backgrounds are shown in Fig. 7.9 for two di-tau final states.

The uncertainty on the normalization of the reducible background comes from the fits of the misidentification rates, which are statistically limited. The fit functions are modified within their uncertainties, and the yields of the reducible processes are recomputed for the variations, which permits to compute a yield uncertainty related to the modifications of the fit functions. It can be seen that a 20 or 30% uncertainty band can cover the variations of the $j \to \tau_h$ or $j \to e/\mu$ fit functions respectively. The uncertainty associated to a given fit function is fully correlated between the final states where it is used to compute the reducible background yield, while uncertainties associated to different fit functions are fully uncorrelated. The uncertainties by final state range from 15% ($\ell\ell\tau_h\tau_h$) to 30% ($\ell\ell e\mu$). The smaller yield uncertainty in the $\ell\ell\tau_h\tau_h$ final state is the consequence of the better statistical precision in the fit functions because the $j \to \tau_h$ misidentification rate is more than one order of magnitude larger than the $j \to \ell$ misidentification rates.

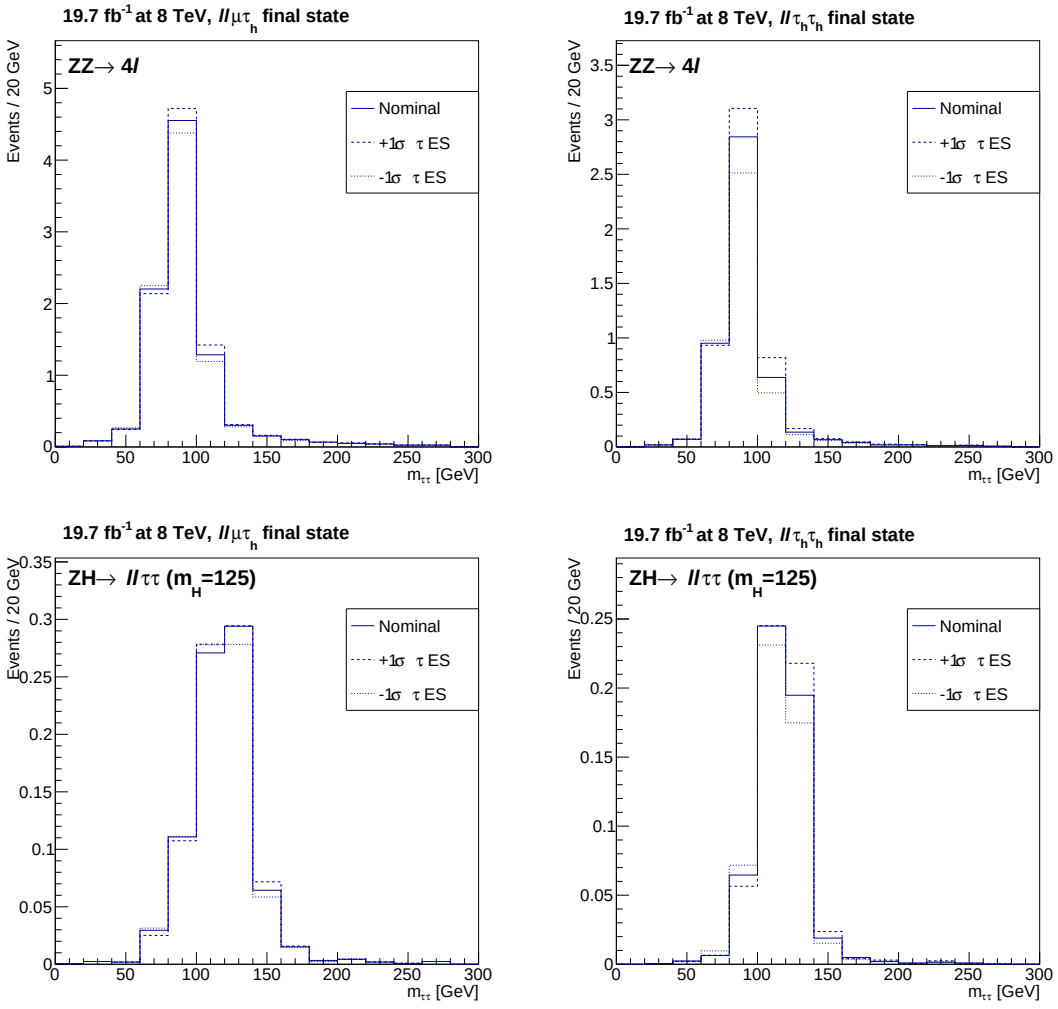

Figure 7.9: Nominal $m_{\tau\tau}$ distributions and their corresponding contributions when the tau energy scale is varied by ± 1 standard deviation, for the $ZH \to \ell\ell\tau\tau$ signal (top) and $ZZ \to 4\ell$ background (bottom), in the $\ell\ell\tau_\mu\tau_h$ (left) and $\ell\ell\tau_h\tau_h$ (right) final states.

Because the number of events after all selection criteria is low for the MC-estimated processes, an uncertainty between 5 and 50%, depending on the final number of events, is assigned to the MC processes [2]. This uncertainty is not correlated between final states as it only has a statistical origin, and is not correlated between processes either.

Finally, bin-by-bin errors are taken into account for every process, estimated from MC simulations or with data-driven method. Because this results in a large number of additional shape uncertainties, these uncertainties are pruned: only those that modify the yield in a bin by more than 10%, or in a 50 GeV $m_{\tau\tau}$ window around 125 GeV, are kept. This pruning is checked to have a very limited impact on the final results.

A summary of the systematic uncertainties and of their effects on the yields of the different processes can be found in Tab. 7.3.

	Systematic Source	Effect on yield							
		$\mu\mu\tau_h\tau_h$	$ee\tau_h\tau_h$	$\mu\mu\tau_e\tau_h$	$ee\tau_e\tau_h$	$\mu\mu\tau_\mu\tau_h$	$ee\tau_\mu\tau_h$	$\mu\mu\tau_e\tau_\mu$	$ee\tau_e\tau_\mu$
Experiment	Luminosity (2011)	2.2%							
	Luminosity (2012)	2.6%							
	Muon trigger	1%	-	1%	-	1%	-	1%	-
	Electron trigger	-	1%	-	1%	-	1%	-	1%
	Muon ID/iso.	4%	-	4%	-	6%	2%	6%	2%
	Electron ID/iso.	-	4%	2%	6%	-	4%	2%	6%
	Tau ID/iso.	12%	12%	6%	6%	6%	6%	-	-
	Tau energy scale	shape						-	
	b-Jet veto	1%							
Theory	PDF $q\bar{q} \to ZZ$	5%							
	PDF $gg \to ZZ$	10%							
	PDF $q\bar{q} \to ZH$	2.5%							
	Scale variation $q\bar{q} \to ZZ$	6%							
	Scale variation VH (2011)	3.1%							
	Scale variation VH (2012)	2.9%							
	$t\bar{t}Z$ cross section	50%							
	$gg \to ZZ$ cross section	44%							
Background estimation	Loose $j \to \tau_h$ rate	-		20%				-	
	Medium $j \to \tau_h$ rate	15%		-					
	Tight $j \to e$ rate	-		10%		-			
	Loose $j \to e/\mu$ rate	-						30%	
	Tight $j \to \mu$ rate	-				10%		-	
	Bin-by-bin errors	shape							
	Limited $gg \to ZZ$ sample	5%	5%	5%	5%	5%	5%	5%	5%
	Limited $q\bar{q} \to ZZ$ sample	5%	5%	5%	5%	5%	5%	5%	5%
	Limited $t\bar{t}Z$ sample	50%	50%	30%	30%	30%	30%	15%	15%

Table 7.3: Sources of systematic uncertainties, and the effects their variations by ± 1 standard deviation have on the yield of the different signal and background processes.

2. The most limited MC samples after selection, which are assigned an uncertainty as large as 50%, contribute to the expected yield by a negligible amount.

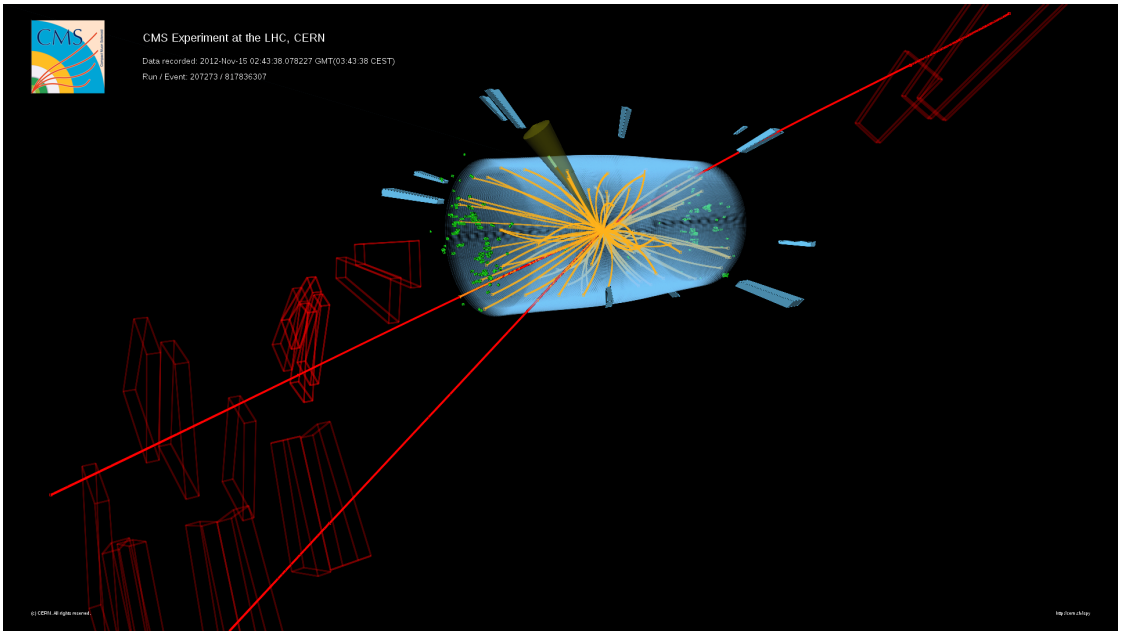

Figure 7.10: 3D view of a event compatible with a $ZH \to \mu\mu\tau_\mu\tau_h$ decay, recorded by CMS at 8 TeV center-of-mass energy in November 2012. In the figure, starting from the upper left corner and proceeding clockwise, the green cone indicates the hadronic tau ($p_T = 19.0$ GeV) potentially coming from the SM scalar boson decay, the first red line in the negative pseudorapidity region represents the first muon ($p_T = 18.4$ GeV), daughter of the Z boson, then, in the positive pseudorapidity, region the second red line indicates the muon ($p_T = 47.5$ GeV) coming from the decay of the tau from the scalar boson decay, and the third red line represents the second muon coming from the Z boson ($p_T = 22.0$ GeV). The Z boson candidate has a mass of 91.0 GeV and the full di-tau mass of the scalar boson candidate, $m_{\tau\tau}$, is 122.8 GeV. [116]

7.6 Results

After the selection, only 84 data events remain, and some of them have a di-tau mass $m_{\tau\tau}$ compatible with 125 GeV. This is the case for example of an event recorded on the 15th of November 2012: the event is selected with the $\mu\mu\tau_\mu\tau_h$ selection and has $m_{\tau\tau}$ equal to 122.8 GeV. A three-dimensional view of this particular event is shown in Fig. 7.10.

A simultaneous maximum likelihood fit is performed in all final states; the resulting postfit distributions are shown in Fig. 7.11 and 7.12 at 7 and 8 TeV center-of-mass energy respectively. The predicted and observed yields for the different final states and data taking periods are detailed in Tab. 7.4. The maximum likelihood fit permits to extract the best-fit signal strength, as well as the pulls on the nuisance parameters. The signal strength for the combination of the eight final states at 7 and 8 TeV is found to be:

$$\hat{\mu} = 1.61 \pm 1.85. \tag{7.11}$$

The spread of the measured signal strengths for the different di-tau final states and the

Process	Signal	Background	Data	$\frac{S}{S+B}$
$ee + e\mu$ 7 TeV	0.045 ± 0.002	1.0 ± 0.1	1	0.077
$\mu\mu + e\mu$ 7 TeV	0.051 ± 0.002	1.0 ± 0.1	3	0.100
$ee + \tau_h\tau_h$ 7 TeV	0.061 ± 0.004	1.1 ± 0.1	1	0.127
$\mu\mu + \tau_h\tau_h$ 7 TeV	0.073 ± 0.006	0.8 ± 0.1	0	0.195
$ee + e\tau_h$ 7 TeV	0.075 ± 0.004	2.2 ± 0.1	4	0.077
$\mu\mu + e\tau_h$ 7 TeV	0.078 ± 0.004	2.2 ± 0.1	1	0.092
$ee + \mu\tau_h$ 7 TeV	0.087 ± 0.004	1.5 ± 0.1	2	0.135
$\mu\mu + \mu\tau_h$ 7 TeV	0.111 ± 0.005	2.4 ± 0.3	2	0.103
$ee + e\mu$ 8 TeV	0.185 ± 0.007	4.0 ± 0.2	4	0.082
$\mu\mu + e\mu$ 8 TeV	0.202 ± 0.008	5.1 ± 0.3	9	0.105
$ee + \tau_h\tau_h$ 8 TeV	0.260 ± 0.020	4.8 ± 0.4	9	0.148
$\mu\mu + \tau_h\tau_h$ 8 TeV	0.285 ± 0.022	5.8 ± 0.4	4	0.150
$ee + e\tau_h$ 8 TeV	0.279 ± 0.013	10.2 ± 0.5	13	0.063
$\mu\mu + e\tau_h$ 8 TeV	0.293 ± 0.014	12.2 ± 0.6	8	0.081
$ee + \mu\tau_h$ 8 TeV	0.385 ± 0.018	7.6 ± 0.4	11	0.149
$\mu\mu + \mu\tau_h$ 8 TeV	0.427 ± 0.021	10.5 ± 0.6	12	0.092

Table 7.4: Observed and predicted event yields in all final states and data taking periods. Background contributions are measured after a simultaneous maximum likelihood fit of all final states, whereas the signal at $m_H = 125$ GeV is normalized to the SM expectation. The last column, $S/(S+B)$ represents the ratio of the signal and signal-plus-background yields in the central $m_{\tau\tau}$ range containing 68% of the signal events for $m_H = 125$ GeV.

different data taking periods is shown in the left-hand side of Fig. 7.13. Computing the chi-square of this set of measured signal strengths with respect to the best-fit value $\hat{\mu}$ for the combination, and comparing it to the chi-square distribution for toys generated with the background-plus-signal hypothesis with $\mu = \hat{\mu}$, one can see that such a spread is expected and reasonable. This is illustrated in the right-hand side part of Fig. 7.13.

As no excess of data above the expected backgrounds is observed, upper limits on the signal strength are set at 95% CL, using the asymptotic CL_s method. The limits obtained in the four di-tau final states are shown in Fig. 7.14. The $\ell\ell\mu\tau_h$ final state is the most sensitive channel because of the clear signature left by muons in the detector, while the $\ell\ell\tau_h\tau_h$ is the second one because of the large branching fractions for taus to decay hadronically. They can be combined together, as illustrated in Fig. 7.15. The upper expected limits on the signal strength range from about 2.5 to 20 depending on the H boson mass probed. These results are compatible with those obtained by the ATLAS Collaboration [117].

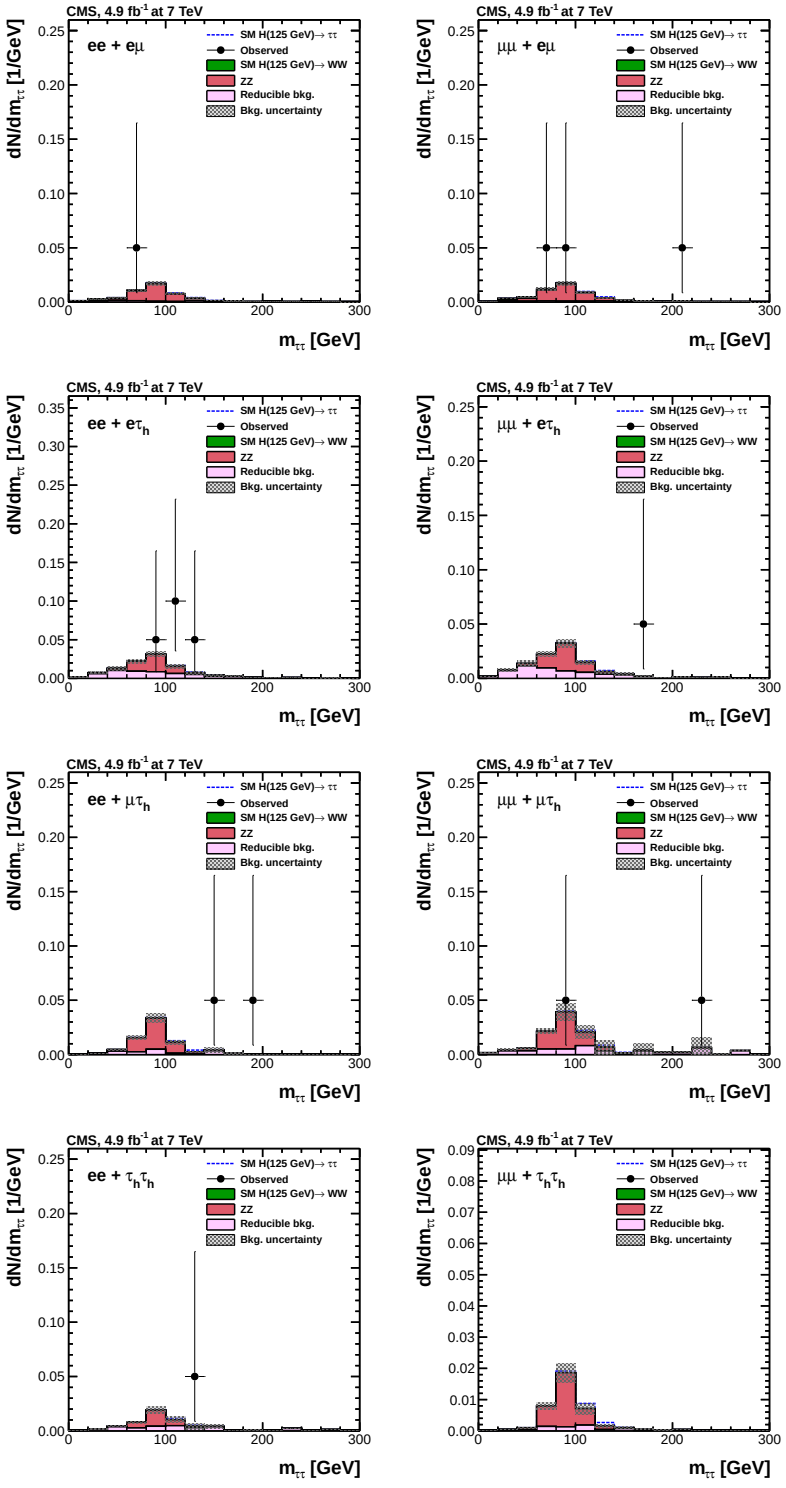

Figure 7.11: Expected and observed $m_{\tau\tau}$ distributions in the eight different final states at 7 TeV. The distributions are obtained after a maximum likelihood fit that includes the nuisance parameters discussed previously. [16]

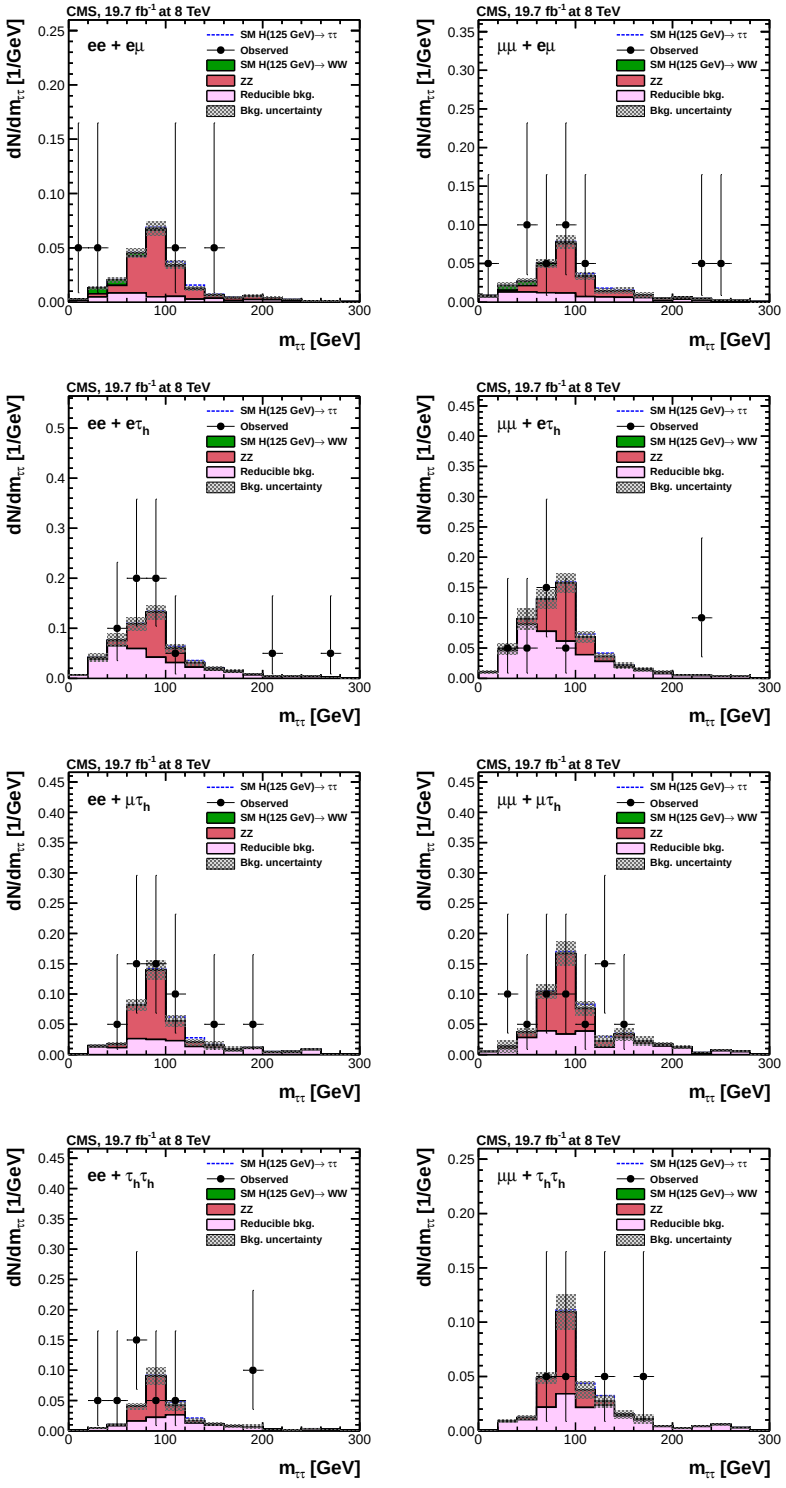

Figure 7.12: Expected and observed $m_{\tau\tau}$ distributions in the eight different final states at 8 TeV. The distributions are obtained after a maximum likelihood fit that includes the nuisance parameters discussed previously. [16]

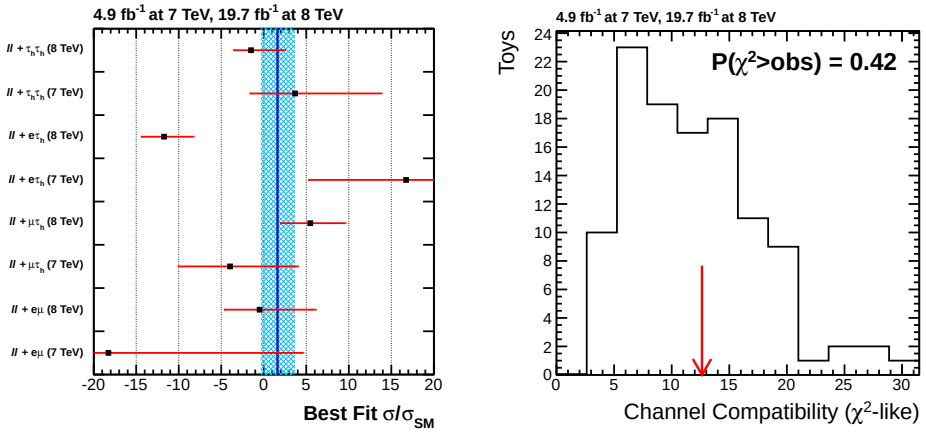

Figure 7.13: Left: Best-fit signal strengths per period and di-tau final state (black squares and red uncertainty lines), and combined measured signal strength (blue). Right: Observed chi-square (red arrow) and chi-square distribution for toys generated with a signal strength equal to the best-fit combined value. 42% toys have a chi-square larger than the observed one, which indicates a very reasonable spread of measured individual strengths.

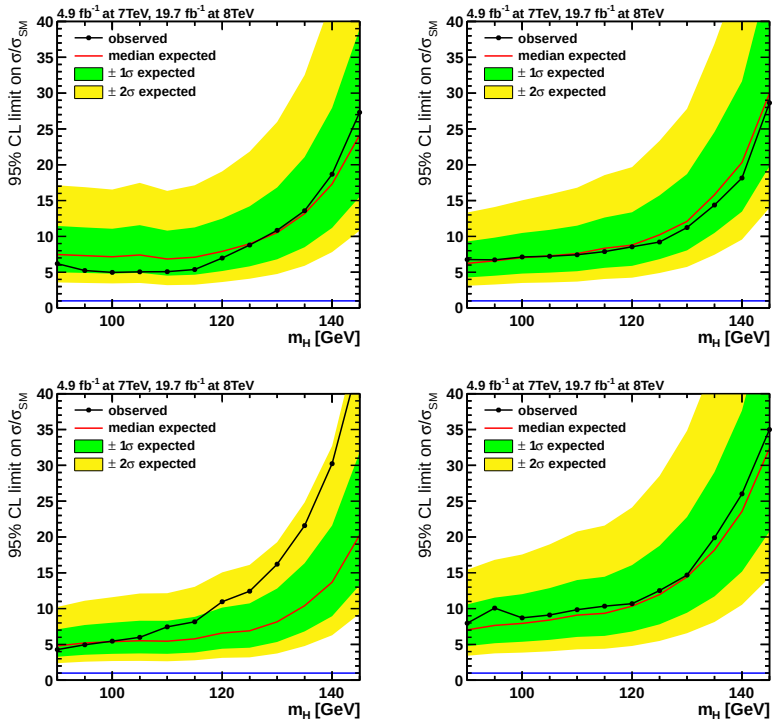

Figure 7.14: Observed and expected 95% CL upper limits on the signal strength in the $\ell\ell\tau_h\tau_h$ (top left), $\ell\ell e\tau_h$ (top right), $\ell\ell\mu\tau_h$ (bottom left) and $\ell\ell e\mu$ final states.

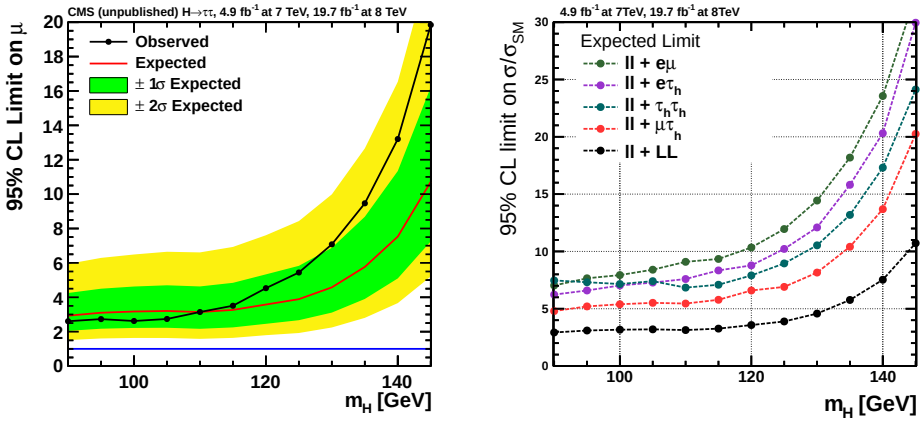

Figure 7.15: Expected and observed 95% CL upper limits on the scalar boson signal strength for the combination of all final states at 7 and 8 TeV [116] (left) and decomposition of the expected limit between different di-tau final states (right).

7.7 Chapter summary and personal contributions

Search for the SM scalar in the $Zh \to \ell\ell\tau\tau$ channel

$H \to \tau\tau$ is the most sensitive decay channel to test the Yukawa couplings of the recently discovered boson. Because of the large $j \to \tau_h$ fake rate, studying this decay in the dominant gluon-gluon fusion production mode leads to large Drell-Yan and QCD multijet background. Even though the associated production with a Z boson has a cross section more than one order of magnitude lower, searching for $ZH \to \ell\ell\tau\tau$ events is viable due to the large background reduction that can be achieved by selecting the two light leptons originating from the Z boson. The irreducible $ZZ \to 4\ell$ background is estimated from MC samples, while reducible processes are determined via the misidentification rate method. The analysis is sensitive to about four times the expected signal cross section in the SM.

My contributions

Figures: 7.2-7.6, 7.8-7.9, 7.11-7.15.

I have participated in the $ZH \to \ell\ell\tau\tau$ results, at all stages of the analysis (selection optimization, background estimation, ...), and have been responsible for the limit setting.

Chapter 8

Search for the SM scalar in the $WH \to e\mu\tau_h$ channel

The cross section for the associated production of the SM scalar boson with a W boson is several times larger compared to the associated production with a Z boson, but the background reduction is less strong because of a less clean signature. Two analyses have been performed with the data collected in Run-1 by the CMS detector [16]: one for fully hadronic tau decays $WH \to \ell\tau_h\tau_h$ and the second one for semi-leptonic di-tau final states $WH \to \ell\tau_\ell\tau_h$. The $e\mu\tau_h$ final state of the latter channel, where the W boson decays to a light lepton and a neutrino, one of the taus to a light lepton of the other flavor, and the other tau hadronically, is the object of this chapter.

8.1 Selection

This analysis targets leptonic W boson decays with one light lepton (electron or muon), leptonic decays of one of the taus, and hadronic decays of the other tau. The $e\mu\tau_h$ final state is described in this chapter, whereas the $\mu\mu\tau_h$ final state is included in [16], and the $ee\tau_h$ final state is not studied because of its lower sensitivity [1].

The events are selected with asymmetric electron-muon trigger paths, for which the leading lepton is required to have a transverse momentum greater than 17 GeV, and the subleading one greater than 8 GeV. Offline, the lepton matched to the leading trigger leg is required to have a transverse momentum greater than 20 GeV, while the lepton matched to the subleading trigger leg should have a transverse momentum greater than 10 GeV. In addition, the electron candidate is selected with $|\eta| < 2.5$, $|d_z| < 0.2$ cm, loose MVA identification and a relative isolation less than 0.15 (0.10) for $|\eta| < 1.479$ (> 1.479). Requiring the three charge estimates to be consistent with each other reduces the electron charge

1. The lower sensitivity of the $ee\tau_h$ final state compared to the $\mu\mu\tau_h$ final state can be explained by the more efficient muon reconstruction and identification, and by the larger electron charge misidentification, which plays a role because the light leptons are required to carry the same electric charge to reduce the Drell-Yan background.

misidentification rate. The muon candidate is selected with $|\eta| < 2.4$, $|d_z| < 0.2$ cm, tight PF identification, and a relative isolation less than 0.15 (0.10) for $|\eta| < 1.479$ (> 1.479). Both light leptons are required not to be associated to a jet that has a CSV discriminator greater than 0.8. The $t\bar{t}$ background is drastically reduced by requiring the electron and the muon to have the same electric charge. The τ_h candidate is required to have a different electric charge, to have $p_T > 20$ GeV, $|\eta| < 2.3$, $|d_z| < 0.2$ cm, and to pass the decay mode finding discriminator, the loose working point of the cut-based isolation, the loose working point of the cut-based discriminator against electrons, and the loose working point of the cut-based discriminator against muons. In the case where the invariant mass between the electron (muon) and tau candidates is in a 40-GeV wide window around the Z boson mass, the tight working point of the discriminator against electrons (muons) is chosen to reduce the Drell-Yan background $Z/\gamma^* \to ee$ and $Z/\gamma^* \to \mu\mu$ contribution. All three objects are required to be separated by at least $\Delta R = 0.5$. Events that contain a b-tagged jet (tight CSV working point), or additional identified electrons, muons or taus, are vetoed. The extra lepton veto prevents any overlap with the $ZH \to \ell\ell\tau\tau$ analysis described in Chapter 7.

Events collected at a center-of-mass energy of 8 TeV are divided into two categories according to L_T, the scalar p_T sum of the three leptons: the L_T-high category is characterized by $L_T > 130$ GeV and the L_T-low one by $L_T < 130$ GeV. Because of the lower integrated luminosity in 2011, 7 TeV events are grouped in a single category with $L_T > 70$ GeV. This categorization improves the sensitivity of the analysis because signal events typically have a larger L_T than background events.

8.2 Background estimation

Irreducible backgrounds correspond to processes with at least three real leptons in the final state, namely $WZ \to 3\ell\nu$ and $ZZ \to 4\ell$. The $ZZ \to 4\ell$ process is reduced by requiring the event not to have more than three identified leptons. These diboson contributions are estimated from MC samples, and normalized to their predicted NLO cross sections [118].

Other backgrounds feature at least one misidentified object, and are classified as reducible. Reducible processes include among others W+jets, $t\bar{t}$, though greatly reduced by the same sign charge requirement on the light leptons, QCD multijet, and Z+jets events. These backgrounds are estimated together with a misidentification rate method. The principle of the method is the same as described in Chapter 7 for the $ZH \to \ell\ell\tau\tau$ analysis. In this case, the "fakeable" objects are considered to be the muon and the electron, and the $j \to e$ and $j \to \mu$ rates therefore have to be measured in data. These misidentification rates are measured in a W+jets-enriched region in data, defined in the same way as the signal region except that the events should not include a τ_h candidate. In addition, the region is enriched in W+jets events by requiring the transverse mass between the "tag" lepton (the lepton that passes all identification and isolation conditions) and the $\not{E}_T$ to be greater than 55 GeV, and the transverse mass between the "probe" lepton (the

lepton without identification and isolation conditions for which the misidentification rate is measured) and the $\vec{\not{E}}_T$ to be less than 35 GeV. In order to make the topology as close as possible to the signal region, an additional jet with p_T greater than 20 GeV is required to mimic the presence of the hadronically decaying tau.

The misidentification rates for electrons and muons are determined independently with a k-Nearest Neighbors (kNN) classifier (see Section 3.7). This allows the rates to depend on a large number of variables. In practice, three variables are chosen in this analysis: the probe lepton p_T, the p_T of the jet closest to the probe lepton, and the number of jets with $p_T > 20$ GeV in the event. The rate measured in collected data for jets to be misidentified as muons is shown in Fig. 8.1 as a function of these three variables. As seen in the context of the $ZH \to \ell\ell\tau\tau$ analysis, the misidentification rates strongly decrease with the transverse momentum of the closest jet. The dependence with the lepton p_T is more complicated because of the contamination of real leptons from WZ events in the high-p_T region. The number of jets variable is particularly useful to parameterize the difference in the misidentification rates in different topologies; these rates indeed tend to be lower for events with a large number of jets, such as $t\bar{t}$ events because of the higher hadronic activity that spoils the probe lepton isolation. The number of nearest neighbors is chosen to be equal to fifty, which ensures a good local description with limited statistical fluctuations.

However, applying such a technique leads to an overestimation of the misidentification rates, especially at high lepton p_T, because of the contamination of ZZ and WZ events with real leptons in the W+jets enriched region. To remove these contributions, two additional kNN per lepton (muon or electron) are trained, respectively for ZZ and WZ events in MC simulations that pass the W+jets enriched region selection. The two kNN outputs are subtracted from the data kNN output according to the expected contributions of WZ and ZZ events in the data region, estimated from the process cross sections. In particular, the kNN outputs of these two MC samples are scaled by:

$$\frac{N^{MC}\mathcal{L}^{data}}{N^{data}\mathcal{L}^{MC}}, \tag{8.1}$$

where N^{MC} and N^{data} are respectively the raw number of events in MC simulations and data in the W+jets control region where the training is done, and $\mathcal{L}^{MC}$ and $\mathcal{L}^{data}$ are the respective integrated luminosities of the MC simulations and data samples.

The rates measured in such a way are applied to data events that pass the signal region selection, except that the muon and/or the electron candidates do not pass the isolation and/or identification conditions. Assuming a misidentication rate f_e for the electron candidate (f_e depends on the electron p_T, on the p_T of its closest jet, and on the number of jets with $p_T > 20$ GeV in the event), and a misidentification rate f_μ for the muon candidate, events with two leptons failing the isolation and/or identification conditions are weighted with $\frac{f_e f_\mu}{(1-f_e)(1-f_\mu)}$, events with the electron passing but the muon failing the identification

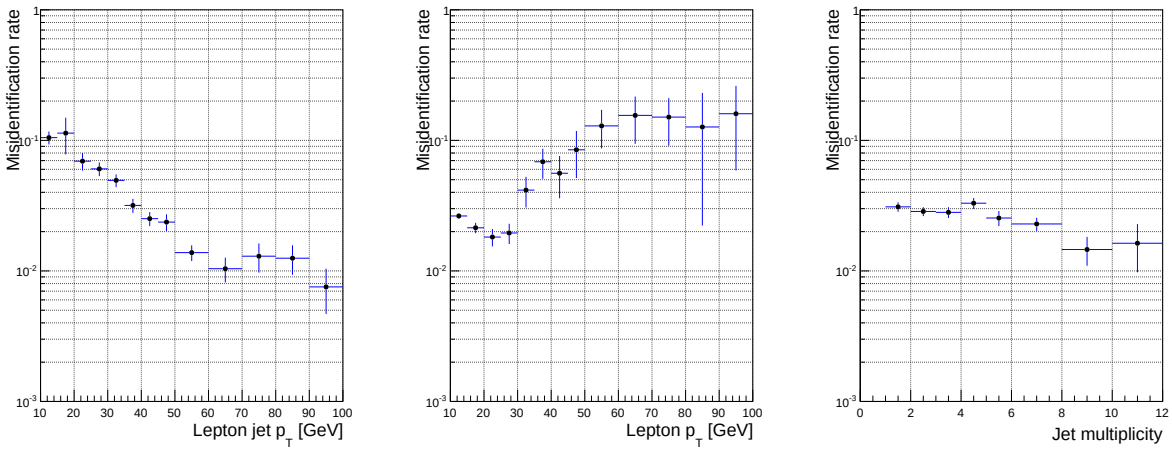

Figure 8.1: Rates with which jets are misidentified as muons, as a function of the p_T of the jet closest to the lepton candidate (left), of the lepton candidate p_T (center), and of the number of jets with $p_T > 20$ GeV in the event. The misidentification rates are measured in a W+jets enriched region in data collected in 2012 at 8 TeV center-of-mass energy. The increase of the misidentification rate with the lepton p_T is due to the contamination of real leptons from WZ events in the high p_T region, while the decrease with the number of jets is caused by the higher hadronic activity, which spoils the lepton isolation.

and/or isolation conditions are weighted with $\frac{f_\mu}{1-f_\mu}$, and events with the muon passing but the electron failing the identification and/or isolation conditions are weighted with $\frac{f_e}{1-f_e}$. As described in Chapter 7, the double counting of events with two fake leptons is removed by subtracting the weighted contribution of events with two leptons failing the isolation and/or isolation conditions, to the sum of the two other weighted categories.

The reducible background estimation method is validated in a control region where the τ_h candidate has the same sign as the electron and the muon, and does not pass the loose working point of the cut-based isolation. This region is signal-free, and enriched in reducible background. Fig. 8.2 illustrates the L_T and m_{vis} distributions; predicted backgrounds agree with observed data both in terms of normalization and distribution. A band corresponding to 30% uncertainty on the reducible background prediction is drawn.

The method of the e/μ misidentification rate is cross-checked with an independent method, which considers the τ_h candidate as the possibly misidentified object. The $j \to \tau_h$ misidentification rate is measured in a W+jets enriched region in data. The events in the control region are selected with a single muon trigger; the muon candidate is required to have $p_T > 24$ GeV, $|\eta| < 2.1$, to pass the tight PF identification, and to have a relative isolation less than 0.1 and a longitudinal impact parameter of the track with respect to the primary vertex less than 0.2 cm. The region is enriched in W+jets events by requiring the transverse mass of the muon and the $\not\!\!E_T$ to be greater than 40 GeV. Two same-sign τ_h candidates, with an opposite charge with respect to the muon, are also selected. Events

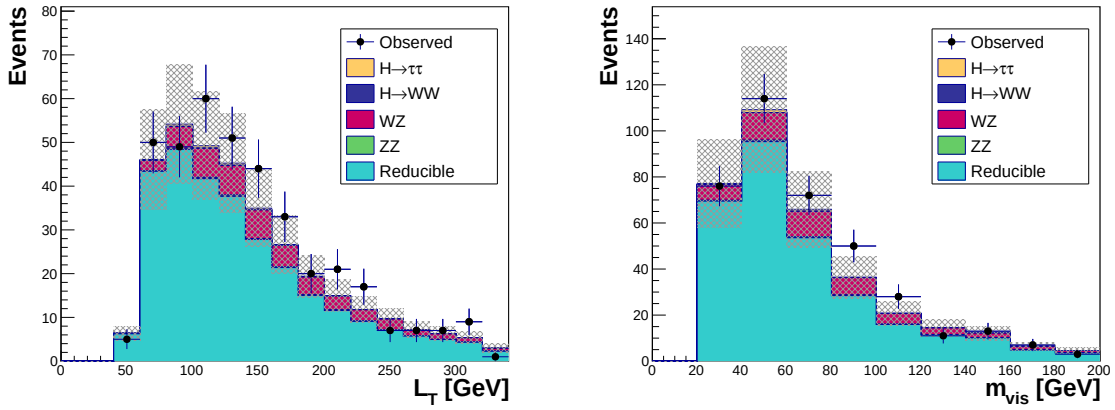

Figure 8.2: Distributions of L_T (left) and of the visible invariant mass between the τ_h candidate and the subleading light lepton (right), when all three objects have the same sign and the τ_h isolation condition is inverted. An uncertainty of 30% for the reducible background is drawn as a shaded area. No maximum likelihood fit to the observed data has been applied. Only 8 TeV data are used in this figure.

that contain an extra light lepton (with $p_T > 15$ GeV), or a b-tagged jet (with $p_T > 20$ GeV) are vetoed. The $j \to \tau_h$ misidentification rate is measured in three pseudorapidity regions ($|\eta| < 0.8$, $0.8 \leq |\eta| < 1.6$, $1.6 \leq |\eta| < 2.3$), separately for 2011 and 2012 data. The dependence of the misidentification rates with the τ_h transverse momentum is parameterized with Landau functions, as illustrated in Fig. 8.3. The mathematical form of Landau distributions is:

$$f(p_T) = \frac{1}{\pi} \int_0^\infty e^{-x \log x - x p_T} \sin(\pi x) dx. \tag{8.2}$$

Events in data that have a loose τ_h candidate that does not pass the isolation condition are reweighted with a weight w:

$$w(p_T) = \frac{f(p_T)}{1 - f(p_T)}, \tag{8.3}$$

in order to estimate the reducible background contribution in the signal region. This method estimates backgrounds that have jets misidentified as τ_h, but does not take into account events where the τ_h corresponds to a real hadronically decaying tau or to a $e/\mu \to \tau_h$ object. Therefore, the small Drell-Yan background contribution is not included in the reducible background estimated with this method, and is instead directly taken from MC samples. The reducible background obtained with the τ_h misidentification method is compared to the one obtained with the e/μ misidentification method described previously. The comparison in the high- and low-L_T regions, shown in Fig. 8.4, demonstrates an excellent agreement between both techniques within statistical uncertainties. The background estimated with the e/μ misidentification rate method is considered as the default one, while the background estimated with the τ_h misidentification rate method is considered as an alternative with a shape uncertainty.

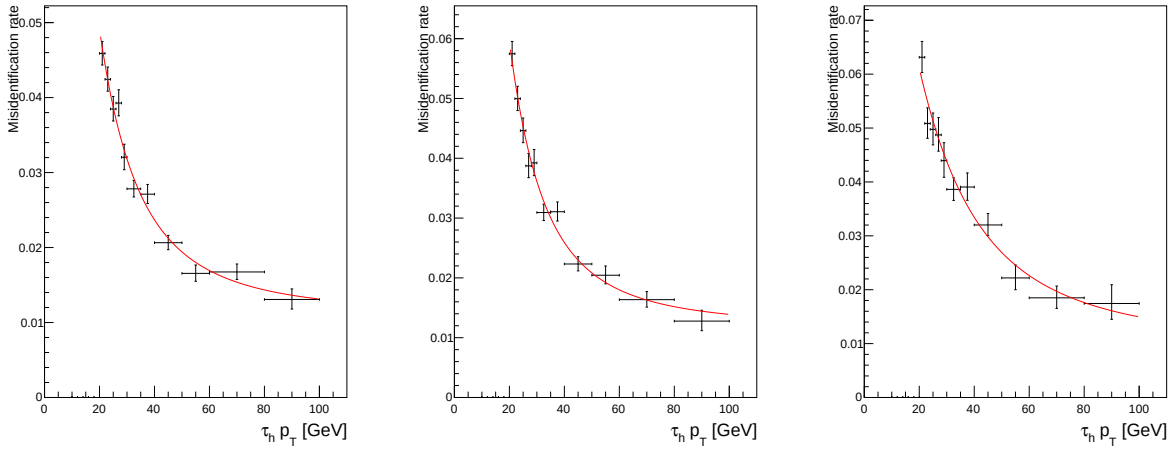

Figure 8.3: Rates with which jets are misidentified as hadronically decaying taus in the barrel ($|\eta| < 0.8$, left), transition ($0.8 \leq |\eta| < 1.6$, center), and endcap ($1.6 \leq |\eta| < 2.3$, right) regions. The misidentification rates are measured in data collected in 2012 at 8 TeV center-of-mass energy, and are fitted with Landau functions.

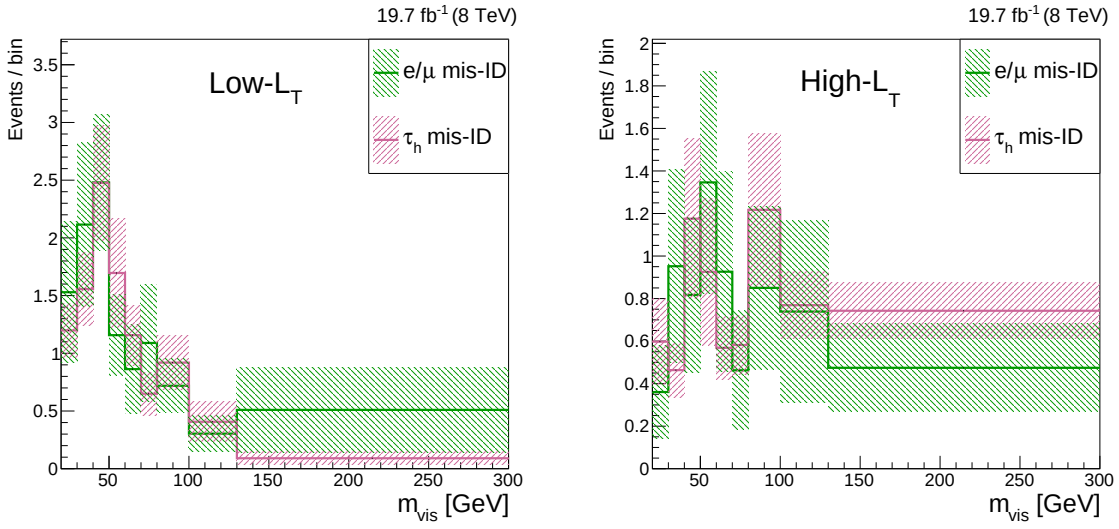

Figure 8.4: Comparison between the reducible background distributions obtained with the e/μ and τ_h misidentification rate methods, in the low-L_T (left) and high-L_T (right) regions. The shaded areas correspond to statistical uncertainties only.

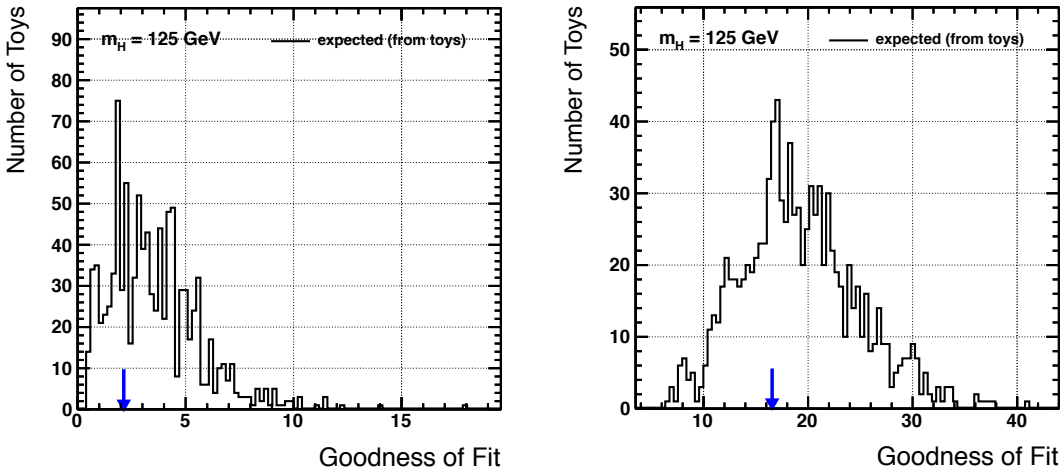

Figure 8.5: Goodness-of-fit test in the $e\mu\tau_h$ final state, in data collected at 7 TeV (left) and 8 TeV (right) center-of-mass energy.

8.3 Results

The observable used to extract the upper exclusion limits is the visible invariant mass between the τ_h candidate and the subleading light lepton. Leptons from leptonic decays of taus originating from H bosons indeed tend to have a lower transverse momentum than light leptons directly originating from W boson decays. The correct di-tau pair is reconstructed in about 70% of cases with this method. The SVfit mass is not used for the WH analyses with $H \to \tau\tau$ because the $\not\!\!E_T$ coming from the W boson decay is mixed to the $\not\!\!E_T$ from the tau decays.

Many systematic uncertainties, such as the trigger efficiency, muon and electron identification and identification, tau identification, tau energy scale, b-tagged jet veto, and luminosity uncertainties are in common with the $ZH \to \ell\ell\tau\tau$ analysis described in Chapter 7. Uncertainties that differ include 30% uncertainty on the normalization of the reducible background due to the e/μ misidentification rate method, and the alternative reducible background distribution from the τ_h misidentification rate method. Additionally, diboson backgrounds estimated from MC samples (WZ and ZZ) are attributed PDF and QCD renormalization scale uncertainties (about 4% each), and a statistical uncertainty between 3 and 10% to account for the limited number of events remaining after the full signal selection.

Goodness-of-fit tests are performed for the 7 and 8 TeV distributions; the results are shown in Fig. 8.5. The observed goodness-of-fit lies in both cases in the bulk of the goodness-of-fit distribution for toys experiments, which indicates a good agreement between the process predictions and the observed data.

m_H	-2σ	-1σ	Median	$+1\sigma$	$+2\sigma$	Obs. Limit
90 GeV	1.40	1.90	2.73	3.96	5.56	3.36
95 GeV	1.59	2.15	3.09	4.49	6.29	3.76
100 GeV	1.77	2.41	3.45	5.04	7.04	4.10
105 GeV	1.48	2.01	2.88	4.18	5.88	2.88
110 GeV	2.13	2.89	4.14	6.02	8.46	4.09
115 GeV	2.14	2.91	4.17	6.08	8.59	3.60
120 GeV	2.33	3.17	4.58	6.71	9.50	4.02
125 GeV	2.84	3.88	5.58	8.18	11.58	4.62
130 GeV	3.53	4.83	6.97	10.27	14.58	5.53
135 GeV	4.31	5.90	8.59	12.67	18.19	6.54
140 GeV	5.82	7.98	11.59	17.09	24.40	8.81
145 GeV	7.42	10.20	14.91	22.10	31.81	11.04

Table 8.1: Expected and observed limits at 95% CL on the signal strength for the $WH \to e\mu\tau_h$ process, for H boson masses between 90 and 145 GeV.

The visible mass distributions obtained with the 7 TeV data, and the 8 TeV data in the two categories, are shown in Fig. 8.6. A good agreement between predicted processes and observed data is seen, and upper limits on the signal cross section are set at 95% CL. At $m_H = 125$ GeV, the analysis is sensitive to about 4.6 times the cross section expected in the SM. All values for H boson masses between 90 and 145 GeV are indicated in Tab. 8.1.

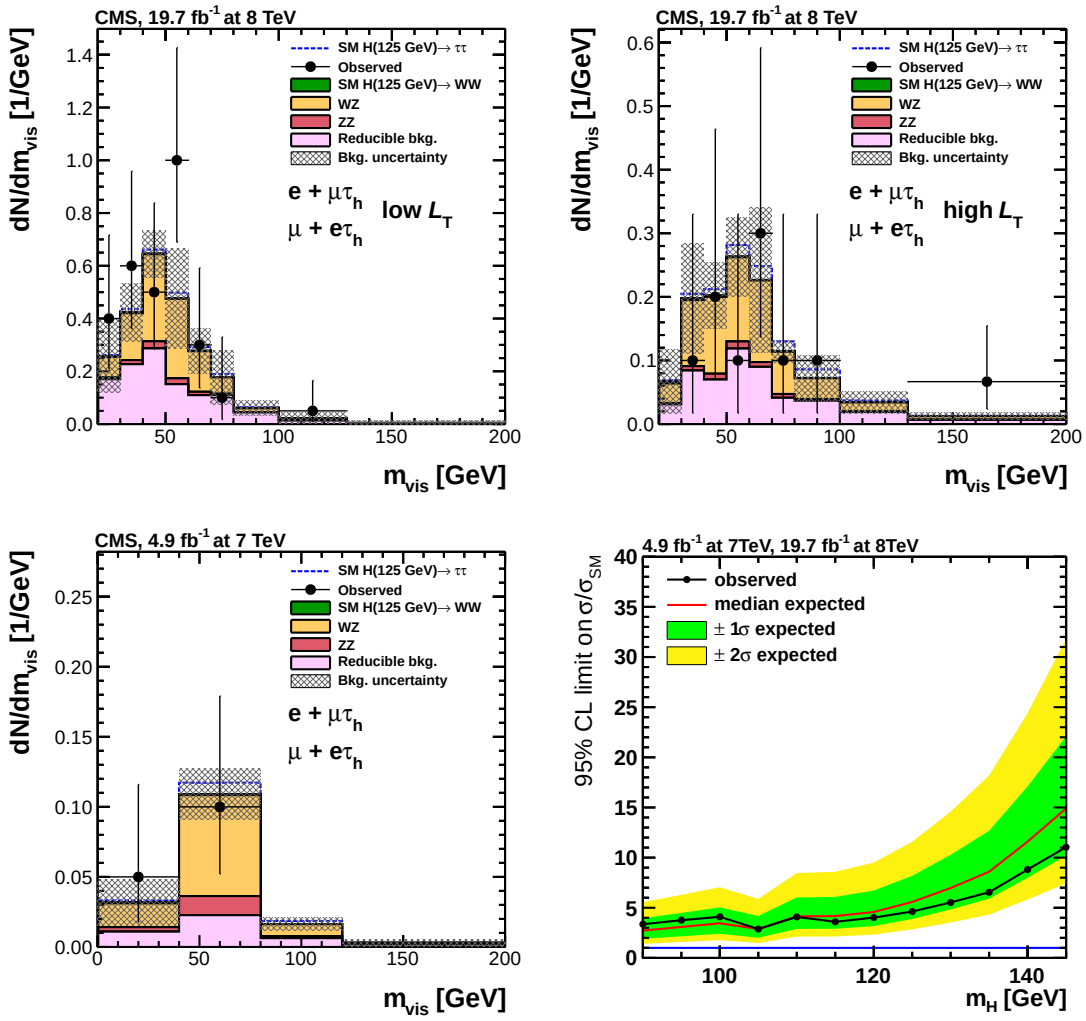

Figure 8.6: Observed and expected distributions of the visible invariant mass between the τ_h candidate and the subleading lepton, at 8 TeV in the low-L_T (top left) and high-L_T (top right) regions, and at 7 TeV (bottom left). [16] The expected and observed limits at 95% CL on the signal cross section for the combination of these distributions is shown in the bottom right part of the figure.

8.4 Chapter summary and personal contributions

Search for the SM scalar in the $WH \to e\mu\tau_h$ channel

The WH production cross section is several times larger than the ZH production cross section, but the level of background is higher because the W boson decay products are less efficient to select than the Z boson decay products. The $e\mu\tau_h$ decay channel, where one of the light lepton promptly comes from the W boson whereas the other one comes from the decay of one of the taus originating from the H boson, is described in this chapter. A great background rejection is achieved by requiring the two light leptons to have the same electric charge. The reducible background is estimated with a misidentification rate method that relies on the probability for jets to be identified as light leptons. No excess of events is observed, and the analysis is sensitive to about five times the expected cross section times branching fraction for the process under study.

My contributions

Figures: 8.1-8.6.

I have cross-checked all $WH \to e\mu\tau_h$ results up to the final limits for the publication in [16].

Chapter 9

Combination of searches for the SM scalar boson decaying to taus

The two searches presented in Chapter 7 and 8, respectively $ZH \to \ell\ell\tau\tau$ and $WH \to e\mu\tau_h$, are combined with searches for the SM scalar boson decaying to taus and produced in gluon-gluon fusion and vector boson fusion productions, as well as with searches in the WH channel but with other final states ($WH \to \ell\tau_h\tau_h$ and $WH \to \mu\mu\tau_h$). This combination provides an important test of the H boson Yukawa couplings.

9.1 Gluon-gluon fusion and vector boson fusion production modes

The gluon-gluon fusion and vector boson fusion production modes are studied simultaneously. Events are separated into different exclusive categories to increase the signal/background discrimination based on kinematic properties of the signal:

- 2-jet: This category targets the VBF production. The events are required to have at least two jets with p_T greater than 30 GeV, and to pass additionally some criteria to increase the VBF signal purity, based on the invariant mass of the jets and their separation in the η-direction.
- 1-jet: This category targets the gluon-gluon fusion production with a jet from initial state radiation.
- 0-jet: This category targets the gluon-gluon fusion production.

The 2-jet and 1-jet categories are the most sensitive. Meanwhile the 0-jet category is the least sensitive because of the overwhelming Drell-Yan background, but is useful to constrain nuisance parameters. Events are further divided according to the transverse momentum of the H boson candidate ($p_T^H = |\vec{p_T}(\tau_1) + \vec{p_T}(\tau_2) + \vec{\not{E}_T}|$, where $\vec{p_T}(\tau_1)$ and $\vec{p_T}(\tau_2)$ are the reconstructed visible transverse momenta of the taus), in order to select H boson candidates boosted in the transverse plane, and according to the transverse momentum of the tau candidates, as they are typically larger than the p_T of taus originating from Z bosons if $m_H > m_Z$.

The six possible di-tau final states are studied. The most sensitive final state is $\tau_\mu\tau_h$, whereas the least sensitive final states $\tau_e\tau_e$ and $\tau_\mu\tau_\mu$ because of the small expected di-tau branching fraction. All details can be found in [16].

9.2 Vector boson associated production

Despite the small production cross section compared to the gluon-gluon fusion and vector boson productions, searching for a scalar boson decaying to taus and produced in association with a vector boson permits to constrain the scalar couplings to vector bosons. Three final states studied in Run-1 in the context of the search for a SM scalar boson decaying to taus and produced in association with a vector boson, have not been presented in the previous chapters: $WH \to \mu\tau_h\tau_h$, $WH \to e\tau_h\tau_h$ and $WH \to \mu\mu\tau_h$. The latter final state is covered with background estimation methods very similar to those used in the $WH \to e\mu\tau_h$ analysis detailed in Chapter 8, and the $Z/\gamma^* \to \mu\mu$ background is greatly reduced by requiring the two muon candidates in the event to have the same electric charge. The large reducible background in the $WH \to \ell\tau_h\tau_h$ final states is reduced by training a BDT and selecting events with a BDT output above a certain threshold. The BDT takes as input the τ_h candidate p_T, the distance between the τ_h candidates, the missing transverse energy, as well as the ratio between the vectorial and scalar sums of the τ_h candidate p_T. The observable used to extract the results is the invariant mass between the τ_h candidates.

The results of the combination between all VH analyses with H decays to taus performed in Run-1 are shown in Fig. 9.1 and Tab. 9.1. The limits increase with the mass of the scalar boson probed because of the expected decrease of the branching fraction $\mathcal{B}(H \to \tau\tau)$. Although there is a small deficit of observed events compared to the expected SM processes, the results are compatible both with the existence and the absence of a SM scalar boson at a mass of 125 GeV. For this particular mass, the observed upper limit at 95% CL on the signal strength lies at 2.1. The combined best-fit signal strength is $\hat{\mu} = -0.33 \pm 1.02$, which corresponds to $\hat{\mu} = 1.61 \pm 1.85$ for the ZH channels, $\hat{\mu} = -3.15 \pm 2.03$ for the WH channels with two hadronically decaying taus, and $\hat{\mu} = -1.57 \pm 1.65$ for the WH channels with exactly one hadronically decaying tau. The VH analyses are expected to reach the SM sensitivity in Run-2 with the increase of integrated luminosity and the increase of center-of-mass energy.

9.3 Combination of all production modes

A comparison of the expected sensitivity of all the final states and categories combined, in terms of upper limits on the signal strength, is shown in Fig. 9.2. The searches in all production modes are combined together, and their uncertainties are correlated when applicable. An excess of events is observed on top of the SM background predictions, as seen in Fig. 9.3 in the combined distribution of the decimal logarithm $\log(S/(S+B))$ obtained

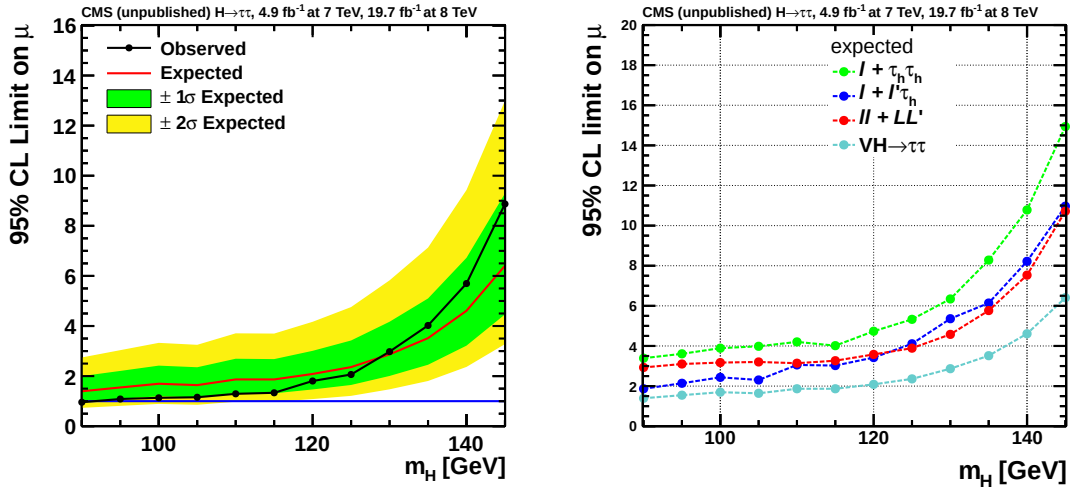

Figure 9.1: Left: Combined expected and observed 95% CL upper limit on the signal strength parameter $\mu = \sigma/\sigma_{SM}$ for the VH analyses. The background-only hypothesis includes the $pp \to H(125\text{GeV}) \to WW$ process for every value of m_H. Right: Expected 95% CL upper limit on the signal strength parameter $\mu = \sigma/\sigma_{SM}$ in the background-only hypothesis, shown separately for each VH channel. [116]

m_{H}	-2σ	-1σ	Median	$+1\sigma$	$+2\sigma$	Obs. Limit
90 GeV	$7.33 \cdot 10^{-1}$	$9.89 \cdot 10^{-1}$	1.40	2.00	2.74	$9.58 \cdot 10^{-1}$
95 GeV	$8.13 \cdot 10^{-1}$	1.09	1.55	2.21	3.04	1.09
100 GeV	$8.91 \cdot 10^{-1}$	1.20	1.70	2.42	3.33	1.13
105 GeV	$8.52 \cdot 10^{-1}$	1.15	1.63	2.36	3.24	1.16
110 GeV	$9.77 \cdot 10^{-1}$	1.32	1.87	2.69	3.71	1.29
115 GeV	$9.70 \cdot 10^{-1}$	1.31	1.87	2.68	3.70	1.33
120 GeV	1.08	1.47	2.09	3.01	4.17	1.81
125 GeV	1.21	1.65	2.36	3.42	4.76	2.06
130 GeV	1.47	2.01	2.87	4.16	5.82	2.98
135 GeV	1.87	2.45	3.52	5.10	7.13	4.02
140 GeV	2.36	3.21	4.61	6.72	9.43	5.70
145 GeV	3.28	4.46	6.41	9.29	12.99	8.87

Table 9.1: Observed and expected 95% CL upper limits on the signal strength for the combination of all VH analyses with H decays to taus performed with Run-1 data.

Final state	$\tau_e\tau_e$	$\tau_\mu\tau_\mu$	$\tau_e\tau_\mu$	$\tau_h\tau_h$
$\hat{\mu}$	0.05 ± 1.60	-0.54 ± 1.38	0.90 ± 1.03	1.31 ± 0.63
Final state	$\tau_e\tau_h$	$\tau_\mu\tau_h$	VH	All
$\hat{\mu}$	0.31 ± 0.55	1.01 ± 0.41	-0.33 ± 1.02	0.78 ± 0.27

Table 9.2: Best-fit signal strengths for every final state for the gluon-gluon fusion and VBF analyses, for the combination of the VH analyses, and for all $H \to \tau\tau$ searches combined.

in each bin of the final discriminating variables for all event categories and channels, where S denotes the expected signal yield at $m_H = 125$ GeV and B the expected background yield in a given bin. This results in the first evidence for the decay of the H boson to a pair of tau leptons, with an observed (expected) significance of 3.2 (3.7) standard deviations for a mass of 125 GeV. The best-fit signal strengths in the different di-tau final states are given in Tab. 9.2; the slight deficit of events relative to the SM expectations for the scalar boson essentially comes from the $\tau_\mu\tau_\mu$ and $\tau_e\tau_h$ final states in gluon-gluon fusion and VBF production modes, and from the VH analyses as described in Section 9.2.

The best-fit value for the signal strength is well compatible with the SM hypothesis: $\hat{\mu} = 0.78 \pm 0.27$ at $m_H = 125$ GeV. The combined measured mass of the excess is obtained after a parabolic fit, illustrated in Fig. 9.3, and amounts to $\hat{m}_H = 122 \pm 7$ GeV. A likelihood scan is shown in Fig. 9.4 for the combination of the analyses in the (k_V, k_f) plane, where the coupling modifiers k_V and k_f quantify the ratio between the measured and the SM values for the couplings of the scalar boson to vector bosons and fermions respectively; the observed couplings are well compatible with the SM expectation. The constraints in the k_V direction essentially come from the searches for a scalar boson produced in association with a vector boson and in vector boson fusion. After combination of the $H \to \tau\tau$ analysis with the search for the decay of the H boson to a pair of b quarks [119], the CMS Collaboration could show an evidence for the decay of the H boson to fermions, with a significance of 3.8 standard deviations (for 4.4 standard deviations expected) [120]. The ATLAS Collaboration also announced an evidence for the H boson Yukawa couplings to taus during LHC Run-1 [121].

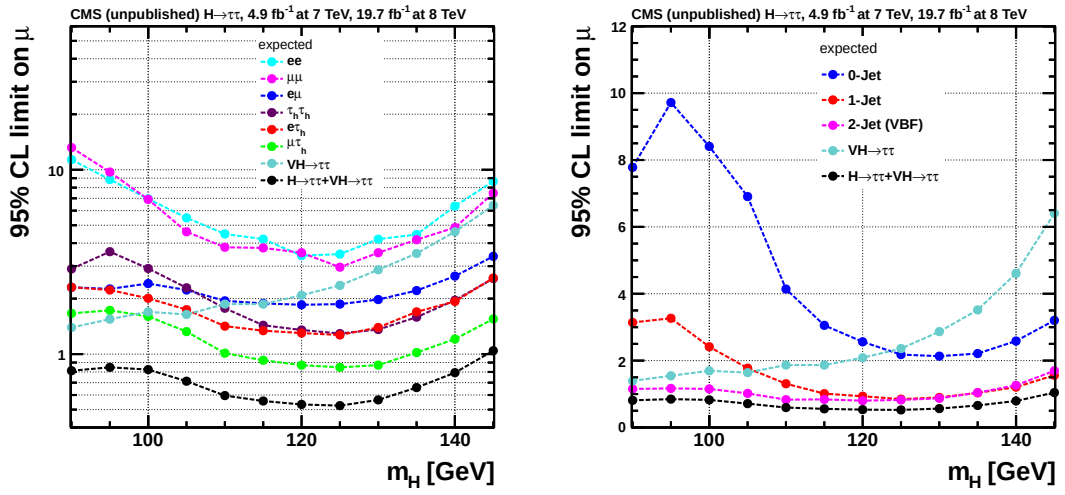

Figure 9.2: Expected 95% CL upper limit on the signal strength parameter $\mu = \sigma/\sigma_{SM}$ in the background-only hypothesis, shown separately for the seven channels (left), and for the 0-jet, 1-jet, 2-jets and VH categories (right). [16]

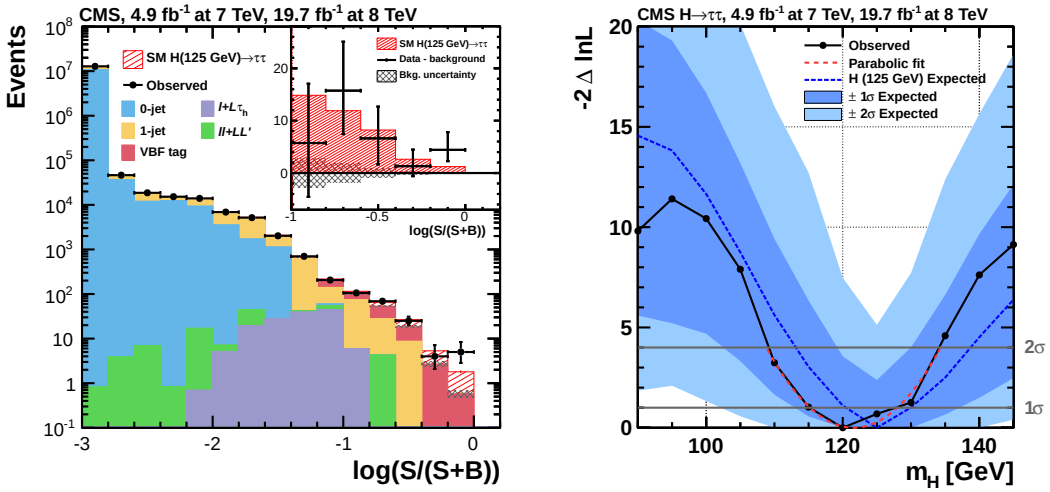

Figure 9.3: Left: Combined distribution of the decimal logarithm $\log(S/(S+B))$ obtained in each bin of the final discriminating variables for all event categories and channels, where S denotes the expected signal yield at $m_H = 125$ GeV and B the expected background yield in a given bin. Right: Scan of the negative log-likelihood difference as a function of m_H. [16]

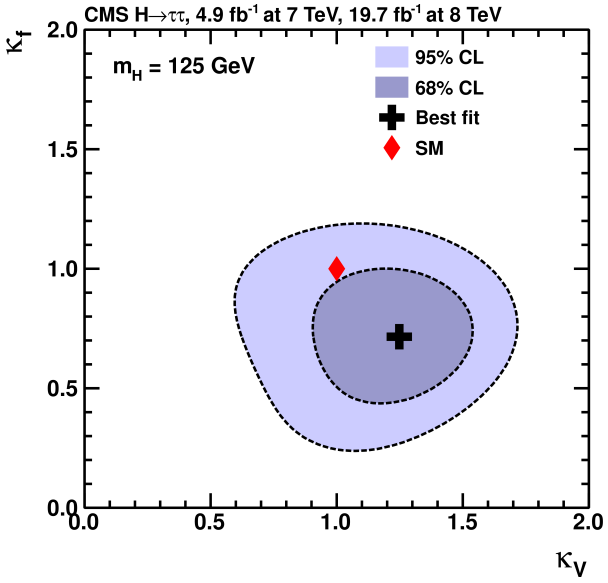

Figure 9.4: Scan of the negative log-likelihood difference as a function of the coupling modifiers k_V and k_f. The $H \to WW$ contribution is treated as a signal process. The red diamond indicates the SM expectation. [16]

9.4 Chapter summary and personal contributions

Combination of searches for the SM scalar boson decaying to taus

The combination of all searches for H boson decays to taus, in the gluon-gluon fusion, vector boson fusion and VH associated productions, leads to an evidence for the decay of the H boson to taus. The results are perfectly compatible with the SM expectation, and the measured signal strength at $m_H = 125$ GeV is $\hat{\mu} = 0.78 \pm 0.27$. The measured mass of the excess is $\hat{m}_H = 122 \pm 7$ GeV.

My contributions

I have participated in the $ZH \to \ell\ell\tau\tau$ and $WH \to e\mu\tau_h$ results, at all stages of the analysis (selection optimization, background estimation, ...). I have been responsible for computing and combining the statistical results (goodness-of-fit tests, maximum likelihood fits, upper limits) of all VH analyses.

Part IV

BSM physics analyses

The next chapters detail four searches for an extended scalar sector, which cover different parts of the phase space of 2HDM type-2 and/or MSSM, or of 2HDM+S type-3. Chapter 10 is devoted to the search for a heavy pesudoscalar boson decaying to a Z boson and a scalar boson in the context of the MSSM and 2HDM type-2, Chapter 11 to the search for exotic decays of the 125-GeV particle to light pseudoscalar bosons in the $h \to aa \to \mu\mu\tau\tau$ channel in 2HDM+S, Chapter 12 to the search for a pseudoscalar lighter than the Z boson decaying to taus and produced in association with b quarks in 2HDM type-2, and Chapter 13 to the search for a heavy scalar decaying to tau leptons in the MSSM.

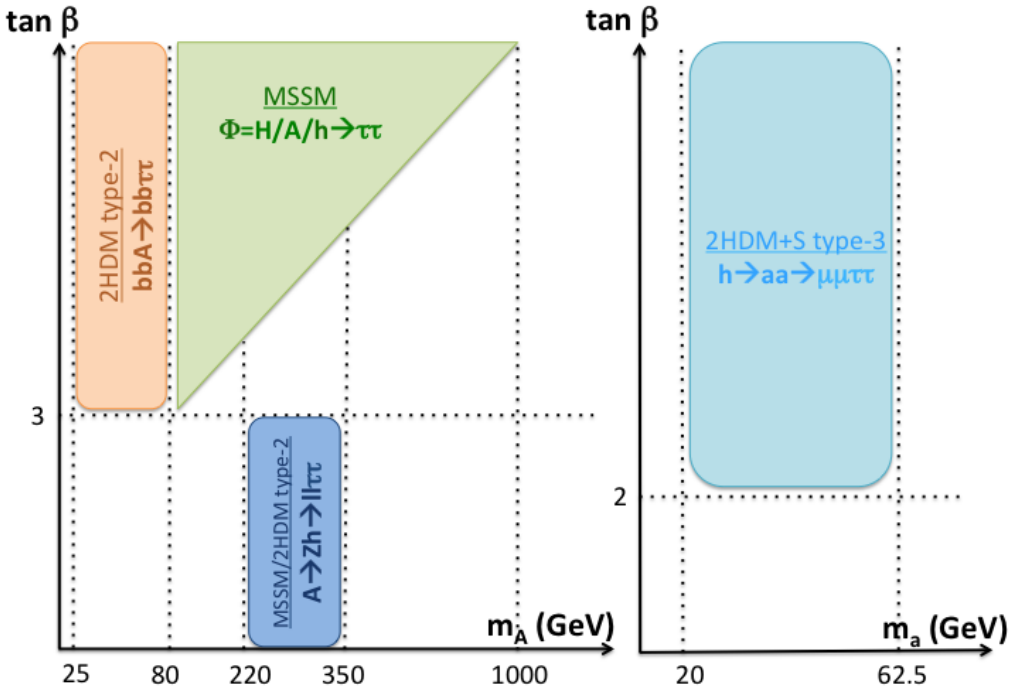

Chapter 10

Search for a heavy pseudoscalar boson A decaying to Zh in the $\ell\ell\tau\tau$ final state

The $A \to Zh$ decay channel is studied to uncover a hypothetical extended scalar sector in the MSSM, or more generally in 2HDM type-2. It is sensitive to pseudoscalar boson masses between about 215 GeV (sum of the masses of the h and Z bosons) and 350 GeV (twice the top quark mass), in the low $\tan\beta$ regions. The most sensitive final states are $\ell\ell bb$ and $\ell\ell\tau\tau$ because they cover the largest h boson branching fractions, and, unlike the case of the SM H production in gluon-gluon fusion, do not suffer from high backgrounds or high triggering thresholds thanks to the additional leptons coming from the Z boson decay. Both analyses have been performed using CMS data collected in 2012; the results from the $A \to Zh \to \ell\ell bb$ search are available in [122], while the $A \to Zh \to \ell\ell\tau\tau$ search results are published in [123] and described below. The analysis workflow is close to the search for the SM H boson produced in association with a Z boson, presented in Chapter 7.

10.1 Differences with respect to the SM $ZH \to \ell\ell\tau\tau$ analysis

Because there are many similarities between the selection and background estimation methods of the present analysis and the SM $ZH \to \ell\ell\tau\tau$ analysis detailed in Chapter 7, this section only highlights the differences; everything not mentioned should be assumed identical to what was done for the SM $ZH \to \ell\ell\tau\tau$ analysis. The same eight final states (corresponding to $Z \to \mu\mu$ or $Z \to ee$, and $h \to \tau_h\tau_h$, $h \to \tau_e\tau_h$, $h \to \tau_\mu\tau_h$ or $h \to \tau_e\tau_\mu$) are studied, but only in data collected in 2012 at a center-of-mass energy of 8 TeV.

The signal samples, with A boson masses between 220 and 350 GeV, are generated with Madgraph. Some rare processes, generated with Madgraph as well, are added to the list of irreducible backgrounds: WWZ ($\sigma = 0.0580$ pb at 8 TeV), WZZ ($\sigma = 0.0197$ pb at 8 TeV) and ZZZ ($\sigma = 0.0055$ pb at 8 TeV) triboson productions. A 50% uncertainty is assigned to the production cross sections of these rare triboson processes [124].

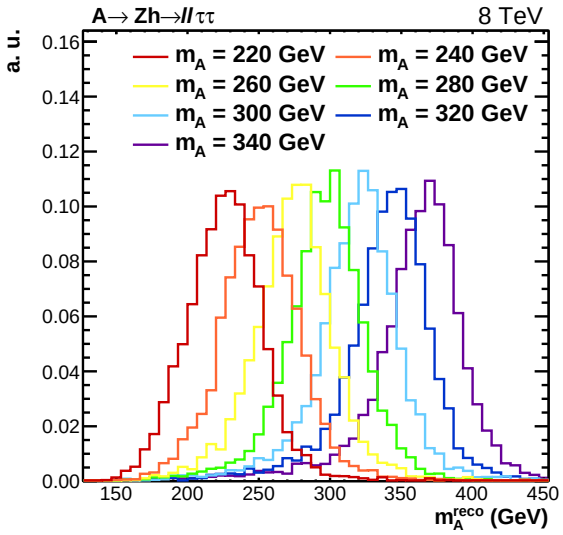

Figure 10.1: Reconstructed A boson mass, using the SVfit-reconstructed di-tau system. The full signal selection is applied, and all eight final states are superimposed. The resolution is between 15 and 20% for all masses.

The observable used in this analysis is the reconstructed mass of the pseudoscalar A boson, m_A^{reco}. It is computed as the invariant mass between the Z candidate and the SVfit-reconstructed di-tau system. A mass resolution between 15 and 20% is obtained for all masses. Fig. 10.1 illustrates the reconstructed mass distributions for different signal mass hypotheses, after the full signal selection.

The τ_h p_T threshold is raised to 21 GeV instead of 15 GeV. This improves the sensitivity of the analysis because signal events typically have harder hadronic taus than background events (mostly reducible processes, but also $ZZ \to 4\ell$). The L_T thresholds described in Chapter 7 are found to be optimal in this case also for all A boson masses probed, using the expected upper limits as a figure of merit. The L_T distributions for the signal, and the reducible and irreducible backgrounds are shown in Fig. 10.2 for the $\ell\ell\tau_h\tau_h$ final state; the threshold at 70 GeV is seen to remove a large contribution from backgrounds while keeping a good signal efficiency. All the selection criteria are summarized in Tab. 10.1, while a cut-flow table, Tab. 10.2, gives indications about the efficiency of the different selection criteria on signal events. It can be noted that no selection criterion is applied to the mass of the di-tau system $m_{\tau\tau}$, which is expected to be close to 125 GeV for signal events. The reason is that such a criterion would bring a negligible improvement in the limits because $m_{\tau\tau}$ is highly correlated to the observable m_A^{reco} in signal and in background events, and because the analysis is statistically limited.

		$Z \to ee$	$Z \to \mu\mu$
$Z \to \ell\ell$	e	$p_T > 10/20$ GeV, $\lvert\eta\rvert < 2.5$ $I_{rel} < 0.3$, vLoose MVA ID	- -
	μ	-	$p_T > 10/20$ GeV, $\lvert\eta\rvert < 2.4$ $I_{rel} < 0.3$, Loose PF ID
	$m_{\ell\ell}$	$60 < m_{\ell\ell} < 120$ GeV	
	Charge	Opposite sign charges	

		$h \to e\mu$	$h \to e\tau_h$	$h \to \mu\tau_h$	$h \to \tau_h\tau_h$
$h \to \tau\tau$	e	$p_T > 10$ GeV, $\lvert\eta\rvert < 2.5$		-	-
		vLoose MVA ID $I_{rel} < 0.3$	Loose MVA ID $I_{rel} < 0.2$		
	τ_h	-	$p_T > 21$ GeV, $\lvert\eta\rvert < 2.3$		
			Loose isolation Tight anti-e Loose anti-μ	Loose isolation Loose anti-e Tight anti-μ	Medium isolation Loose anti-e Loose anti-μ
	μ	$p_T > 10$ GeV $\lvert\eta\rvert < 2.4$ Loose PF ID $I_{rel} < 0.3$	-	$p_T > 10$ GeV $\lvert\eta\rvert < 2.4$ Tight PF ID $I_{rel} < 0.3$	-
	Charge	Opposite sign charges			

		$h \to e\mu$	$h \to e\tau_h$	$h \to \mu\tau_h$	$h \to \tau_h\tau_h$
Others	L_T	> 25 GeV	> 30 GeV	> 45 GeV	> 70 GeV
	b–Jet veto	No b–tagged jet (medium CSV working point)			
	Lepton veto	No additional identified and isolated electron or muon			
	ΔR between leptons	> 0.5			

Table 10.1: Selection criteria for the eight final states of the $A \to Zh \to \ell\ell\tau\tau$ analysis.

	$\mu\mu\tau_h\tau_h$	$\mu\mu e\tau_h$	$\mu\mu\mu\tau_h$	$\mu\mu e\mu$	$ee\tau_h\tau_h$	$eee\tau_h$	$ee\mu\tau_h$	$eee\mu$
Initial number	99 794							
Trigger	61 577							
At least 4 loose leptons	12 136	11 717	6 212	2 876	8 504	7 310	5 755	1 865
b-Jet veto	10 109	10 276	5 551	2 660	7 018	6 332	5 045	1 711
Z candidate	7 825	7 758	4 571	2 142	4 903	5 266	2 720	1 340
h candidate	1 106	919	1 485	718	764	735	950	531
L_T cut	842	919	1 362	707	612	735	892	522

Table 10.2: Number of unweighted signal events after every selection criterion, for a sample with $m_A = 300$ GeV.

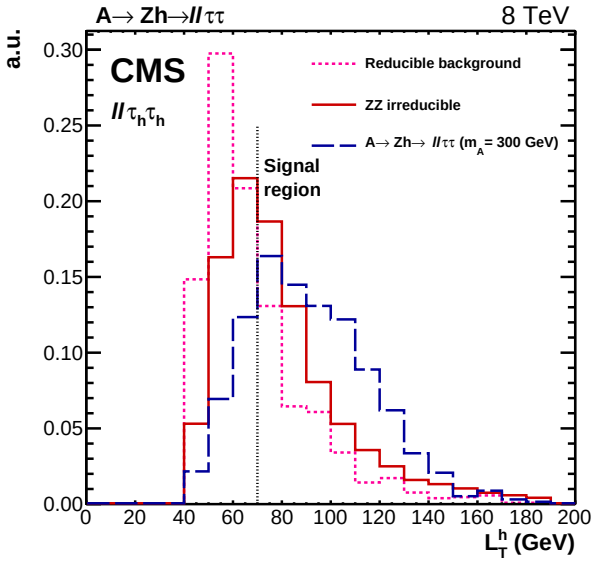

Figure 10.2: Normalized distribution of the variable L_T for events selected in the $\ell\ell\tau_h\tau_h$ final state. The reducible background is estimated from data, instead the ZZ irreducible background comes from MC simulation. The events are selected, in the signal region, with $L_T > 70$ GeV. [123]

The normalization of the reducible processes is again taken from a control region where the two tau candidates have a same-sign charge and pass relaxed isolation criteria. The relaxed isolation and identification criteria have been slightly modified with respect to the SM ZH analysis, and are namely:

- $\ell\ell\tau_h\tau_h$: output of the MVA discriminator without lifetime information greater than 0 for both hadronic taus;
- $\ell\ell\tau_e\tau_h$: output of the MVA discriminator without lifetime information greater than -0.95 for the hadronic tau, loose MVA electron ID, relative electron isolation less than 0.3;
- $\ell\ell\tau_\mu\tau_h$: output of the MVA discriminator without lifetime information greater than -0.95 for the hadronic tau, loose PF muon ID, relative muon isolation less than 0.7;
- $\ell\ell\tau_e\tau_\mu$: loose PF muon ID, no electron ID, electron and muon relative isolations less than 2.0.

These criteria have been chosen to ensure a selection efficiency as large as possible without biasing the background composition. Indeed, in the semi-leptonic final states, relaxing the isolation of the light lepton might lead to an over-representation of the Z+jets background (no real isolated light lepton) over the WZ+jets background (one real isolated light lepton).

The $j \to e$, $j \to \mu$ and $j \to \tau_h$ misidentification rates are reevaluated with the new selection; and the functions for the loose electron and loose muon ID/isolation are now

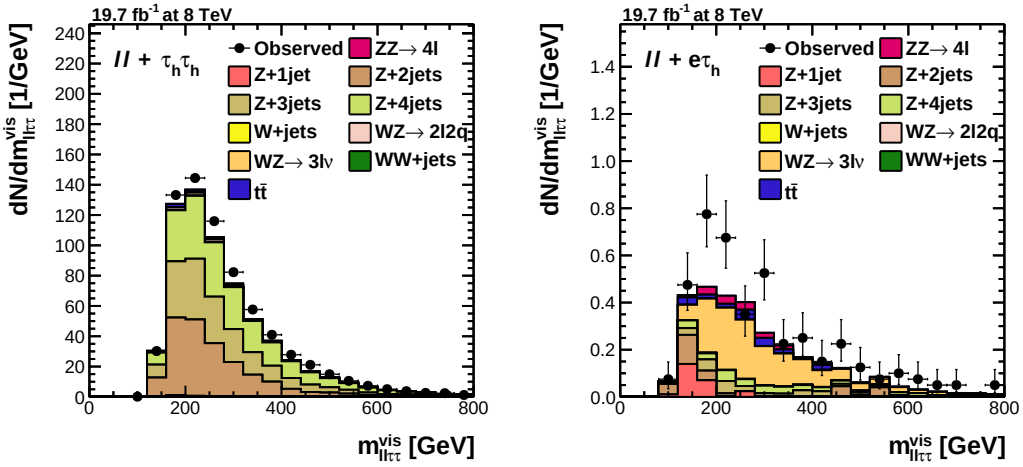

Figure 10.3: Visible invariant mass of the four leptons in the $\ell\ell\tau_h\tau_h$ (left) and $\ell\ell\tau_e\tau_h$ (right) final states, in a reducible background-dominated region, where the tau candidates carry a same sign charge, the L_T selection criteria are not applied, and the hadronic tau isolation is inverted. Filled areas represent background contributions estimated directly from MC simulations: the Z+jets processes by far dominate in the $\ell\ell\tau_h\tau_h$ final state, while the WZ+jets contribution is not negligible in the other final states. The agreement between MC predictions and data is not perfect because of large statistical and systematic uncertainties on the MC-estimated processes.

divided into barrel and endcap regions. The systematic uncertainties on the normalization are again computed by varying the fit functions within their uncertainties and propagating these to the reducible processes yield.

10.2 Background estimation validation

The main components of the reducible background are Z+jets and WZ+jets processes, where one or two jets are misidentified as leptons. The first one is by far dominant in the $\ell\ell\tau_h\tau_h$ final state, whereas the WZ+jets contribution becomes non negligible in all other final states, with at least three identified light leptons. Fig. 10.3 shows some reducible background distributions, obtained by inverting the charge requirement on the tau candidates, relaxing the L_T selection criteria and inverting the hadronic tau isolation. Contributions from MC processes are superimposed; they permit to see the background composition, but suffer from large statistical (limited number of selected events) and systematic (jet misidentification rates not well modeled in MC) uncertainties. The same selection is applied to produce the distributions in Fig. 10.4, except that the hadronic tau isolation is not inverted, but simply relaxed to the very loose working point of the MVA-based isolation with lifetime information. The data-driven reducible background prediction is shown with the light blue line; the agreement between prediction and observation is good within the uncertainties.

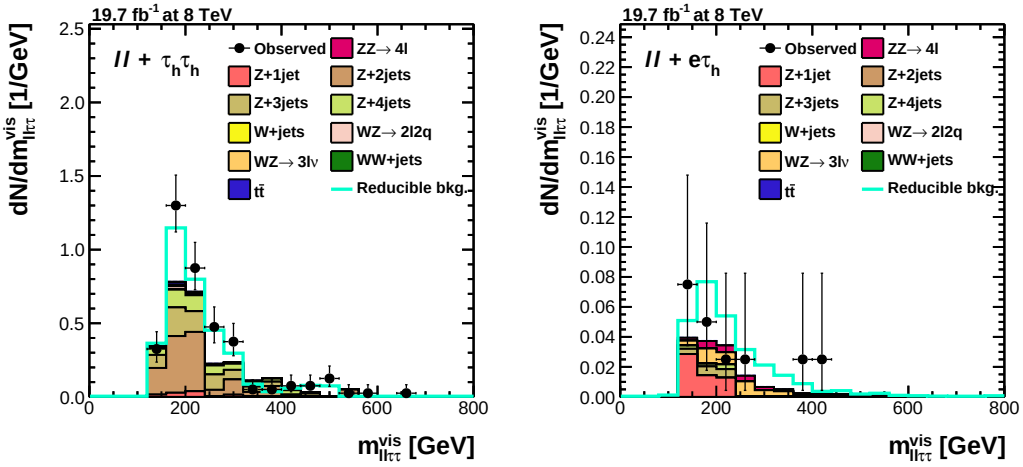

Figure 10.4: Visible invariant mass of the four leptons in the $\ell\ell\tau_h\tau_h$ (left) and $\ell\ell\tau_e\tau_h$ (right) final states, in a reducible background-dominated region, where the tau candidates carry a same sign charge, the L_T selection criteria are not applied, and the very loose MVA discriminator is used for hadronic tau isolation. Filled areas represent background contributions estimated directly from MC simulations: the Z+jets processes by far dominate in the $\ell\ell\tau_h\tau_h$ final state, while the WZ+jets contribution is not negligible in the other final states. The agreement between MC predictions and data is not perfect because of large statistical and systematic uncertainties on the MC-estimated processes. The blue line represents the data-driven prediction for the reducible background; the agreement with observed data is good.

Two di-tau final states have not been considered in this analysis: $\tau_e\tau_e$ and $\tau_\mu\tau_\mu$. The reason is two-fold: they have the lowest branching fractions (about 3% each) and suffer from very large contributions from the $ZZ \to 4\ell$ background. Even if signal events typically have a larger $\not\!\!E_T$ than background events due to the neutrinos from tau decays, adapting the selection does not permit to obtain a significant background rejection for a reasonable signal efficiency. It has been shown that adding these two final states would bring less than 5% to the combined limit, with an almost zero effect for low m_A signal hypotheses. However, the $\ell\ell ee$ and $\ell\ell\mu\mu$ final states can be used to validate the estimation of the $ZZ \to 4\ell$ background. Fig. 10.5 shows a good agreement between the ZZ background, taken from MC simulations, and the observed data, in an $\ell\ell ee$ and an $\ell\ell\mu\mu$ control regions.

10.3 High $\not\!\!E_T$ excess

The $\not\!\!E_T$ distributions obtained after the full signal selection are shown in Fig. 10.6. An excess of events is observed at large $\not\!\!E_T$ values in four final states: $eee\mu$, $\mu\mu\mu e$, $eee\tau_h$ and $\mu\mu e\tau_h$. The expected and observed yields in these four final states for $\not\!\!E_T > 120$ GeV can be found in Tab. 10.3. These events pass the filters to remove events with abnormally high $\not\!\!E_T$, as described in Section 5.2.7. The characteristics of the eight events that pass the full signal selection and have $\not\!\!E_T > 120$ GeV, are shown in Tab. 10.4. Most backgrounds, such

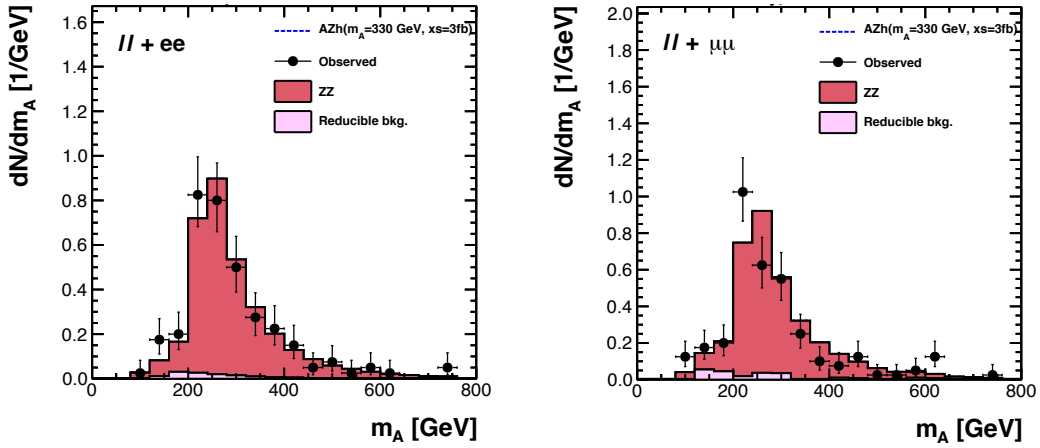

Figure 10.5: Reconstructed A boson mass distribution in the $\ell\ell ee$ (left) and $\ell\ell\mu\mu$ (right) control regions states. The prediction for the ZZ background is well in agreement with the observed data, without any maximum likelihood fit being applied. The $A \to Zh$ signal contribution is negligible in both final states.

as $ZZ \to 4\ell$ or Z+jets, have a low $\not\!\!E_T$, whereas triboson processes including W bosons essentially contribute in high $\not\!\!E_T$ regions. The signal processes have real $\not\!\!E_T$ from the tau decays, but the typical $\not\!\!E_T$ for such events lies below 100 GeV. All observed events with high $\not\!\!E_T$ have two light leptons very compatible with a Z boson (invariant mass between 85 and 93 GeV), while the two tau candidates do not correspond to a particular resonance. The excess is interpreted as an upward statistical fluctuation, particularly of triboson processes.

10.4 Results

Goodness-of-fit tests (see Section 3.5) are performed for the four di-tau final states, as illustrated in Fig. 10.7. The observed goodness-of-fit values generally lie in the bulk of the toys distributions, which indicates a reasonable background description given the observed data. Some limited tensions appear in the $\ell\ell\tau_\mu\tau_h$ and $\ell\ell\tau_e\tau_\mu$ final states.

No significant excess of events is observed on top of the predicted backgrounds in any of the final states, and model-independent limits can be set on the cross section times branching ratio for different mass hypotheses, as illustrated in Fig. 10.8. The observed combined limit at 95% CL ranges from about 4 to 16 fb. Another search for $A \to Zh$ decays was performed with the CMS detector in Run-1, in the final state with two light leptons (from the Z boson) and two b quarks (from the h boson). In the hypothesis that the ratio of the branching fractions of the h boson to taus and b quarks is the same as in the SM, the search for $A \to Zh \to \ell\ell bb$ is a few times more powerful than the $A \to Zh \to \ell\ell\tau\tau$ search presented here. However, this hypothesis might not hold and BSM phenomena could intervene; the $A \to Zh \to \ell\ell\tau\tau$ analysis therefore has an

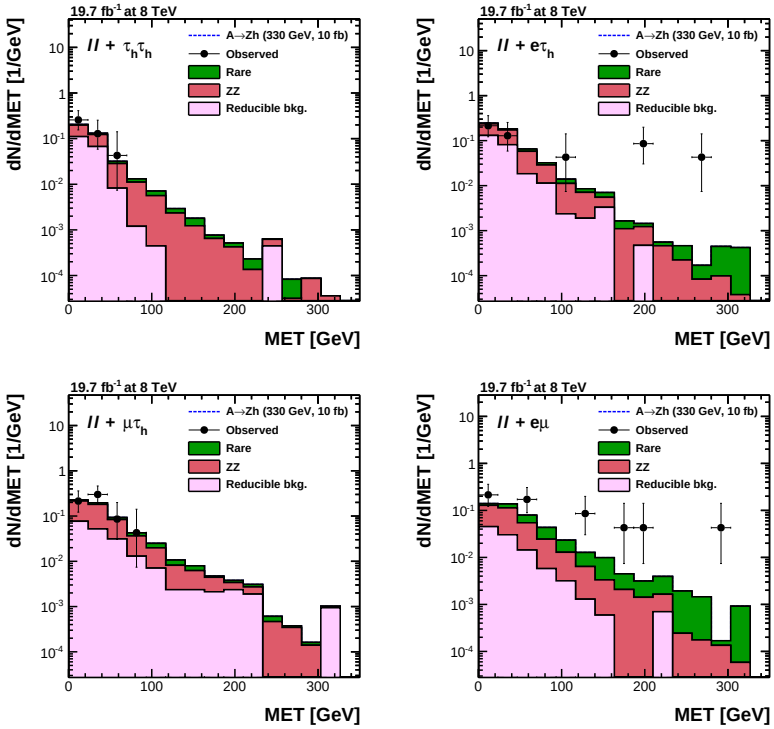

Figure 10.6: $\not\!\!E_T$ distributions in the $\ell\ell\tau_h\tau_h$ (top left), $\ell\ell\tau_e\tau_h$ (top right), $\ell\ell\tau_\mu\tau_h$ (bottom left) and $\ell\ell\tau_e\tau_\mu$ (bottom right) final states. In the $\ell\ell\tau_e\tau_h$ and $\ell\ell\tau_e\tau_\mu$ final states, an excess of events is observed at high $\not\!\!E_T$. No maximum likelihood fit is performed on the predicted backgrounds and systematic uncertainties are not taken into account.

Process	$ee + e\tau_h$	$\mu\mu + e\tau_h$	$ee + e\mu$	$\mu\mu + \mu e$
$q\bar{q} \to ZZ \to 4\ell$	0.010	0.096	0.119	0.117
$gg \to ZZ \to 4\ell$	0.010	0.007	0.014	0.014
Reducible	0.090	0.027	0.018	0.016
WWZ	0.027	0.021	0.085	0.129
WZZ	0.004	0.002	0.006	0.001
ZZZ	0.000	0.001	0.000	0.001
$t\bar{t}Z$	0.000	0.019	0.150	0.054
$ZH \to \ell\ell\tau\tau$	0.018	0.017	0.019	0.020
$ZH \to \ell\ell WW$	0.002	0.001	0.025	0.027
Total background	0.247±0.105	0.191±0.073	0.436±0.164	0.378±0.120
Observed data	1	2	3	2

Table 10.3: Predicted background and observed yields for $\not\!\!E_T > 120$ GeV in the four final states where an excess is observed, corresponding to the right side of Fig. 10.6.

	$ee + e\mu$	$ee + e\mu$	$ee + e\mu$	$ee + e\tau_h$	$\mu\mu + e\tau_h$	$\mu\mu + e\mu$	$\mu\mu + e\tau_h$	$\mu\mu + e\mu$
PF $\not\!\!E_T$ (GeV)	298	132	173	197	201	186	256	131
$p_T(\ell_1)$ (GeV)	106	311	138	50	196	133	30	326
$p_T(\ell_2)$ (GeV)	25	79	104	41	72	83	27	51
$p_T(\tau_1)$ (GeV)	76	10	43	139	26	63	206	23
$p_T(\tau_2)$ (GeV)	86	277	34	23	51	31	30	42
$m_{\ell\ell}$ (GeV)	91	93	85	91	91	90	86	93
$m_{\tau\tau}$ (GeV)	370	159	41	213	81	229	233	260
$m_{\tau\tau}^{vis}$ (GeV)	167	127	19	130	25	120	144	130
m_T (GeV)	308	719	346	343	307	360	330	540
Iso (ℓ_1)	0.107	0.022	0.006	0.009	0.000	0.015	0.000	0.000
Iso (ℓ_2)	0.024	0.086	0.000	0.012	0.130	0.076	0.240	0.190
Iso (τ_1)	0.185	0.000	0.000	0.008	0.000	0.019	0.000	0.220
Iso (τ_2)	0.042	0.008	0.000	0.000	0.000	0.000	1.800	0.000
Number of jets	6	3	0	1	1	0	5	3

Table 10.4: Characteristics of the observed events with $\not\!\!E_T$ larger than 120 GeV. For hadronic taus, the absolute isolation in GeV is quoted, while for light leptons it is the relative isolation.

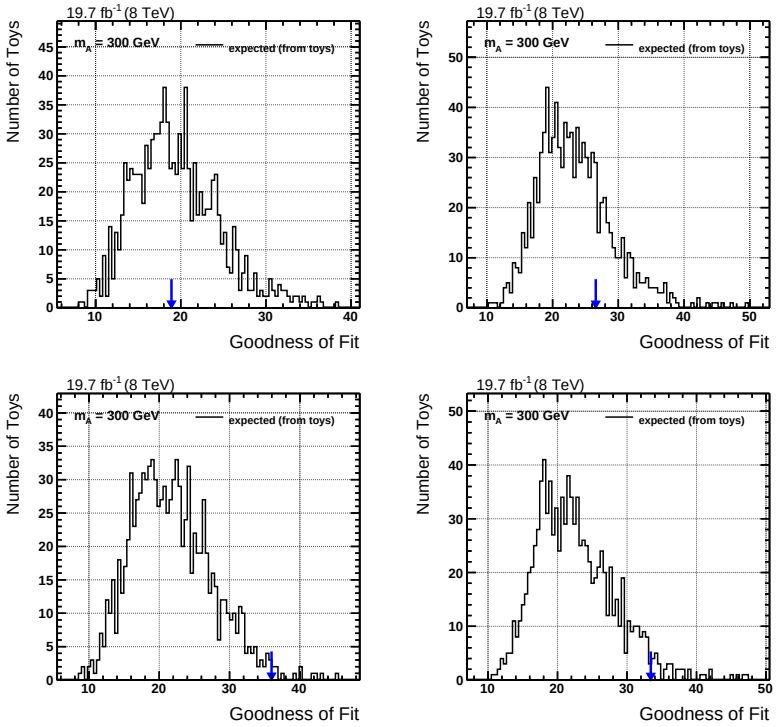

Figure 10.7: Observed values (blue arrows) and expected distributions (black histograms) of goodness-of-fit values in the $\ell\ell\tau_h\tau_h$ (top left), $\ell\ell\tau_e\tau_h$ (top right), $\ell\ell\tau_\mu\tau_h$ (bottom left) and $\ell\ell\tau_e\tau_\mu$ (bottom right) final states, for a pseudoscalar boson mass hypothesis of 300 GeV.

interest by itself, in addition to the sensitivity it could add if it was combined to the $A \to Zh \to \ell\ell bb$ search.

The results are also interpreted in the contexts of the MSSM and 2HDM, as shown in Fig. 10.10, where the production cross sections and the branching fractions of the scalar bosons are calculated as described in [126]. In the MSSM, the results are interpreted in the so-called low $\tan\beta$ scenario [127], for which the SUSY scale, M_{SUSY}, is increased up to the point where the mass of the lightest scalar boson is compatible with 125 GeV over a range of low $\tan\beta$ and m_A values. The $A \to Zh \to \ell\ell\tau\tau$ analysis is sensitive to low $\tan\beta$ values (95% CL exclusion of regions with up to $\tan\beta \simeq 2.5$) because the $gg \to A$ production cross section is very large in this region [1], and because the $A \to Zh$ decay mode largely dominates when the $A \to \tau\tau$ and $A \to bb$ decays are not enhanced by large values of $\tan\beta$. The limit steeply falls down around 350 GeV, where the $A \to tt$ channel opens. In 2HDM type-2, the interpretation of the search results is based on these inputs: the scalar boson masses [2], $\tan\beta$, α and $m_{12}^2 = m_A^2 \frac{\tan\beta}{1+\tan^2\beta}$. In the alignment limit, where $\cos(\beta-\alpha) \to 0$, the $A \to Zh$ branching fraction vanishes as the h boson becomes SM-like. The other region where the analysis is not sensitive at low $\tan\beta$, for $\cos(\beta-\alpha)$ values between 0 and 1, corresponds to vanishing values for $\mathcal{B}(h \to \tau\tau)$ when $\alpha \to 0$, as the couplings of the h boson to leptons in 2HDM type-2 are proportional to $(-\sin\alpha/\cos\beta)$ (see Tab. 2.2).

10.5 Combination with $H \to hh \to bb\tau\tau$

The results of the search presented in this chapter are combined with those of the search for a heavy neutral scalar decaying to a pair of SM-like scalar bosons ($m_h = 125$ GeV) with two taus and two b quarks in the final state [123]. These analyses are both sensitive in comparable mass ranges for the heavy scalars ($m_H \simeq m_A$): above the sum of the h and Z masses or twice the h boson mass, and below twice the top quark mass. No excess is observed in any of the analyses, and the results are combined in the models already described in the previous section, as shown in Fig. 10.11. The $H \to hh \to bb\tau\tau$ analysis is also sensitive to low $\tan\beta$ values in the MSSM, because it has very large production rates in this region. In 2HDM type-2, both $\mathcal{B}(h \to bb)$ and $\mathcal{B}(h \to \tau\tau)$ vanish when $\alpha \to 0$. The results from the ATLAS Collaboration about h boson pair production do not show any excess of data either [128].

1. It is higher than the SM $gg \to H$ cross section for $\tan\beta \simeq 1$.
2. We assume here that $m_A = m_H = m_{H^\pm} = 300$ GeV.

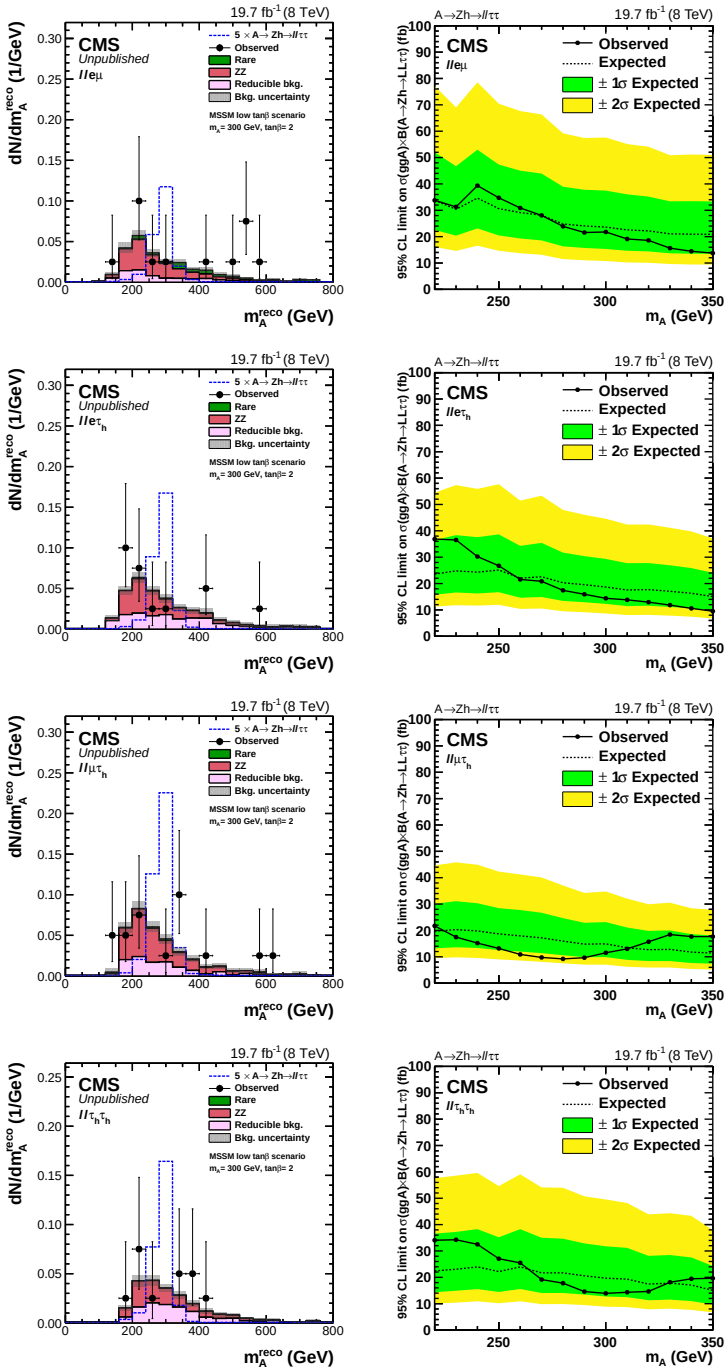

Figure 10.8: Expected and observed distributions of the reconstructed m_A in the four different di-tau final states at 8 TeV (left) and their corresponding upper limits on the signal cross section times branching fraction (right). The distributions are obtained after a maximum likelihood fit. The signal is scaled to five times its expected cross section in the MSSM low $\tan\beta$ scenario for $m_A = 300$ GeV and $\tan\beta = 2$. Limits are shown up to $m_A = 350$ GeV, where the predicted $A \to Zh$ branching fraction drastically decreases because of the opening of the $t\bar{t}$ decay mode. [123, 125]

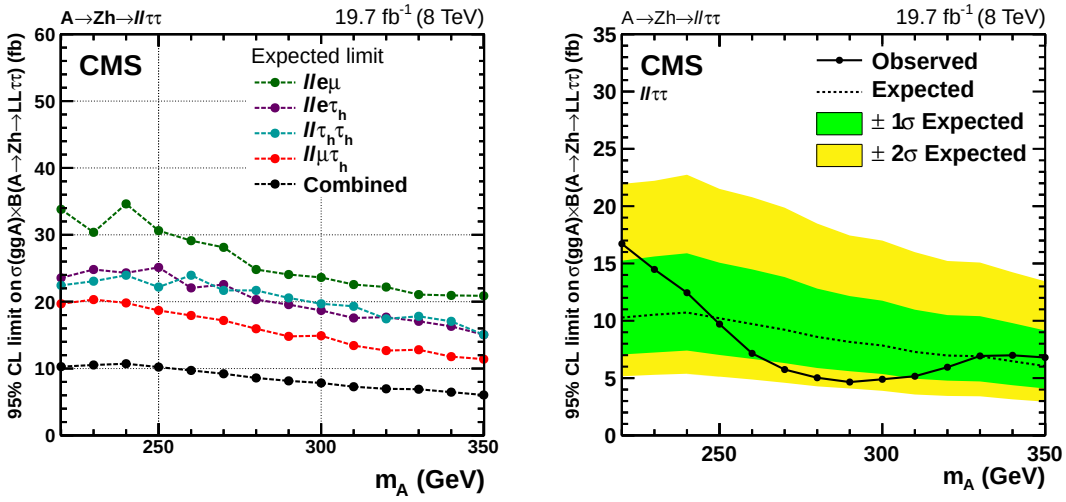

Figure 10.9: Left: Comparison between the expected limits in the four di-tau final states. Right: Observed and expected upper limits at 95% on the production cross section times branching fraction, for the combination of all the final states studied in this analysis. [123]

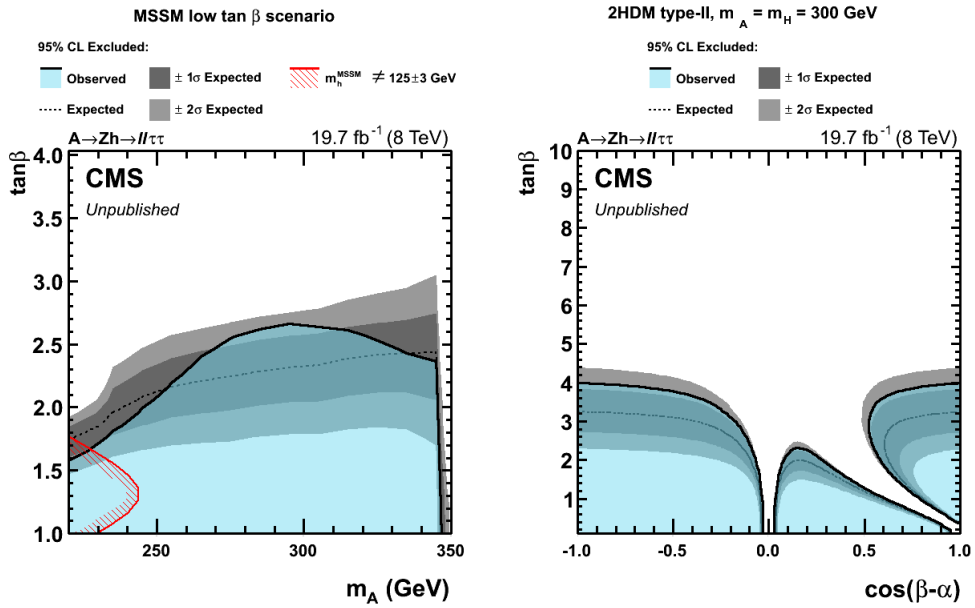

Figure 10.10: Left: Exclusion region at 95% CL in the $m_A - \tan\beta$ plane for the low-tan β scenario of the MSSM. The red area indicates the region excluded by the mass of the SM-like scalar being inconsistent with 125 GeV. Right: Exclusion region at 95% CL in the $\cos(\beta - \alpha) - \tan\beta$ plane in 2HDM type-2 for $m_A = m_H = 300$ GeV. [125]

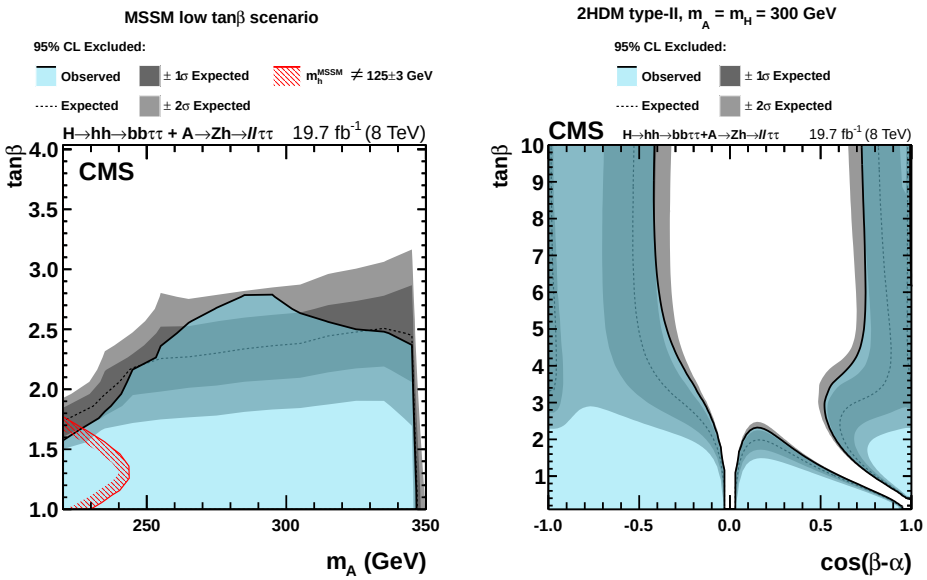

Figure 10.11: Left: Exclusion region at 95% CL in the $m_A - \tan\beta$ plane for the low-tan β scenario of the MSSM, for the combination of the $A \to Zh \to \ell\ell\tau\tau$ and $H \to hh \to bb\tau\tau$ analyses . The red area indicates the region excluded by the mass of the SM-like scalar being inconsistent with 125 GeV. Right: Exclusion region at 95% CL in the $\cos(\beta - \alpha) - \tan\beta$ plane in 2HDM type-2 for $m_A = m_H = 300$ GeV, for the combination of the $A \to Zh \to \ell\ell\tau\tau$ and $H \to hh \to bb\tau\tau$ analyses. [123]

10.6 Chapter summary and personal contributions

Search for a heavy pseudoscalar A boson decaying to Zh in the $\ell\ell\tau\tau$ final state

Searching for a heavy pseudoscalar boson, A, decaying to a Z and an h bosons is powerful to uncover an MSSM scalar sector, at low $\tan\beta$ and intermediate A boson masses (between the sum of the h and Z boson masses, and twice the top quark mass). In the analysis presented in this chapter, the Z boson decays to a pair of electrons or muons, which allows to suppress the SM backgrounds, and the h boson decays to a pair of tau leptons, which is characterized by a large branching fraction. The analysis methods are close to those used in the context of the search for a SM scalar boson produced in association with a Z boson and decaying to a pair of taus; differences include among others the definition of the reconstructed A boson mass as observable. As no excess of events is observed, limits are set on the cross section times branching fraction. The results are also interpreted in the MSSM and in 2HDM type-2. Finally, model-dependent results are shown for the combination with the $H \to hh \to bb\tau\tau$ analysis.

My contributions

Figures: 10.1-10.9.

I have produced all the $A \to Zh \to \ell\ell\tau\tau$ results presented in this chapter from the generation of the signal samples to the model-independent exclusion limits.

Chapter 11

Search for exotic decays of the SM-like scalar boson in the $\mu\mu\tau\tau$ final state

As explained in Section 2.4, motivations for the existence of exotic decays of the 125-GeV scalar boson are numerous. This chapter describes the search for the decay of the 125-GeV particle to a pair of lighter pseudoscalar bosons, decaying to a di-muon pair and a di-tau pair [129]. The di-muon pair exhibits an excellent mass resolution, which can be used to separate the signal from background contributions. Selecting a di-tau pair on top of the di-muon pair allows for a larger branching fraction than if two di-muon pairs were selected, and for a better background rejection than if a b quark pair was probed. The $\mu\mu\tau\tau$ final state is especially sensitive in 2HDM+S type-3 with large $\tan\beta$*, where pseudoscalar decays to leptons are enhanced over decays to quarks, and can complement analyses with other final states such as $\mu\mu bb$. It can be noticed that the $\mu\mu\tau\tau$ final state has also been studied in the context of the search of the SM scalar boson produced in association with a Z boson and decaying to taus (Chapter 7); these two analyses therefore share similarities in the event selection and background estimation methods and references will be made in time. A major difference lies in the modeling of the reconstructed discriminant variable, $m_{\mu\mu}$ for the signal and background processes. The last part of the chapter is devoted to the interpretation of the results in the different types of 2HDM+S, and to the comparison with other searches for exotic decays of the 125-GeV particle performed with the CMS detector in Run-1.*

11.1 Selection

The possibility of exotic decays of the 125-GeV particle is studied in the $h \to aa \to \mu\mu\tau\tau$ channel, the Feynman diagram of which can be found in Fig. 11.1 for the gluon-gluon fusion production. Among the six possible di-tau final states, only $\tau_\mu\tau_\mu$ is not studied. In addition of the low branching fraction and large $ZZ \to 4\ell$ background, shared with the $\tau_e\tau_e$ final state, it also suffers from combinatorial difficulties in grouping the

four final state muons into two correct pairs. The selection of the four di-tau final states common to the SM $ZH \to \ell\ell\tau\tau$ and BSM $A \to Zh \to \ell\ell\tau\tau$ analyses is close to what has been presented in Chapter 7 and 10 respectively, but slightly looser to allow for a signal acceptance times efficiency as large as possible. The signal acceptance times efficiency is lower in this analysis than in the $ZH \to \ell\ell\tau\tau$ and $A \to Zh \to \ell\ell\tau\tau$ cases as the final state leptons typically have lower transverse momenta because they originate from lighter particles. Signal samples are generated with Pythia using its built-in 2HDM functionality, for pseudoscalar boson masses ranging between 20 and 60 GeV with 5-GeV steps.

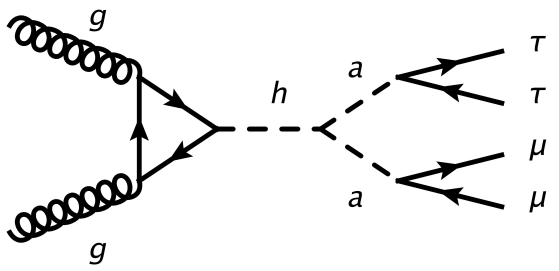

Figure 11.1: Feynman diagram for the $gg \to h \to aa \to \mu\mu\tau\tau$ process.

The selection criteria for the five di-tau final states studied in this analysis are summarized in Tab. 11.1. The events are again selected with a double muon trigger path. The offline muon p_T thresholds are chosen to be as low as possible, while still on the trigger efficiency plateau: they are one GeV above the HLT thresholds, which means 18 GeV for the leading muon and 9 GeV for the subleading one. In case there are more than two muons in the event ($\mu\mu\tau_e\tau_\mu$ and $\mu\mu\tau_\mu\tau_h$ final states), the one with the highest p_T is considered as decaying promptly from a pseudoscalar a boson, and is paired with the next highest p_T muon with an opposite-sign charge, while the last muon is considered as coming from a muonic tau decay. The correct pairing is obtained in more than 90% of cases, for all pseudoscalar masses. The p_T of the third muon in these final states should be larger than 5 GeV. The di-muon pair originating from the pseudoscalar boson is formed from two opposite sign muons that pass the loose PF identification, have a relative isolation less than 0.4 and satisfy $|\eta| < 2.4$. There is no selection criterion on their invariant mass because signal events do not have a real Z boson.

The five di-tau decays are selected as follows, from two opposite-sign charge particles:
- $a \to \tau_e\tau_e$: This decay is reconstructed from two opposite-sign electrons that pass the loose MVA identification, have a relative isolation less than 0.4, a transverse momentum greater than 7 GeV and $|\eta| < 2.5$. The contribution from the background $h \to ZZ^* \to \mu\mu ee$ is reduced by requiring the visible invariant pass of the four leptons not to lie in a 30 GeV wide window around the h boson mass.
- $a \to \tau_e\tau_\mu$: This decay is reconstructed from an electron with $p_T > 7GeV$, $|\eta| < 2.5$, having a relative isolation less than 0.4 and passing the loose MVA identification, and from a muon with $p_T > 5/9$ GeV (depending on whether it is responsible for

firing the trigger path), $|\eta| < 2.4$, passing the tight PF identification and having a relative isolation less than 0.4.
- $a \to \tau_e\tau_h$: This decay is reconstructed from an electron with $p_T > 7GeV$, $|\eta| < 2.5$, having a relative isolation less than 0.2 and passing the loose MVA identification, and from a hadronic tau with $p_T > 15$ GeV, $|\eta| < 2.3$, and passing the decay mode finding, the loose MVA-based isolation, the loose rejection against muons and the loose rejection against electrons discriminators.
- $a \to \tau_\mu\tau_h$: This decay is reconstructed from a muon with $p_T > 5/9$ GeV (depending on whether it is responsible for firing the trigger path), $|\eta| < 2.4$, passing the tight PF identification and having a relative isolation less than 0.5, and from a hadronic tau with $p_T > 15$ GeV, $|\eta| < 2.3$, and passing the decay mode finding, the loose MVA-based isolation, the loose rejection against muons and the very loose rejection against electrons discriminators.
- $a \to \tau_h\tau_h$: This decay is reconstructed from two hadronic taus with $p_T > 15$ GeV, $|\eta| < 2.3$, and passing the decay mode finding, the medium MVA-based isolation, the loose rejection against muons and the very loose rejection against electrons discriminators.

The leptons are required to be separated from each other by at least $\Delta R = 0.4$. Events that contain a jet with $p_T > 20$ GeV, $|\eta| < 2.4$ and that passes the tight working point of the CSV discriminator, or additional identified and isolated light leptons, are discarded. There is no selection on the L_T variable anymore, but two additional criteria are applied to reduce the background contribution in the signal region. First, the invariant mass of the four leptons, with the di-tau system reconstructed with the SVfit algorithm, is required to lie in a 50 GeV-wide window around the h boson mass: $|m_{\mu\mu\tau\tau} - 125| < 25$ GeV. Second, as the di-tau pair and the di-muon pair are expected to have the same mass in signal events, their normalized mass difference is on average low and the following selection criterion is found efficient to reject background events: $|m_{\mu\mu} - m_{\tau\tau}|/m_{\mu\mu} < 0.8$. Typical distributions of theses two variables are illustrated in Fig. 11.2. Both criteria have a signal efficiency greater than 90%.

The signal acceptance times efficiency after the full selection ranges from 1 to 5% depending on the final state. The efficiency to pass the double muon trigger is about 70%, and the smallest efficiencies are generally associated to the selection of the four leptons because of the p_T threshold requirements.

The signal samples are generated for the gluon-gluon fusion production mode only, but non negligible contributions from other production modes should also be taken into account. Indeed, if the h boson has SM-like production modes, with a theoretical cross section of 22.1 pb, the ggh, VBF, Wh, Zh and $t\bar{t}h$ productions represent respectively 87.2, 7.1, 3.2, 1.9 and 0.6% of the total production cross section. Signal samples for a pseudoscalar boson mass of $m_a = 40$ GeV are generated for every production mode, and their acceptance times efficiency is compared to the one of the gluon-gluon fusion produced samples. The efficiency for the VBF sample is roughly the same as for the

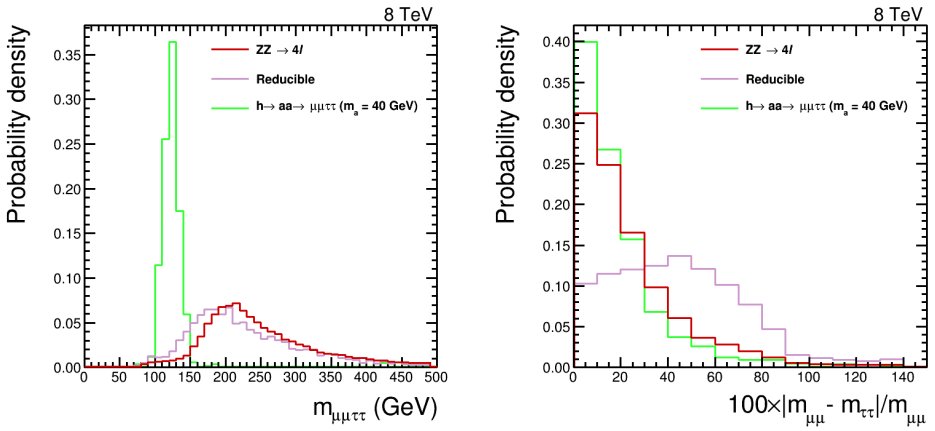

Figure 11.2: Normalized distributions of the $m_{\mu\mu\tau\tau}$ (left) and 100 times $|m_{\mu\mu}-m_{\tau\tau}|/m_{\mu\mu}$ (right) variables in signal and background events.

	$\mu\mu\tau_e\tau_e$	$\mu\mu\tau_e\tau_\mu$	$\mu\mu\tau_e\tau_h$	$\mu\mu\tau_\mu\tau_h$	$\mu\mu\tau_h\tau_h$
μ_1	p_T >18 GeV, $\|\eta\| < 2.4$, $I_{rel} < 0.4$, Loose PF ID				
μ_2	$I_{rel} < 0.4$, Loose PF ID, $\|\eta\| < 2.4$				
	$p_T > 9$ GeV	$p_T > 5/9$ GeV	$p_T > 9$ GeV	$p_T > 5/9$ GeV	$p_T > 9$ GeV
τ_e	$p_T > 7$ GeV, $\|\eta\| < 2.5$, MVA ID			-	-
	$I_{rel} < 0.4$	$I_{rel} < 0.4$	$I_{rel} < 0.2$		
τ_h	-	-	$p_T > 15$ GeV, $\|\eta\| < 2.3$, Loose anti-μ		
			Loose iso. Loose anti-e	Loose iso. vLoose anti-e	Medium iso. vLoose anti-e
τ_μ	-	$p_T > 9/5$ GeV $\|\eta\| < 2.4$ Loose PF ID $I_{rel} < 0.4$	-	$p_T > 9/5$ GeV $\|\eta\| < 2.4$ Tight PF ID $I_{rel} < 0.5$	-
b–Jet veto	No b–tagged jet in the event.				
Lepton veto	No additional electron or muon.				
$\|m_{\mu\mu\tau\tau} - 125\|$	< 25 GeV				
$\|m_{\mu\mu} - m_{\tau\tau}\|/m_{\mu\mu}$	< 0.8				
ΔR **between leptons**	> 0.4				
$\|m^{vis}_{\mu\mu ee} - 125\|$	> 15 GeV	-			

Table 11.1: Selection criteria in the five studied final states. The two p_T and η values quoted for the muons in the $\mu\mu\tau_\mu\tau_h$ and $\mu\mu\tau_e\tau_\mu$ final states correspond to the case where the muons are responsible or not for firing the trigger path.

gluon-gluon fusion signal, because the lepton kinematics is basically unchanged and there is no selection focuse based on the number of jets. The case of the Wh and Zh productions is different: leptons might be produced in vector boson decays and make the event fail the additional lepton veto, or neutrinos from the vector bosons may change the $m_{\tau\tau}$ computation and make the event fail the selection criteria on $m_{\mu\mu\tau\tau}$ or $|m_{\mu\mu} - m_{\tau\tau}|/m_{\mu\mu}$. Because of these effects, the selection efficiency for signal events produced in association with vector bosons is approximately 40% lower than in the gluon-gluon fusion case. The relative efficiencies with respect to the gluon-gluon fusion production for the VBF, Wh and Zh production modes are shown in Fig. 11.3. Meanwhile, the $t\bar{t}h$ contribution is negligible because of its small cross section, of the b jet veto, and of the additional lepton veto. Therefore, signal samples produced in gluon-gluon fusion are reweighted with a modified cross section σ computed as:

$$\sigma = 22.1 \times (0.872 \times 1.00 + 0.071 \times 1.00 + 0.032 \times 0.60 + 0.019 \times 0.60 + 0.006 \times 0.00) \text{ pb.} \quad (11.1)$$

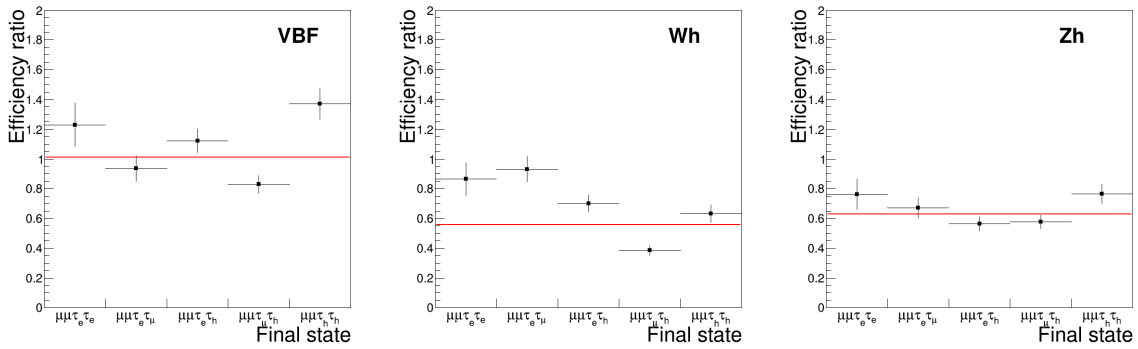

Figure 11.3: Ratio of the signal acceptance times efficiency in the VBF (left), Wh (center) and Zh (right) production modes, to the signal efficiency in gluon-gluon fusion production. The acceptance times efficiency in VBF is comparable to the acceptance times efficiency in ggh, while it is about 40% lower for the Wh and Zh production modes.

11.2 Background estimation and its validation

The background estimation methods are generally similar to those used in the context of the SM $ZH \to \ell\ell\tau\tau$ and MSSM $A \to Zh \to \ell\ell\tau\tau$ searches. The ZZ background is directly taken from MC simulations and normalized to its NLO cross section [118], while the reducible processes are estimated with data-driven methods.

The normalization of the reducible processes comes from the misidentification rate method. The $j \to \mu$, $j \to e$ and $j \to \tau_h$ misidentification rates are measured for the identification and isolation working points used in this analysis; they are shown in Fig. 11.4. They are parameterized with decreasing exponential functions as a function of the transverse momentum of the closest jet, but in the case of light leptons with p_T less than 15 GeV,

	$\mu\mu\tau_e\tau_e$	$\mu\mu\tau_e\tau_\mu$	$\mu\mu\tau_e\tau_h$	$\mu\mu\tau_\mu\tau_h$	$\mu\mu\tau_h\tau_h$	Combination
Data	13 ± 3.6	14 ± 3.7	65 ± 8.1	24 ± 4.9	56 ± 7.5	172 ± 13.1
Mis-ID rate method	11.2 ± 5.6	13.3 ± 6.6	57.5 ± 21.8	25.8 ± 9.8	68.9 ± 17.2	176.7 ± 30.7

Table 11.2: Comparison between the yield in data with two SS tau candidates, and the yield obtained in the SS region with the misidentification rate method.

they are measured in two five-GeV wide bins. The low-p_T behavior of the muon misidentification rate is due to events with a very low p_T spurious track with potentially one hit in the muon chambers, which are reconstructed as muon candidates but do not pass the muon identification. Because of the large pileup, many such muons are reconstructed, but their misidentification rate is small because they do not pass the identification conditions. The normalization of the reducible processes is estimated by subtracting the contribution of events with two tau candidates that fail the isolation or identification conditions, weighted by a factor that depends on the misidentification rates, from the weighted contribution of events with exactly one tau candidate that fails the identification or isolation conditions.

To validate the estimation of the reducible background, the yields obtained with the misidentification rate method are compared with the observed data in a region where the two tau candidates have the same electric charge. The statistical uncertainties are reduced by relaxing the selection criteria on $|m_{\mu\mu} - m_{\tau\tau}|/m_{\mu\mu}$, $m_{\mu\mu\tau\tau}$ and $m_{\mu\mu}$. The results are presented in Tab. 11.2; the yields from the misidentification rate method are very compatible with the observation. An additional cross-check consists in comparing the yields of the misidentification rate method when the rates are parameterized as a function of the p_T of the closest jet or of the lepton. The difference between both methods is limited (between 5 and 30%) and well covered by the uncertainty assigned to the reducible background normalization [1]. Nevertheless, the parametrization as a function of the p_T of the closest jet is chosen because it gives the best agreement between prediction and observation in the closure test described in the previous paragraph.

The di-muon mass ($m_{\mu\mu}$) distribution of the reducible background is taken from data in a region where both tau candidates have the same electric charge and are selected with relaxed isolation and identification criteria, namely:

- $\mu\mu\tau_e\tau_e$: relative isolation less than 1.0 for both electrons;
- $\mu\mu\tau_e\tau_\mu$: relative isolation less than 2.0 for both leptons;
- $\mu\mu\tau_e\tau_h$: loose MVA electron identification, relative electron isolation less than 5.0, BDT output of the tau isolation including lifetime information greater than -0.95;
- $\mu\mu\tau_\mu\tau_h$: loose PF muon identification, relative muon isolation less than 5.0, BDT output of the tau isolation including lifetime information greater than -0.95;
- $\mu\mu\tau_h\tau_h$: BDT output of the tau isolation including lifetime information greater than -0.90.

The $m_{\mu\mu}$ distribution obtained in this way is compatible, within the large statistical un-

1. The uncertainties range from 25 to 50% depending on the final state, as explained in Section 11.4.

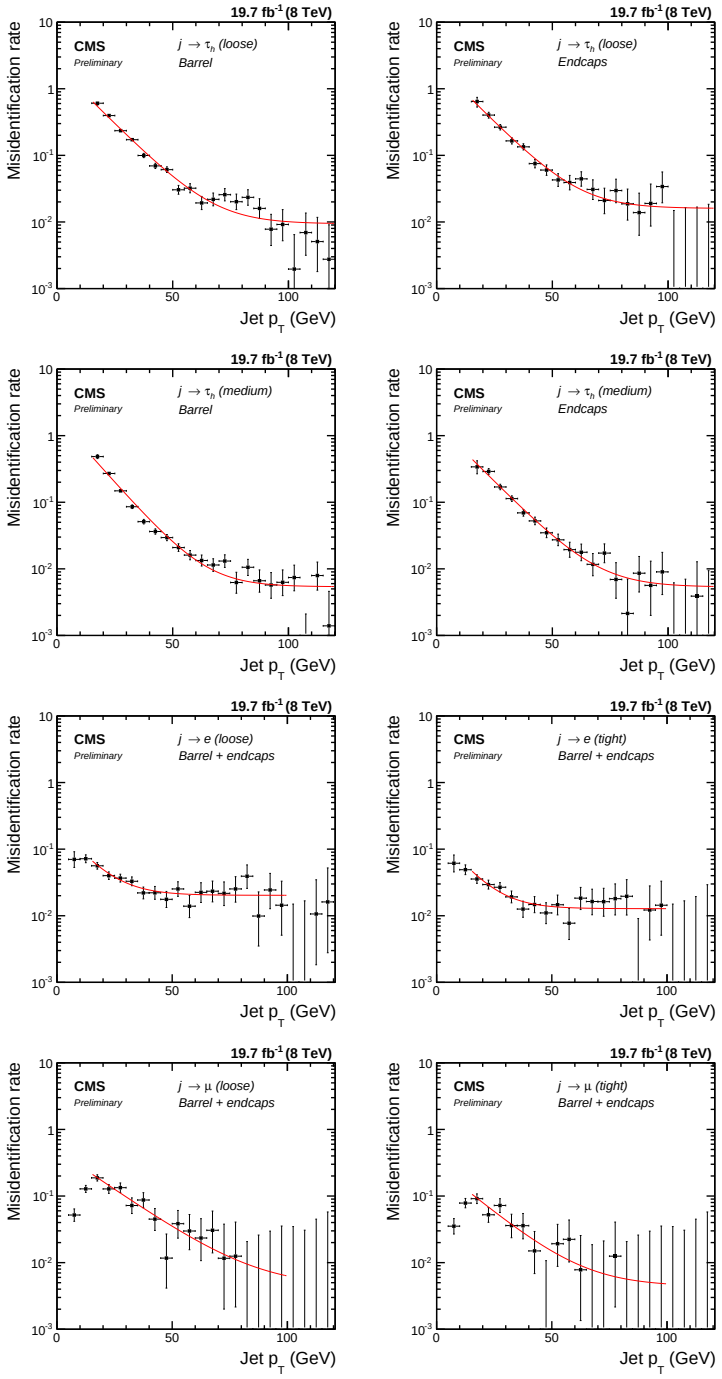

Figure 11.4: Misidentification rates of the tau candidates. [130]

certainties, with the distribution coming from the misidentification rate method, as shown in Fig. 11.5.

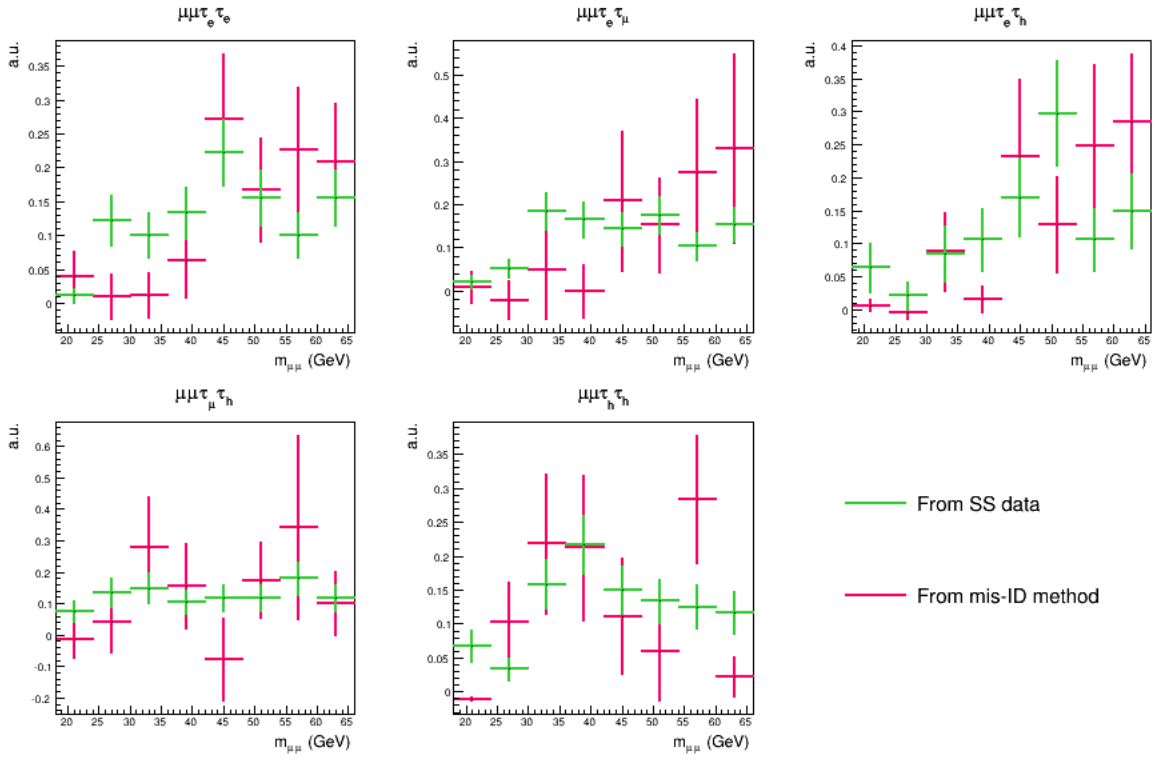

Figure 11.5: Comparison between the $m_{\mu\mu}$ distributions obtained via the misidentification rate method and from data with SS tau candidates (default method), in the five different final states.

Distributions of the $m_{\mu\mu}$ variable observed in data and their predictions for SM processes, before cutting on $|m_{\mu\mu} - m_{\tau\tau}|/m_{\mu\mu}$ nor $m_{\mu\mu\tau\tau}$ are shown in Fig. 11.6 and demonstrate a good background description in the full mass range, and especially in the more populated Z peak region.

11.3 Modeling of the experimental $m_{\mu\mu}$ distributions

Because of the excellent di-muon mass resolution, an unbinned shape analysis, using $m_{\mu\mu}$ as observable, is performed. All processes are parameterized separately in the five final states.

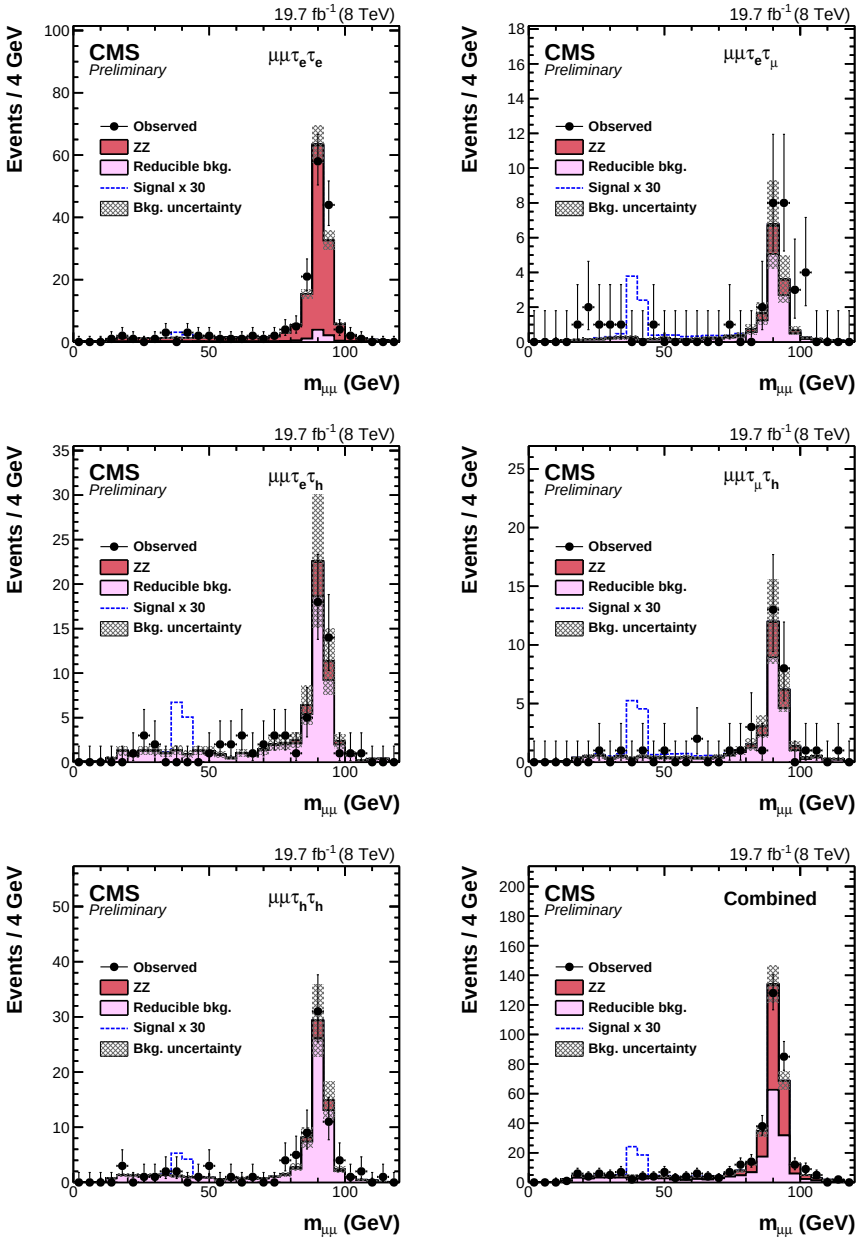

Figure 11.6: Data, predicted SM backgrounds, and signal (m_a = 40 GeV) di-muon mass distributions in the $\mu\mu\tau_e\tau_e$ (top left), $\mu\mu\tau_e\tau_\mu$ (top right), $\mu\mu\tau_e\tau_h$ (center left), $\mu\mu\tau_\mu\tau_h$ (center right), and $\mu\mu\tau_h\tau_h$ (bottom left) final states, and their combination (bottom right). The cuts on the variables $m_{\mu\mu\tau\tau}$ and $|m_{\mu\mu} - m_{\tau\tau}|/m_{\mu\mu}$ are not applied to increase the number of selected events. The signal samples are scaled as thirty times the normalization obtained with $\sigma(h)$ as predicted in the SM, $\mathcal{B}(h \to aa) = 10\%$, and considering decays of the pseudoscalar a boson to leptons only. No maximum likelihood fit to the data has been performed. [129]

11.3.1 Signal

Signal distributions are parameterized with Voigtian functions, which are convolutions of Gaussian and Lorentzian profiles:

$$V(m) = \int_{-\infty}^{+\infty} G(m', \sigma) L(m - m', \alpha) dm', \tag{11.2}$$

where the Gaussian profile is centered on 0 and defined as:

$$G(m, \sigma) = \frac{e^{-m^2/(2\sigma^2)}}{\sigma\sqrt{2\pi}}, \tag{11.3}$$

and the centered Lorentzian distribution is:

$$L(m, \alpha) = \frac{\alpha}{\pi(m^2 + \alpha^2)}. \tag{11.4}$$

In practice, the Voigtian function, and its components, are centered close to the a boson mass hypothesis. The Lorentzian component reflects the natural width of the signal, while the Gaussian component takes into account experimental resolution effects.

Signal samples are generated with Pythia, for masses between 20 and 60 GeV, with 5 GeV steps. Fits are performed for every mass hypothesis and every final state, after the full selection has been applied. The Gaussian component is seen to vanish in the final states with three muons ($\mu\mu\tau_e\tau_\mu$ and $\mu\mu\tau_\mu\tau_h$), and the signal distributions in these final states are therefore fitted with simple Lorentzian functions. The signal fits in the different final states for $m_a = 40$ GeV are shown in Fig. 11.7; a good fit quality is observed for all of them.

A method is designed to interpolate the signal description to any mass between 20 and 60 GeV, and to extrapolate it up to $m_h/2 = 62.5$ GeV. The fit parameters extracted from the fits to the signal samples, are parameterized as a function of the generated a boson mass with polynomials with three degrees of freedom. The mean of the distributions is, as expected, close to the generated a boson mass, while the width parameters, α and σ, show a more complex behavior. The distributions of the fit parameters are shown in Fig. 11.8 for all final states. The signal acceptance times efficiency, measured for all masses in every final state, is also parameterized as a function of the mass hypothesis, as shown in Fig. 11.9. These parameterizations allow the description of the signal distribution and normalization at any mass, as illustrated in Fig. 11.10

A closure test is performed to validate the interpolation procedure. A signal sample is removed from the fit of the Lorentzian and Voigtian parameters as a function of the a boson mass, and the signal distributions resulting from the extrapolation with this parameterization are compared to the direct fits to this signal sample. The test is performed for intermediary masses, and for an extreme mass ($m_a = 60$ GeV): interpolating to intermediary masses and extrapolating outside the range of generated masses both give a

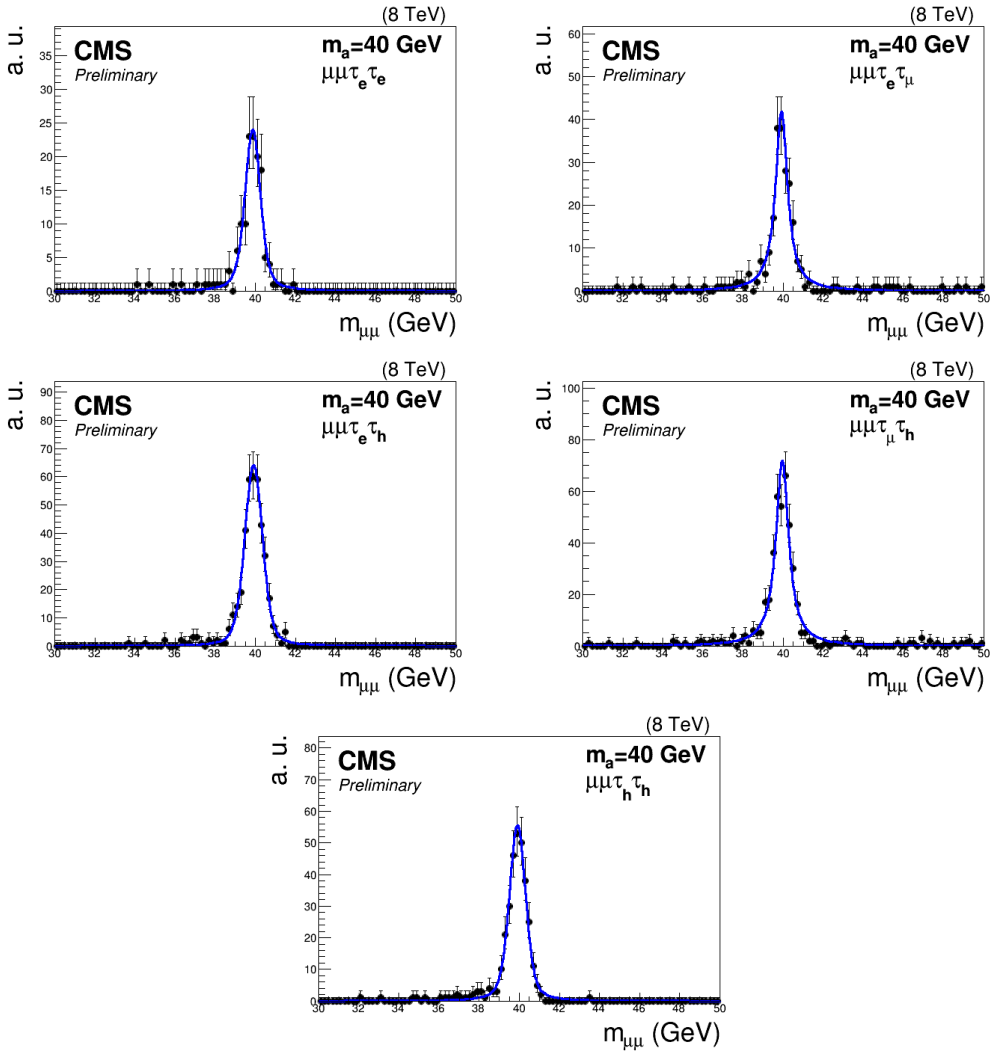

Figure 11.7: Modeling of the signal with $m_a = 40$ GeV using Lorentzian or Voigtian functions, in the $\mu\mu\tau_e\tau_e$ (top left), $\mu\mu\tau_e\tau_\mu$ (top right), $\mu\mu\tau_e\tau_h$ (center left), $\mu\mu\tau_\mu\tau_h$ (center right), and $\mu\mu\tau_h\tau_h$ (bottom) final states. The black dots correspond to events selected in MC samples. [130]

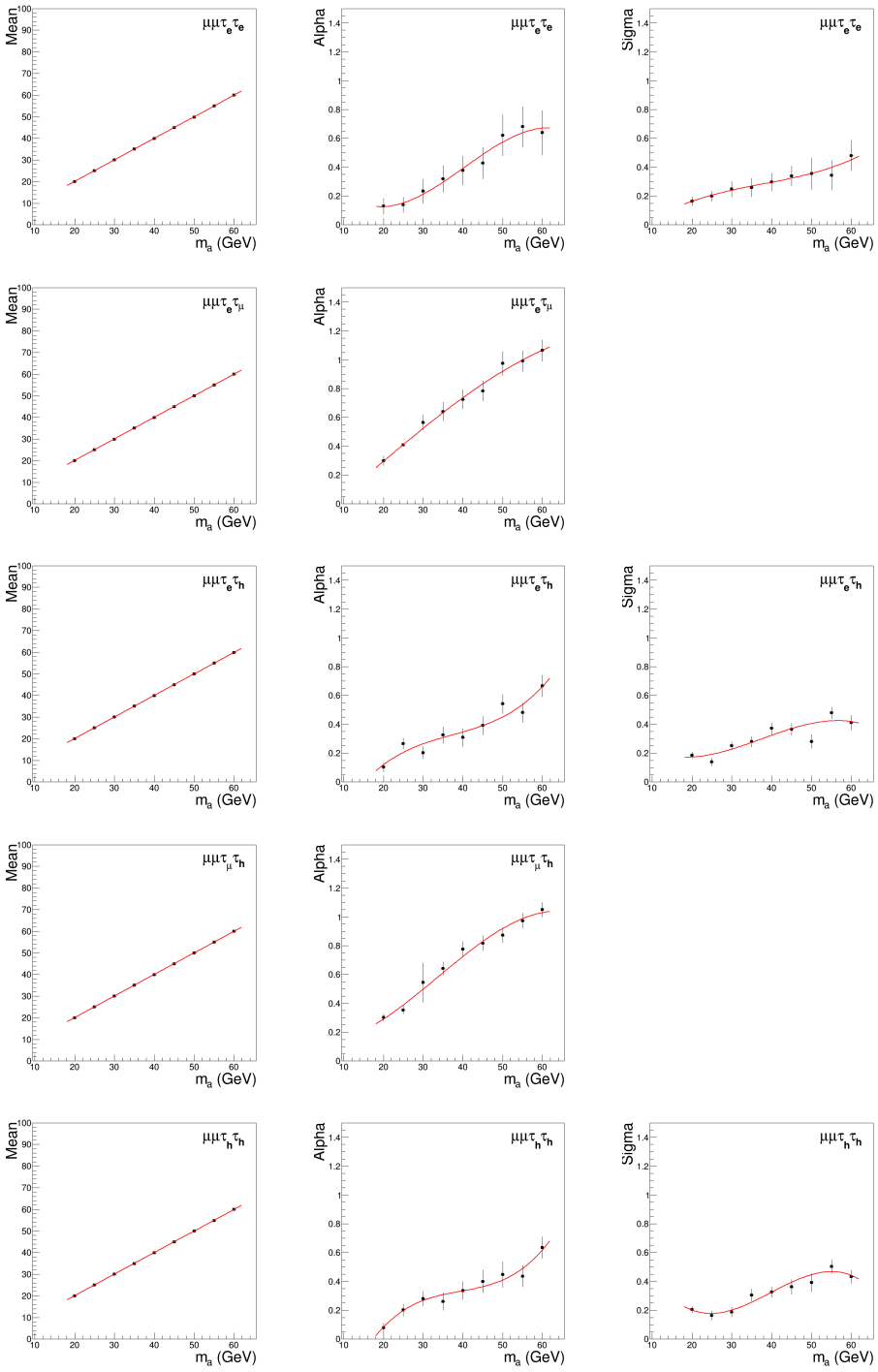

Figure 11.8: Lorentzian or Voigtian fit parameters extracted from fits to signal samples in the different final states, with pseudoscalar boson masses ranging from 20 to 60 GeV.

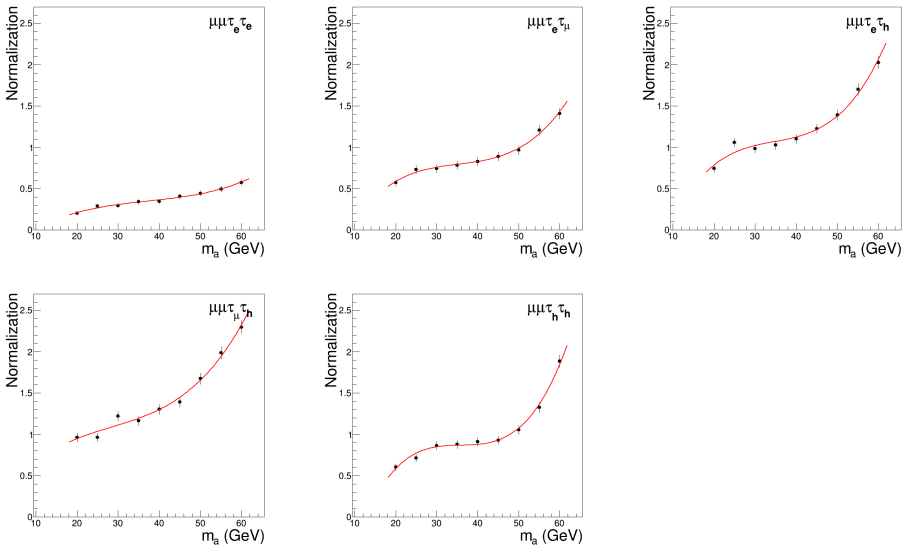

Figure 11.9: Signal normalization as a function of the pseudoscalar boson mass, for an h boson production cross as expected in the SM, a decays to leptons only and $\mathcal{B}(h \to aa) = 10\%$. The plateau trend between 30 and 50 GeV is due to the interplay between the boost of the a bosons at low m_a and the boost of the tau leptons at high m_a.

good agreement with the direct fits. The results of the closure test for $m_a = 55$ GeV are shown in Fig. 11.11.

11.3.2 ZZ background

The ZZ background is parameterized with Bernstein polynomials, which are linear combinations of Bernstein-basis polynomials. The $n+1$ Bernstein-basis polynomials used to build a Bernstein polynomial with n degrees of freedom are defined as:

$$b_{i,n}(x) = \binom{n}{i} x^i (1-x)^{n-i}, \text{ with } i = 0, ..., n, \tag{11.5}$$

where $\binom{n}{i}$ are binomial coefficients. Bernstein polynomials are positively defined for x between 0 and 1, which makes them a good choice to describe data limited by statistics.

The polynomial coefficients are extracted from a fit to the events selected in the ZZ MC simulation. As the number of selected events is extremely low in the $\mu\mu\tau_h\tau_h$ final state, the hadronic tau isolation is relaxed from the medium to the loose HPS working point. This does not bias the bias the $m_{\mu\mu}$ distribution, and increases the number of selected events by more than 50%. The fits are shown in Fig. 11.12 for all final states.

The degree of the Bernstein polynomial is chosen to be the lowest that gives a good data description; in other words, the degree n is chosen if the degree $n+1$ does not bring

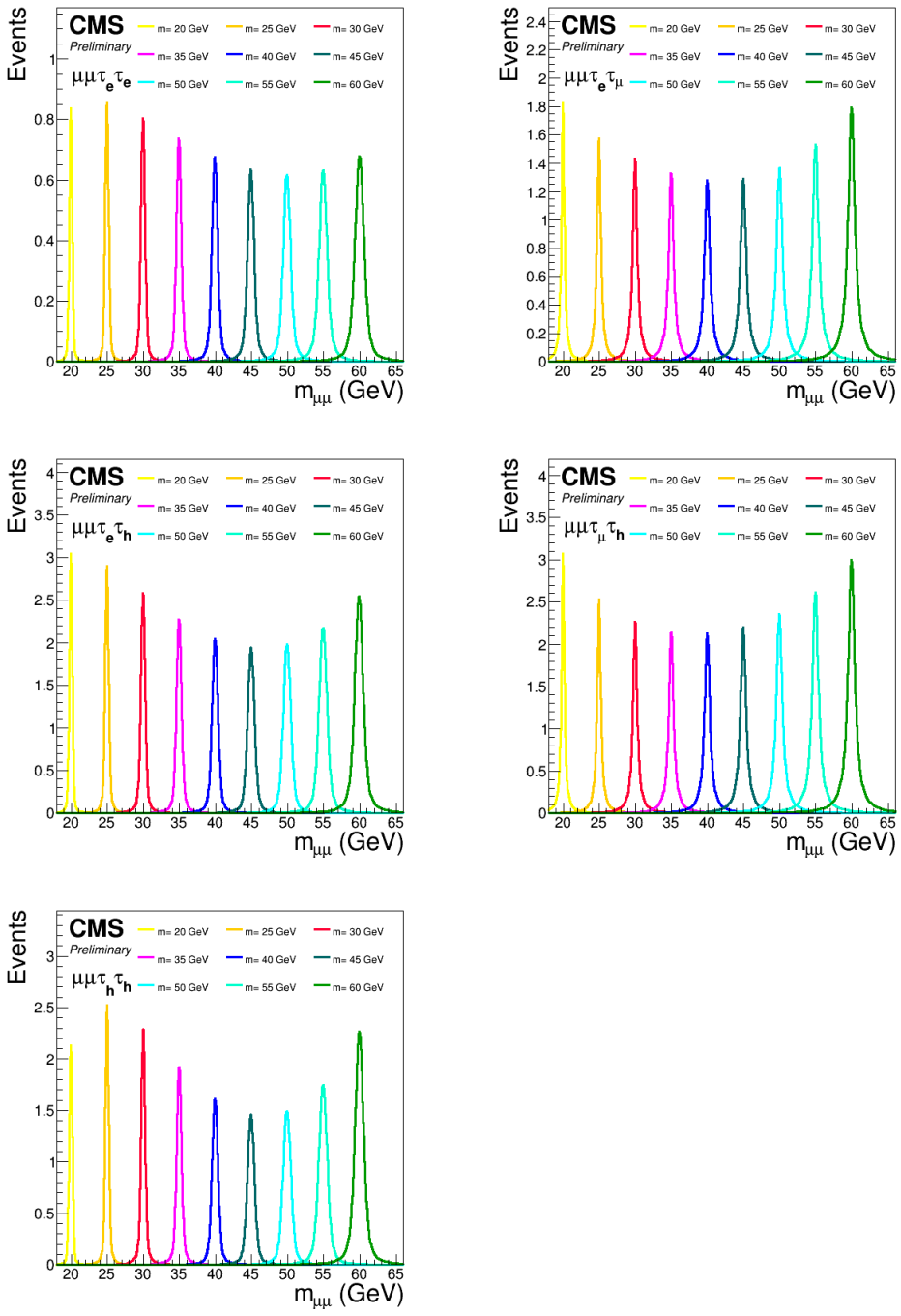

Figure 11.10: Signal description extracted from the parameterization of the Voigtian and Lorentzian fit parameters. The normalization corresponds to an h boson production cross as expected in the SM, a decays to leptons only and $\mathcal{B}(h \to aa) = 10\%$. [130]

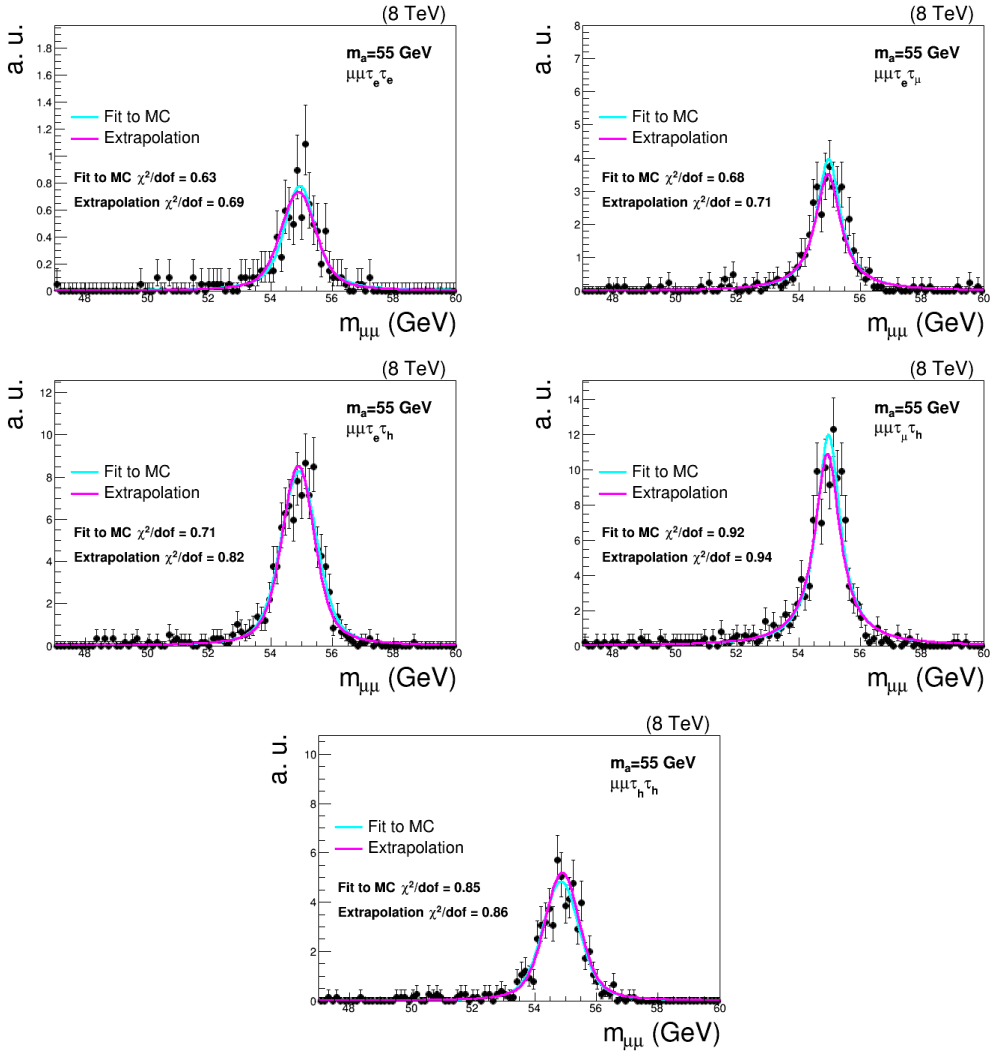

Figure 11.11: Comparison between the interpolation from the parameterization and the direct fit for a signal with $m_a = 55$ GeV.

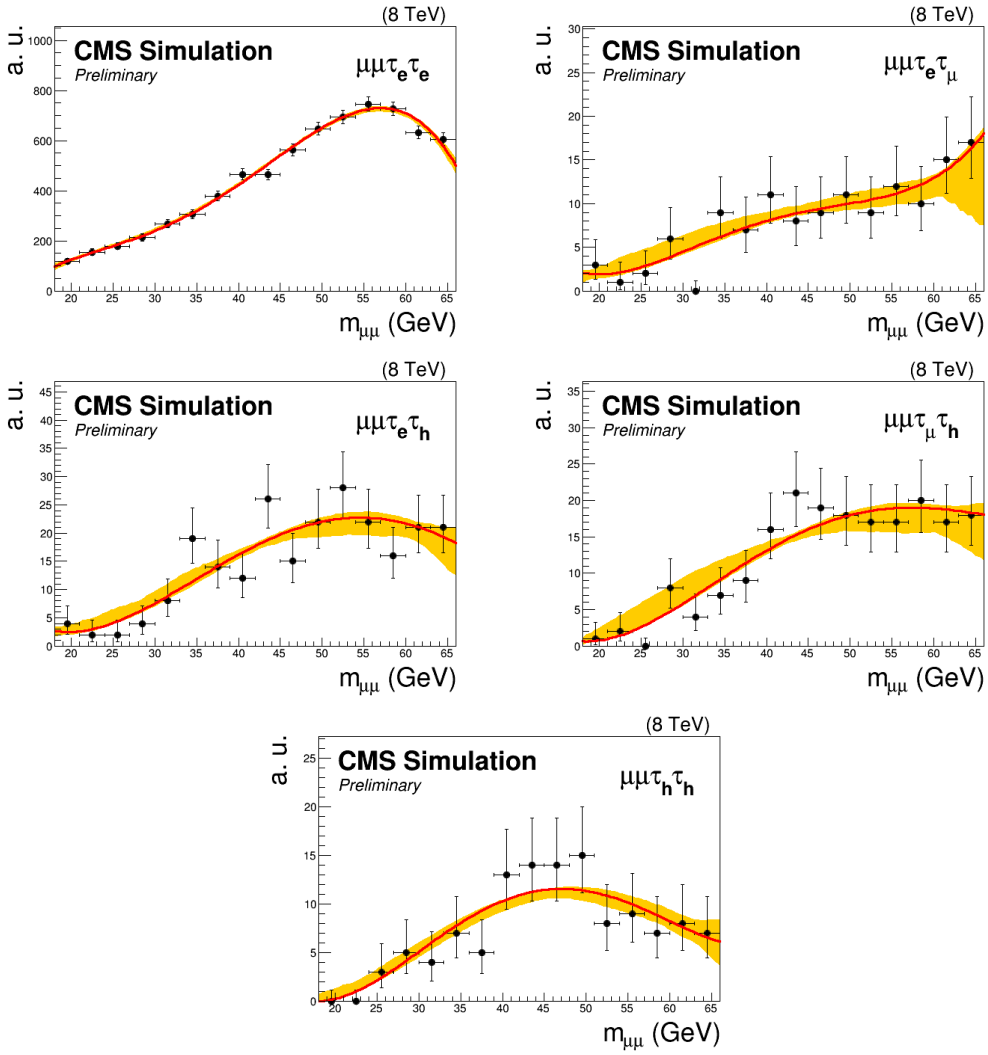

Figure 11.12: Modeling of the ZZ background, estimated from MC simulations, using fifth-degree Bernstein polynomials, in the $\mu\mu\tau_e\tau_e$ (top left), $\mu\mu\tau_e\tau_\mu$ (top right), $\mu\mu\tau_e\tau_h$ (center left), $\mu\mu\tau_\mu\tau_h$ (center right), and $\mu\mu\tau_h\tau_h$ (bottom) final states. The black dots correspond to events selected in MC samples. [129]

Polynomial degree ($n \to n+1$)	$2 \times (NLL_n - NLL_{n+1})$				
	$\mu\mu\tau_e\tau_e$	$\mu\mu\tau_e\tau_\mu$	$\mu\mu\tau_e\tau_h$	$\mu\mu\tau_\mu\tau_h$	$\mu\mu\tau_h\tau_h$
$3 \to 4$	94.8	0.05	9.07	4.29	6.17
$4 \to 5$	18.2	1.65	0.78	0.67	2.99
$5 \to 6$	0.20	0.61	2.87	2.22	2.01

Table 11.3: Twice the difference between the minimum negative log-likelihood values for two adjacent polynomial degrees in the different final states, for the fit of the ZZ background. The improvement brought by the additional degree of freedom is judged significant if this value is larger than 3.85. The sixth degree does not improve the fit quality significantly for any of the final states, and the fifth degree is thus chosen.

a significant improvement to the fit quality. The minimized negative log-likelihood, NLL, which describes the level of agreement between the fit function and the distribution of the selected events, can be measured for the fits with polynomials with degree n or $n+1$. It can be shown that twice their difference follows a chi-square distribution with one degree of freedom: $2 \times (NLL_n - NLL_{n+1}) \sim \chi^2_1$. The number of degrees of freedom $n+1$ is chosen over n if the chi-square between these two fits shows no significant improvement (p-value < 0.05 with a F-distribution [131]): $P(\chi^2_1 \geq 2 \times (NLL_n - NLL_{n+1})) < 0.05$. A significant improvement therefore consists in $2 \times (NLL_n - NLL_{n+1}) > 3.85$. Such a method has been used in [132]. The differences for the fits with Bernstein polynomials of different degrees are shown in Tab. 11.3: the fifth degree is the one that permits to describe efficiently all final states. The fourth degree would have been optimal for all final states except $\mu\mu\tau_e\tau_e$, which is the most populated by ZZ events; this choice does not impact the final results because the ZZ background is negligible with respect to the reducible processes in these final states.

11.3.3 Reducible background

Like the ZZ background, reducible processes are modeled with Bernstein polynomials. The same method is used to determine the optimal polynomial degree; as shown in Tab. 11.4, the third degree is the best choice. It can be noticed that the reducible background is described with a polynomial with less degrees of freedom than the ZZ background, which is subdominant. The reason is that the distribution of the ZZ background is better constrained by the large statistics from the MC sample, especially in the $\mu\mu\tau_e\tau_e$ final state, whereas the reducible background distribution comes from a statistically limited number of observed events in a control region in data. The results of the fits, together with their uncertainties, are illustrated in Fig. 11.13.

11.4 Uncertainties

The systematic uncertainties that affect the yields of the signal and background processes are:

– **Theoretical signal prediction**: A 10% uncertainty affects the signal yield, to account for uncertainties on the theoretical signal prediction.

Polynomial degree ($n \to n+1$)	$2 \times (NLL_n - NLL_{n+1})$				
	$\mu\mu\tau_e\tau_e$	$\mu\mu\tau_e\tau_\mu$	$\mu\mu\tau_e\tau_h$	$\mu\mu\tau_\mu\tau_h$	$\mu\mu\tau_h\tau_h$
$2 \to 3$	6.80	9.35	0.84	0.76	12.5
$3 \to 4$	0.41	0.12	1.55	0.11	0.07

Table 11.4: Twice the difference of the minimum negative log-likelihood values for two adjacent polynomial degrees in the different final states, for the fit of the reducible background. The improvement brought by the additional degree of freedom is judged significant if this value is larger than 3.85. The fourth degree does not improve the fit quality significantly for any of the final states, and the third degree is thus chosen.

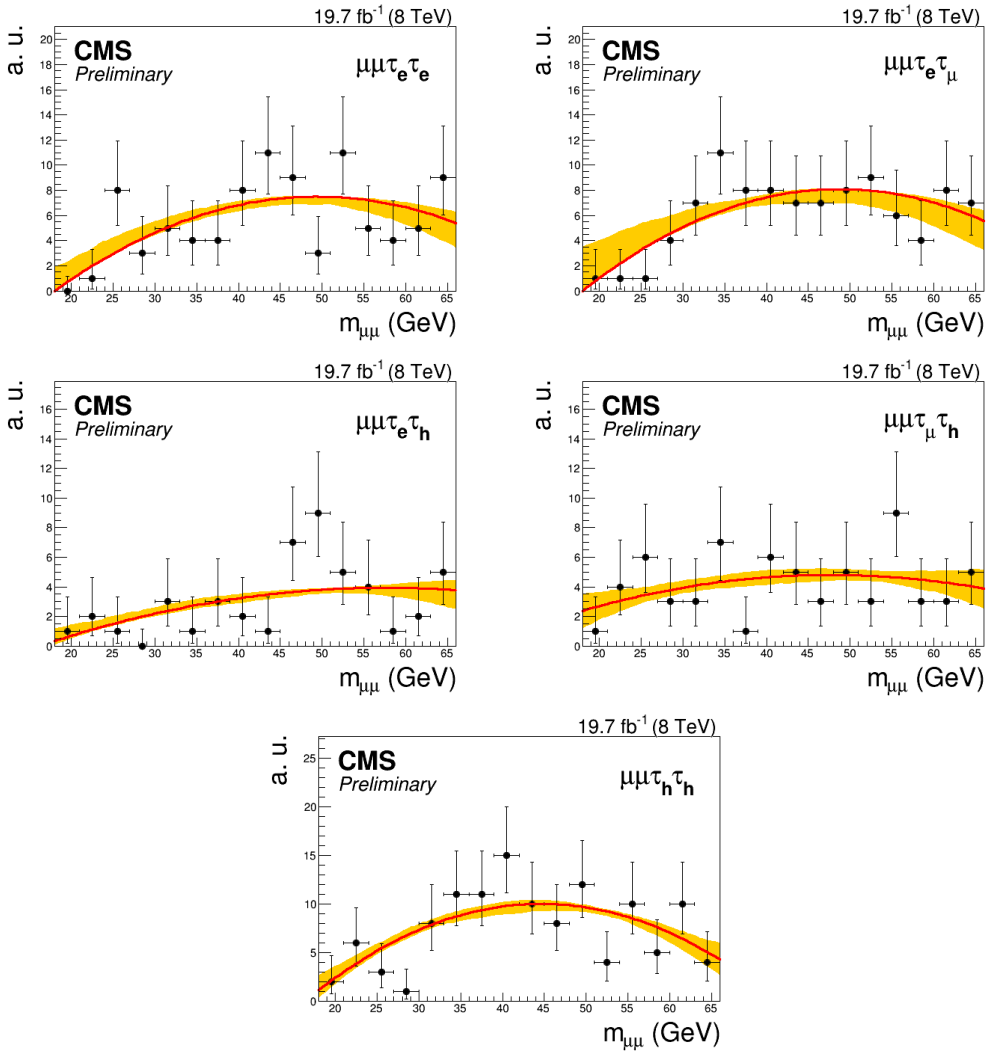

Figure 11.13: Modeling of the reducible background with third-order Bernstein polynomials, in the $\mu\mu\tau_e\tau_e$ (top left), $\mu\mu\tau_e\tau_\mu$ (top right), $\mu\mu\tau_e\tau_h$ (center left), $\mu\mu\tau_\mu\tau_h$ (center right), and $\mu\mu\tau_h\tau_h$ (bottom) final states. The black dots correspond to observed events selected in control regions. [129]

- **Signal efficiency**: An uncertainty between 5 and 8% is considered in each final state to account for the uncertainty on the parameterization of the normalization of the signal as a function of the mass, illustrated in Fig. 11.9.
- **Luminosity**: The uncertainty on the luminosity, which affects the ZZ background and the signal, is measured to be 2.6% [109].
- **Tau energy scale**: As discussed in Chapter 6, the tau energy scale in data is known with 3% precision [103]. This does not affect the $m_{\mu\mu}$ distributions, but has an effect on the estimated yield of processes from MC simulations because of the p_T thresholds applied to select hadronic taus. When the tau energy scale is varied by $\pm 3\%$, the acceptance for the signal and ZZ processes is modified by up to 10% in the $\mu\mu\tau_h\tau_h$ final state, and up to 4% in the $\mu\mu\tau_e\tau_h$ and $\mu\mu\tau_\mu\tau_h$ final states. The yield uncertainties in the $\mu\mu\tau_h\tau_h$ final state, and in the $\mu\mu\tau_e\tau_h$ and $\mu\mu\tau_\mu\tau_h$ final states, are uncorrelated because different HPS isolation working points are used.
- **Tau identification**: An uncertainty of 6% is considered for any single hadronic tau [103]; and this number is conservatively doubled in the $\mu\mu\tau_h\tau_h$ final state.
- **Muon identification**: A 1% uncertainty is considered, conservatively multiplied by the number of muons in the final state.
- **Electron identification**: A 2% uncertainty is considered, conservatively multiplied by the number of electrons in the final state.
- **Trigger efficiency**: The uncertainty on the double muon trigger efficiency is estimated to amount to 2%.
- **B jet veto**: Applying a b jet veto brings a 1% uncertainty on the yield of the signal and ZZ processes, both estimated from MC simulations.
- ZZ **theoretical cross section**: Uncertainties in the parton distribution functions (PDF) and variations of the renormalization and factorization scales lead to respectively 5 and 6% yield uncertainties on the ZZ background.
- **Limited number of** ZZ **events in MC samples**: After the full selection, the number of MC events remaining for the ZZ process is limited, and an uncertainty ranging between 1 and 15% depending on the final state is associated the global normalization of the ZZ background.
- **Reducible background normalization estimation**: The uncertainty on the normalization of the reducible background is estimated by recomputing the yields after modifying the misidentification rate fit functions within their uncertainties. An uncertainty is associated to every fit function, and the total uncertainty in a given final state varies between 25 and 50%

Meanwhile, the shape uncertainties considered in the analysis are:

- **Signal modeling**: Statistical uncertainties on the parameterization of the signal are accounted for through the uncertainties on the fit parameters (α, σ) describing the signal distribution.
- **Muon energy scale and muon momentum resolution**: The muon energy scale and momentum resolution uncertainties are found to shift the mean of the signal distributions by up to 0.2% when they are varied by ± 1 standard deviation. This

Systematic uncertainty	Relative change in yield		
	Signal	ZZ	Reducible backgrounds
Luminosity	2.6%	2.6%	-
Trigger	1%	1%	-
Tau identification	0-12%	0-12%	-
b-Jet veto	1%	1%	-
Tau energy scale	0-10%	0-10%	-
Electron identification	0-4%	0-4%	-
Muon identification	2-4%	2-4%	-
Signal prediction	10%	-	-
Signal efficiency	5-8%	-	-
PDF	-	5%	-
QCD scale VV	-	6%	-
ZZ statistics in MC	-	1-15%	-
Reducible background normalization	-	-	25-50%
Reducible background distribution	-	-	shape only
Signal modeling	shape only	-	-
Muon energy scale	shape only	-	-

Table 11.5: Systematic uncertainties on the yields or shapes of the signal, ZZ and reducible processes. The relative change in yields resulting from a variation of the nuisance parameter equivalent to one standard deviation is indicated.

is accounted for as a parametric uncertainty on the mean of the Lorentzian and Voigtian functions.

– **Reducible background distribution estimation**: The three uncertainties associated to the three degrees of freedom of the Bernstein polynomials used to model the reducible background, are decorrelated and considered as shape uncertainties.

All the uncertainties are summarized in Tab. 11.4. Given the very low expected yields expected over the full mass range, and the excellent di-muon mass resolution, the analysis is mostly statistically limited, and the systematic uncertainties described above generally play a little role in the results.

11.5 Results

The expected and observed $m_{\mu\mu}$ distributions in the different final states are shown in Fig. 11.14. The expected distributions are the result of a simultaneous background-only maximum likelihood fit to the observed data. Every observed event is indicated together with its precise $m_{\mu\mu}$ value. The yields are detailed in Tab. 11.6: the number of observed events is compatible with the SM expectation.

Upper limits can be set on the cross section times branching fraction for the process $h \to aa \to \mu\mu\tau\tau$, but a more easily interpretable result consists in upper limits on $\sigma(h)/\sigma_{SM} \times \mathcal{B}(h \to aa) \times \mathcal{B}(a \to \tau\tau)^2$. Indeed, if the production cross section of the h

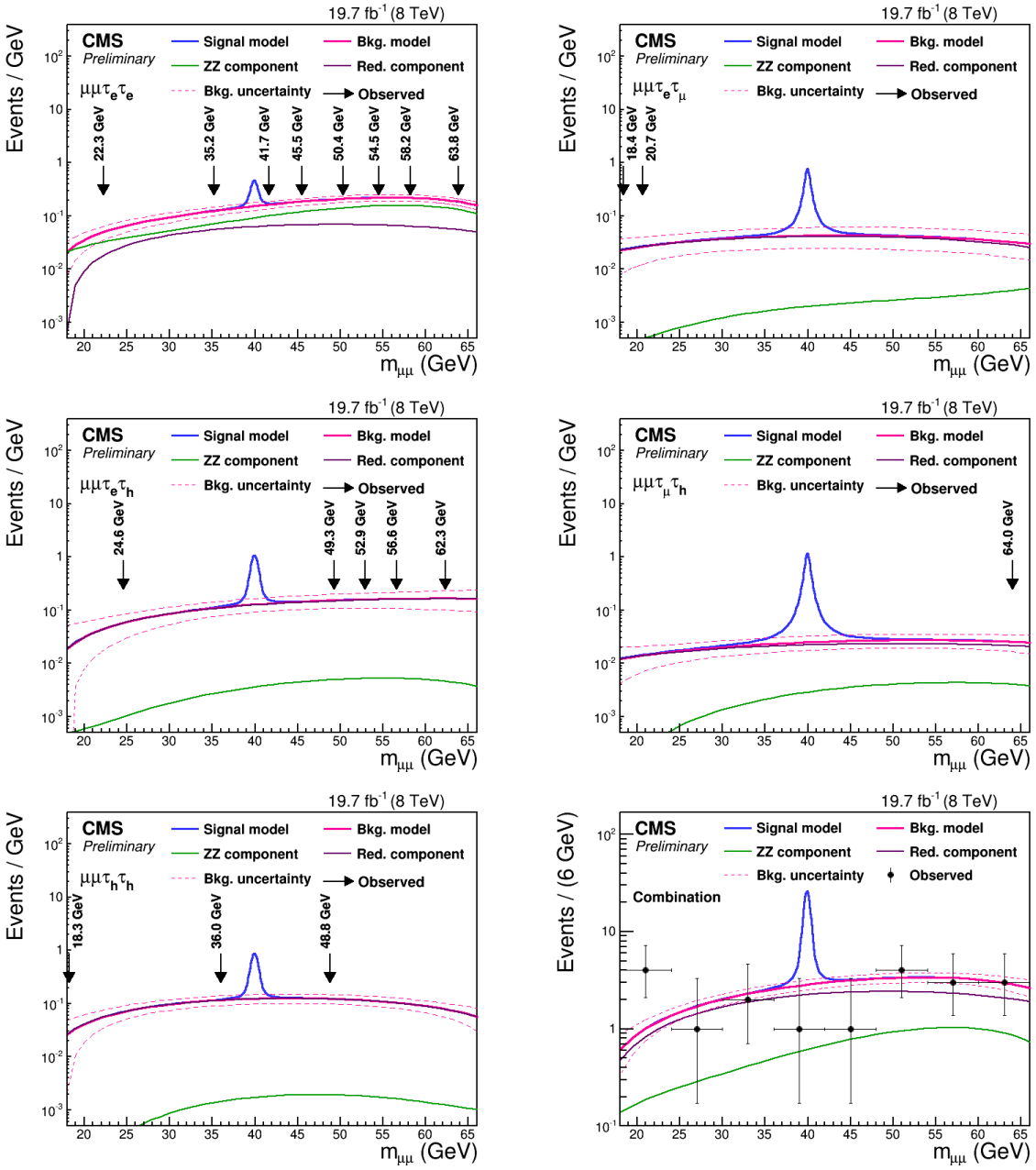

Figure 11.14: Background and signal (m_a = 40 GeV) models, scaled to their expected yields, in the $\mu\mu\tau_e\tau_e$ (top left), $\mu\mu\tau_e\tau_\mu$ (top right), $\mu\mu\tau_e\tau_h$ (middle left), $\mu\mu\tau_\mu\tau_h$ (middle right), and $\mu\mu\tau_h\tau_h$ (bottom left) final states, and their combination (bottom right). The two components that form the background model, ZZ and reducible processes, are drawn. Every observed event in the individual decay channels is represented by an arrow, together with its measured $m_{\mu\mu}$ value; while in the combined mass plot data are binned in a histogram. The signal samples are scaled with $\sigma(h)$ as predicted in the SM, $\mathcal{B}(h \to aa)$ = 10% and considering decays of the pseudoscalar a boson to leptons only. The results are shown after a simultaneous maximum likelihood fit that takes into account the systematic uncertainties. [129]

	Signal		Backgrounds			Obs.
	m_a = 20 GeV	m_a = 60 GeV	ZZ	Reducible	Total	
$\mu\mu\tau_e\tau_e$	0.20±0.02	0.58±0.06	4.64±0.39	2.49±1.03	7.13±1.10	8
$\mu\mu\tau_e\tau_\mu$	0.58±0.08	1.42±0.16	0.10±0.01	1.70±0.74	1.80±0.74	2
$\mu\mu\tau_e\tau_h$	0.74±0.08	2.02±0.20	0.16±0.02	5.65±1.77	5.81±1.77	5
$\mu\mu\tau_\mu\tau_h$	0.96±0.10	2.30±0.22	0.13±0.02	0.99±0.31	1.12±0.31	1
$\mu\mu\tau_h\tau_h$	0.60±0.06	1.90±0.18	0.06±0.01	4.64±0.98	4.70±0.98	3
Combined	3.08±0.31	8.22±0.82	5.09±0.39	15.47±2.41	20.56±2.44	19

Table 11.6: Expected and observed yields in the different final states. The signal samples are scaled with $\sigma(h)$ as expected in the SM, $\mathcal{B}(h \to aa) = 10\%$ and considering decays of the pseudoscalar a boson to leptons only. The background yields are obtained after a maximum likelihood fit to observed data, taking into account the systematic uncertainties described previously.

boson is the same as predicted in the SM, the first term is equal to 1, while the last term is also almost equal to 1 in the hypothesis that the a boson does not decay to quarks [2]. The latter hypothesis is a good approximation at large $\tan\beta$ in 2HDM+S type-3. The $\mathcal{B}(a \to \mu\mu)$ branching fraction can easily be expressed as a multiple of $\mathcal{B}(a \to \tau\tau)$, given that in 2HDM and their extensions, one has:

$$\frac{\Gamma(a \to \mu\mu)}{\Gamma(a \to \tau\tau)} = \frac{m_\mu^2\sqrt{1-(4m_\mu^2/m_a^2)}}{m_\tau^2\sqrt{1-(4m_\tau^2/m_a^2)}}. \tag{11.6}$$

The asymptotic approximation cannot be used to extract the CL_s limits because of the low expected event yield, and other techniques have to be used [67]. Indeed the test statistic distributions in this analysis do not follow chi-squares, as supposed by the asymptotic approximation. Therefore toys need to be generated for every mass point and every final state to obtain the exact test statistic distributions. The limits obtained with the full CL_S calculation are shown in Fig. 11.15. Under the hypotheses that the h boson production cross section is the same as expected in the SM and that the a boson does not decay to quarks, $\mathcal{B}(h \to aa)$ larger than values between 4 and 15% can be excluded for pseudoscalar masses ranging from 20 to 62.5 GeV. An excess of events is seen at low m_a in the $\mu\mu\tau_e\tau_\mu$ final state. The local significance of the excess is about three standard deviations, but a large look-elsewhere effect, due to the narrow signal resolution, the large mass range probed and the five different final states needs to be taken into account. The up-crossing method (see Section 3.4) is not appropriate in this case to evaluate the look-elsewhere effect because there exists a correlation between the background description in neighbor bins, but the trial factor, which relates the global to the local p-value is measured by throwing toys based on the background-only expectation and counting the fraction of times an excess as the one in the $\mu\mu\tau_e\tau_\mu$ final state is observed. The trial factor is larger than thirty, which leads to a global significance less than two standard deviations.

2. $\mathcal{B}(a \to \tau\tau) > 0.995$ for all a boson masses larger than 20 GeV if there is no decay to quarks.

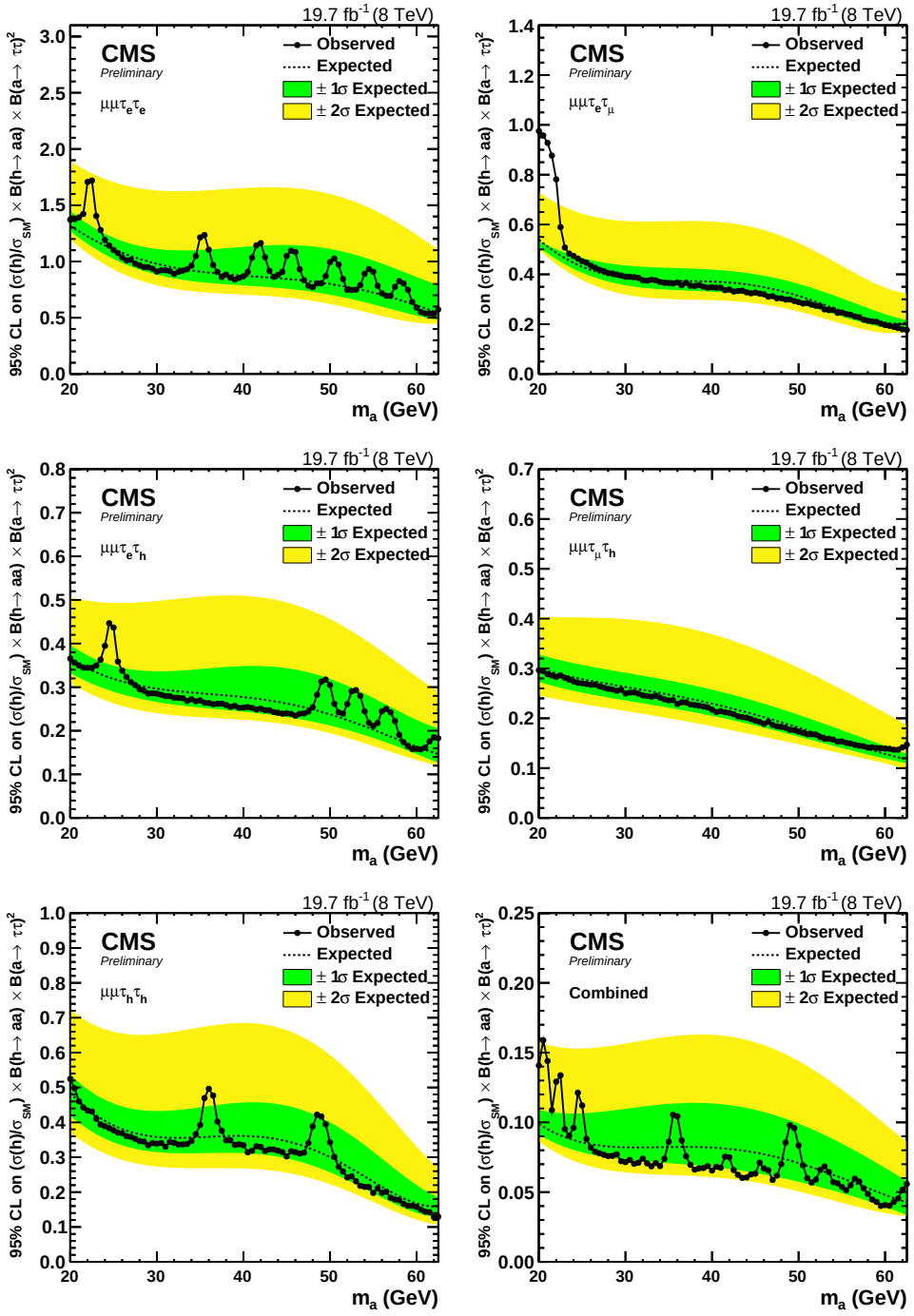

Figure 11.15: Expected upper limits at 95% CL on the production of $h \to aa$ relative to the SM h production, scaled by $\mathcal{B}(a \to \tau\tau)^2$, in the $\mu\mu\tau_e\tau_e$ (top left), $\mu\mu\tau_e\tau_\mu$ (top right), $\mu\mu\tau_e\tau_h$ (middle left), $\mu\mu\tau_\mu\tau_h$ (middle right), and $\mu\mu\tau_h\tau_h$ (bottom left) final states, and for the combination of these five final states (bottom right). $\mathcal{B}(a \to \tau\tau)^2$ is close to 1 in the hypothesis where the pseudoscalar a boson does not decay to quarks. No excess has a global significance larger than 2 standard deviations. [129]

The ATLAS Collaboration has also published results on the search for the exotic decay of the 125-GeV particle to a pair of light pseudoscalar bosons in the final state with two muons and two taus [133]. The analysis targets masses of the pseudoscalar boson between twice the tau mass, and 50 GeV, and makes use of special techniques to reconstruct boosted di-tau pairs. Because the strategy used by ATLAS is optimized for boosted di-tau pairs and thus low pseudoscalar masses, the CMS analysis described in this chapter is roughly one order of magnitude more sensitive for pseudoscalar masses above 20 GeV.

If a type of 2HDM+S and a value of $\tan\beta$ are chosen, the branching fractions of the pseudoscalar boson to any SM particle can be determined univocally for any mass m_a. Assuming that the production cross section for the h boson is the same as predicted in the SM, this analysis is sensitive to $\mathcal{B}(h \to aa) < 1$ values at large $\tan\beta$ ($\tan\beta > 1.8$) in 2HDM+S type-3, and small $\tan\beta$ ($\tan\beta < 0.5$) in 2HDM+S type-4, as illustrated in Fig. 11.16. It is however not sensitive to branching fractions less than unity for any $\tan\beta$ in 2HDM+S type-1 and type-2.

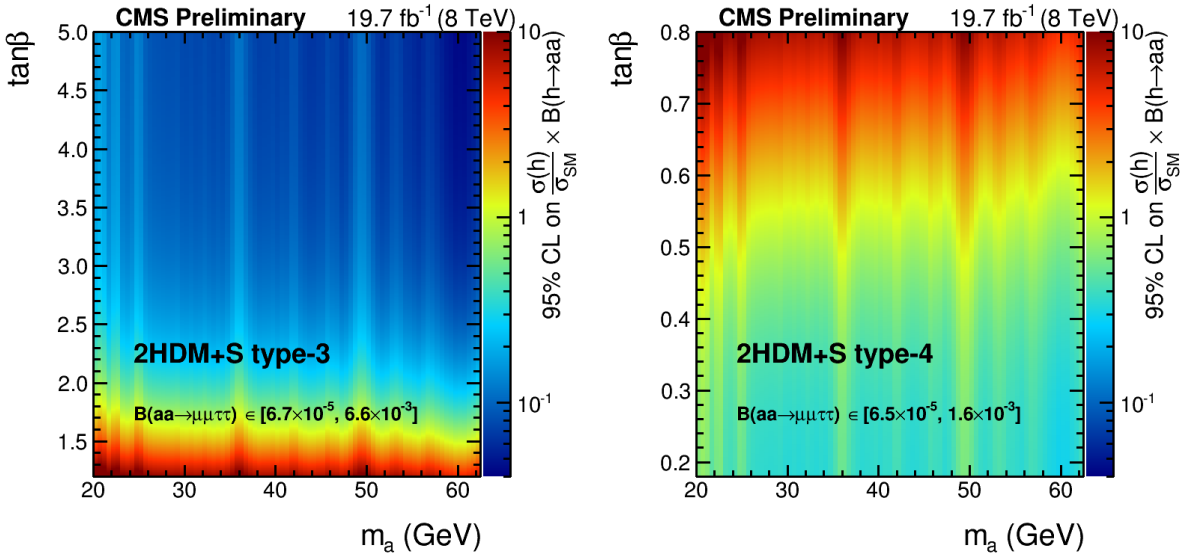

Figure 11.16: Observed upper limits at 95% CL on $\frac{\sigma(h)}{\sigma_{SM}} \times \mathcal{B}(h \to aa)$ for the combination of all di-tau final states, in 2HDM+S type-3 (left) and type-4 (right). [129]

11.6 Interpretation and comparison with other CMS searches

A large variety of exotic h decays is allowed in 2HDM+S, with little indirect constrains from other CMS measurements. It is therefore a favored model to compare the reach of different exotic h decay searches. Five decay modes with two light pseudoscalar bosons have been studied with the data collected by CMS in Run-1:

1. $h \to aa \to \mu\mu\tau\tau$, $20 < m_a < 62.5$ GeV [129]. It is the analysis described at length

in this chapter.

2. $h \to aa \to \mu\mu bb$, $20 < m_a < 70$ GeV [134]. This analysis is pretty similar to the first one, but suffers from larger backgrounds because of the difficulty to identify b jets.
3. $h \to aa \to \tau\tau\tau\tau$, $5 < m_a < 9$ GeV [135]. Because of the low pseudoscalar mass, the di-tau pairs are boosted, and special boosted reconstruction techniques have been used.
4. $h \to aa \to \tau\tau\tau\tau$, $5 < m_a < 15$ GeV [136]. Even if the final state is the same as in the previous analysis, different boosted reconstruction techniques are used, and this analysis particularly targets the Wh associated production mode.
5. $h \to aa \to \mu\mu\mu\mu$, $0.25 < m_a < 3$ GeV [137]. Apart from its reach in 2HDM+S, this analysis is also interpreted in dark SUSY models. A similar analysis has also been published by the ATLAS Collaboration [138].

In 2HDM+S, the pseudoscalar a inherits its couplings to fermions from the SM-like scalar, while it cannot decay to gauge bosons. The branching fractions of the a boson depend on the type of 2HDM+S, and on the value of $\tan\beta$, the ratio between the vacuum expectation values of the two scalar doublets. The formulae presented in Section 1.3.3 still apply, with some notable differences due to the pseudoscalar nature of the boson and to the presence of a second doublet [18, 52].

The partial decay width of the pseudoscalar to fermions reads:

$$\Gamma(a \to f\bar{f}) = \frac{N_c G_F}{4\sqrt{2}\pi} g_{af\bar{f}}^2 m_a m_f^2 \sqrt{1 - \frac{4m_f^2}{m_a^2}}, \tag{11.7}$$

where the differences with the SM case lie in the power of the last term (1 for a pseudoscalar, 3 for a scalar), and in the scaling by the square of $g_{af\bar{f}}$, which multiplies the coupling from the SM, depends on $\tan\beta$ and is given in Tab. 2.2 for all types of 2HDM. It can be noticed that, for two different kinds of leptons, the ratio of the branching fractions is simply the ratio of their squared masses when $m_a \gg 2m_f$, for example:

$$\frac{\mathcal{B}(a \to \mu\mu)}{\mathcal{B}(h \to \tau\tau)} \simeq \frac{m_\mu^2}{m_\tau^2}. \tag{11.8}$$

In the case of decays to quarks, the previous formula still holds with $N_C = 3$ and specific QCD corrections, amounting to about 20%. The QCD corrections can be decomposed in two terms: Δ_{qq} and Δ_a^2, with

$$\Delta_{qq} = 5.67\frac{\bar{\alpha}_S}{\pi} + (35.94 - 1.35N_f)\left(\frac{\bar{\alpha}_S}{\pi}\right)^2, \tag{11.9}$$

$$\Delta_a^2 = \frac{\bar{\alpha}_S^2}{\pi^2}\left(3.83 - \log\frac{m_a^2}{m_t^2} + \frac{1}{6}\log^2\frac{\bar{m_q^2}}{m_a^2}\right). \tag{11.10}$$

The symbol $\bar{\alpha}_S$ indicates the running of the strong coupling constant at the renormalization scale m_a, and $\bar{m}_q$ is the running of the quark mass in the modified minimal subtraction ($\overline{\text{MS}}$) scheme [139–141] at the same renormalization scale. In 2HDM+S type-1 and type-2, when neglecting the QCD correction terms, and for pseudoscalar boson masses large compared to twice the b quark mass, the ratio between the branching fractions of the pseudoscalar to b quarks and to tau leptons is given by:

$$\frac{\mathcal{B}(a \to bb)}{\mathcal{B}(h \to \tau\tau)} \simeq 3\frac{m_b^2}{m_\tau^2}, \tag{11.11}$$

where the factor 3 comes from the number of colors.

The partial decay width to a photon pair via b- or t-quark loops [3], is given by:

$$\Gamma(a \to \gamma\gamma) = \frac{G_F \alpha^2 m_a^3}{128\sqrt{2}\pi^3} \left| \sum_f N_c q_f^2 g_{af\bar{f}} A_{1/2}^a \left(\frac{m_a^2}{4m_f^2} \right) \right|^2, \tag{11.12}$$

where q_f is the electric charge relative to that of the electron. The form factor $A_{1/2}^a$ is simply given by:

$$A_{1/2}^a(x) = 2x^{-1} f(x), \tag{11.13}$$

with

$$f(x) = \begin{cases} \arcsin^2 \sqrt{x}, \text{ if } x \leq 1; \\ -\frac{1}{4}\left(\log \frac{1+\sqrt{1-1/x}}{1-\sqrt{1-1/x}} - i\pi \right)^2 \text{ otherwise.} \end{cases} \tag{11.14}$$

There is no QCD correction to take into account.

Finally, the partial decay width to a pair of gluons, through c-, b- or t-quark loops is:

$$\Gamma(a \to gg) = \frac{G_F \bar{\alpha}_S^2 m_a^3}{36\sqrt{2}\pi^3} \left| \sum_{q=t,b,c} g_{aqq} A_{1/2}^a \left(\frac{m_a^2}{4m_q^2} \right) \right|^2 \left(1 + \left(\frac{97}{4} - \frac{7}{6} N_f \right) \frac{\bar{\alpha}_S}{\pi} \right). \tag{11.15}$$

The NLO corrections in the last term are computed with the renormalization scale of the strong coupling constant equal to the pseudoscalar mass.

The branching fraction for each decay can be obtained by dividing the partial decay width over the total decay width. Fig. 11.17 shows the branching fractions of the pseudoscalar a to SM particles, in the four types of 2HDM+S, for different values of $\tan\beta$.

The largest branching fraction for the $\mu\mu\tau\tau$ final state, $\mathcal{B}(aa \to \mu\mu\tau\tau)$, is obtained for large $\tan\beta$ values in 2HDM+S type-3, where the decays to leptons are enhanced over the decays to quarks. The largest $\mathcal{B}(aa \to \mu\mu bb)$ is also obtained in 2HDM+S type-3, but for $\tan\beta \simeq 2$: it is the best compromise between the enhancement of the couplings

3. Unlike the SM case, there is no contribution from W loops because of the pseudoscalar nature of a.

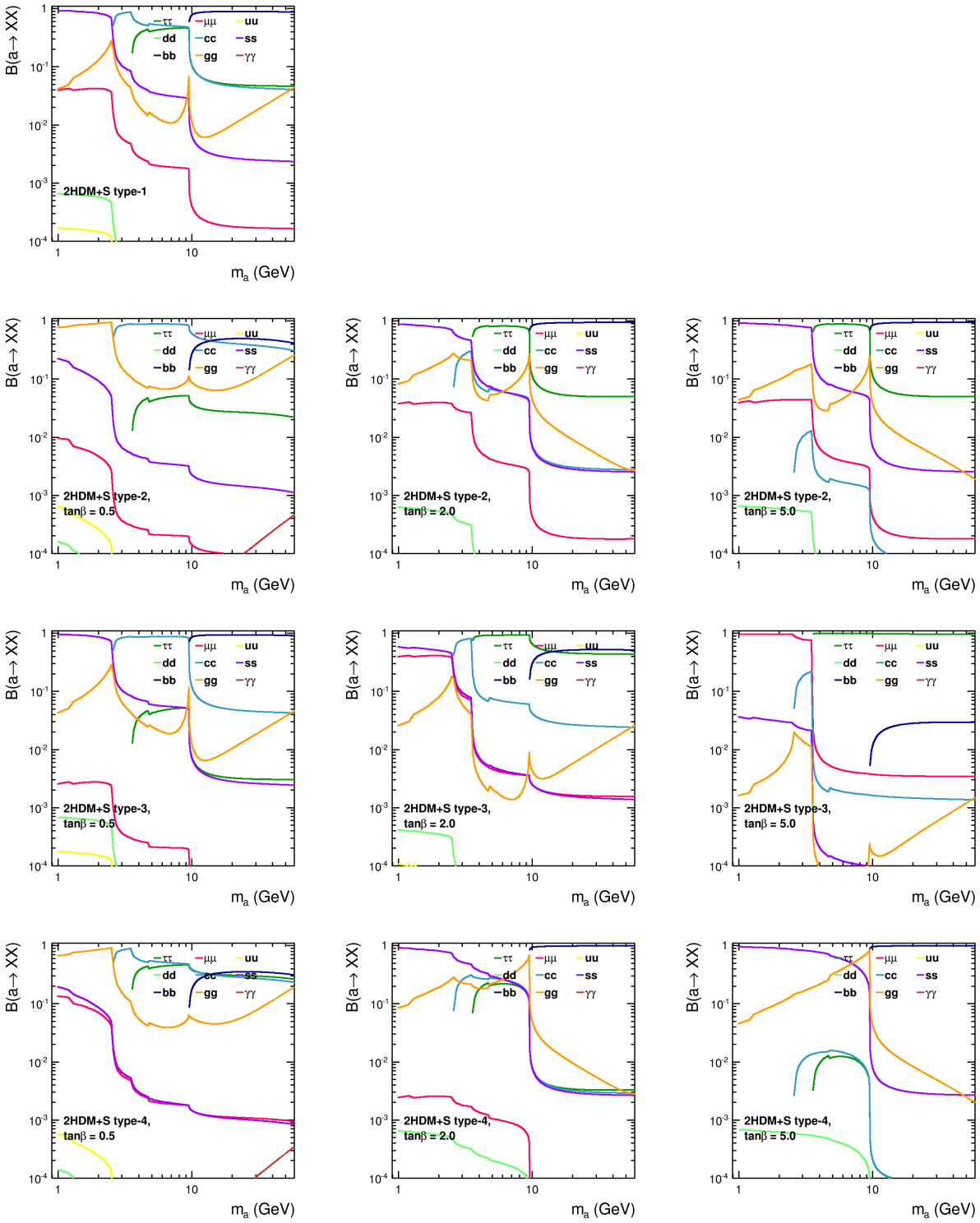

Figure 11.17: Branching fractions of the pseudoscalar boson a to SM particles for different types of 2HDM+S and different $\tan\beta$ values. There is no $\tan\beta$ dependence in 2HDM+S type-1. The calculations in the [3,5] and [9,11] GeV mass ranges are most likely invalid due to decays to quarkonia.

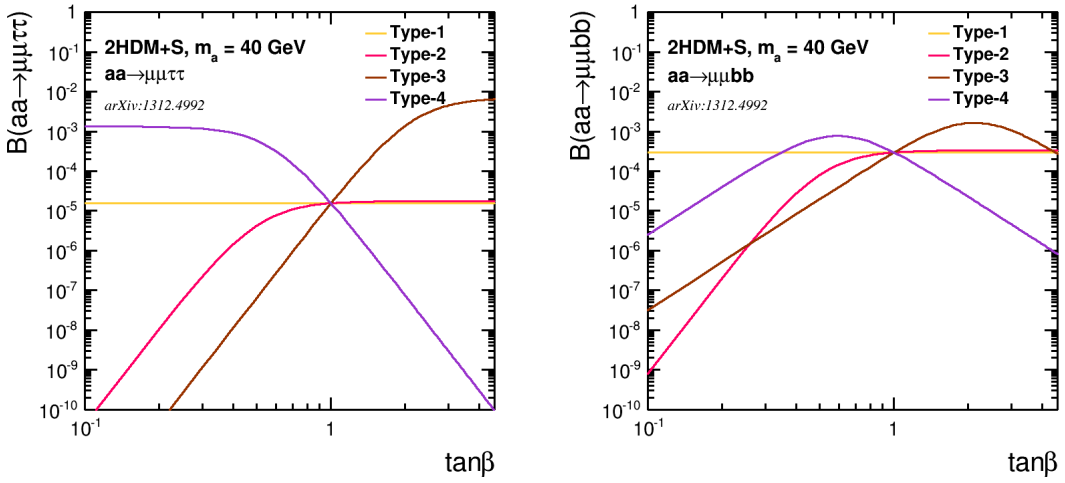

Figure 11.18: Branching fractions of a pair of a bosons to $\mu\mu\tau\tau$ (left) and $\mu\mu bb$ (right) as a function of $\tan\beta$, in the four types of 2HDM+S without tree-level FCNC.

to leptons and the reduction of the couplings to quarks. The branching fractions to both final states are shown in Fig. 11.18 for a pseudoscalar with a mass of 40 GeV as a function of $\tan\beta$ in all four types of 2HDM+S without tree-level FCNC. The interplay between the $h \to aa \to \mu\mu bb$ and $h \to aa \to \mu\mu\tau\tau$ analyses in type-3 and type-4 is shown in Fig. 11.19: $h \to aa \to \mu\mu\tau\tau$ is more sensitive in type-3 for $\tan\beta \geq 1.8$ and in type-4 for $\tan\beta \leq 0.5$.

In 2HDM+S type-1 and type-2, the ratio between the branching fractions of the pseudoscalar to down-type quarks and to leptons does not depend on $\tan\beta$. The results of all analyses can therefore be rescaled to limits on $(\sigma(h)/\sigma_{SM}) \times \mathcal{B}(h \to aa) \times \mathcal{B}(a \to \tau\tau)^2$, or equivalently on $(\sigma(h)/\sigma_{SM}) \times \mathcal{B}(h \to aa) \times \mathcal{B}(a \to \mu\mu)^2$, as shown in Fig. 11.20. In type-3 and type-4 however, down-type quarks and leptons do not couple to the same scalar doublet, and the ratio between their branching fractions depends on $\tan\beta$.

The branching fractions of the pseudoscalar boson to muons and taus hugely depend on the pseudoscalar mass; and more intuitive limits can be set on $(\sigma(h)/\sigma_{SM}) \times \mathcal{B}(h \to aa)$. This requires to make a hypothesis both on the model and on $\tan\beta$. The results are shown for three $\tan\beta$ values in every type of 2HDM+S in Fig. 11.21.

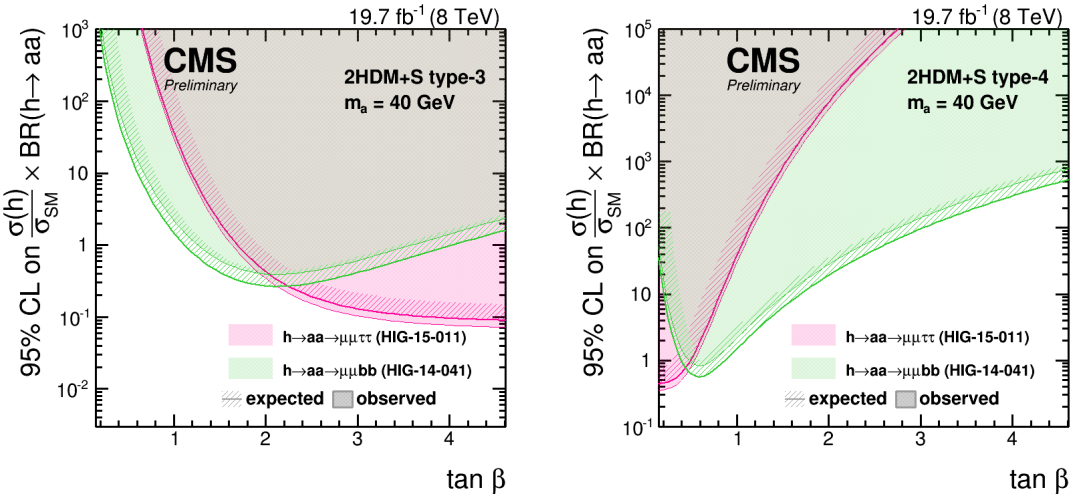

Figure 11.19: Comparison between the reach of the $h \to aa \to \mu\mu bb$ and $h \to aa \to \mu\mu\tau\tau$ as a function of $\tan\beta$ for a pseudoscalar mass of 40 GeV, in 2HDM/S type-3 (left) and type-4 (right).

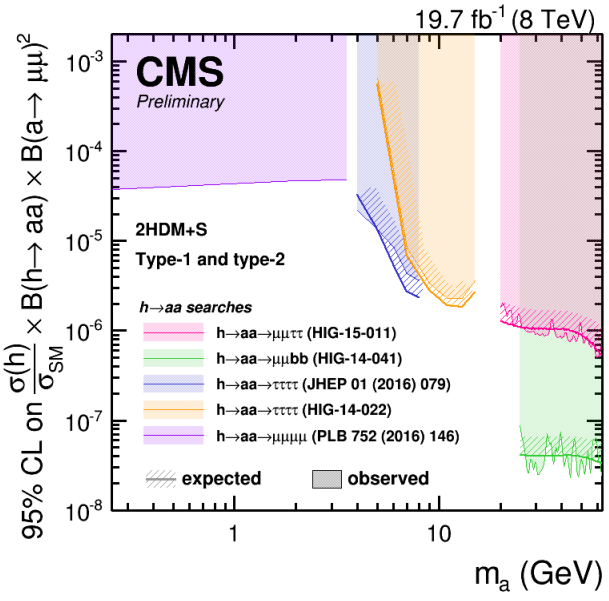

Figure 11.20: Comparison between the different analyses $h \to aa$ searches performed in Run-1 with the CMS detector, in 2HDM+S type-1 and type-2. The white areas between 3.55 and 5 GeV, and between 15 and 20 GeV, correspond to mass regions where no analysis was performed.

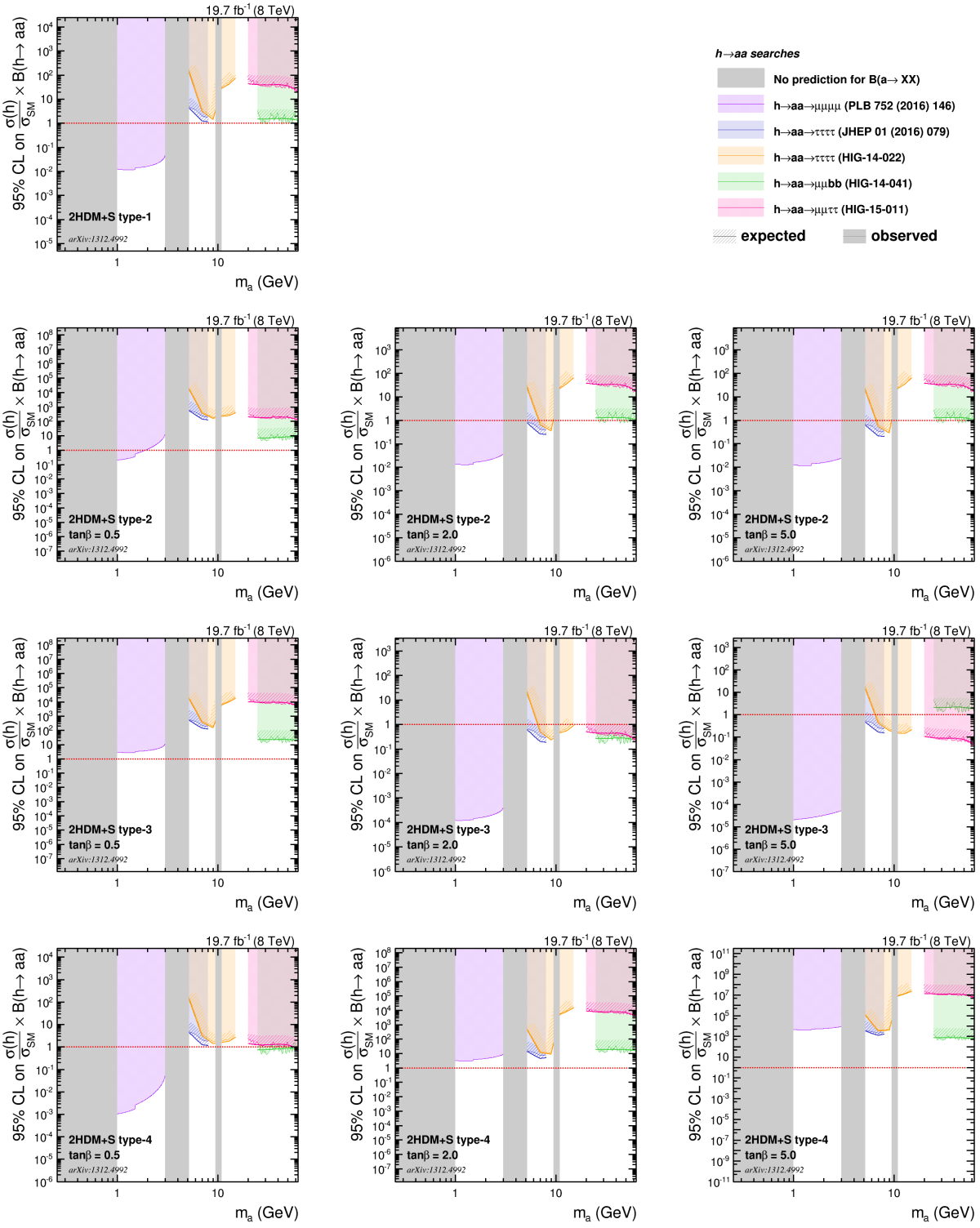

Figure 11.21: Comparison between the different analyses in 2HDM+S type-1 (first row), type-2 (second row), type-3 (third row), and type-4 (fourth row), for $\tan\beta = 0.5$ (left), $\tan\beta = 2.0$ (center) and $\tan\beta = 5.0$ (right) in terms of 95% CL limits on $(\sigma(h)/\sigma_{SM}) \times \mathcal{B}(h \to aa)$.

11.7 Chapter summary and personal contributions

Search for exotic decays of the SM-like scalar in the $\mu\mu\tau\tau$ final state

The existence of exotic decays of the 125-GeV boson is still allowed with relatively large branching fractions by the precision measurements on this 125-GeV state. This chapter presents a search for the $h \to aa \to \mu\mu\tau\tau$ decay, which is particularly enhanced at large $\tan\beta$ in 2HDM+S type-3. The observable is the invariant mass of the two muons, and given its excellent resolution, an unbinned shape analysis is performed. No excess is observed over the tiny predicted SM backgrounds, and exclusion limits can be set. Branching fractions of the h boson to a pair of light pseudoscalar a bosons as low as 4% can be excluded, in 2HDM+S type-3 with large $\tan\beta$. The performance of this analysis is then compared with those of the other exotic h decay searches performed with the CMS detector in Run-1, in the four different types of 2HDM+S without FCNC.

My contributions

Figures: 11.1-11.21.
I have produced all the results of the $h \to aa \to \mu\mu\tau\tau$ search presented in this chapter, and have made the summary plots combining the five different searches for exotic h decays performed with the data collected by CMS in Run-1.

Chapter 12

Search for a light pseudoscalar decaying to taus

In some particular scenarios of 2HDM type-2, light pseudoscalar A bosons can be produced in association with b jets with a large cross section accessible with LHC Run-1 data, as explained in Section 2.2.3. This low mass region, below the Z boson mass, has been barely explored at the LHC, unlike the high mass region where many analyses test various hypotheses. A difficulty in analyzing such a mass region is that the final state leptons typically have low transverse momenta and do not pass the trigger thresholds. In this chapter, we study the $bbA \to bb\tau\tau$ process, as published in [142]. Whereas the $bbA \to bb\mu\mu$ process is more easily accessible because of the efficient identification and triggering of muons, the branching ratio of the A boson to muons is more than two orders of magnitude lower than its branching fraction to taus.

12.1 Analysis overview

The Feynman diagram of the signal process considered in this analysis is shown in Fig. 12.1. Three di-tau final states among the six possible ones are studied: $\tau_e\tau_\mu$, $\tau_\mu\tau_h$ and $\tau_e\tau_h$. The $\tau_e\tau_e$ and $\tau_\mu\tau_\mu$ final states are discarded because of their low branching fractions and of the large backgrounds, while the trigger thresholds in the $\tau_h\tau_h$ final state are too high (45 GeV per hadronic tau) to study a light resonance.

Signal samples are generated with Pythia, for pseudoscalar masses between 25 and 80 GeV. Because the selection efficiency is low given the low average transverse momentum of final state leptons, all events are generated with at least one lepton with p_T greater than 15 GeV, and a reweighting is performed to account for the generator level efficiency. The Drell-Yan, W+jets, $t\bar{t}$ (fully leptonic, semi leptonic and fully hadronic) and diboson (WW, WZ and ZZ) processes are also generated with Madgraph. Finally, single top and SM H boson processes are generated with Powheg. The W+jets and Z+jets samples are produced inclusively, and exclusively for different numbers of generated jets. This permits to increase the selection efficiency for these important processes with large cross sections,

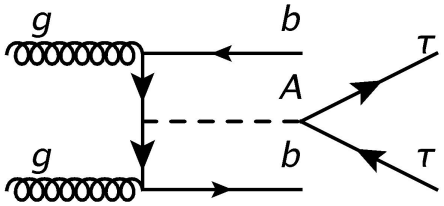

Figure 12.1: Feynman diagram for the production of a light pseudoscalar with a pair of b quarks, and decaying to taus.

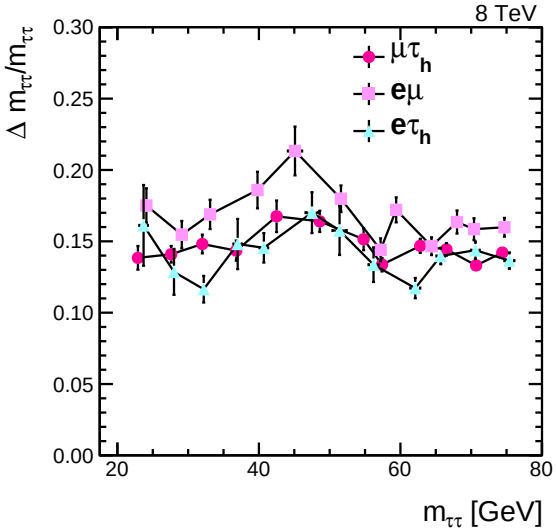

Figure 12.2: Measured masses and mass resolutions obtained with the SVfit algorithm in the three final states studied in the analysis, for signal samples with generated A boson masses between 25 and 80 GeV with 5 GeV steps. The resolution in the $e\mu$ final state is a few percent worse because of the presence of one additional neutrino in the final state.

and to obtain more precise templates. The different samples can be combined with the stitching technique. The $Z/\gamma^* \to 2\ell$ samples are further divided into two mass regions: $m_{\ell\ell} > 50$ GeV and $10 < m_{\ell\ell} < 50$ GeV. It has been checked that both mass regions can be joined smoothly. The data have been collected in 2012 at 8 TeV center-of-mass energy, and amount to 19.7 fb^{-1} integrated luminosity. A summary of the MC processes with their cross sections, as well as the collected datasets, can be found in Appendix A.

A binned analysis is performed, using the full di-tau invariant mass $m_{\tau\tau}$ as observable, and upper limits on the cross section times branching fraction are set with the asymptotic CL_s method. The SVfit algorithm is seen to perform well for low mass resonances, and a mass resolution of about 15% is obtained for all final states and all masses between 25 and 80 GeV, as shown in Fig. 12.2.

12.2 Selection

A vertex with at least four degrees of freedom is required in the event, with a position with respect to the beam interaction such that $-24 < z < 24$ cm and $|r| < 2$ cm. If there are more than one vertex satisfying these conditions, the one with the highest scalar p_T sum of the tracks is chosen as the vertex of the hard-scatter interaction. In all final states, the events are required to have at least one jet with $p_T > 20$ GeV, $|\eta| < 2.4$ and passing the medium CSV b-tagging working point. The next sections describe the selection criteria specific to the three different di-tau final states.

12.2.1 $\tau_e\tau_\mu$ final state

The events in the $\tau_e\tau_\mu$ di-tau final state have to fire a trigger path that requires at HLT level a muon and an electron with p_T greater than 8 and 17 GeV respectively for the leading and subleading lepton. At analysis level, the p_T requirements are chosen such that the trigger efficiency is close to the plateau, and either a muon with p_T greater than 10 GeV and an electron with p_T greater than 20 GeV, or a muon with p_T greater than 18 GeV and an electron with p_T greater than 10 GeV are required. The 2 GeV difference between the leading electron and muon criteria comes from the slower trigger efficiency turn-on for electrons. The pseudorapidity conditions on the leptons also come from trigger constrains and are $|\eta| < 2.3$ for muons and $|\eta| < 2.1$ for electrons. In addition, the selected objects are required to correspond within $\Delta R < 0.5$ to the objects that fired the trigger paths.

The electron and the muon are required to be isolated, with relative isolation less than 0.15 in the endcaps ($|\eta| > 1.479$) and 0.10 in the barrel ($|\eta| < 1.479$). The electron should pass the conversion veto and the loose MVA identification, while the muon should be tightly identified. The $|d_z|$ and d_{xy} parameters are required to be less than 0.2 and 0.02 cm respectively for both leptons. The electron and the muon need to carry an opposite-sign charge, and to be separated by at least $\Delta R = 0.5$.

In order to reduce the backgrounds from Drell-Yan or diboson productions, events that have more than one isolated and identified electron and muon are vetoed. In particular, the extra electrons are selected with the following characteristics:

- $p_T > 10$ GeV, $|\eta| < 2.5$;
- $d_{xy} < 0.045$ cm, $|d_z| < 0.2$ cm;
- relative isolation less than 0.3;
- loose MVA identification and conversion veto,

while extra muons pass the following conditions:

- $p_T > 10$ GeV, $|\eta| < 2.4$;
- $d_{xy} < 0.045$ cm, $|d_z| < 0.2$ cm;
- relative isolation less than 0.3;
- tight PF identification.

The $t\bar{t}$ contribution is reduced by selecting events with P_ζ, defined in Chapter 6, greater than -40 GeV. In addition, the transverse mass between the dilepton system and the $\vec{\not{E}}_T$

is required to be less than 25 GeV; this further reduces the $t\bar{t}$ contribution and removes a large fraction of electroweak backgrounds. Over the probed mass range, the expected upper limits on the signal cross section times branching fraction improve by 40-55% by applying the P_ζ selection, and by 8-20% by additionally applying the transverse mass selection; the largest improvement is seen at low m_A.

12.2.2 $\tau_\mu\tau_h$ final state

The trigger path used to select events in the $\tau_\mu\tau_h$ final state requires at HLT a muon with p_T greater than 17 GeV and a hadronic tau with p_T greater than 20 GeV. At analysis level, a muon with p_T greater than 18 GeV and $|\eta|$ less than 2.1, and well as a tau with p_T greater than 22 GeV and $|\eta|$ less than 2.3, are required. The reconstructed objects should correspond to the objects that fired the trigger paths within $\Delta R < 0.5$. The muon should pass the tight PF identification, and have a relative isolation less than 0.1. Its d_{xy} and its $|d_z|$ are required to be less than 0.045 and 0.2 cm respectively. The hadronic tau should pass the decay mode finding discriminator, the tight MVA identification including lifetime information, the loose cut-based rejection against electrons, as well as the medium MVA rejection against muons. Both leptons are required to carry an opposite-sign charge and to be separated by at least $\Delta R = 0.5$.

To remove contributions from $Z/\gamma^* \to \mu\mu$ events, the events are vetoed if they contain a second muon that has an opposite-sign charge compared to the selected muon, and with a relative isolation less than 0.3, $p_T > 15$ GeV, $|\eta| < 2.4$, $|d_z| < 0.2$ cm, separated from the tau candidate by at least $\Delta R = 0.15$, and being identified as a global, PF and tracker muon. In a more general way, all events that have an electron ($p_T > 10$ GeV, $|\eta| < 2.5$, loose MVA identification, relative isolation less than 0.3, $|d_z| < 0.2$ cm, separated from the muon and tau candidates by at least $\Delta R = 0.15$) or a second muon ($p_T > 10$ GeV, $|\eta| < 2.4$, tight PF identification, relative isolation less than 0.3, $|d_z| < 0.2$ cm, separated from the muon and tau candidates by at least $\Delta R = 0.15$) on top of the already selected muon and tau candidates are vetoed. The contribution from W+jets and $t\bar{t}$ events is reduced by requiring the transverse mass between the muon and $\vec{\not{E}}_T$ less than 30 GeV.

12.2.3 $\tau_e\tau_h$ final state

At HLT level, an electron with transverse momentum greater than 22 GeV and a hadronic tau with transverse momentum greater than 20 GeV are required. Offline, the events are selected with an electron with $p_T > 24$ GeV and $|\eta| < 2.1$ and a hadronic tau with $p_T > 22$ GeV and $|\eta| < 2.3$. The electron is required to pass the tight MVA identification, and to have a relative isolation less than 0.1, whereas the hadronic tau passes the decay mode finding discriminator, the tight MVA isolation including lifetime information, the medium MVA discriminator against electrons as well as the loose cut-based discriminator against muons. Both candidates have $|d_z| < 0.2$ cm, and are matched to trigger level objects. Moreover, the electron and the tau have an opposite-sign charge and are separated from each other by at least $\Delta R = 0.5$.

Extra lepton vetoes are applied to reduce the contribution from Drell-Yan and multi-lepton processes. Any event with an additional electron ($p_T > 10$ GeV, $|\eta| < 2.5$, loose MVA identification, relative isolation less than 0.3, $|d_z| < 0.2$ cm, separated from the electron and tau candidates by at least $\Delta R = 0.15$) or muon ($p_T > 10$ GeV, $|\eta| < 2.4$, tight PF identification, relative isolation less than 0.3, $|d_z| < 0.2$ cm, separated from the electron and tau candidates by at least $\Delta R = 0.15$) is discarded. To reject more specifically the $Z/\gamma^* \to ee$ background, the events are also not selected if they contain a second electron that has an opposite-sign charge to the other electron, and has the following characteristics: $p_T > 15$ GeV, $|\eta| < 2.4$, tight MVA-based identification, relative isolation less than 0.3, $|d_z| < 0.2$ cm, separated from the electron and tau candidates by at least $\Delta R = 0.15$. The contribution from W+jets and $t\bar{t}$ backgrounds is reduced by requiring the transverse mass between the electron and $\vec{\not{E}}_T$ to be below 30 GeV.

12.3 Background estimation

12.3.1 $Z/\gamma^* \to \tau\tau$

The $Z/\gamma^* \to \tau\tau$ process is a major irreducible background, and it is therefore crucial to estimate it correctly. To do so, so-called embedded samples are used [143]. They are produced from $Z/\gamma^* \to \mu\mu$ observed events collected with a muon trigger. The reconstructed muons are replaced by simulated taus that are subsequently decayed with Tauola, and polarization effects are modeled with TauSpinner [144]. The detector response to the tau decay products is modeled via Geant. Jets, $\not{E}_T$, and hadronic taus are then reconstructed with the PF algorithm, while lepton isolations are recomputed given the new set of particles. Embedded samples based on the full collected data are generated for every di-tau final state. Such a method implies that most event properties, for example the $\not{E}_T$ or the jet characteristics, are directly taken from data and do not suffer from modeling uncertainties. The normalization is taken from the MC simulation for the selection without any requirement on the number of b jets, and a scale factor derived from the embedded samples is applied to account for the differences in the selection. Because $t\bar{t} \to WbWb \to \mu\nu b\mu\nu b$ events contaminate the di-muon events selected in data, embedded $t\bar{t}$ samples generated from MC samples are also produced, and subtracted from the embedded $Z/\gamma^* \to \tau\tau$ after reweighting. Generally, the contribution from $t\bar{t}$ events is low, but it can become significant if b jets are required in the selection. In addition, the $m_{\tau\tau}$ distributions of the $t\bar{t}$ and Drell-Yan samples are extremely different, and the $t\bar{t}$ process becomes proportionally more important in the $m_{\tau\tau}$ tails, where searches are performed.

Embedded samples are produced for invariant masses of the leptons greater than 50 GeV, while MC samples are used to model $Z/\gamma^* \to \tau\tau$ events with $m_{\ell\ell}$ below 50 GeV. More precise distributions are obtained for the MC samples by relaxing the b-tagging CSV working point.

12.3.2 $Z/\gamma^* \to \mu\mu/ee$

These processes contribute essentially to the $\mu\tau_h$ and $e\tau_h$ final states, when one of the light leptons is misidentified as a hadronic tau. Because the $e \to \tau_h$ and even more so the $\mu \to \tau_h$ misidentification rates are low, these processes represent only a small contribution to the total background. They are entirely estimated from MC samples.

12.3.3 W+jets

The W+jets background is composed of events where a jet is misidentified as a hadronic tau ($e\tau_h$ and $\mu\tau_h$ final states) or as a light lepton ($e\mu$ final state). It is estimated with different methods depending on the final state.

In the $e\tau_h$ and $\mu\tau_h$ final states, this background is strongly reduced by requiring the transverse mass between the light lepton and the $\vec{\not{E}}_T$ to be less than 30 GeV. While its distribution comes from MC samples, its normalization is estimated directly from observed data. In the region where the transverse mass is greater than 70 GeV, the W+jets process is by far the dominant background, and a scale factor can be estimated in such a way as the normalization of the MC sample corresponds to the number of observed events, from which the other small background contributions, estimated from MC samples, have been subtracted. The scale factor measured in the high m_T region is then applied to the MC simulation in the low m_T signal region. As the tau p_T distribution is seen to differ in MC simulations and data, an event-by-event correction that accounts for the differences between data and MC simulations in the energy scale of hadronic taus arising from $j \to \tau_h$ misidentification is applied. It is measured in a control region with $m_T > 50$ GeV, and depends on the transverse momentum of the hadronic tau in the MC sample. The weight w can be expressed as a function of the hadronic tau p_T as:

$$w = 0.79 - 0.15.x - 0.03.x^2 - 0.08.x^3, \tag{12.1}$$

$$\text{where } x = (p_T/\text{GeV} - 149.83)/100. \tag{12.2}$$

In the $e\mu$ final state, all backgrounds that have at least one jet misidentified as a muon or an electron are estimated together with a data-driven method, which is explained in the next section.

12.3.4 QCD multijet

The QCD multijet background is an important event contribution in the low di-tau mass region. It arises from jets misidentified as hadronic taus, muons or electrons, and from real light leptons from the semi-leptonic decays of jets from heavy flavor quarks. The QCD multijet background is estimated with data-driven methods that depend on the final state.

In the $e\tau_h$ and $\mu\tau_h$ final states, the normalization of the QCD multijet background is obtained from a same-sign (SS) charge region, where the charge requirement on the two leptons has been inverted. The contribution from other processes, such as W+jets or $t\bar{t}$ production, is estimated from MC simulations and subtracted from the observed data, which gives the QCD multijet $m_{\tau\tau}$ distribution. The normalization of this process is not necessarily the same in the SS and opposite-sign (OS) regions, and a scale factor to extrapolate the SS normalization to the OS normalization is needed. It is measured in data, by taking the ratio between OS and SS events with inverted light lepton isolation and hadronic taus passing the very loose working point of the MVA isolation instead of the tight one. The relaxation of the tau isolation and the inversion of the light lepton isolation permit to obtain a signal-free QCD-enriched region, from which the tiny contributions from other processes are subtracted. The ratio is measured as a function of the di-tau mass as some dependence is observed, and is applied to events in the isolated SS region to extract the QCD multijet normalization in the signal region.

The $m_{\tau\tau}$ distribution of the QCD multijet background in the $e\tau_h$ and $\mu\tau_h$ final states is also taken from an SS region. Compared to the signal region, the tau isolation is relaxed to the loose MVA working point instead of the tight one to obtain more populated templates, and the muon isolation is required to lie between 0.2 and 0.5 to remove the W+jets contribution. A bias in the $m_{\tau\tau}$ distribution of the QCD multijet template is introduced by relaxing the tau isolation; this is corrected by applying an event-by-event weight that represents the probability for a hadronic tau that has passed the very loose MVA-based isolation to pass the tight working point. This weight is measured in three different pseudorapidity regions, as a function of the tau transverse momentum. Additionally, the bias introduced by selecting events in the SS region instead of the OS one is corrected with the same $m_{\tau\tau}$-dependent weight derived to extract the QCD multijet normalization. Fig. 12.3 shows a schematic summary of how the QCD multijet normalization and $m_{\tau\tau}$ distribution are estimated in the $e\tau_h$ and $\mu\tau_h$ final states.

In the $e\mu$ final state, all processes where at least one jet is misidentified as one of the light leptons, are estimated together with a method that relies on the $j \to e$ and $j \to \mu$ misidentification rates. The probability for loosely preselected, or so-called "fakeable", leptons to pass the full lepton identification and isolation as required in the signal region are measured in signal-free regions. Fakeable electrons have the following characteristics: GSF candidate, $p_T > 10$ GeV, $|\eta| < 2.3$, $d_{xy} < 0.2$ cm, $|d_z| < 0.1$ cm, conversion veto, transverse shower shape parameter $\sigma_{i\eta i\eta} < 0.01(0.01)$ in the barrel (endcaps), $|\Delta\phi_{in}| < 0.15(0.10)$ in the barrel (endcaps), $|\Delta\eta_{in}| < 0.007(0.009)$ in the barrel (endcaps), and relative track, electromagnetic and HCAL isolations all less than 0.2. Meanwhile fakeable muons are selected as global muons with $p_T > 10$ GeV, $|\eta| < 2.1$ and $d_{xy} < 0.2$ cm. If the muon transverse momentum is greater than 20 GeV, the fakeable candidate is required to have its relative track, electromagnetic and HCAL isolations all less than 0.4; otherwise its absolute track, electromagnetic and HCAL isolations should all be less than 8 GeV. The complete signal selection is applied to data events with fakeable electrons and muons,

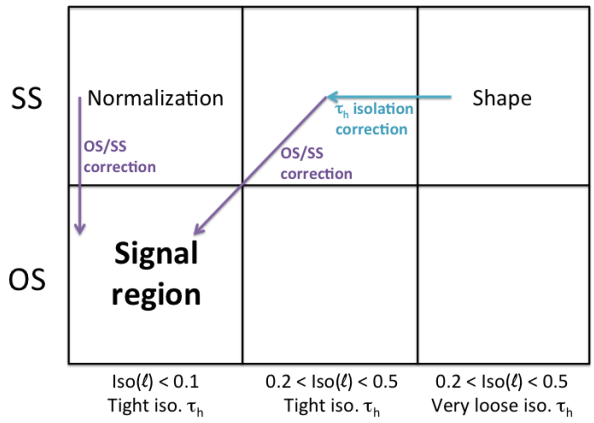

Figure 12.3: Schematic overview of the QCD multijet background estimation in the $e\tau_h$ and $\mu\tau_h$ final states.

and the events are divided into three categories:

- N_{ff}: The fakeable electron and the fakeable muon both fail the lepton identification or isolation requirements. These events are weighted by $w = \frac{f_e f_\mu}{(1-f_e)(1-f_\mu)}$.
- N_{pf}: The fakeable electron passes the full electron requirements but the fakeable muon fail the identification or isolation criteria. These events are weighted by $w = \frac{f_\mu}{1-f_\mu}$.
- N_{fp}: The fakeable muon passes the full muon requirements but the fakeable electron fail the identification or isolation criteria. These events are weighted by $w = \frac{f_e}{1-f_e}$.

In order to remove double-counted events, which have both a misidentified muon and a misidentified electron, the normalization of the reducible background is estimated with a weighted combination of the three categories: $N_{pf} + N_{fp} - N_{ff}$. The contamination from events with real leptons is estimated to 17% and the yield of the reducible background estimated with the misidentification rate method is reduced by this amount.

12.3.5 $t\bar{t}$ production

The top quark pair production is another large irreducible background, which contributes over the entire di-tau mass range. This contribution is particularly important because of the b jet requirement in the selection of all channels. The $t\bar{t}$ process is estimated from MC samples, and reweighted to the cross section measured in a $t\bar{t}$-enriched region in data, obtained by selecting events with an electron, a muon and two b jets. Because the distributions of the top quark transverse momentum differ in data and MC samples, a weight is assigned event-by-event to correct the MC distribution.

12.3.6 Other backgrounds

Single top and diboson backgrounds are only a small fraction of the background, and are fully estimated from MC samples and scaled to their NLO cross section [118]. The contribution from the SM-like scalar with a mass of 125 GeV is taken into account in all its dominant production modes. The $H \to WW$ decay mainly contributes in the $e\mu$ final state.

12.3.7 Control distributions

The agreement between data and predicted backgrounds is shown for a set of variables in Fig. 12.4 for the $e\mu$ final state, and in Fig. 12.5 for the other two final states.

12.4 Systematic uncertainties

The systematic uncertainties considered in this analysis are detailed in Tab. 12.4.

The uncertainties on the lepton trigger, identification and isolation efficiencies are treated together, and amount to 2% per muon, 2% per electron and 8% per hadronic tau. Because some hadronic taus are selected with p_T in trigger turn-on efficiency curves, a shape uncertainty consisting in the difference between the measured and plateau efficiencies is considered for low p_T taus. All processes estimated from MC simulations are affected by a 2.6% uncertainty related to the luminosity measurement [109]

The $Z/\gamma^* \to ee$ and $Z/\gamma^* \to \mu\mu$ processes are attributed a 30% uncertainty related to the $e \to \tau_h$ and $\mu \to \tau_h$ misidentification rates respectively, while all Drell-Yan events with $m_{\ell\ell} > 50$ GeV have a 3% uncertainty related to the theoretical predicted cross section [146]. A 10% uncertainty is considered for the low mass Drell-Yan events. The other processes also have normalization uncertainties: 15% for the diboson production theoretical cross section, 10% for the measured $t\bar{t}$ cross section, 30% for the reducible background in $e\mu$ related to the misidentification rate method, 30% for the $h \to \tau\tau$ process because of the uncertainty on the measured signal strength, 20% for the QCD multijet because of the uncertainties on the OS/SS and misidentification rate functions, and finally 30% for the W+jets background in the $e\tau_h$ and $\mu\tau_h$ final states due to the propagation of the $\not\!\!E_T$ uncertainties to the scale factor measured in the high-m_T region.

Shape uncertainties include the uncertainties on the electron and tau energy scales, and on the $t\bar{t}$ p_T reweighting. Bin-by-bin uncertainties are considered for all processes to account for the limited number of events in every single bin of the distributions, while the W+jets and QCD multijet processes also have a shape uncertainty related to their data-driven estimation methods.

Theory uncertainties affecting the signal include the differences in acceptance observed when using an LO generator instead of NLO (20%). Theoretical uncertainties arising from the underlying event and parton showering matching scale, PDF [147], and the dependence

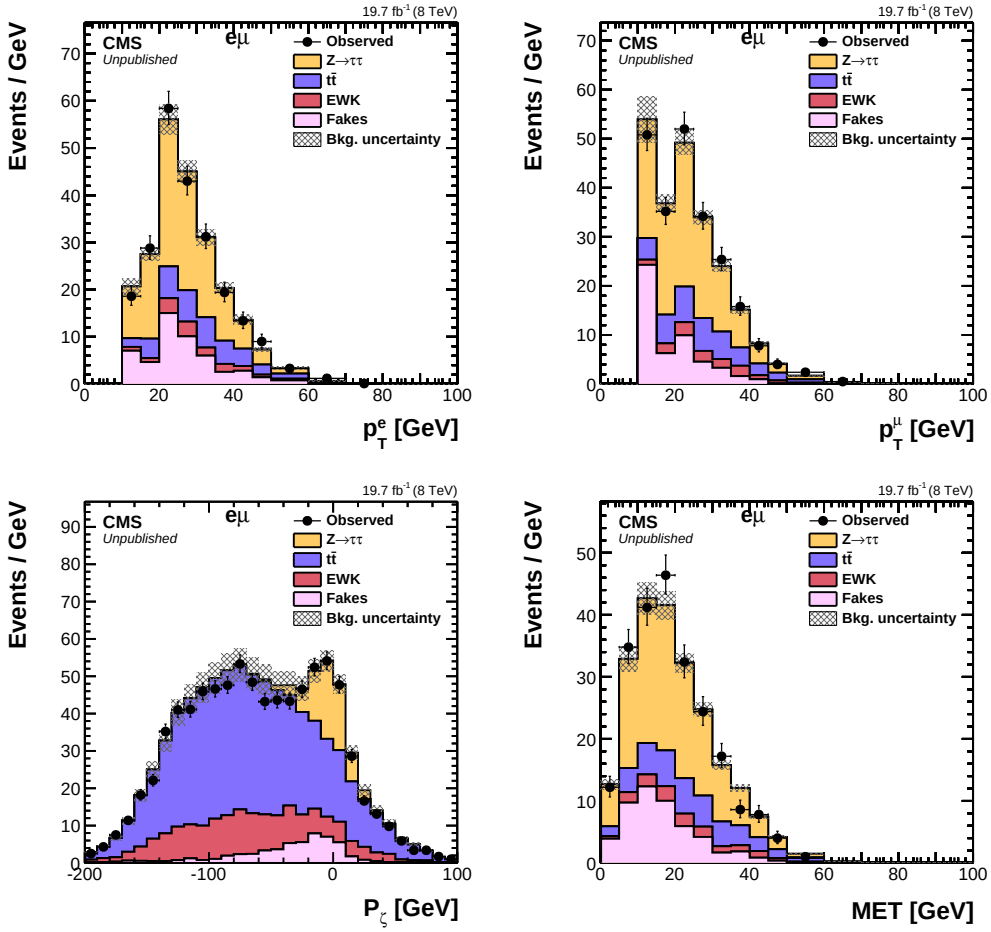

Figure 12.4: Control distributions in the $e\mu$ final state. The events are selected as in the signal region except that there is no requirement on the number of b-tagged jets. The electroweak background is composed of diboson and single top backgrounds, while the misidentified e/μ background is due to QCD multijet and W+jets events. The contributions from the SM scalar boson and from the signal are negligible and therefore not shown. A maximum likelihood fit to data, taking into account systematic uncertainties, is performed [145]

	Systematic source	Yield uncertainty		
		$\mu\tau_h$	$e\tau_h$	$e\mu$
Normalization	Integrated luminosity	2.6%	2.6%	2.6%
	Muon ID/trigger	2%	-	2%
	Electron ID/trigger	-	2%	2%
	Tau ID/trigger	8%	8%	-
	$\mu \to \tau_h$ misidentification rate	30%	-	-
	$e \to \tau_h$ misidentification rate	-	30%	-
	b tagging efficiency	1-4%	1-4%	1-4%
	b mistag rate	1-9%	1-9%	1-9%
	$\not\!\!E_T$ scale	1-2%	1-2%	1-2%
	$Z/\gamma^* \to \tau\tau$ normalization	3%	3%	3%
	$Z/\gamma^* \to \tau\tau$ low-mass normalization	10%	10%	10%
	QCD multijet normalization	20%	20%	-
	Reducible background normalization	-	-	30%
	W+jets normalization	30%	30%	-
	$t\bar{t}$ cross section	10%	10%	10%
	Diboson cross section	15%	15%	15%
	$H \to \tau\tau$ signal strength	30%	30%	30%
Distribution	Electron energy scale	-	-	shape
	Tau energy scale	shape	shape	-
	Distribution of QCD multijet and W+jets	shape	shape	-
	Trigger efficiency	shape	shape	-
	Limited number of events	shape	shape	shape
	$t\bar{t}$ p_T reweighting	shape	shape	shape
Theory	Underlying event and parton shower	1-5%	1-5%	1-5%
	Scales for A boson production	10%	10%	10%
	PDF for generating signal	10%	10%	10%
	NLO vs. LO	20%	20%	20%

Table 12.1: Systematic uncertainties considered in the $bbA \to bb\tau\tau$ analysis.

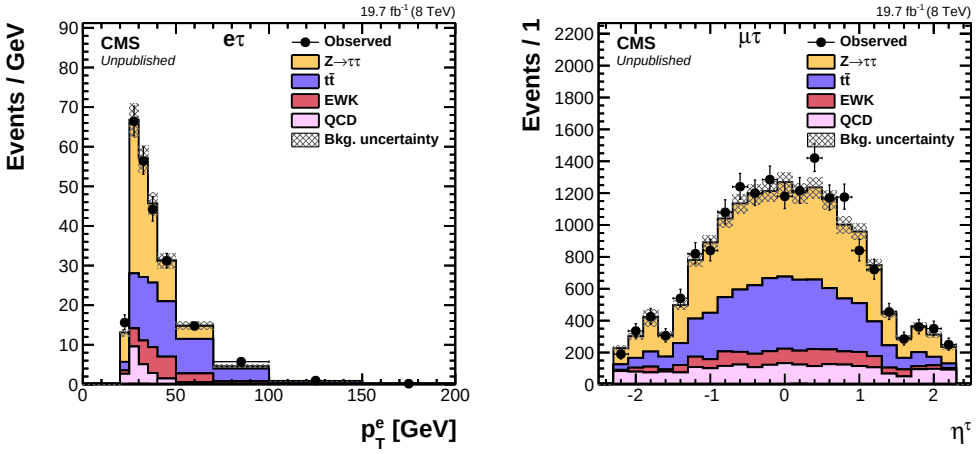

Figure 12.5: Control distributions in the $e\tau_h$ (left) and $\mu\tau_h$ (right) final states. The events are selected as in the signal region except that there is no requirement on the number of b-tagged jets. The electroweak background is composed of $Z \to ee$, $Z \to \mu\mu$, W+jets, diboson, and single top quark contributions. The contribution from the SM scalar boson and from the signal are negligible and therefore not shown. A maximum likelihood fit to data, taking into account systematic uncertainties, is performed. [145]

on factorization and normalization scales are considered for signal. The PDFs uncertainty is taken as the difference in the signal acceptance for the signal simulation with CTEQ6L1, MSTW2008NLO [148], and NNPDF2.3NLO [149] PDF sets, leading to a 10% uncertainty.

12.5 Results

A simultaneous maximum likelihood fit is performed in the three final states with all the systematic uncertainties taken into account. The pulls and goodness-of-fit tests indicate a good description of the processes. The di-tau mass plots after the fit are shown in Fig 12.6, together with their zoomed-in versions at low $m_{\tau\tau}$. A slight excess is observed in the $\mu\tau_h$ mass spectrum around 35 GeV, but it is compatible with the background-only hypothesis within the statistical and systematic errors. Model-independent upper limits can be set on the cross section times branching ratio using the asymptotic CL_s technique; they are shown for each final state in Fig. 12.7. Even though the level of background is higher at large $m_{\tau\tau}$, the exclusion limits improve sharply with the A mass; this is due to the rapidly increasing signal acceptance times efficiency with the pseudoscalar mass, illustrated in Fig. 12.8. The combination of the three final states is shown in Fig. 12.9, which contains also colorful points indicating theoretically viable scenarios. All red-orange points have cross sections above the ones excluded by the analysis: this process is excluded in 2HDM type-2 with wrong sign Yukawa couplings. The theoretical points are shown up to $m_A = m_h/2$, but the exclusion is even stronger for heavier A pseudoscalar bosons due to the absence of h boson decays to a pair of pseudoscalars.

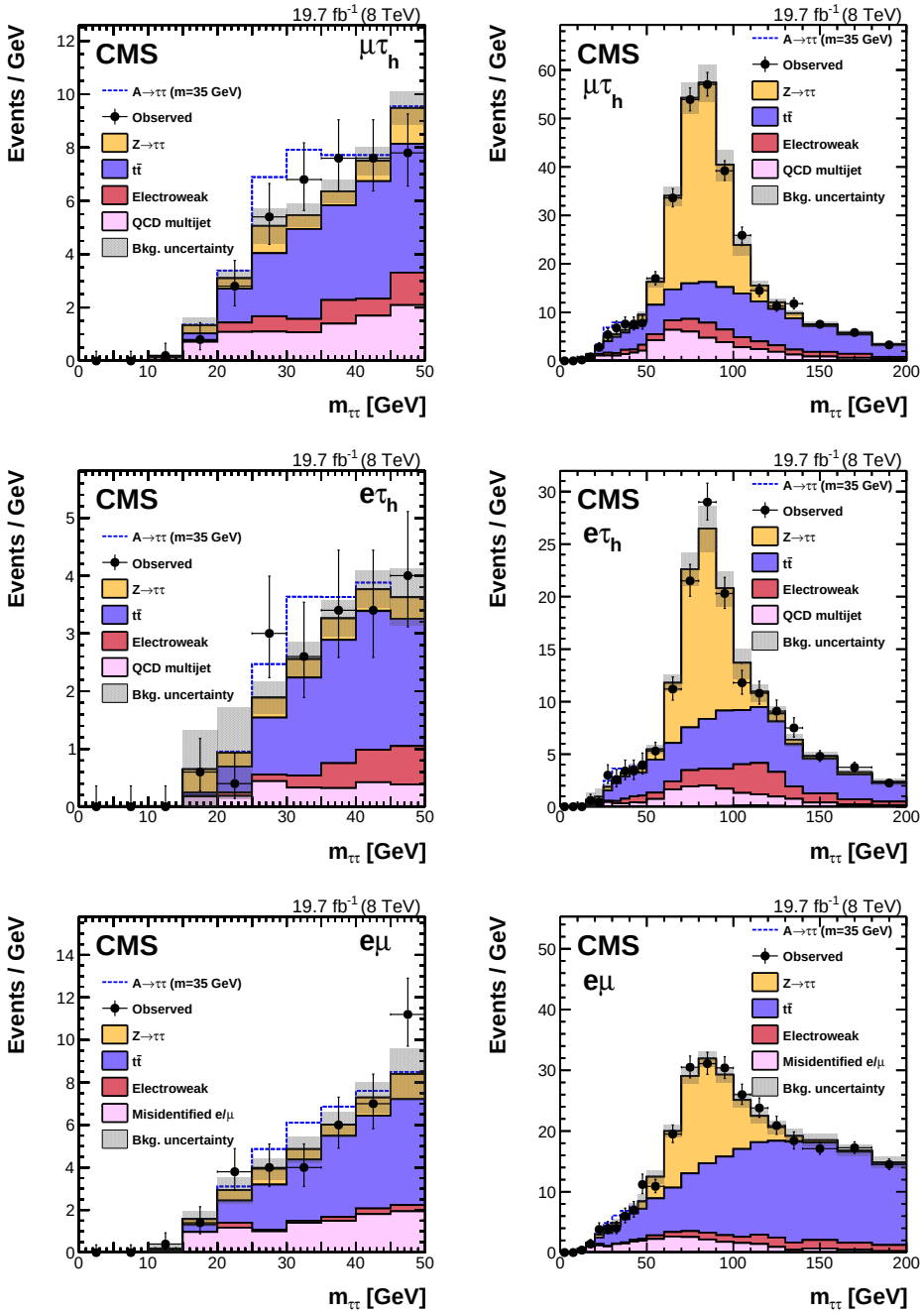

Figure 12.6: Observed and predicted $m_{\tau\tau}$ distributions in the $\mu\tau_h$ (top), $e\tau_h$ (center) and $e\mu$ (bottom) final states. The plots on the left are the zoomed-in versions for $m_{\tau\tau}$ distributions below 50 GeV. A signal for a mass of $m_A = 35$ GeV is shown for a cross section of 40 pb. In the $\mu\tau_h$ and $e\tau_h$ final states, the electroweak background is composed of $Z \to ee$, $Z \to \mu\mu$, W+jets, diboson, and single top quark contributions. In the $e\mu$ final state, the electroweak background is composed of diboson and single top backgrounds, while the misidentified e/μ background is due to QCD multijet and W+jets events. The contribution from the SM H boson is negligible and therefore not shown. [142]

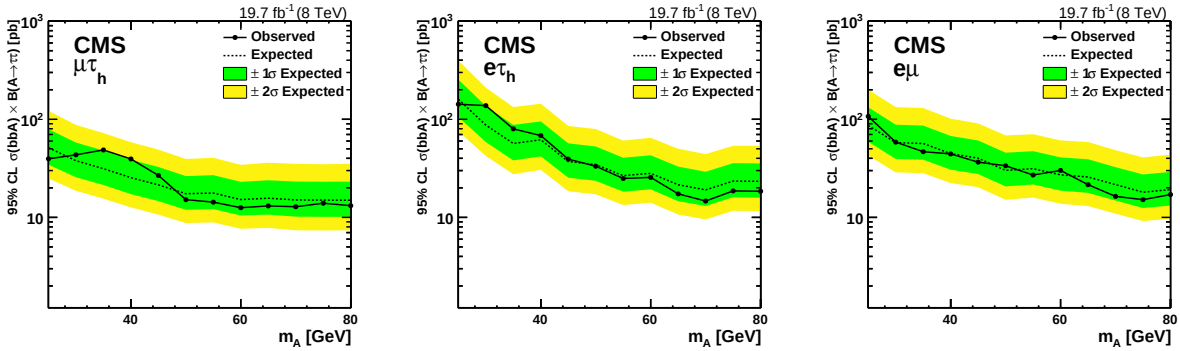

Figure 12.7: Observed and expected upper limits at 95% on the cross section times branching fraction for a light pseudoscalar boson produced in association with two b quarks and decaying to taus, in the $\mu\tau_h$ (left), $e\tau_h$ (center) and $e\mu$ (right) final states. [142]

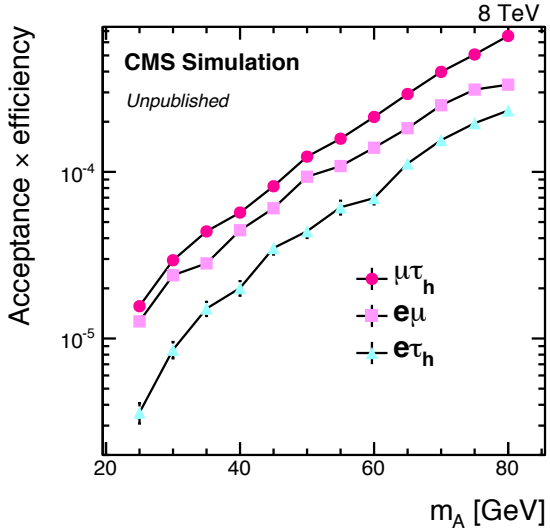

Figure 12.8: Signal acceptance and efficiency for different A masses for the three di-tau final states. The acceptance times efficiency increases sharply with the pseudoscalar boson mass. [145]

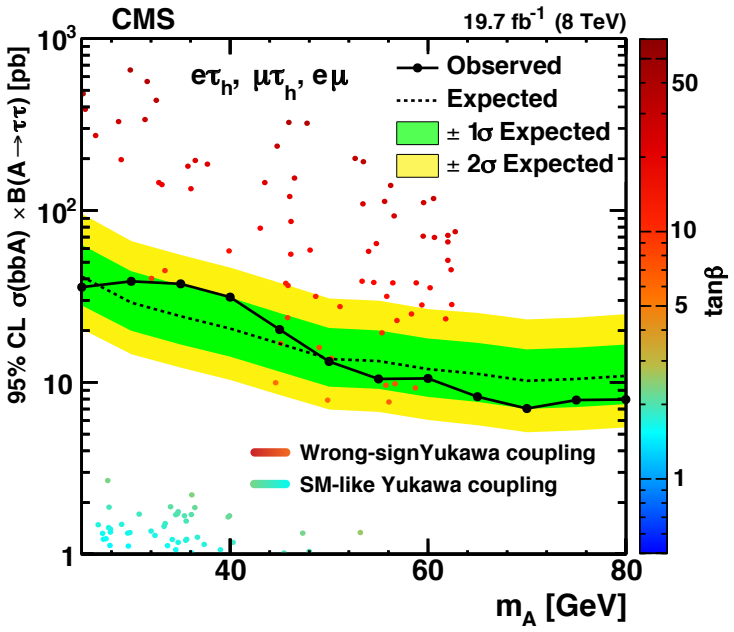

Figure 12.9: Expected and observed upper limits at 95% confidence level on the cross section times branching fraction for the combination of all three final states. The points represent typical expected cross sections in 2HDM type-2. The blue and green points correspond to models with SM-like Yukawa couplings, with low $\tan\beta$, $\sin(\beta-\alpha) \simeq 1$, $\cos(\beta-\alpha) > 0$ and low m_{12}^2; while the orange and red points correspond to models with a wrong-sign Yukawa coupling, with large $\tan\beta$, $\sin(\beta+\alpha) \simeq 1$ and small $\cos(\beta-\alpha) < 0$. Theoretical points are shown up to A boson masses equal to half of the h boson mass. [142]

12.6 Chapter summary and personal contributions

Search for a light pseudoscalar decaying to taus

In some parameter space of 2HDM type-2, a pseudoscalar lighter than the Z boson mass can be produced with a large cross section, while still being consistent with the results from all high-energy experiments. The search is performed in a mass range from 25 to 80 GeV, which was previously almost unexplored at the LHC. The associated production with b quarks is studied, and the search is performed in three di-tau final states: $\tau_e\tau_\mu$, $\tau_\mu\tau_h$ and $\tau_e\tau_h$. The dominant backgrounds are estimated from data-driven methods. No significant excess is observed in the low di-tau mass region, and limits between 7 and 39 pb are set on the production cross section times branching fraction. These results exclude the signal hypothesis in 2HDM type-2 with wrong-sign Yukawa coupling, where the sign of the Yukawa couplings of the h boson is not SM-like.

My contributions

Figures: 12.1-12.9.

I have been responsible for the results in the $e\mu$ final state, and for the combination results of the three final states.

Chapter 13

Search for a heavy di-tau resonance in the MSSM

Supersymmetry is the most elegant solution to many shortcomings of the SM, such as the existence of dark matter or the hierarchy problem. Its simplest version, the MSSM, can be probed at the LHC. Searching for heavy neutral resonances ($\Phi = A/H/h$) decaying to a pair of tau leptons is the most powerful way at the LHC to uncover an MSSM scalar sector at large $\tan\beta$, given the increased scalar couplings to leptons and down-type quarks. This chapter presents such a search, for resonance masses between 90 and 1000 GeV [42]. This analysis supersedes the previous results obtained with the same dataset by the CMS Collaboration [150]. The differences between the analyses are the categorization according to the τ_h candidate p_T, described later in the text, and the MVA-based identification of τ_h in the latest analysis. The six possible di-tau final states are studied with 7 and 8 TeV data collected by CMS in 2011 and 2012. The treatment of the $\tau_e\tau_h$, $\tau_\mu\tau_h$ and $\tau_e\tau_\mu$ decay modes is similar to a large extent to the one described in Chapter 12, and only the differences will be mentioned. The $\tau_e\tau_e$ and $\tau_\mu\tau_\mu$ final states are by far the least sensitive, because of the small branching fractions and large levels of backgrounds; and they will not be described in details in this chapter. Finally, the $\tau_h\tau_h$ channel, which has not been studied in Chapter 12 because of the high p_T thresholds at trigger level, is in this analysis particularly sensitive thanks to the large branching fraction and the typically high p_T decay products of heavy resonances. The analysis in this channel will be described at length in the next sections.

13.1 Categorization

In the MSSM, neutral scalar bosons can be produced either by gluon-gluon fusion, or by b-associated production. The gluon-gluon fusion proceeds essentially via top and bottom quark loops, but contributions from light squarks can also play a limited role. The first production mechanism is dominant for small and moderate $\tan\beta$ values, whereas the

latter becomes more important at large $\tan\beta$ due to the enhancement of the couplings to down-type quarks. It can also be noticed that at large $\tan\beta$, the couplings to leptons are increased in the same proportions, and the branching fraction of the heavy resonance to tau leptons can reach up to 10% [1]. The first step of the categorization aims at separating the two different production modes.

The events are divided into two categories, depending on their number of b-tagged jets:

- **B-tag**: This category targets the $gg \to \Phi bb$ production mode. The events should contain at least one jet with $p_T > 20$ GeV, $|\eta| < 2.4$ and passing the medium CSV working point. The large $t\bar{t}$ contribution is reduced by limiting the number of jets (b-tagged or not) with $p_T > 30$ GeV to maximum one.
- **No-b-tag**: This category targets the $gg \to \Phi$ production mode. The events are required not to contain any jet with $p_T > 20$ GeV, $|\eta| < 2.4$ and passing the medium CSV working point.

These two categories permit to measure the cross sections independently for the two production modes, and ensure a better analysis sensitivity because the signal over background ratio is larger in the b-tag case, especially at large $\tan\beta$. It can be noticed that the requirement on the maximum number of jets with $p_T > 30$ GeV in the b-tag category is not applied in the $bbA \to bb\tau\tau$ analysis detailed in Chapter 11.

The events collected at 8 TeV in the $e\tau_h$, $\mu\tau_h$ and $\tau_h\tau_h$ final states are further categorized based on the transverse momentum of the hadronic taus. The b-tag category is divided into two sub-categories:

- **Low**: The hadronic tau p_T, in the $e\tau_h$ and $\mu\tau_h$ channels, is between 30 and 45 GeV. In the $\tau_h\tau_h$ final state, the subleading hadronic tau is required to have a transverse momentum between 45 and 60 GeV.
- **High**: The hadronic tau p_T, in the $e\tau_h$ and $\mu\tau_h$ channels, is greater 45 GeV. In the $\tau_h\tau_h$ final state, the subleading hadronic tau is required to have a transverse momentum greater than 60 GeV.

Meanwhile the no-b-tag category is divided into three sub-categories:

- **Low**: The hadronic tau p_T, in the $e\tau_h$ and $\mu\tau_h$ channels, is between 30 and 45 GeV. In the $\tau_h\tau_h$ final state, the subleading hadronic tau is required to have a transverse momentum between 45 and 60 GeV.
- **Medium**: The hadronic tau p_T, in the $e\tau_h$ and $\mu\tau_h$ channels, is between 45 and 60 GeV. In the $\tau_h\tau_h$ final state, the subleading hadronic tau is required to have a transverse momentum between 60 and 80 GeV.
- **High**: The hadronic tau p_T, in the $e\tau_h$ and $\mu\tau_h$ channels, is greater 60 GeV. In the $\tau_h\tau_h$ final state, the subleading hadronic tau is required to have a transverse momentum greater than 80 GeV.

The classification is summarized in Tab. 13.1. These sub-categories also have different signal-to-background ratios, which improves the sensitivity for signal events with high p_T

1. In this case, the resonance only decays to b quarks and tau leptons, and the ratio between both branching fractions does not depend on $\tan\beta$ because they couple to the same doublet.

Channel	$30 < p_T^{\tau_h} < 45$ GeV	$45 < p_T^{\tau_h} < 60$ GeV	$60 < p_T^{\tau_h} < 80$ GeV	$p_T^{\tau_h} > 80$ GeV
$e\tau_h/\mu\tau_h$ b-tag	Low	High		
$e\tau_h/\mu\tau_h$ no-b-tag	Low	Medium	High	
$\tau_h\tau_h$ b-tag	-	Low	High	
$\tau_h\tau_h$ no-b-tag	-	Low	Medium	High

Table 13.1: Categorization based on the p_T of the τ_h candidates, according to the final state and the b-tagging category.

hadronic taus. The categorization according to the hadronic tau p_T is seen to improve the expected upper limits by about 20% in $e\tau_h$, 30% in $\mu\tau_h$ and 40% in $\tau_h\tau_h$ for all signal mass hypotheses. This corresponds to increasing the dataset size by a factor between 1.5 and 2.

The $\mu\mu$ and $e\mu$ channels, as well as all data collected at 7 TeV, are not categorized based on the final state lepton transverse momenta because they are either limited by the small number of selected events, or much less sensitive than the others.

13.2 $\tau_h\tau_h$ final state

The $\tau_h\tau_h$ channel has not been studied in the $bbA \to bb\tau\tau$ analysis because of the high p_T thresholds imposed by trigger constraints. In the case of the search for a heavy resonance however, the taus are produced with a larger transverse momentum, and the signal acceptance grows with the resonance mass. The $\tau_h\tau_h$ channel has the largest di-tau branching fraction (about 44%) and as such, improves considerably the sensitivity of the analysis in the regions with large m_Φ.

13.2.1 Selection

A combination of two triggers is used to select events in the $\tau_h\tau_h$ channel. If the transverse momentum of the leading tau in the event is less than 350 GeV, the events should pass a trigger path requiring two hadronic taus with p_T greater than 35 GeV at HLT. Otherwise, a single jet trigger path, requiring at HLT level a PF jet with p_T greater than 320 GeV, is applied to the events. The latter path is seen to be more efficient for events with high p_T taus. The double tau trigger path was deployed during the year 2012, and only 18.3 fb^{-1} are exploitable for this analysis.

Offline, the events are selected if they contain two hadronic taus with visible p_T greater than 45 GeV and $|\eta| < 2.1$, corresponding within $\Delta R < 0.5$ to the objects that fired the trigger path. Both tau candidates are required to pass the tight working point of the MVA isolation including lifetime information. The subleading tau should additionally pass the loose working point of the MVA discriminator against electrons. The two taus are required to be of opposite charge. In case more than two taus pass these selection criteria, the two most isolated [2] taus that have an opposite charge are chosen.

2. The decision is based on the raw output of the MVA isolation including lifetime information.

13.2.2 Background estimation

The estimation of the $Z/\gamma^* \to \tau\tau$ background is similar in all the final states studied in this analysis. Embedded samples are used, and they are normalized in an inclusive category (combination of all five event categories) to the yield obtained from MC samples. The normalization in the individual exclusive categories is obtained by multiplying the yield in the inclusive category by an acceptance factor measured in the embedded samples. The contamination from $t\bar{t}$ events is estimated and subtracted.

The QCD multijet process is a particularly overwhelming background in the $\tau_h\tau_h$ channel, because of the large $j \to \tau_h$ misidentification rate. The QCD multijet estimation relies on the measurement of the probabilities for the leading τ_h to pass the tight MVA isolation working point, as required in the signal region, or to pass a relaxed isolation working point (loose or very loose) but fail the tight one. These probabilities are measured in a QCD-enriched control region, obtained by inverting the charge requirement on the tau candidates, and subtracting the limited contribution of other processes, based on MC samples. The probabilities are measured as a function of the tau transverse momentum, and in three pseudo-rapidity regions ($|\eta| < 1.2$, $1.2 < |\eta| < 1.7$ and $1.7 < |\eta| < 2.1$). The ratios f_τ between the probabilities to pass the tight isolation and to pass the relaxed but to fail the tight isolations are fitted with linear functions as a function of the τ_h p_T. The shape and normalization of the QCD multijet background are obtained by selecting events that pass the full signal selection except that the leading tau does not pass the tight isolation working point but a relaxed one, and reweighting them by the ratios measured in the previous step. The contribution from other small processes is estimated from MC predictions and subtracted. The relaxed working point is the loose one in the no-b-tag category and the very-loose one in the b-tag category. In addition, because the number of selected events in the b-tag category is still low, the CSV working point is relaxed to loose, which is checked not to bias the QCD multijet background distribution. The ratios are illustrated in Fig. 13.1.

The estimation of all other backgrounds ($t\bar{t}$, W+jets, diboson, ...) is the same as described in Chapter 12 for the $bbA \to \tau\tau$ analysis in the $e\tau_h$ and $\mu\tau_h$ channels.

The resulting distributions in the five different categories are shown in Fig. 13.2.

13.2.3 Trigger efficiency

The efficiency of the double tau trigger is measured in data and in MC simulations in order to derive correction factors for the simulations. The efficiency is measured for one tau, and the total efficiency is given by the product between the efficiencies for the two taus. The measurement is performed in a region enriched in $Z/\gamma^* \to \tau_\mu\tau_h$ events.

To perform the measurement, the events are first triggered with a single muon trigger, and the presence of a muon with $p_T > 25$ GeV, $|\eta| < 2.1$, tightly identified and with a relative isolation less than 0.1 is required. The τ_h candidate is selected with $p_T > 20$

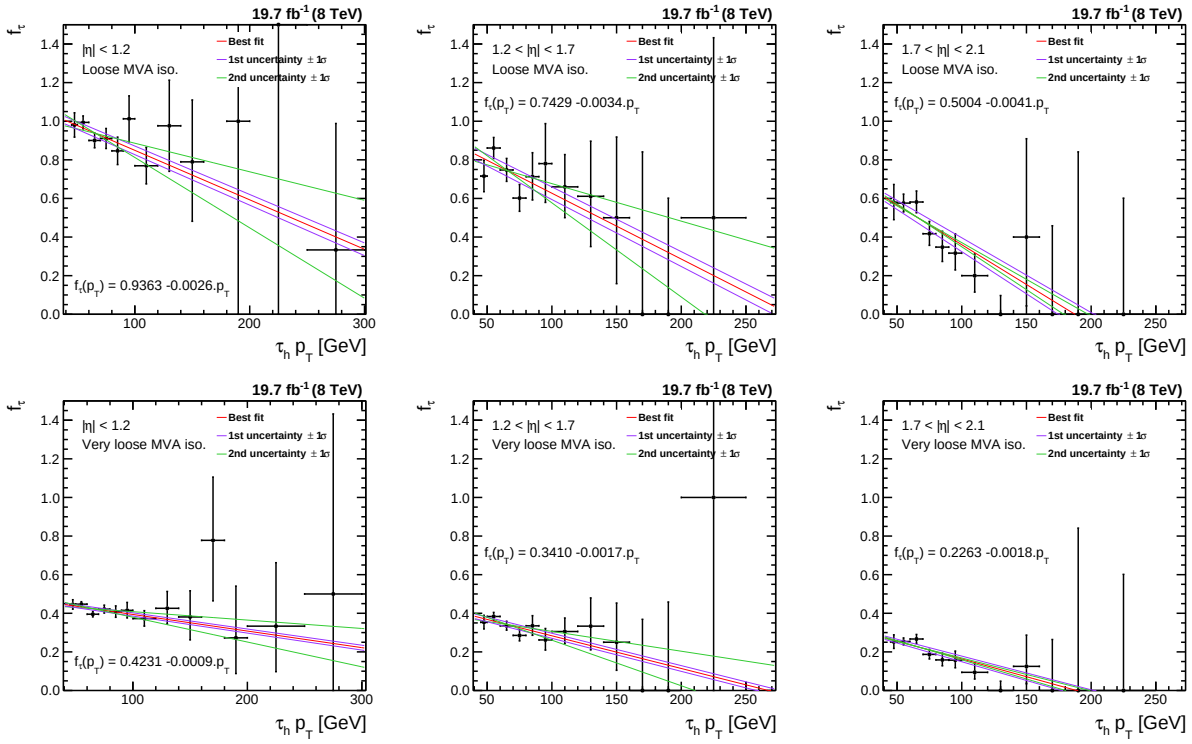

Figure 13.1: Ratios f_τ between the probabilities for the leading hadronic tau to pass the tight isolation, and to pass the loose (top) or very loose (bottom) but to fail the tight isolations, for $|\eta| < 1.2$ (left), $1.2 < |\eta| < 1.7$ (center) and $1.7 < |\eta| < 2.1$ (right). They are fitted linearly with functions of the τ_h p_T: the red line indicates the best fit, while the green and violet lines indicate the variations by $\pm 1\sigma$ of the decorrelated fit uncertainties.

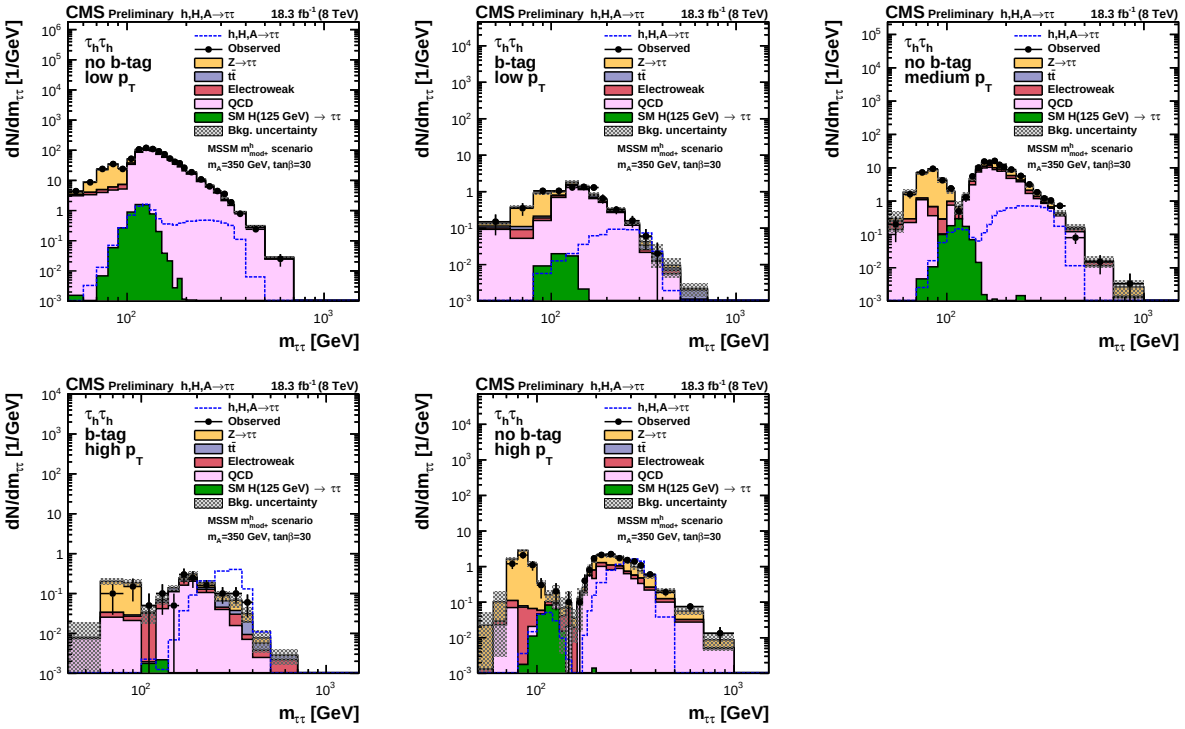

Figure 13.2: Observed and expected $m_{\tau\tau}$ distributions in the $\tau_h\tau_h$ channel, in the five subcategories. The expectation is shown after a maximum likelihood fit to data. [42]

GeV, $|\eta| < 2.1$, and has to pass the decay mode finding and the tight working point of the MVA-based isolation. The muon and the tau should be separated by at least $\Delta R = 0.5$, and to have an opposite sign charge. The W+jets background is reduced by requiring the transverse mass between the muon and the $\not\!\!E_T$ to be less than 20 GeV. The set of events selected in such a way constitutes the denominator of the efficiency ratio.

The numerator of the efficiency ratio is obtained by requiring the events to pass a trigger path that requires a muon and a hadronic tau. The muon selection at trigger level is looser compared to the single muon trigger applied in the previous step, and all events pass this part of the trigger. The tau requirements of this muon+tau trigger are the same for a single tau as those used by the double tau trigger under study, except that the tau p_T threshold at L2 and L3 is 25 GeV for the first one and 35 GeV for the latter one. To correct for this, the muon+tau trigger path is required to be fired and an offline cut on the L2 and L3 tau p_T is applied to emulate the double tau trigger operation.

The efficiency is measured as a function of the tau p_T by dividing the numerator and denominator events, both in data and in MC events. It is fitted with the convolution of a Heaviside step function and of a Gaussian curve, which reflects resolution effects:

$$f(p_T) = \frac{\epsilon}{2}\left[1 + erf\left(\frac{p_T - \mu}{\sqrt{2}\sigma\sqrt{p_T}}\right)\right], \tag{13.1}$$

where μ and σ are the mean and width of the Gaussian, representing the inflection point of the curve and its spread, and ϵ is a normalization factor, representing the efficiency at the plateau. The error function is defined as:

$$erf(x) = \frac{2}{\sqrt{\pi}}\int_0^x e^{-t^2}dt. \tag{13.2}$$

An unbinned fit is performed. The resulting curves in MC simulations and in data are shown in Fig. 13.3.

The division between the data and MC efficiency curves gives a p_T dependent scale factor to be applied to correct simulations. The correction amounts to up to 10% for taus with $p_T > 45$ GeV as used in the analysis. The uncertainty on the correction is estimated to be 4.5% per single tau. The trigger efficiency for high p_T taus is seen to decrease steeply in MC samples because of a problem in simulations, and reaches efficiencies below half its plateau value. The decrease is parametrized by a second order polynomial for taus with $p_T > 140$ GeV, which is used to correct the simulations. A 100% uncertainty is associated to this correction.

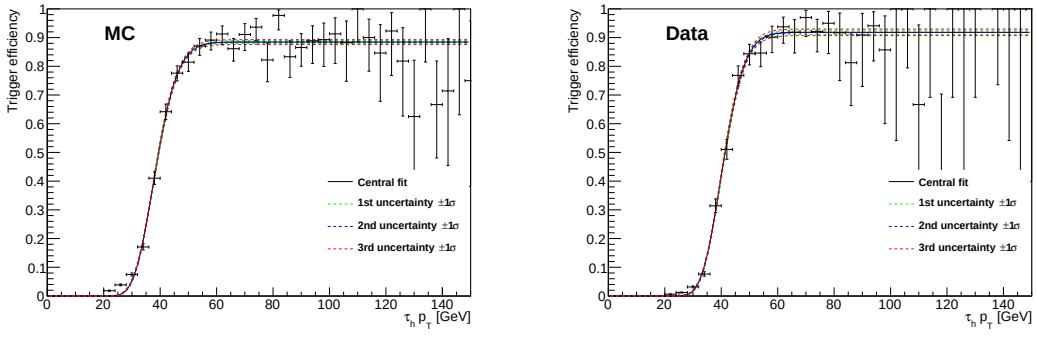

Figure 13.3: Trigger efficiency measured in MC simulations (left) and data (right). The uncertainties obtained by varying the three decorrelated fit uncertainties by one standard deviation are shown with dashed lines.

13.3 Differences from the light pseudoscalar boson search analysis in the $e\tau_h$, $\mu\tau_h$ and $e\mu$ final states

The selection of the $e\tau_h$, $\mu\tau_h$ and $e\mu$ final states proceeds almost similarly as in the case of the search for a light pseudoscalar decaying to taus and produced in association with b jets. The main differences lie in the categorization according to the number of b-tagged jets and to the transverse momentum of the τ_h candidates. Additionally, these final states are also studied here with data collected at 7 TeV center-of-mass energy. Because the search concentrates on heavy resonances, the Drell-Yan contributioncriterion is estimated only for an invariant mass of the leptons above 50 GeV.

13.3.1 Differences specific to the $e\mu$ channel

The leading muon is required to have a transverse momentum greater than 20 GeV instead of 18 GeV. There is no selection on the transverse mass between the dilepton system and $\not{E}_T$, and P_ζ is required to be greater than -20 GeV.

13.3.2 Differences specific to the $e\tau_h$ and $\mu\tau_h$ channels

The selection of the $e\tau_h$ and $\mu\tau_h$ final states is almost identical, except for the categorization discussed before. Another difference is that the OS/SS scale factor measured to scale the QCD multijet background extracted from a region where the two tau candidates have the same sign, is not measured as a function of the di-tau mass anymore, but is estimated to be a constant equal to 1.06, with a 5% uncertainty. The lepton thresholds are also modified compared to the $bbA \to bb\tau\tau$ analysis: the taus are selected with $p_T > 30$ GeV (instead of 20 GeV), and the muons with $p_T > 20$ GeV (instead of 18 GeV). The distributions obtained with 8 TeV data are shown for the $e\tau_h$ and $\mu\tau_h$ channels in Fig. 13.5 and 13.6 respectively.

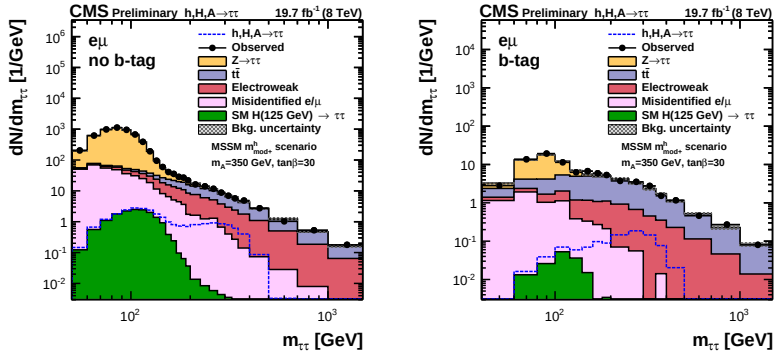

Figure 13.4: Observed and expected $m_{\tau\tau}$ distributions in the $e\mu$ channel, in the two subcategories. The expectation is shown after a maximum likelihood fit to data. [42]

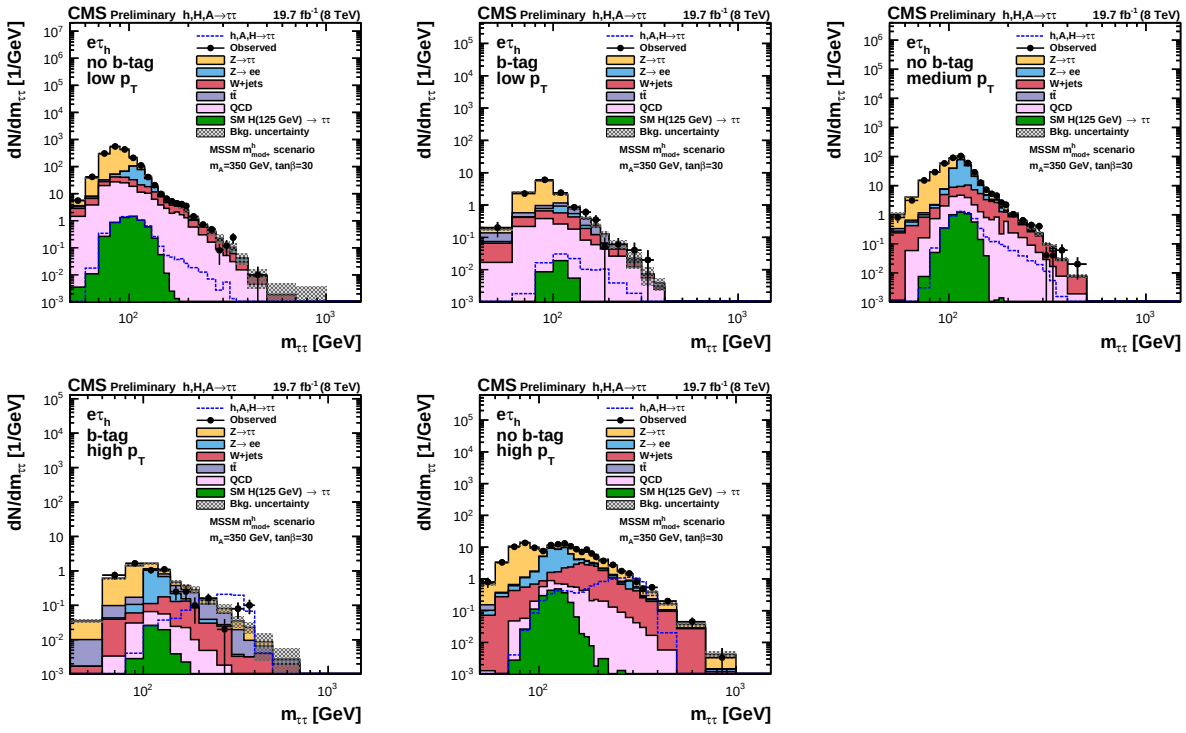

Figure 13.5: Observed and expected $m_{\tau\tau}$ distributions in the $e\tau_h$ channel, in the five subcategories. The expectation is shown after a maximum likelihood fit to data. [42]

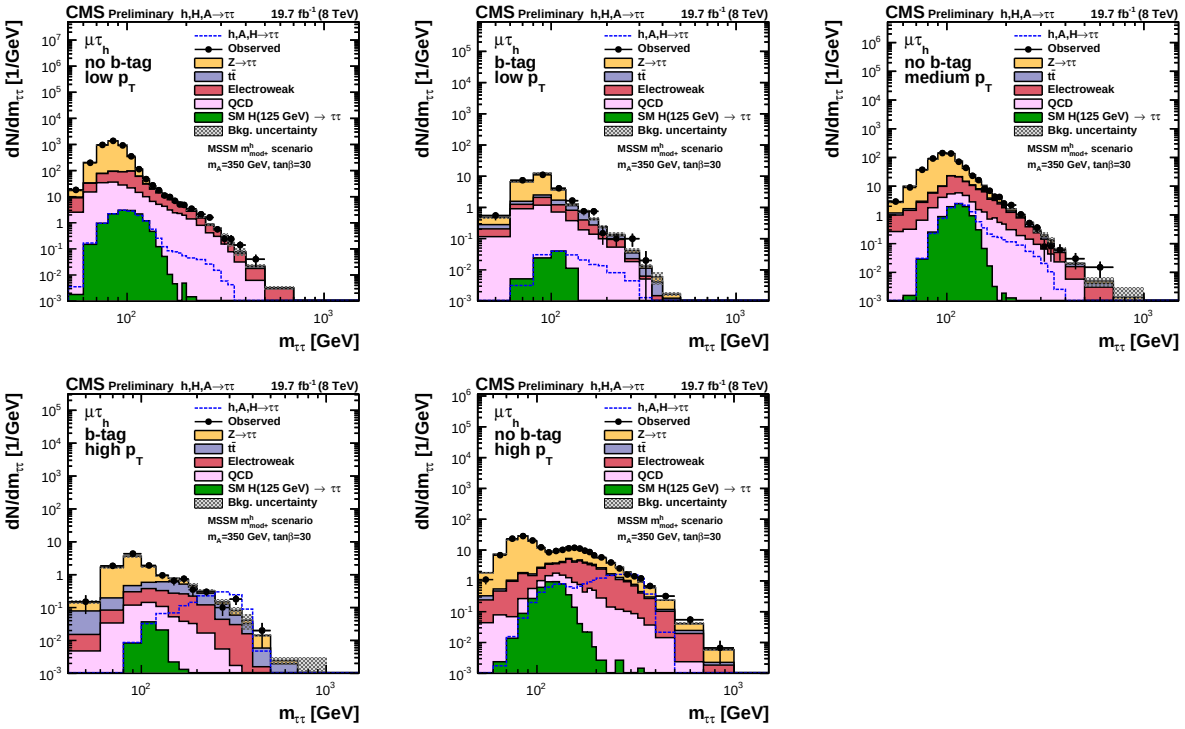

Figure 13.6: Observed and expected $m_{\tau\tau}$ distributions in the $\mu_h\tau_h$ channel, in the five subcategories. The expectation is shown after a maximum likelihood fit to data. [42]

13.4 Φ p_T reweighting

The transverse momentum of the Φ resonance produced in gluon-gluon fusion depends on the relative contributions from top, bottom, stop and sbottom quark loops, and therefore is related to $\tan\beta$. This variable is not directly used in the analysis, but it has an influence on the transverse momenta of its daughter tau leptons. A modification of the Φ transverse momentum will cause changes on the signal acceptance due to p_T thresholds, and event migrations from a p_T category to another. Signal samples are generated at LO with Pythia, and the Φ bosons are produced without any transverse momentum other than coming from initial state radiations. The description of the Φ p_T variable is corrected using the procedure outlined in [151] and briefly explained here. The Φ p_T spectra are computed at NLO level with Powheg, and some weights are derived to correct the p_T spectra obtained via Pythia. The reweighting factor is taken as the average between the factors obtained with $\tan\beta = 2$ and $\tan\beta = 30$, and the difference is considered as a shape systematic uncertainty. Reweighting the Pythia distributions typically makes the p_T spectra softer, and therefore contributes to a decrease of the analysis sensitivity, especially for small m_Φ. The effect of the shape uncertainty on the final upper limits is limited to less than 5%.

13.5 Result interpretation

The statistical uncertainties in the tail of the $m_{\tau\tau}$ distributions are large, and a fit of the form $f(m_{\tau\tau}) = \exp\left(-\frac{m_{\tau\tau}}{c_0+c_1\times m_{\tau\tau}}\right)$ is performed for every major background, where c_0 and c_1 are constant terms. The binned distributions are used at low $m_{\tau\tau}$, while the fit functions are used to model the different processes at higher $m_{\tau\tau}$ values [3]. The uncertainties on the decorrelated parameters are considered as nuisance parameters in the likelihood functions. Simulation corrections and other systematic uncertainties are generally similar to those considered in the context of the $bbA \to bb\tau\tau$ analysis. Additional uncertainties are related to the categorization. The full invariant mass $m_{\tau\tau}$, reconstructed with the SVfit algorithm, is again used as observable to extract the results. Fig. 13.7 illustrates the difference between the visible invariant mass and $m_{\tau\tau}$ distributions for the $Z \to \tau\tau$ background and for the signal with different masses. The $m_{\tau\tau}$ distributions are centered on the true mass, and have a typical resolution of 20%. Their high mass tail is due to $\not\!\!E_T$ resolution effects, while the low mass tail comes from events where the tau candidates are back-to-back and have little visible p_T.

No significant excess compatible with a heavy resonance is observed in any of the final states or categories, and model-independent limits on the cross section times branching fraction can be set for the two production modes. Upper limits are set at 95% CL with the CL_s asymptotic technique, and are shown in Fig. 13.8. The fact that both production modes contribute to the b-tag and non b-tag categories is taken into account. The signal

3. The threshold where the parameterization starts is between 150 and 325 GeV depending on the final state and on the category.

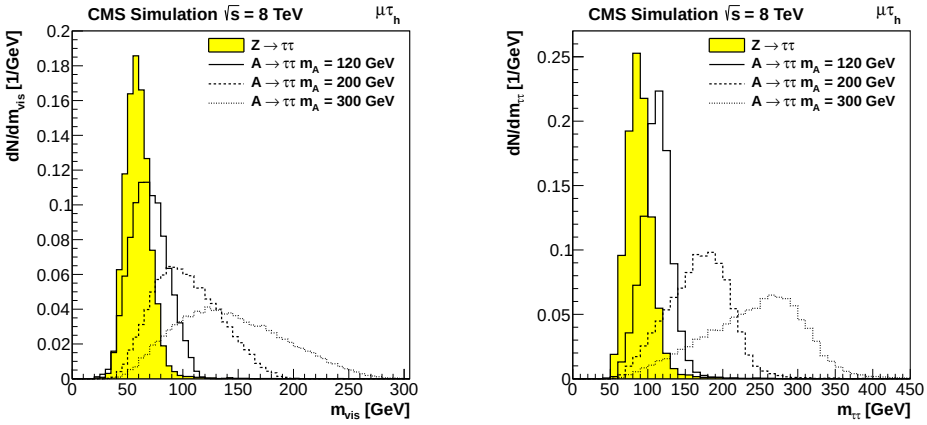

Figure 13.7: Visible mass m_{vis} and full SVfit mass $m_{\tau\tau}$ distributions for the $Z \to \tau\tau$ background and different signal hypotheses. [42]

templates are considered as the sum of the contributions of the two MSSM neutral bosons degenerated in mass, while the third boson contribution is seen to be negligible.

The results can also be interpreted in some specific MSSM benchmark scenarios, as illustrated in Fig. 13.9. The six benchmark scenarios considered are:

- m_h^{max}: The parameters are designed to maximize the mass of the lightest scalar, up to about 135 GeV. As the mass of the SM-like scalar has been measured to be 125 GeV, a large part of the parameter space in this benchmark scenario is already excluded by this indirect constraint, but this scenario can be used to set conservative lower bounds on m_A and $\tan\beta$.
- m_h^{mod+}: The parameters are modified such that the h mass is compatible with the mass of the observed SM-like scalar, by reducing the amount of mixing in the stop sector. The stop mixing parameter is chosen to give the best agreement with the measured value of muon anomaly $(g-2)_\mu$.
- m_h^{mod-}: The mass of the h boson is compatible with 125 GeV, and the stop mixing parameter is chosen to give the best agreement with the measured rate of $b \to s\gamma$.
- Light-stop scenario: The mass of the h boson is compatible with 125 GeV, and the rate for the h boson production through gluon-gluon fusion is reduced.
- Light-stau scenario: The mass of the h boson is compatible with 125 GeV, and the rate for the decay of the h boson to photons is increased.
- Tau-phobic scenario: The mass of the h boson is compatible with 125 GeV, and the couplings of the h boson to leptons and down-type quarks are reduced.

More details about these benchmark scenarios can be found in [152, 153].

Similar results have been obtained by the ATLAS Collaboration in Run-1 [154], and results with an almost equal sensitivity have been published with the data collected at 13 TeV center-of-mass energy in 2015 [155].

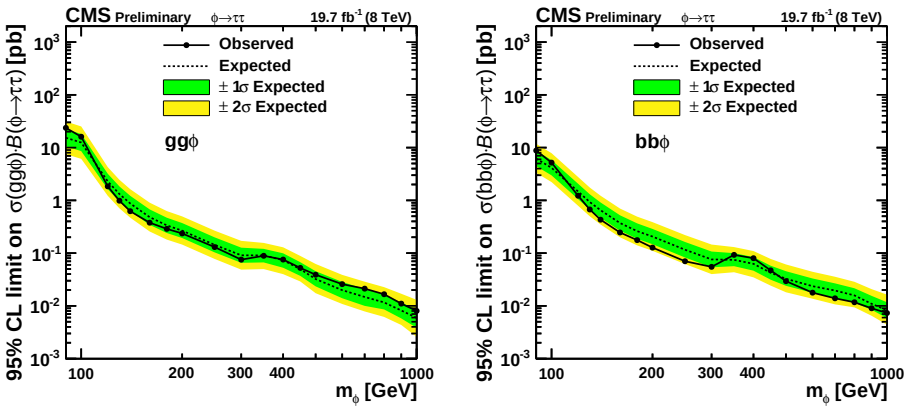

Figure 13.8: Model-independent observed and expected upper limits at 95% CL on $\sigma(gg\Phi).\mathcal{B}(\Phi \to \tau\tau)$ (left) and $\sigma(bb\Phi).\mathcal{B}(\Phi \to \tau\tau)$ (right), for the production of a narrow resonance that decays into tau pairs, beyond the discovered SM-like boson of mass 125 GeV. [42]

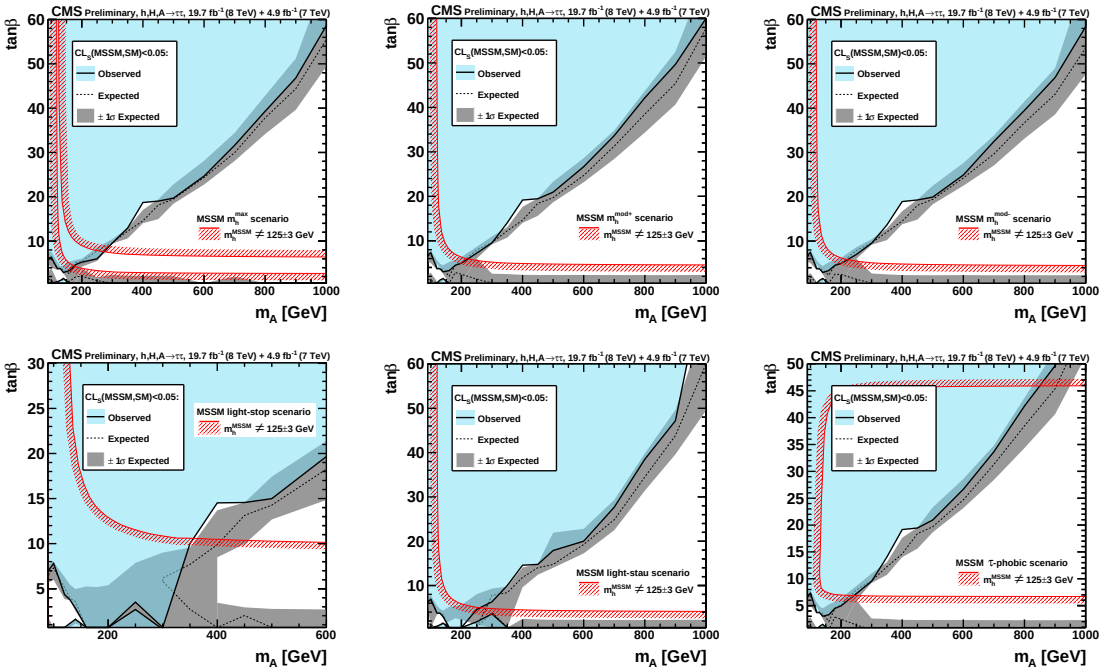

Figure 13.9: Regions of the $m_A - \tan\beta$ plane excluded by this analysis (blue) and by the constraint $m_h^{MSSM} = 125 \pm 3$ GeV (red) in the m_h^{max} (top left), m_h^{mod+} (top center), m_h^{mod-} (top right), light-stop (bottom left), light-stau (bottom center) and tau-phobic (bottom right) MSSM benchmark scenarios. The 3 GeV uncertainty on the h mass comes from theoretical predictions on m_h in supersymmetric models. [42]

13.6 Chapter summary and personal contributions

Search for a heavy di-tau resonance in the MSSM

The search for a heavy resonance decaying to a pair of taus is by far the most powerful way to discover an extended scalar sector in the MSSM when $\tan\beta$, the ratio between the vacuum expectation values of the two scalar doublets, is large. At large $\tan\beta$ values, the decays of the heavy resonance $\Phi = A/H/h$ to taus are enhanced, as is its production in association with b quarks. The analysis sensitivity is improved by categorizing events according to their number of b-tagged jets, and to the transverse momentum of their leading hadronic tau if applicable. As no excess of data is observed on top of the predicted SM backgrounds, limits are set on the cross section times branching fraction of a signal in the $bb\Phi$ and $gg\Phi$ production modes, for resonance masses between 90 and 1000 GeV. Results are also interpreted in different MSSM scenarios, and are seen to exclude a large part of the parameter space, especially at large $\tan\beta$.

My contributions

Figures: 13.1-13.3.

I have synchronized with the LLR Polytechnique group in the $\tau_h\tau_h$ final state, which consists in reproducing all results from scratch up to the final limits and reaching a better than 10% agreement between the two analyses. I have also measured the tau trigger efficiency in data and MC simulations.

Part V

Status and prospects

Chapter 14

Overview of LHC results and prospects for future colliders

After the discovery of a particle compatible with the scalar boson of the SM, many fundamental questions remain. Searches performed at the LHC in Run-1 have not permitted to discover BSM physics, but a few deviations from the SM expectations have been observed with a low significance. These will require more data, collected in Run-2 or later, to be confirmed or invalidated. Next sections describe the status of the results of the CMS experiment after Run-1 and their projections in the coming runs, with particular emphasis on the scalar sector, as well as the prospects for the next collider experiments.

14.1 Overview of CMS measurements in the scalar sector

14.1.1 SM precision measurements

The significance of the excess of events at a mass of about 125 GeV has long since exceeded five standard deviations, and physicists are now performing precision measurements on the recently discovered particle, to assess its compatibility with the SM scalar hypothesis. The most precise decay channels are $H \to \gamma\gamma$ and $H \to ZZ^* \to 4\ell$. The $H \to \gamma\gamma$ analysis [132] is characterized by a small narrow resonance above a large falling continuum background. To increase the sensitivity of this analysis, different categories are defined, with various signal purity and mass resolution. Results are extracted from a fit of the parameterized background and signal distributions to the observed data. In the $H \to ZZ^* \to 4\ell$ channel [60], at least one of the Z bosons is produced off-shell. The so-called golden channel corresponds to the case where both Z bosons decay to leptons (essentially ee or $\mu\mu$). Despite the low cross section times branching fraction, this decay channel is extremely powerful and is one of the main components of the discovery in 2012, because of the low level of backgrounds and the excellent lepton identification and reconstruction.

As detailed in Chapter 7, the fermionic decay channels, despite their large branching fractions at $m_H = 125$ GeV, are less sensitive because of the large level of backgrounds in the gluon-gluon fusion production mode. The decay channel $H \to bb$ has the largest branching fraction in the SM, but is extremely complicated experimentally because the difficult distinction between jets originating from b quarks – b jets – and other jets makes the QCD multijet background overwhelm the signal. Luckily, some production modes of the scalar boson give handle to reduce the backgrounds: this is the case of the vector boson fusion production with two additional energetic forward jets, and of the associated production with a vector boson where the decay products of this vector boson may be easy to identify. These two production modes have been studied at CMS, and although the results are still far from a discovery in the bb decay mode, an excess at a mass close to 125 GeV has been observed with a significance of 2.1 and 2.2 standard deviations respectively in the associated production and vector boson fusion production modes [119, 156]. The main challenges in searching for $H \to \tau\tau$ decays are to distinguish tau leptons decaying hadronically from jets originating from quarks or gluons, and to reduce the large multijet backgrounds coming from Drell-Yan QCD processes. Additionally the invariant mass of the tau pair can only be reconstructed with a poor resolution ($\simeq 20\%$). The analysis of data taken in 2011 and 2012 at the LHC has shown an evidence for the existence of H decays to tau leptons, and all measurements (signal strength, mass, ...) are compatible with SM expectations. More details can be found in Chapter 7. The combined significance of the $H \to bb$ and $H \to \tau\tau$ searches exceeds three standard deviations, which leads to an evidence for the decay of the 125-GeV particle to fermions [120].

Although the branching fractions of the SM scalar boson to a pair of electrons or muons are tiny and not accessible with a low amount of data such as that collected during LHC Run-1, the searches $H \to \mu\mu$ and $H \to ee$ are still performed because the observation of such decays would be a clear evidence for BSM physics. In these analyses [157], the signal hypothesis forms a narrow resonance on top of SM backgrounds, which enables the analysts to use shape-based techniques to extract a potential signal. No excess has been observed in any of the decay channels, and upper limits have been set by the CMS Collaboration at 95%CL on the branching fraction of the new particle to electrons ($\mathcal{B}(H \to ee) < 0.0019$) or muons ($\mathcal{B}(H \to \mu\mu) < 0.0016$), assuming the SM production cross section for scalar boson.

The combination of ATLAS and CMS results in the $H \to \gamma\gamma$ and $H \to ZZ^* \to 4\ell$ channels led to the most precise measurement of the new particle mass [158]:

$$\hat{m}_H = 125.09 \pm 0.21 \text{ (stat.)} \pm 0.11 \text{ (syst.) GeV}. \tag{14.1}$$

All production and decay channels have been taken into account in a CMS-only combination [54]; the combined signal strength is found to be very compatible with the SM expectation:

$$\hat{\mu} = 1.00 \pm 0.09 \text{ (stat.)}^{+0.08}_{-0.07} \text{ (theo.)} \pm 0.07 \text{ (syst.)}. \tag{14.2}$$

The signal strengths measured for the different production and decay modes are all in a good agreement with the SM expectations, as shown in Fig. 14.1. An interesting feature is

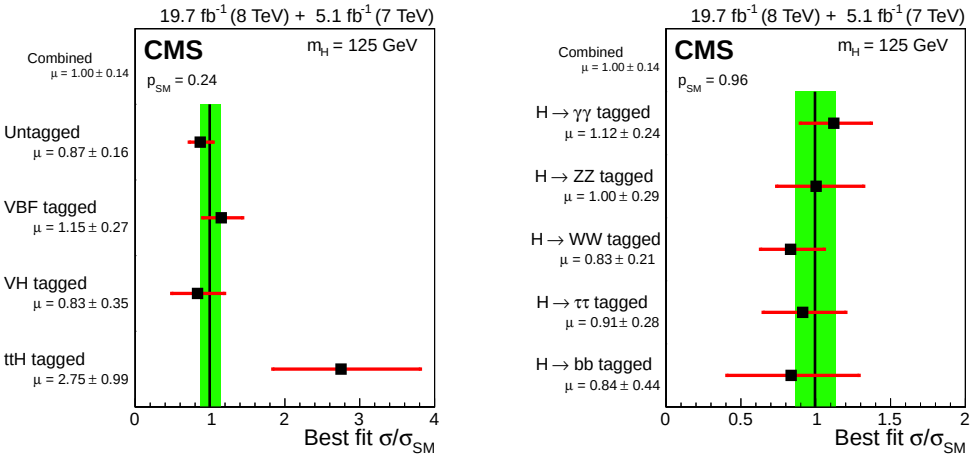

Figure 14.1: Measured signal strengths in different event categories that tag different production (left) and decay (right) modes. [54]

the excess observed in the $t\bar{t}H$ production mode [159]. Table 14.1 summarizes the signal strengths and significances measured in the different production and decay channels of the SM scalar boson, with the data collected in Run-1 by the CMS detector.

Such a mass for the scalar boson, associated to the measured top quark mass [160]:

$$\hat{m}_t = 172.44 \pm 0.13 \text{ (stat.)} \pm 0.47 \text{ (syst.) GeV}, \tag{14.3}$$

implies that in the SM without addition of new physics, the universe lies at the boundary between stability and instability of the electroweak vacuum [161, 162], as illustrated in Fig. 14.2. The electroweak vacuum lifetime in this meta-stability region fortunately exceeds the age of the universe. The fact that the universe lies at the edge of the electroweak vacuum expectation value raises many questions: why did early fluctuations not destabilize the potential?, does it play a role in inflation?, ... This apparent meta-stability might be a hint in understanding deeper physics.

Another great achievement of Run-1 is the extraction of an upper bound on the H boson width, equal to 5.4 times the value predicted in the SM for a boson mass of 125 GeV [163]. This bound is obtained under the SM hypothesis, in the $gg \to H \to ZZ$ channel, and relies on the determination of the relative off-shell and on-shell productions. Indeed, the respective cross sections are:

$$\sigma^{\text{on-shell}}_{gg\to H\to ZZ^*} \simeq \frac{g^2_{ggH} g^2_{HZZ}}{m_H \Gamma_H}, \tag{14.4}$$

$$\sigma^{\text{off-shell}}_{gg\to H^*\to ZZ} \simeq \frac{g^2_{ggH} g^2_{HZZ}}{4 m^2_Z}, \tag{14.5}$$

	ggH	VBF	VH	$t\bar{t}H$	All
$H \to \gamma\gamma$	$\hat{\mu} = 1.12^{+0.37}_{-0.32}$	$\hat{\mu} = 1.58^{+0.77}_{-0.68}$	$\hat{\mu} = -0.16^{+1.16}_{-0.79}$	$\hat{\mu} = 2.7^{+2.6}_{-1.8}$	$\hat{\mu} = 1.12 \pm 0.24$ 5.6σ
$H \to ZZ$	$\hat{\mu} = 0.83^{+0.31}_{-0.25}$ (0/1-jet, 4ℓ)	$\hat{\mu} = 1.45^{+0.89}_{-0.62}$ (2-jet, 4ℓ)		$\hat{\mu} = -4.7^{+5.0}_{-1.3}$ (4ℓ) $\hat{\mu} = 3.1^{+2.4}_{-2.0}$ (3ℓ) $\hat{\mu} = 5.3^{+2.1}_{-1.8}$ (SS 2ℓ)	$\hat{\mu} = 1.00 \pm 0.29$ 6.5σ
$H \to WW$	$\hat{\mu} = 0.74^{+0.22}_{-0.20}$	$\hat{\mu} = 0.60^{+0.57}_{-0.46}$	$\hat{\mu} = 0.56^{+1.27}_{-0.95}$ ($3\ell 3\nu$) $\hat{\mu} = 0.39^{+1.97}_{-1.87}$ ($2\ell 2\nu 2q$)		$\hat{\mu} = 0.83 \pm 0.21$ 4.7σ
$H \to \tau\tau$	$\hat{\mu} = 0.34 \pm 1.09$ (0-jet) $\hat{\mu} = 1.07 \pm 0.46$ (1-jet)	$\hat{\mu} = 0.94 \pm 0.41$	$\hat{\mu} = -0.33 \pm 1.02$	$\hat{\mu} = -1.3^{+6.3}_{-5.5}$ ($\tau_h\tau_h$)	$\hat{\mu} = 0.91 \pm 0.28$ 3.2σ
$H \to bb$	-	$\hat{\mu} = 2.8^{+1.6}_{-1.4}$ 2.2σ	$\hat{\mu} = 1.0 \pm 0.5$ 2.1σ	$\hat{\mu} = 0.7 \pm 1.9$	$\hat{\mu} = 0.84 \pm 0.44$
$H \to \mu\mu$	$\mu < 7.4$			-	$\mu < 7.4$ $< 0.1\sigma$
$H \to ee$	$\mu < 3.7 \times 10^{-5}$			-	$\mu < 3.7 \times 10^{-5}$
All	$\hat{\mu} = 0.85^{+0.19}_{-0.16}$	$\hat{\mu} = 1.16^{+0.37}_{-0.34}$	$\hat{\mu} = 0.92^{+0.38}_{-0.36}$	$\hat{\mu} = 2.90^{+1.08}_{-0.94}$	$\hat{\mu} = 1.00 \pm 0.14$

Table 14.1: Best-fit signal strengths and observed significances, measured in Run-1, for different production and decay modes of the SM scalar boson. Results come from [16, 54, 59, 60, 119, 132, 156, 157, 159].

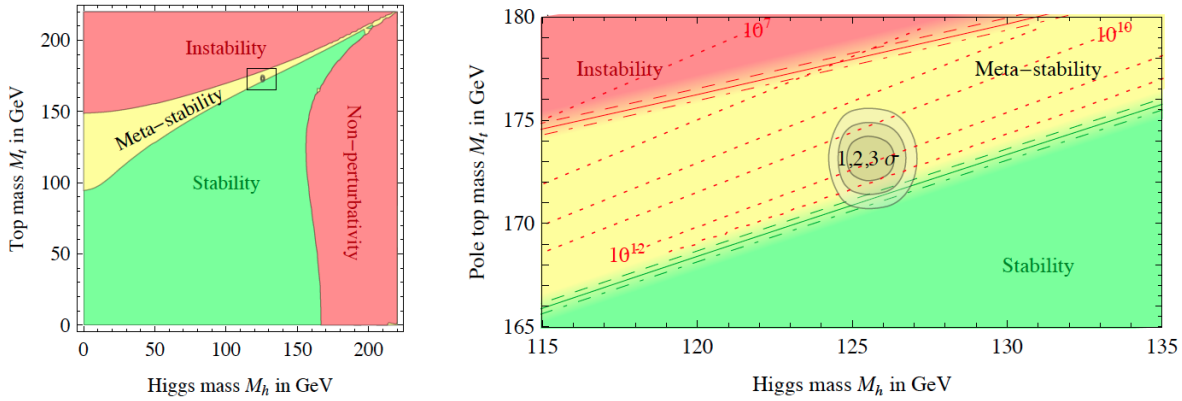

Figure 14.2: Regions of stability, meta-stability and instability of the electroweak vacuum without any BSM physics at the TeV scale. [161]

where g_{ggH} and g_{HZZ} are the H boson couplings to gluons and Z bosons respectively, and Γ_H is the H boson width. The indirect upper limit of $\Gamma_H < 22$ MeV at 95% CL complements the existing experimental results on the H boson width, and gives a value more precise by more than two orders of magnitude.

All the above-mentioned physics analyses have shown a good agreement between the properties of the 125-GeV particle and those predicted for the scalar boson of the SM. This is however not the end of the story, as many BSM theories with an extended scalar sector have an alignment limit, where the properties of one of their scalars tend to be SM-like. Highlighting deviations from the SM expectations therefore requires to reach a greater precision, and to analyze larger datasets. The LHC is expected to collect about 300 fb^{-1} of proton-proton data by 2022, after which a long shutdown is planned for upgrades of the machine and detectors. The High Luminosity LHC (HL-LHC) will eventually permit to collect about 3000 fb^{-1} data with an increased instantaneous luminosity and larger average pileup. Projections of the precision measurements on the scalar boson have been extrapolated from the Run-1 operation in the 300 and 3000 fb^{-1} cases [164]. An optimistic and a pessimistic scenarios have been studied: the first one supposes the theoretical uncertainties are reduced by a factor two and the other uncertainties are scaled by the square root of the luminosity, while the second one assumes the systematic uncertainties are the same as in Run-1. In any case, the performance of the detector and trigger is considered to be the same as in Run-1. The projections of the precision on the measurements of the signal strength for a SM-like boson are shown in Fig. 14.3: in particular the precision on the $H \to \tau\tau$ signal strength, equal to approximately 30% in Run-1 can be reduced to 8-14% with 300 fb^{-1} data at 14 TeV, and 5-8% with 3000 fb^{-1} data at 14 TeV. The increased precision obtained at the HL-LHC might lead to the observation of deviations with respect to the SM predictions, and be an indication of the existence of BSM physics.

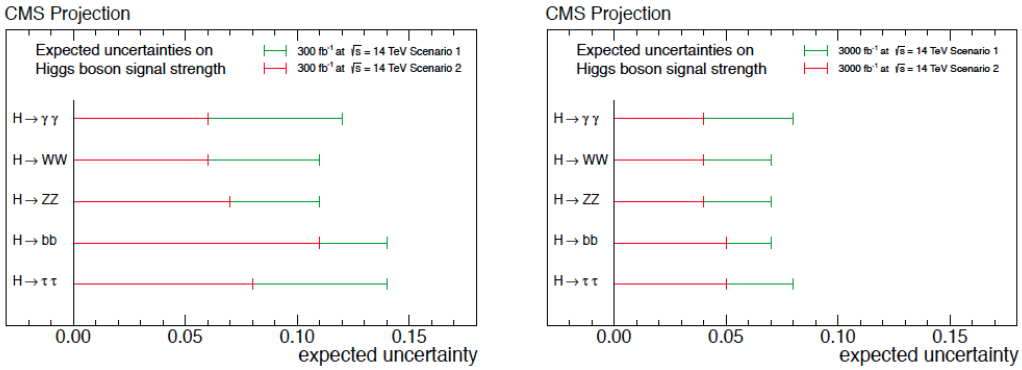

Figure 14.3: Projected precisions on the measurement of the signal strength for a SM-like H boson with 300 (left) and 3000 (right) fb^{-1} data collected at 14 TeV. The two scenarios are described in the text. [164]

14.1.2 Exotic scalar decays

Three categories of searches for exotic scalar decays are explored with data collected at the LHC:

- A summary of the CMS searches for the exotic decay of the 125-GeV particle to two light pseudoscalar bosons has been presented in Chapter 11. The results of the searches are interpreted in the context of 2HDM+S; the analyses can exclude branching fraction $\mathcal{B}(h \to aa)$ values less than one in some scenarios (especially large $\tan\beta$ in type-3, where the decays to leptons are enhanced over the decays to quarks) and in some pseudoscalar mass ranges. These analyses will be performed with Run-2 data, and new final states and mass ranges will be covered to probe a larger phase space.

- Lepton-flavor violating scalar decays are also studied with CMS data [165]. Decays such as $H \to \mu\tau$ or $H \to e\tau$ are not allowed in the SM if the theory is renormalizable, and their observation would be an evidence for the existence of BSM physics above a finite mass scale. An excess of events compatible with $H \to \mu\tau$ decays is observed with a significance of 2.4 standard deviations, and corresponds to a best-fit branching fraction $\mathcal{B}(H \to \mu\tau) = (0.84^{+0.39}_{-0.37})\%$. The ATLAS experiment does not confirm the excess seen by CMS [166] but does not exclude its existence, and more precise results from the next LHC runs are looked forward to.

- In some BSM models, the SM-like scalar boson could decay to invisible particles with a large branching fraction. Such a possibility is investigated through final states with a large transverse missing energy coming from H decays to invisible particles, and other physics objects from H production in association with a Z boson, in the vector boson fusion production mode, or in the gluon-gluon fusion mode with a jet from initial state radiation. The combination leads to an upper limit at 95% CL of 36% on the branching fraction of the 125-GeV state to invisible particles [167].

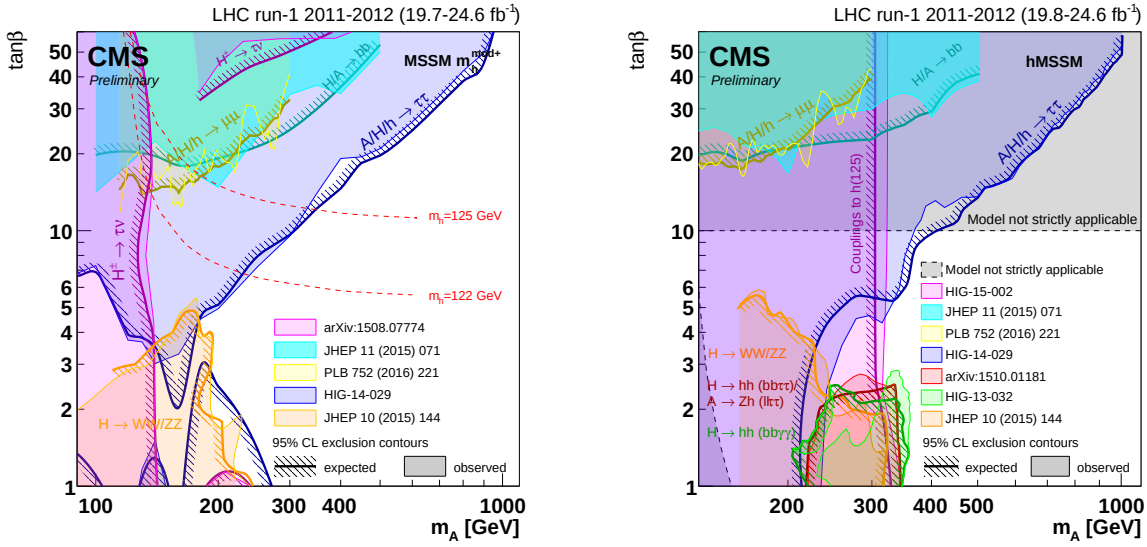

Figure 14.4: 95% CL exclusions contours as obtained by the most sensitive CMS analyses in the context of the MSSM that have been performed on the LHC Run-1 dataset. The colored filled areas correspond to the regions in m_A and $\tan\beta$ that have been excluded at 95% CL. The colored (slightly darker shaded) lines with hatches correspond to the regions that were expected to be excluded. The exclusions are shown for the (left) MSSM m_h^{mod+} scenario with $\mu = 200$ GeV, and the (right) hMSSM scenario. The regions in m_A and $\tan\beta$ where the hMSSM is not strictly applicable are marked in gray. The theoretical uncertainty of the MSSM predictions on m_h has been estimated to be ± 3 GeV. [168, 169]

14.1.3 MSSM and 2HDM scalar searches

Different parts of the MSSM parameter space can be covered by the study of a variety of scalar decays. As described in Chapter 13, the search for resonances decaying to a pair of tau leptons can exclude scenarios with large $\tan\beta$, for which the scalar couplings to leptons and down-type quarks are enhanced. Decays sensitive in the same high $\tan\beta$ region, but less powerful, include $H \to \mu\mu$ and $H \to bb$. At low $\tan\beta$, different final states can uncover an MSSM scalar sector: $H \to WW$, $H \to ZZ$, $A \to Zh$ and $H \to hh$. Meanwhile the search for a charged scalar boson is sensitive to the low m_A region. A summary of the searches for an MSSM scalar sector performed with the CMS data in Run-1 is presented in Fig. 14.4, in the m_h^{mod+} [152, 153] and hMSSM [44] benchmark scenarios [168]. As the MSSM is a special type of 2HDM, these searches can also be interpreted in 2HDM [168]. However, because of the larger number of free parameters, the comparison of the results of several analyses is not as straightforward. No excess has been observed in any search for a 2HDM scalar sector in Run-1 or Run-2 as of now.

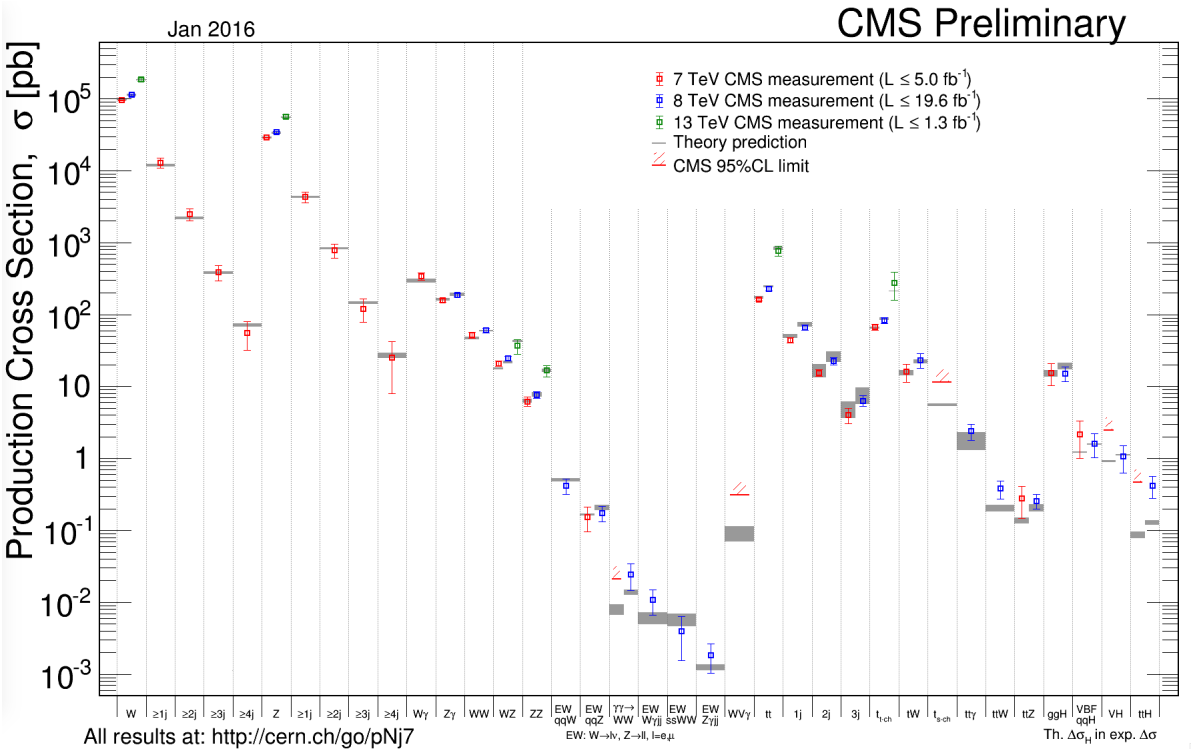

Figure 14.5: Comparison of theoretically-predicted cross sections for various SM processes at 7, 8 and 13 TeV, with experimental measurements made with the CMS detector in Run-1 and Run-2. [173]

14.2 Overview of other SM and BSM results of the CMS experiment

14.2.1 Standard model

With the 25 fb^{-1} proton-proton data collected by the CMS detector in Run-1, unprecedented precision on the measurement of the cross section of SM processes could be achieved [170,171]. All measurements and theory predictions are in remarkable agreement at 7, 8, and 13 TeV center-of-mass energy, as presented in Fig. 14.5. The top quark mass measurement precision reached a great accuracy in Run-1 at CMS: $m_t = 172.44 \pm 0.13$ (stat.) ± 0.47 (syst.) GeV [160]. This value supplants the "world combination" performed in 2014 with the results of the ATLAS, CDF, CMS and D0 experiments [172]. More SM measurements were made in Run-1 [170, 171], but are not be detailed here.

14.2.2 Dark matter

Unlike direct and indirect detection experiments, collider experiments not only search for dark matter (DM) candidates, but could also in principle produce them. DM candidates produced at the LHC are assumed to have weak-scale mass and interaction cross

section with baryonic matter, and therefore to escape the detector leaving as signature a momentum imbalance. Most CMS searches for dark matter look for pair-produced dark matter candidates, characterized by a large transverse missing energy $\not{E}_T$, produced in association with an object identifiable in the detector; such analyses are generically called mono-X + $\not{E}_T$. The most sensitive mono-X + $\not{E}_T$ channel is the monojet, where one jet is produced from initial state radiation (ISR) and can be triggered on. Other mono-X + $\not{E}_T$ analyses include the mono-photon, mono-scalar, mono-Z, mono-top and mono-lepton channels. Collider experiments are complementary to direct and indirect detection experiments, and are typically more sensitive to low DM particle masses ($m_{DM} < 10$ GeV) and spin-dependent interactions. Assuming a simplified model with a vector particle decaying to a pair of DM particles, the CMS experiment excludes at 90% confidence level (CL) in the monojet channel, mediator masses up to 1.6 TeV with Run-1 and 1.3 TeV with Run-2 data, for low DM particle masses [174, 175].

14.2.3 Supersymmetry

A broad variety of analyses have searched for SUSY particles and processes in Run-1, without finding any hint of BSM physics [176]. If they are light enough to be produced at the LHC, strongly-produced SUSY particles are expected to have the largest production cross section of all sparticles. CMS analyses set limits on simplified models where gluinos or squarks are pair-produced, with inclusive searches. Other searches target processes with smaller production cross sections, such as the direct production of stop quarks, sbottom quarks or electroweakinos. Results from different gluino and stop quark searches, interpreted in Simplified Model Spectra (SMS) are shown in Fig. 14.6. Even though the masses probed almost reach the highest possible mass for superparticles, many SUSY models have not been addressed yet, and a large parameter space remains unexplored. The SUSY physics program at the LHC will continue in the next runs.

14.2.4 Others

Many searches for exotic models (Z' boson, W' boson, leptoquarks, heavy stable charged particles, excited leptons, heavy Majorana neutrinos, ...) have been performed at the LHC [178]. As of now only one promising excess has been reported by both the ATLAS and CMS collaborations: an excess of events in the diphoton mass spectrum at a mass of about 750 GeV [179,180]. The global significance is about two standard deviations in the ATLAS analysis with Run-2 data, and somewhat lower for CMS, but it is intriguing that an excess is seen at the same place in both experiments. Many theoretical models have been proposed to address such a deviation from the SM if it were to be confirmed with larger datasets in Run-2.

14.3 Future collider experiments

The HL-LHC program extends until about 2035, but it is already time to design its successor, as many fundamental questions will remain. If no new physics is observed at the LHC, the reason could be that the new physics mass scale is beyond the LHC reach,

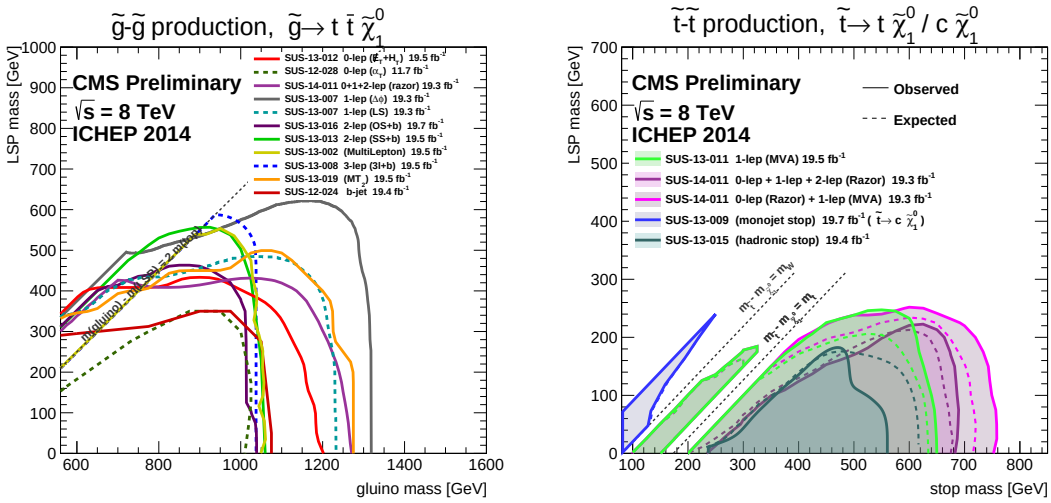

Figure 14.6: Summary of exclusion limits in Simplified Model Spectra from several SUSY gluino (left) and stop (right) searches performed with the data collected by the CMS detector in 2012. [177]

or that the mass scale is accessible at the LHC but the final states are elusive to the direct search. Different options of linear and circular colliders are studied to address both cases. In general, electron-positron colliders have the advantage to provide an extremely clean experimental environment, with an absence of strong-interaction backgrounds and with controlled electroweak backgrounds, allowing for very precise measurements. Additionally, such colliders do not suffer from underlying event and pileup collision contamination, and the triggering is easy with a 100% efficiency. On the other hand, hadronic colliders have a larger mass reach for the exploration of new physics, but require carefully-designed subdetectors for the identification of particles in a crowded environment. Circular colliders, relative to linear colliders, can provide a much higher luminosity because of larger collision rates, continuous injection and multiple collision points, and their beam energy can be measured with great accuracy. However, the center-of-mass energy they can reach is lower because of synchrotron radiation, they consume a large power, and their beams are difficult to polarize. A comparison between the luminosity and center-of-mass energy linear and circular colliders can reach is shown in Fig. 14.7 for some collider projects. Different collider projects are described in the next paragraphs.

The FCC-ee (also known as TLEP) [181] program involves electron-positron collisions at a center-of-mass energy of 91 (Z boson pole), 160 (WW threshold), 240 (H production peak, dominated by Higgsstrahlung) and 350 ($t\bar{t}$ threshold) GeV in a circular collider with a circumference between 80 and 100 km situated in the Geneva basin. The FCC-ee would allow for extremely precise SM process measurements with permille-level uncertainties, and could set indirect constrains on heavy BSM particles. The dominant uncertainty associated to the measurement of SM processes would be theoretical. The scalar physics program of the FCC-ee consists in determining all scalar boson couplings in a model-

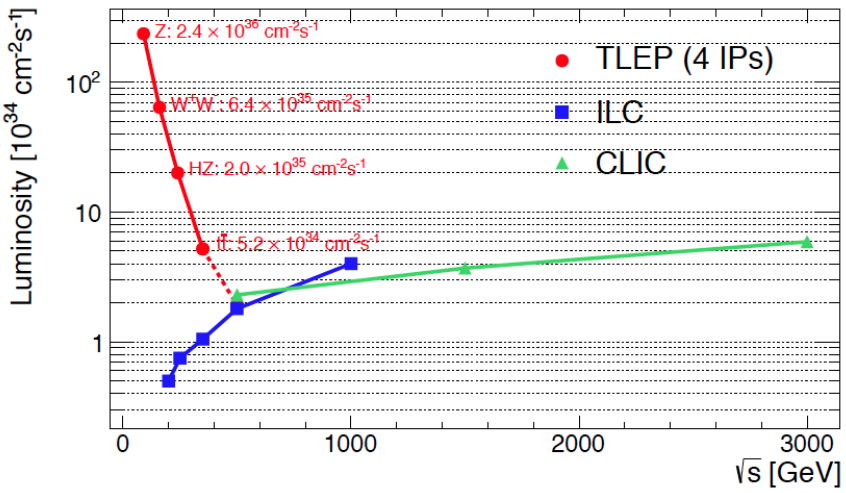

Figure 14.7: Comparison between the instantaneous luminosity linear (ILC and CLIC) and circular (TLEP/FCC-ee with four interaction points) colliders can deliver as a function of the center-of-mass energy. [181]

independent way, in measuring its total decay width indirectly and evaluating its rare or exotic decays. The FCC-ee physics program for electroweak precision measurements relies on the production of about 10^{13} Z bosons, 10^8 W bosons and 10^6 $t\bar{t}$ pairs.

After a dozen years of operation (about two years at the Z pole, one or two years at the WW threshold, five years as a "Higgs factory", and five years at the $t\bar{t}$ threshold), and more than two million scalar bosons produced, the FCC-ee could potentially be upgraded to become a proton-proton collider, FCC-hh, with a center-of-mass energy of around 100 TeV [182]. Because the energy is proportional to the magnetic field and to the collider radius, such an energy can be achieved by multiplying the magnetic field by a factor two and the radius by a factor four relative to the LHC. The combination of FCC-ee and FCC-hh reduces the costs of having two experiments, and would permit to obtain the best precision, sensitivity and reach for new physics among all other collider options. The FCC-hh could collect between 250 and 1000 fb^{-1} every year, which would lead to about 20 ab^{-1} after twenty-five years of operation. The option of a circular collider between electrons and hadrons, FCC-eh, is also under study [183].

The International Linear Collider (ILC) [184] is a linear electron-positron collider that could be built in Japan in a few years. The ILC would in a first phase collect 500 fb^{-1} at an energy in the electron-positron center-of-mass of 250 GeV, 200 fb^{-1} at 350 GeV, and 500 fb^{-1} at 500 GeV, and in a second phase 3500 fb^{-1} at 500 GeV and 1500 fb^{-1} at 250 GeV. Such a machine has a low beamstrahlung, and its luminosity and energy can be determined precisely. The ILC provides a clean environment to measure the scalar boson couplings with a great accuracy, which would allow to eventually highlight deviations

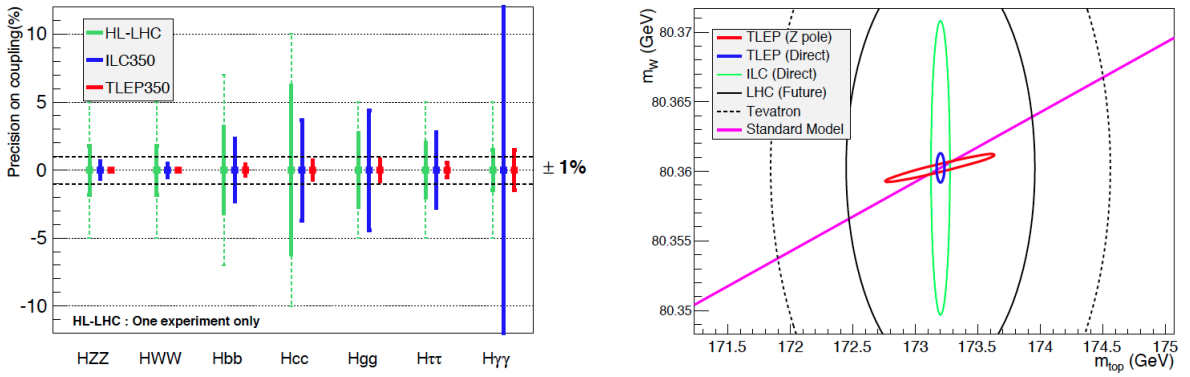

Figure 14.8: Left: Expected precision on the measurement of the H boson signal strength at the HL-LHC, ILC and TLEP/FCC-ee. The TLEP and ILC indications correspond to the data expected to be collected during the run at 350 GeV center-of-mass energy and during the previous runs at lower energy. Right: Precision on the top quark and W boson mass measurements achievable with different projects of colliders. [181]

from the SM predictions. Its physics program also covers measurements of the properties of the top quark with a great accuracy, and searches for new particles at the TeV scale.

A comparison of the expected reach of the HL-LHC, FCC-ee and ILC in terms of scalar boson signal strength precision, top quark mass and scalar boson mass measurements is shown in Fig. 14.8.

14.4 Chapter summary

Overview of LHC results and prospects for future colliders

The CMS physics program has covered an impressive range of new physics searches and precision measurements as of now. The highlight of the Run-1 is the discovery of a new particle compatible with the SM scalar boson and the measurement of some of its properties, but the fact that searches for BSM physics, such as dark matter or SUSY, do not observe any deviation from the SM in a large parameter space is not less interesting. Future collider studies and designs have started in order to take over the LHC physics program and to address the unanswered questions after the LHC stops running.

Conclusion

The LHC started operating in 2010, at an unprecedented center-of-mass energy of 7 TeV. Its Run-1 extended until the end of 2012 with a center-of-mass energy of 8 TeV. After a first long shutdown, the LHC resumed its operations in 2015 with proton-proton collisions at a center-of-mass energy of 13 TeV. The discovery of a new particle, H, compatible with the Brout-Englert-Higgs boson of the standard model (SM) is without contest the highlight of the Run-1 of the LHC.

The discovery of the new particle was driven by the searches in the $H \to \gamma\gamma$ and $H \to ZZ$ decay channels, but many other decay modes are open in the SM for a mass of the scalar boson equal to 125 GeV. Measuring the production cross sections and the branching fractions of the new boson for all possible production and decay modes is essential to assess its compatibility with the SM predictions. In Chapters 7 and 8 is described a search for the SM scalar boson, produced in association with a Z boson or a W boson respectively, and decaying to a pair of tau leptons. The di-tau final state is the most sensitive fermionic decay channel, and therefore gives the most precise measurement of the Yukawa couplings of the scalar particle. While the vector boson associated production has a small cross section relative to the gluon-gluon fusion and vector boson fusion production modes, an efficient background rejection is obtained by selecting the light leptons originating from the vector boson decays. Both analyses are not sensitive yet to the cross section predicted in the SM for the scalar boson, but their results are compatible with the SM scalar boson hypothesis. After combination with the dominant production modes, the first evidence for the decay of the H boson to a pair of tau leptons is achieved with a significance of 3.2 standard deviations, as detailed in Chapter 9.

In the SM, the H boson decays approximately 6% of the time to tau leptons if it has a mass of 125 GeV. The $H \to \tau\tau$ decay channel is challenging because of the similarity between hadronically decaying taus, and quark and gluon jets. In CMS, the Hadrons Plus Strips (HPS) algorithm is used to reconstruct and identify hadronic taus (τ_h), as described in Chapter 6. It first proceeds by checking that tau candidates correspond to one of the possible tau decay modes by counting the number of tracks and deposits in strips of the electromagnetic calorimeter, and measuring their compatibility with a hadronic tau hypothesis. The second step consists in rejecting jets, electrons and muons by applying further selection criteria, based among others on the isolation of the tau candidates. A

typical selection efficiency of 50% can be reached, for a $j \to \tau_h$ misidentification rate at the percent level, and $e \to \tau_h$ and $\mu \to \tau_h$ misidentification rates at the permille level or below. The performance is also measured in data collected both in Run-1 and Run-2: it is generally compatible with the performance in MC simulations, but some data-to-simulation scale factors not equal to unity are also derived, for example for the $e \to \tau_h$ and $\mu \to \tau_h$ misidentification rates. The uncertainties on the tau identification efficiency and tau energy scale in data amount to 6% and 3% respectively.

The SM is known not to answer a series of questions, and is thought to be a good approximation at low energies of a more fundamental theory. This is motivated among others by the existence of dark matter and dark energy, the hierarchy problem, describing the fact that the H boson mass receives huge corrections, or the will to unify all fundamental interactions. Many of the models that address some of these questions introduce an extended scalar sector. This is the case of the minimal supersymmetric SM (MSSM), which contains three neutral and two charged scalars. The MSSM can be described at tree level by two parameters: m_A the mass of the neutral pseudoscalar, and $\tan\beta$ the ratio between the vacuum expectation values of the two scalar doublets. Different searches should be performed to cover the full parameter space of the MSSM; for example $H/A/h \to \tau\tau$ is sensitive at large $\tan\beta$ while $A \to Zh$ searches are powerful at low $\tan\beta$ only. More general models are two-Higgs-doublet models (2HDM), which also give rise to five (pseudo)scalars. Depending on the choice of its parameters, it can motivate the existence of light pseudoscalars. A simple extension of 2HDM is 2HDM+S, where a scalar singlet is added to the two scalar doublets. Such models make the decay of the 125-GeV particle to non-SM particles possible, even after the precision measurements on the SM-like scalar performed in Run-1. In general, tau leptons are important objects to uncover a potentially extended scalar sector, because the scalar boson Yukawa couplings are proportional to the mass, and taus are by far heavier than muons and electrons.

Chapter 10 details the search for $A \to Zh$ decays in the $\ell\ell\tau\tau$ final states. The light leptons originating from the Z boson allow for an efficient background rejection, while $h \to \tau\tau$ has a large branching fraction relative to most other decay channels. The analysis is performed with 8 TeV data, and combined with $H \to hh \to bb\tau\tau$, which is also sensitive at low $\tan\beta$ and in a comparable mass range. No excess is observed in any of the final states, and the results are interpreted as model-independent upper limits on the cross section times branching fraction, and as model-dependent limits in the $m_A - \tan\beta$ plane in the MSSM and 2HDM type-2. Cross sections times branching fractions between 5 and 17 fb are excluded at 95% CL for pseudoscalar boson masses ranging between 220 and 350 GeV in the $A \to Zh \to \ell\ell\tau\tau$ analysis.

The possibility of exotic decays of the h boson to a pair of light pseudoscalar bosons is studied in Chapter 11. The $h \to aa \to \mu\mu\tau\tau$ is especially sensitive in 2HDM+S type-3, where, for $\tan\beta > 1$, the decays of the pseudoscalar a boson to leptons are enhanced over its decays to quarks. The expected SM backgrounds are particularly low, and an unbinned

shape analysis is performed. No significant excess is observed, and upper limits between 4 and 15% can be set on $\mathcal{B}(h \to aa)$ in the hypotheses that the h production cross section is the same as predicted in the SM, and that the a boson does not decay to quarks, which is a good approximation at large $\tan\beta$ in 2HDM+S type-3. The end of the chapter presents an interpretation of all $h \to aa$ searches performed with the CMS detector in Run-1, in different types of 2HDM+S and for different $\tan\beta$ values; pseudoscalar masses between 1 GeV to half of the h boson mass are covered by the analyses.

In 2HDM and for a given choice of the model parameters, the production of light pseudoscalars is allowed with large cross sections, while not contradicting other LHC measurements. Chapter 12 describes the search for a light pseudoscalar decaying to taus and produced in association with b quarks. The search covers a mass region between 25 and 80 GeV, which was unexplored before at the LHC. No excess is observed in any of the three di-tau final states studied, and stringent upper limits are set on the cross section times branching fraction. The analysis is seen to exclude such a process for pseudoscalar masses between 25 and 80 GeV in 2HDM type-2 with negative Yukawa couplings of the h boson to down-type fermions.

Chapter 13 presents the search for a heavy resonance ($\Phi = A/H/h$) in the MSSM, with an improved sensitivity obtained by categorizing the events according to the p_T of their hadronic taus, and by using the MVA tau identification including lifetime information. The $\Phi \to \tau_h\tau_h$ decay channel, which has the largest branching fraction, is described in details. Again, no excess of data above the predicted SM backgrounds is observed, and limits are set on the production cross section times branching fractions for the $bb\Phi$ and $gg\Phi$ production modes. The excluded cross section times branching fraction ranges approximately from 22 pb to 8 fb depending on the resonance mass and on the production mode. The results are also interpreted in some benchmark scenarios, where large parts of the regions with high $\tan\beta$ are excluded. In particular, $\tan\beta$ values as low as about 3 can be excluded in the m_h^{max} scenario of the MSSM for $m_A \simeq 140$ GeV.

No evidence for BSM physics has been observed in any of the searches presented in this thesis, neither in other CMS measurements performed in Run-1 as detailed in Chapter 14. The Run-2 of the LHC started at the beginning of 2015, with an increased center-of-mass energy, which permits to explore completely new regions. The large luminosity that will be collected together with the increased center-of-mass energy, will make searches for BSM processes with smaller cross sections or heavier particles possible, and allow for more precise measurements of the SM-like scalar properties, which might highlight deviations from the SM expectation. The MSSM parameter space has been impressively well covered in Run-1, though unexplored regions, especially at large and intermediate m_A, still remain. In addition, many new physics signatures have not yet been studied. This is only the beginning of the LHC program, and many discoveries most likely lie ahead of us.

Appendix A

Technical details about physics analyses

A.1 Monte Carlo samples and collected datasets

The collision datasets used in the analyses described throughout this thesis are presented in Tab. A.1, A.2 and A.3, at 7, 8 and 13 TeV center-of-mass energies respectively. The Monte Carlo samples, together with their generators and cross sections are indicated in Tab. A.4, A.5 and A.6.

A.2 Triggers

The trigger paths used in the analyses described throughout this thesis are indicated in Tab. A.7 for every studied final state.

	Dataset	Run-range	$\mathcal{L}$ (fb)	Chapters						
				6	7	8	10	11	12	13
$\mu\mu$	/DoubleMu/Run2011A-16Jan2012-v1	160329–175770	0.211		✓					
	/DoubleMu/Run2011B-16Jan2012-v1	175832–180252	2.562		✓					
ee	/DoubleElectron/Run2011A-16Jan2012-v1	160329–175770	0.211		✓					
	/DoubleElectron/Run2011B-16Jan2012-v1	175832–180252	2.562		✓					
$e\mu$	/MuEG/Run2011A-16Jan2012-v1	160329–175770	0.211		✓					
	/MuEG/Run2011B-16Jan2012-v1	175832–180252	2.562		✓					

Table A.1: Datasets collected at 7 TeV center-of-mass energy, used in the physics analyses detailed in this thesis.

	Dataset	Run-range	$\mathcal{L}$ (fb)	Chapters						
				6	7	8	10	11	12	13
$e\tau_h/\mu\tau_h$	/TauPlusX/Run2012A-22Jan2013-v1	190456–193621	0.887						✓	✓
	/TauPlusX/Run2012B-22Jan2013-v1	193833–196531	4.446						✓	✓
	/TauPlusX/Run2012C-22Jan2013-v1	198022–203742	7.153						✓	✓
	/TauPlusX/Run2012D-22Jan2013-v1	203777–208686	7.318						✓	✓
$\tau_h\tau_h$	/TauParked/Run2012B-22Jan2013-v1	193833–196531	3.885							✓
	/TauParked/Run2012C-22Jan2013-v1	198022–203742	7.153							✓
	/TauParked/Run2012D-22Jan2013-v1	203777–208686	7.318							✓
	/JetHT/Run2012B-22Jan2013-v1	193833–196531	3.885							✓
	/JetHT/Run2012C-22Jan2013-v1	198022–203742	7.153							✓
	/JetHT/Run2012D-22Jan2013-v1	203777–208686	7.318							✓
$e\mu$	/MuEG/Run2012A-22Jan2013-v1	190456–193621	0.887			✓			✓	✓
	/MuEG/Run2012B-22Jan2013-v2	193833–196531	4.446			✓			✓	✓
	/MuEG/Run2012C-22Jan2013-v3	198022–203742	7.153			✓			✓	✓
	/MuEG/Run2012D-22Jan2013-v4	203777–208686	7.318			✓			✓	✓
$\mu\mu$	/DoubleMu/Run2012A-22Jan2013-v1	190456–193621	0.887		✓		✓	✓		
	/DoubleMuParked/Run2012B-22Jan2013-v1	193833–196531	4.446		✓		✓	✓		
	/DoubleMuParked/Run2012C-22Jan2013-v1	198022–203742	7.153		✓		✓	✓		
	/DoubleMuParked/Run2012D-22Jan2013-v1	203777–208686	7.318		✓		✓	✓		
ee	/DoubleElectron/Run2012A-22Jan2013-v1	190456–193621	0.887		✓		✓			
	/DoubleElectron/Run2012B-22Jan2013-v1	193833–196531	4.446		✓		✓			
	/DoubleElectron/Run2012C-22Jan2013-v1	198022–203742	7.153		✓		✓			
	/DoubleElectron/Run2012D-22Jan2013-v1	203777–208686	7.318		✓		✓			
μ	/SingleMu/Run2012A-22Jan2013-v1	190456–193621	0.887	✓						
	/SingleMu/Run2012B-22Jan2013-v1	193833–196531	4.446	✓						
	/SingleMu/Run2012C-22Jan2013-v1	198022–203742	7.153	✓						
	/SingleMu/Run2012D-22Jan2013-v1	203777–208686	7.318	✓						

Table A.2: Datasets collected at 8 TeV center-of-mass energy, used in the physics analyses detailed in this thesis. This table considers only the $e\tau_h$, $\mu\tau_h$, $e\mu$ and $\tau_h\tau_h$ final states of the MSSM $\Phi \to \tau\tau$ analysis described in Chapter 13.

	Dataset	Chapters						
		6	7	8	10	11	12	13
μ	/SingleMuon/Run2015C25ns-16Dec2015-v1	✓						
	/SingleMuon/Run2015D-16Dec2015-v1	✓						

Table A.3: Datasets collected at 13 TeV center-of-mass energy, used in the physics analyses detailed in this thesis.

Process	Generator	XS×$\mathcal{B}$ (pb)	Chapters						
			6	7	8	10	11	12	13
$ZZ \to 4\ell$	Pythia	0.106		✓	✓				
$gg \to ZZ^* \to 2\ell 2\ell$	Pythia	0.005		✓					
$WZ \to 3\ell\nu$	Madgraph	0.868			✓				
$t\bar{t}Z$	Madgraph	0.139		✓					
$WH/ZH/ttH$ with $H \to \tau\tau$	Pythia	0.021		✓	✓				
$H \to WW \to 2\ell 2\nu$, $WH, ZH, t\bar{t}H$	Powheg	0.0053		✓	✓				

Table A.4: MC samples, with their generators and cross sections used in 7 TeV analyses. The cross sections for the SM scalar boson are indicated for $m_H = 125$ GeV.

	Process	Generator	XS×$\mathcal{B}$ (pb)	Chapters						
				6	7	8	10	11	12	13
Di- and tri-boson	$WW \to 2\ell 2\nu$	Madgraph	5.824						✓	✓
	$WZ \to 2\ell 2q$	Madgraph	2.207						✓	✓
	$WZ \to 3\ell\nu$	Madgraph	1.058			✓			✓	✓
	$ZZ \to 4\ell$	Madgraph	0.187				✓	✓	✓	✓
	$ZZ \to 4\ell$	Pythia	0.130		✓	✓				
	$gg \to ZZ^* \to 2\ell 2\ell$	Pythia	0.012		✓		✓			
	$ZZ \to 2\ell 2\nu$	Madgraph	0.716						✓	✓
	$ZZ \to 2\ell 2q$	Madgraph	2.502						✓	✓
	WW (inclusive)	Pythia	69.9	✓						
	WZ (inclusive)	Pythia	33.2	✓						
	ZZ (inclusive)	Pythia	8.4	✓						
	WWZ	Madgraph	0.058				✓			
	WZZ	Madgraph	0.020				✓			
	ZZZ	Madgraph	0.006				✓			
Top	$t\bar{t} \to 2b2\ell 2\nu$	Madgraph	26.198						✓	✓
	$t\bar{t} \to 2b\ell\nu 2q$	Madgraph	109.3						✓	✓
	$t\bar{t} \to 2b4q$	Madgraph	114.02						✓	✓
	$t\bar{t}$ (inclusive)	Madgraph	245.8	✓						
	$t/\bar{t} \to tW$	Powheg	22.2	✓					✓	✓
	$t\bar{t}Z$	Madgraph	0.208		✓		✓			
Drell-Yan	$Z/\gamma^* \to 2\ell$ +jets, $m_{\ell\ell} > 50$ GeV	Madgraph	2950	✓		✓			✓	✓
	$Z/\gamma^* \to 2\ell + 1$ jet, $m_{\ell\ell} > 50$ GeV	Madgraph	561						✓	✓
	$Z/\gamma^* \to 2\ell + 2$ jets, $m_{\ell\ell} > 50$ GeV	Madgraph	181						✓	✓
	$Z/\gamma^* \to 2\ell + 3$ jets, $m_{\ell\ell} > 50$ GeV	Madgraph	51.1						✓	✓
	$Z/\gamma^* \to 2\ell + 4$ jets, $m_{\ell\ell} > 50$ GeV	Madgraph	23						✓	✓
	$Z/\gamma^* \to 2\ell$ +jets, $10 < m_{\ell\ell} < 50$ GeV	Madgraph	11050						✓	
	$Z/\gamma^* \to 2\ell + 1$ jet, $10 < m_{\ell\ell} < 50$ GeV	Madgraph	716.0						✓	
	$Z/\gamma^* \to 2\ell +$ 2 jets, $10 < m_{\ell\ell} < 50$ GeV	Madgraph	309.7						✓	
W+jets	$W \to \ell\nu$ + jets (inclusive)	Madgraph	30400	✓					✓	✓
	$W \to \ell\nu + 1$ jets	Madgraph	5400	✓					✓	✓
	$W \to \ell\nu + 2$ jets	Madgraph	1750	✓					✓	✓
	$W \to \ell\nu + 3$ jets	Madgraph	519	✓					✓	✓
	$W \to \ell\nu + 4$ jets	Madgraph	214	✓					✓	✓
SM scalar	$H \to \tau\tau$, gg fusion	Powheg	1.218						✓	✓
	$H \to \tau\tau$, VBF	Powheg	0.0997						✓	✓
	$WH/ZH/ttH$ with $H \to \tau\tau$	Pythia	0.0789						✓	✓
	$H \to \tau\tau$, ZH	Powheg	0.0265				✓			
	$H \to WW \to 2\ell 2\nu$, ggH	Powheg	0.438						✓	✓
	$H \to WW \to 2\ell 2\nu$, VBF	Powheg	0.0358						✓	✓
	$H \to WW \to 2\ell 2\nu$, $WH, ZH, t\bar{t}H$	Powheg	0.0065				✓			
BSM scalars	$A \to Zh \to \ell\ell\tau\tau$	Madgraph	-				✓			
	$h \to aa \to \mu\mu\tau\tau$, gg fusion	Pythia	-					✓		
	$h \to aa \to \mu\mu\tau\tau$, VBF	Pythia	-					✓		
	$h \to aa \to \mu\mu\tau\tau$, Wh	Pythia	-					✓		
	$h \to aa \to \mu\mu\tau\tau$, Zh	Pythia	-					✓		
	$bbA \to bb\tau\tau$, $m_A < 90$ GeV	Pythia	-						✓	
	$\Phi \to \tau\tau$, gg fusion	Pythia	-							✓
	$\Phi \to \tau\tau$, b-association	Pythia	-							✓

Table A.5: MC samples, with their generators and cross sections used in 8 TeV analyses. The k-factors are respectively for W+jets, $Z/\gamma^* \to 2\ell$+jets $m_{\ell\ell} > 50$ GeV and $Z/\gamma^* \to 2\ell$+jets $10 < m_{\ell\ell} < 50$ GeV, 1.234, 1.188 and 1.33. The cross sections for the SM scalar boson are indicated for $m_H = 125$ GeV.

Process	Generator	XS×$\mathcal{B}$ (pb)	Chapters						
			6	7	8	10	11	12	13
$VV \to 2\ell 2\nu$	aMC@NLO	11.95	✓						
$ZZ \to 2\ell 2q$	aMC@NLO	3.22	✓						
$ZZ \to 4\ell$	aMC@NLO	1.21	✓						
$WW \to 1\ell 1\nu 2q$	aMC@NLO	50.00	✓						
$WZ \to 2\ell 2q$	aMC@NLO	5.60	✓						
WZ jets	aMC@NLO	5.26	✓						
$WZ \to 3\ell 1\nu$	aMC@NLO	4.71	✓						
$WZ \to 1\ell 3\nu$	aMC@NLO	3.05	✓						
$WZ \to 1\ell 1\nu 2q$	aMC@NLO	10.71	✓						
$t\bar{t}$ (inclusive)	Powheg	831.8	✓						
$t/\bar{t} \to tW$	Powheg	71.2	✓						
$Z/\gamma^* \to 2\ell$ +jets, $m_{\ell\ell} > 50$ GeV	Madgraph	6025.2	✓						
$W \to \ell\nu$ + jets (inclusive)	Madgraph	61526.7	✓						

Table A.6: MC samples, with their generators and cross sections used in 13 TeV analyses. W+jets and Z+jets cross sections are quoted at NNLO.

	Year	Path	Chapters						
			6	7	8	10	11	12	13
$\ell\tau_h$	2012	Ele22_eta2p1_WP90Rho_LoosePFIsoTau20						✓	✓
	2012	IsoMu17_eta2p1_LoosePFIsoTau20						✓	✓
$\tau_h\tau_h$	2012	DoubleMediumIsoPFTau35_Trk5_eta2p1							✓
	2012	DoubleMediumIsoPFTau35_Trk1_eta2p1							✓
$e\mu$	2011	Mu8_Ele17_CaloIdL			✓				
	2011	Mu8_Ele17_CaloIdT_CaloIsoVL			✓				
	2012	Mu8_Ele17_CaloIdT_CaloIsoVL_TrkIdVL_TrkIsoVL			✓			✓	✓
	2011	Mu17_Ele8_CaloIdL			✓				
	2011	Mu17_Ele8_CaloIdT_CaloIsoVL			✓				
	2012	Mu17_Ele8_CaloIdT_CaloIsoVL_TrkIdVL_TrkIsoVL			✓			✓	✓
$\mu\mu$	2011	DoubleMu7		✓					
	2011	Mu13_Mu8		✓					
	2011/2012	Mu17_Mu8		✓		✓	✓		
	2012	Mu17_TkMu8		✓		✓	✓		
ee	2011	Ele17_CaloIdL_CaloIsoVL_Ele8_CaloIdL_CaloIsoVL		✓					
	2011/2012	Ele17_CaloIdT_CaloIsoVL_TrkIdVL_TrkIsoVL_ Ele8_CaloIdT_CaloIsoVL_TrkIdVL_TrkIsoVL		✓		✓			
μ	2011/2012	IsoMu24_eta2p1	✓						
	2015	IsoMu18	✓						

Table A.7: Trigger paths used in the analyses detailed in this thesis. For the MSSM $\Phi \to \tau\tau$ analysis of Chapter 13, only the $e\tau_h$, $\mu\tau_h$, $\tau_h\tau_h$ and $e\mu$ final states at 8 TeV center-of-mass energy are covered.

Bibliography

[1] C. Burgess and G. Moore. *The standard model, a primer*. Cambridge University Press, 2013.

[2] D. Griffiths. *Introduction to elementary particles*. Wiley-VCH, 2008.

[3] S. L. Glashow. Partial symmetries of weak interactions. *Nucl. Phys.*, 22:579–588, 1961.

[4] S. Weinberg. A model of leptons. *Phys. Rev. Lett.*, 19:1264–1266, 1967.

[5] A. Salam. Weak and electromagnetic interactions. *Conf. Proc.*, C680519:367–377, 1968.

[6] J. Gunion et al. *The Higgs hunter's guide*. Perseus Publishing, 1990.

[7] P. Ramond. *Journeys beyond the standard model*. Perseus Books, 1999.

[8] J. J. Thomson. Cathode rays. *Phil. Mag.*, 44:293–316, 1897.

[9] Particle Data Group. Review of particle physics. *Chin. Phys.*, C38:090001, 2014.

[10] P. Higgs. Broken symmetries and the masses of gauge bosons. *Phys. Rev. Lett.*, 13:508–509, 1964.

[11] P. Higgs. Broken symmetries, massless particles and gauge fields. *Phys. Lett.*, 12:132–133, 1964.

[12] P. Higgs. Spontaneous symmetry breakdown without massless bosons. *Phys. Rev.*, 145:1156–1163, 1966.

[13] F. Englert and R. Brout. Broken symmetry and the mass of gauge vector mesons. *Phys. Rev. Lett.*, 13:321–323, 1964.

[14] G. S. Guralnik, C. R. Hagen, and T. W. B. Kibble. Global conservation laws and massless particles. *Phys. Rev. Lett.*, 13:585–587, 1964.

[15] T. W. B. Kibble. Symmetry breaking in non abelian gauge theories. *Phys. Rev.*, 155:1554–1561, 1967.

[16] CMS Collaboration. Evidence for the 125 GeV Higgs boson decaying to a pair of τ leptons. *JHEP*, 1405:104, 2014.

[17] LHC Higgs cross section working group. LHC Higgs Cross Section Working Group. https://twiki.cern.ch/twiki/bin/view/LHCPhysics/CrossSections.

[18] A. Djouadi. The anatomy of electro-weak symmetry breaking - Tome I: The Higgs boson in the standard model. 2005. arXiv:0503.172.

[19] CMS Collaboration. Observation of a new boson at a mass of 125 GeV with the CMS experiment at the LHC. *Phys. Lett.*, B716:30–61, 2013.

[20] ATLAS Collaboration. Observation of a new particle in the search for the standard model Higgs boson with the ATLAS detector at the LHC. *Phys. Lett.*, B716:1–29, 2013.

[21] Y. Nagashima. *Beyond the standard model of elementary particle physics*. Wiley-VCH, Weinheim, 2014.

[22] Super-Kamiokande Collaboration. Evidence for oscillation of atmospheric neutrinos. *Phys. Rev. Lett.*, 81:1562–1567, 1998.

[23] Double Chooz Collaboration. Indication for the disappearance of reactor electron antineutrinos in the Double Chooz experiment. *Phys. Rev. Lett.*, 108:131801, 2012.

[24] F. Zwicky. Die Rotverschiebung von extragalaktischen Nebeln. *Helv. Phys. Acta*, 6:110–127, 1933.

[25] Planck Collaboration. Planck 2015 results. XIII. Cosmological parameters. 2015. arXiv:1502.01589.

[26] A. D. Sakharov. Violation of CP invariance, C asymmetry, and baryon asymmetry of the universe. *Pisma Zh. Eksp. Teor. Fiz.*, 5:32–35, 1967.

[27] G. Burdman. New solutions to the hierarchy problem. *Braz. J. Phys.*, 37:506–513, 2007.

[28] G. C. Branco et al. Theory and phenomenology of two-Higgs-doublet models. *Phys. Rept.*, 516:1–102, 2012.

[29] M. Carena and H. Haber. Higgs boson theory and phenomenology. *Prog. Part. Nucl. Phys.*, 50:63–152, 2003.

[30] A. Djouadi. The Higgs particles in the MSSM. `http://ecole-de-gif.in2p3.fr/Cours/GIF01/djouadi.ps`.

[31] S. L. Glashow and S. Weinberg. Natural conservation laws for neutral currents. *Phys. Rev.*, D15:1958, 1977.

[32] N. Deshpande and E. Ma. Pattern of symmetry breaking with two Higgs doublets. *Phys. Rev.*, D18:2574, 1978.

[33] J. Gunion and H. Haber. CP-conserving two-Higgs-doublet model: The approach to the decoupling limit. *Phys. Rev. D*, 67, 2003.

[34] N. Craig, J. Galloway, and S. Thomas. Searching for signs of the second Higgs doublet. 2013. arXiv:1305.2424.

[35] J. Bernon et al. Light Higgs bosons in two-Higgs-doublet models. *Phys. Rev.*, D91(7):075019, 2015.

[36] S. Martin. A supersymmetry primer. 1998. Adv. Ser. Direct. High Energy Phys.18,1.

[37] J. Wess and B. Zumino. Supergauge transformations in four-dimensions. *Nucl. Phys.*, B70:39–50, 1974.

[38] Y. A. Golfand and E. P. Likhtman. Extension of the algebra of Poincare group generators and violation of p invariance. *JETP Lett.*, 13:323–326, 1971.

[39] P. Fayet. Supergauge invariant extension of the Higgs mechanism and a model for the electron and its neutrino. *Nucl. Phys.*, B90:104–124, 1975.

[40] P. Fayet. Spontaneously broken supersymmetric theories of weak, electromagnetic and strong interactions. *Phys. Lett.*, B69:489, 1977.

[41] P. Fayet. Supersymmetry and weak, electromagnetic and strong interactions. *Phys. Lett.*, B64:159, 1976.

[42] CMS Collaboration. Search for additional neutral Higgs bosons decaying to a pair of tau leptons in pp collisions at $\sqrt{s} = 7$ and 8 TeV. CMS Physics Analysis Summary CMS-PAS-HIG-14-029, 2015.

[43] A. Djouadi. The anatomy of electro-weak symmetry breaking. II. The Higgs bosons in the minimal supersymmetric model. *Phys. Rept.*, 459:1–241, 2008.

[44] A. Djouadi et al. Fully covering the MSSM Higgs sector at the LHC. *JHEP*, 06:168, 2015.

[45] A. Djouadi and J. Quevillon. The MSSM Higgs sector at a high M_{SUSY}: reopening the low tanβ regime and heavy Higgs searches. *JHEP*, 10:028, 2013.

[46] J. M. Frere, D. R. T. Jones, and S. Raby. Fermion masses and induction of the weak scale by supergravity. *Nucl. Phys.*, B222:11–19, 1983.

[47] E. Cremmer, P. Fayet, and L. Girardello. Gravity induced supersymmetry breaking and low-energy mass spectrum. *Phys. Lett.*, B122:41, 1983.

[48] U. Ellwanger, C. Hugonie, and A. M. Teixeira. The Next-to-Minimal Supersymmetric Standard Model. *Phys. Rept.*, 496:1–77, 2010.

[49] J. E. Kim and H. P. Nilles. The mu problem and the strong CP problem. *Phys. Lett.*, B138:150, 1984.

[50] C. Englert et al. Exploring the Higgs portal. *Phys. Lett.*, B703:298–305, 2011.

[51] M. Carena et al. Complementarity between non-standard Higgs boson searches and precision Higgs boson measurements in the MSSM. *Phys. Rev.*, D91(3):035003, 2015.

[52] D. Curtin et al. Exotic decays of the 125 GeV Higgs boson. *Phys. Rev.*, D90(7):075004, 2014.

[53] D. Curtin, R. Essig, and Y. Zhong. Uncovering light scalars with exotic Higgs decays to $b\bar{b}\mu^+\mu^-$. *JHEP*, 06:025, 2015.

[54] CMS Collaboration. Precise determination of the mass of the Higgs boson and tests of compatibility of its couplings with the standard model predictions using proton collisions at 7 and 8 TeV. *Eur. Phys. J.*, C75(5):212, 2015.

[55] CMS Collaboration. Search for a light NMSSM Higgs boson produced in supersymmetric cascades and decaying into a b-quark pair. CMS Physics Analysis Summary CMS-PAS-HIG-14-030, 2015.

[56] C. Caillol et al. Precision versus discovery: A simple benchmark. *Eur.Phys.J.Plus*, 129:93, 2014.

[57] CMS Collaboration. Combination of standard model Higgs boson searches and measurements of the properties of the new boson with a mass near 125 GeV. CMS Physics Analysis Summary CMS-PAS-HIG-13-005, 2013.

[58] CMS Collaboration. Search for a heavy Higgs boson in the H to ZZ to 2l2nu channel in pp collisions at $\sqrt{s} = 7$ and 8 TeV. CMS Physics Analysis Summary CMS-PAS-HIG-13-005, 2013.

[59] CMS Collaboration. Measurement of Higgs boson production and properties in the WW decay channel with leptonic final states. *JHEP*, 01:096, 2014.

[60] CMS Collaboration. Measurement of the properties of a Higgs boson in the four-lepton final state. *Phys. Rev.*, D89(9):092007, 2014.

[61] Procedure for the LHC Higgs boson search combination in Summer 2011. Technical Report CMS-NOTE-2011-005. ATL-PHYS-PUB-2011-11, CERN, Geneva, Aug 2011.

[62] J. S. Conway. Incorporating nuisance parameters in likelihoods for multisource spectra. In *Proceedings, PHYSTAT 2011 Workshop on Statistical Issues Related to Discovery Claims in Search Experiments and Unfolding, CERN,Geneva, Switzerland 17-20 January 2011*, 2011.

[63] A. L. Read. Linear interpolation of histograms. *Nucl. Instrum. Meth.*, A425:357–360, 1999.

[64] R. Barlow and C. Beeston. Fitting using finite Monte Carlo samples. *Comput. Phys. Commun.*, 77:219–228, 1993.

[65] A. L. Read. Presentation of search results: The CL(s) technique. *J. Phys.*, G28:2693–2704, 2002.

[66] A. L. Read. Modified frequentist analysis of search results (the CL_s method). CERN-OPEN-2000-205, 2000.

[67] T. Junk. Confidence level computation for combining searches with small statistics. *Nucl. Instrum. Meth.*, A434:435–443, 1999.

[68] G. Cowan et al. Asymptotic formulae for likelihood-based tests of new physics. *Eur. Phys. J.*, C71:1554, 2011.

[69] E. Gross and O. Vitells. Trial factors or the look elsewhere effect in high energy physics. *Eur. Phys. J.*, C70:525–530, 2010.

[70] R. Cousins. Generalization of chisquare goodness-of-fit test for binned data using saturated models, with application to histograms. http://www.physics.ucla.edu/cousins/stats/cousinssaturated.pdf, 2010.

[71] A. Hocker et al. TMVA - Toolkit for multivariate data analysis. *PoS*, ACAT:040, 2007.

[72] B. Roe et al. Boosted decision trees, an alternative to artificial neural networks. *Nucl. Instrum. Meth.*, A543(2-3):577–584, 2005.

[73] LEP Working Group for Higgs boson searches ALEPH L3 OPAL, DELPHI. Search for the standard model Higgs boson at LEP.

[74] CDF and D0 Collaborations. Higgs boson studies at the Tevatron. *Phys. Rev.*, D88(5):052014, 2013.

[75] L. Evans and P. Bryant. LHC machine. *JINST*, 3:S08001, 2008.

[76] CERN. CERN website. `http://home.cern/fr`, 2015.

[77] CMS Collaboration. The CMS experiment at the CERN LHC. *JINST*, 3:S08004, 2008.

[78] ATLAS Collaboration. The ATLAS experiment at the CERN Large Hadron Collider. *JINST*, 3:S08003, 2008.

[79] LHCb Collaboration. The LHCb detector at the LHC. *JINST*, 3:S08005, 2008.

[80] ALICE Collaboration. The ALICE experiment at the CERN LHC. *JINST*, 3:S08002, 2008.

[81] CMS Collaboration. CMS luminosity - Public results. `https://twiki.cern.ch/twiki/bin/view/CMSPublic/LumiPublicResults`, 2015.

[82] J. Butler et al. CMS Phase II upgrade scope document. CERN-LHCC-2015-019. LHCC-G-165, 2015.

[83] CMS Collboration. *CMS Physics: Technical Design Report Volume 1: Detector Performance and Software*. Technical Design Report CMS. CERN, Geneva, 2006. http://cds.cern.ch/record/922757.

[84] P. Adzic et al. Energy resolution of the barrel of the CMS electromagnetic calorimeter. *JINST*, 2:P04004, 2007.

[85] A. Buckley et al. General-purpose event generators for LHC physics. *Phys. Rept.*, 504:145–233, 2011.

[86] S. Jadach et al. The tau decay library TAUOLA: Version 2.4. *Comput. Phys. Commun.*, 76:361–380, 1993.

[87] F. Maltoni and T. Stelzer. MadEvent: Automatic event generation with MadGraph. *JHEP*, 02:027, 2003.

[88] T. Sjostrand, S. Mrenna, and P. Skands. PYTHIA 6.4 physics and manual. *JHEP*, 05:026, 2006.

[89] S. Frixione, P. Nason, and C. Oleari. Matching NLO QCD computations with parton shower simulations: the POWHEG method. *JHEP*, 11:070, 2007.

[90] J. Alwall et al. The automated computation of tree-level and next-to-leading order differential cross sections, and their matching to parton shower simulations. *JHEP*, 07:079, 2014.

[91] S. Agostinelli et al. GEANT4: A simulation toolkit. *Nucl. Instrum. Meth.*, A506:250–303, 2003.

[92] CMS Collaboration. Particle–flow event reconstruction in CMS and performance for jets, taus, and $\not\!\!E_T$. CMS Physics Analysis Summary CMS-PAS-PFT-09-001, 2009.

[93] CMS Collaboration. Commissioning of the particle-flow reconstruction in minimum-bias and jet events from pp collisions at 7 TeV. CMS Physics Analysis Summary CMS-PAS-PFT-10-002, 2010.

[94] CMS Collaboration. Description and performance of track and primary-vertex reconstruction with the CMS tracker. *JINST*, 9(10):P10009, 2014.

[95] CMS Collaboration. Tracking and primary vertex results in first 7 TeV collisions. CMS Physics Analysis Summary CMS-PAS-TRK-10-005, 2010.

[96] M. Cacciari, G. Salam, and G. Soyez. The anti-k(t) jet clustering algorithm. *JHEP*, 04:063, 2008.

[97] CMS Collaboration. Determination of jet energy calibration and transverse momentum resolution in CMS. *JINST*, 6:P11002, 2011.

[98] CMS Collaboration. Identification of b-quark jets with the CMS experiment. *JINST*, 8:P04013, 2013.

[99] CMS Collaboration. Performance of b tagging at $\sqrt{s} = 8$ TeV in multijet, ttbar and boosted topology events. CMS Physics Analysis Summary CMS-PAS-BTV-13-001, 2013.

[100] CMS Collaboration. Performance of electron reconstruction and selection with the CMS detector in proton-proton collisions at $\sqrt{s} = 8$ TeV. *JINST*, 10(06):P06005, 2015.

[101] CMS Collaboration. Performance of CMS muon reconstruction in pp collision events at $\sqrt{s} = 7$ TeV. *JINST*, 7:P10002, 2012.

[102] CMS Collaboration. Performance of tau-lepton reconstruction and identification in CMS. *JINST*, 7:P01001, 2012.

[103] CMS Collaboration. Reconstruction and identification of τ lepton decays to hadrons and ν_τ at CMS. *JINST*, 11(01):P01019, 2016.

[104] CMS Collaboration. Performance of the CMS missing transverse momentum reconstruction in pp data at $\sqrt{s} = 8$ TeV. *JINST*, 10(02):P02006, 2015.

[105] CMS Collaboration. Tau ID performance plots. CMS Detector Performance Summary CMS-DP-14-015, 2014.

[106] CMS Collaboration. Measurement of the inclusive W and Z production cross sections in pp collisions at $\sqrt{s} = 7$ TeV. *JHEP*, 10:132, 2011.

[107] CDF Collaboration. Search for neutral MSSM Higgs bosons decaying to tau pairs in $p\bar{p}$ collisions at $\sqrt{s} = 1.96$ TeV. *Phys. Rev. Lett.*, 96:011802, 2006.

[108] CMS Collaboration. Measurement of the $t\bar{t}$ production cross section in the dilepton channel in pp collisions at $\sqrt{s} = 8$ TeV. *JHEP*, 02:024, 2014.

[109] CMS Collaboration. CMS luminosity based on pixel cluster counting - Summer 2013 update. CMS Physics Analysis Summary CMS-PAS-LUM-13-001, 2013.

[110] CMS Collaboration. Tau reconstruction and identification performance in LHC Run-2. CMS Physics Analysis Summary CMS-PAS-TAU-16-002, 2016. To be made public.

[111] L. Bianchini et al. Reconstruction of the Higgs mass in $H \to \tau\tau$ events by dynamical likelihood techniques. *J. Phys. Conf. Ser.*, 513:022035, 2014.

[112] LHC Higgs Cross Section Working Group. Handbook of LHC Higgs cross sections: 3. Higgs properties. 2013. arXiv:1307.1347.

[113] CMS Collaboration. Measurement of associated production of vector bosons and top quark-antiquark pairs at $\sqrt{s} = 7$ TeV. *Phys. Rev. Lett.*, 110:172002, 2013.

[114] CMS Collaboration. Measurement of top quark-antiquark pair production in association with a W or Z boson in pp collisions at $\sqrt{s} = 8$ TeV. *Eur. Phys. J.*, C74(9):3060, 2014.

[115] CMS Collaboration. Absolute calibration of the luminosity measurement at CMS: Winter 2012 update. CMS Physics Analysis Summary CMS-PAS-SMP-12-008, 2012.

[116] CMS Collaboration. CMS-HIG-13-034 public twiki. `https://twiki.cern.ch/twiki/bin/view/CMSPublic/Hig13004PubTWiki`.

[117] ATLAS Collaboration. Search for the standard model Higgs boson produced in association with a vector boson and decaying into a tau pair in pp collisions at $\sqrt{s} = 8$ TeV with the ATLAS detector. 2015. arXiv:1511.08352, Submitted to PRD.

[118] J. Campbell, R. Ellis, and C. Williams. Vector boson pair production at the LHC. *JHEP*, 07:018, 2011.

[119] CMS Collaboration. Search for the standard model Higgs boson produced in association with a W or a Z boson and decaying to bottom quarks. *Phys. Rev.*, D89(1):012003, 2014.

[120] CMS Collaboration. Evidence for the direct decay of the 125 GeV Higgs boson to fermions. *Nature Phys.*, 10, 2014.

[121] ATLAS Collaboration. Evidence for the Higgs-boson Yukawa coupling to tau leptons with the ATLAS detector. *JHEP*, 04:117, 2015.

[122] CMS Collaboration. Search for a pseudoscalar boson decaying into a Z boson and the 125 GeV Higgs boson in $\ell^+\ell^- b\bar{b}$ final states. *Phys. Lett.*, B748:221–243, 2015.

[123] CMS Collaboration. Searches for a heavy scalar boson H decaying to a pair of 125 GeV Higgs bosons hh or for a heavy pseudoscalar boson A decaying to Zh, in the final states with $h \to \tau\tau$. *Phys. Lett.*, B755:217–244, 2016.

[124] T. Binoth et al. NLO QCD corrections to tri-boson production. *JHEP*, 06:082, 2008.

[125] CMS Collaboration. CMS-PAS-HIG-14-034 public twiki. `http://cms-results.web.cern.ch/cms-results/public-results/publications/HIG-14-034/index.html`.

[126] R. Harlander et al. Interim recommendations for the evaluation of Higgs production cross sections and branching ratios at the LHC in the two-Higgs-doublet model. 2013. arXiv:1312.5571.

[127] E. Bagnaschi et al. Benchmark scenarios for low $\tan\beta$ in the MSSM. 2015. LHCHXSWG-2015-002.

[128] ATLAS Collaboration. Searches for Higgs boson pair production in the $hh \to bb\tau\tau, \gamma\gamma WW^*, \gamma\gamma bb, bbbb$ channels with the ATLAS detector. *Phys. Rev.*, D92:092004, 2015.

[129] CMS Collaboration. Search for the exotic decay of the Higgs boson to two light pseudoscalar bosons with two taus and two muons in the final state at $\sqrt{s} = 8$ TeV. CMS Physics Analysis Summary CMS-PAS-HIG-15-011, 2016.

[130] CMS Collaboration. CMS-PAS-HIG-15-011 public twiki. `http://cms-results.web.cern.ch/cms-results/public-results/preliminary-results/HIG-15-011/index.html`.

[131] E. W. Weisstein. F-distribution. From MathWorld – A Wolfram Web Resource.

[132] CMS Collaboration. Observation of the diphoton decay of the Higgs boson and measurement of its properties. *Eur. Phys. J.*, C74(10):3076, 2014.

[133] ATLAS Collaboration. Search for Higgs bosons decaying to aa in the $\mu\mu\tau\tau$ final state in pp collisions at $\sqrt{s} = 8$ TeV with the ATLAS experiment. *Phys. Rev.*, D92(5):052002, 2015.

[134] CMS Collaboration. Search for exotic decays of the Higgs boson to a pair of new light bosons with two muon and two b jets in the final state. CMS Physics Analysis Summary CMS-PAS-HIG-14-041, 2016.

[135] CMS Collaboration. Search for a very light NMSSM Higgs boson produced in decays of the 125 GeV scalar boson and decaying into τ leptons in pp collisions at $\sqrt{s} = 8$ TeV. *JHEP*, 01:079, 2016.

[136] CMS Collaboration. Search for Higgs decays to new light bosons in boosted tau final states. CMS Physics Analysis Summary CMS-PAS-HIG-14-022, 2015.

[137] CMS Collaboration. Search for a non-standard-model Higgs boson decaying to a pair of new light bosons in four-muon final states. *Phys. Lett.*, B726:564–586, 2013.

[138] ATLAS Collaboration. Search for new light gauge bosons in Higgs boson decays to four-lepton final states in pp collisions at $\sqrt{s} = 8$ TeV with the ATLAS detector at the LHC. *Phys. Rev.*, D92(9):092001, 2015.

[139] N. Gray et al. Three loop relation of quark (modified) Ms and pole masses. *Z. Phys.*, C48:673–680, 1990.

[140] K. G. Chetyrkin and M. Steinhauser. Short distance mass of a heavy quark at order α_s^3. *Phys. Rev. Lett.*, 83:4001–4004, 1999.

[141] K. Melnikov and T. Ritbergen. The three loop relation between the MS-bar and the pole quark masses. *Phys. Lett.*, B482:99–108, 2000.

[142] CMS Collaboration. Search for a low-mass pseudoscalar Higgs boson produced in association with a $b\bar{b}$ pair in pp collisions at $\sqrt{s} = 8$ TeV. 2015. Submitted to Phys. Lett. B, arXiv:1511.03610.

[143] ATLAS Collaboration. Modelling $Z \to \tau\tau$ processes in ATLAS with τ-embedded $Z \to \mu\mu$ data. *JINST*, 10(09):P09018, 2015.

[144] Z. Czyczula, T. Przedzinski, and Z. Was. TauSpinner program for studies on spin effect in tau production at the LHC. *Eur. Phys. J.*, C72:1988, 2012.

[145] CMS Collaboration. CMS-HIG-14-033 public twiki. `http://cms-results.web.cern.ch/cms-results/public-results/publications/HIG-14-033/index.html`.

[146] K. Melnikov and F. Petriello. Electroweak gauge boson production at hadron colliders through O(alpha(s)**2). *Phys. Rev.*, D74:114017, 2006.

[147] PDF4LHC Working Group. The PDF4LHC Working Group interim report. 2011. arXiv:1101.0536.

[148] A. Martin et al. Parton distributions for the LHC. *Eur. Phys. J.*, C63:189–285, 2009.

[149] R. Ball et al. Parton distributions with LHC data. *Nucl. Phys.*, B867:244–289, 2013.

[150] CMS Collaboration. Search for neutral MSSM Higgs bosons decaying to a pair of tau leptons in pp collisions. *JHEP*, 10:160, 2014.

[151] U. Langenegger et al. SM and MSSM Higgs boson production: spectra at large transverse momentum. *JHEP*, 06:035, 2006.

[152] M. Carena et al. Suggestions for benchmark scenarios for MSSM Higgs boson searches at hadron colliders. *Eur. Phys. J.*, C26:601–607, 2003.

[153] M. Carena et al. MSSM Higgs boson searches at the LHC: benchmark scenarios after the discovery of a Higgs-like particle. *Eur. Phys. J.*, C73(9):2552, 2013.

[154] ATLAS Collaboration. Search for neutral Higgs bosons of the minimal supersymmetric standard model in pp collisions at $\sqrt{s} = 8$ TeV with the ATLAS detector. *JHEP*, 11:056, 2014.

[155] ATLAS Collaboration. Search for neutral minimal supersymmetric standard model Higgs bosons $H/A \to \tau\tau$ produced in pp collisions at $\sqrt{s} = 13$ TeV with the ATLAS detector. ATLAS Conference Note ATLAS-CONF-2015-061, 2015.

[156] CMS Collaboration. Search for the standard model Higgs boson produced through vector boson fusion and decaying to $b\bar{b}$. *Phys. Rev.*, D92(3):032008, 2015.

[157] CMS Collaboration. Search for a standard model-like Higgs boson in the $\mu^+\mu^-$ and e^+e^- decay channels at the LHC. *Phys. Lett.*, B744:184–207, 2015.

[158] CMS and ATLAS Collaborations. Combined measurement of the Higgs boson mass in pp collisions at $\sqrt{s} = 7$ and 8 TeV with the ATLAS and CMS experiments. *Phys. Rev. Lett.*, 114:191803, 2015.

[159] CMS Collaboration. Search for the associated production of the Higgs boson with a top-quark pair. *JHEP*, 09:087, 2014.

[160] CMS Collaboration. Measurement of the top quark mass using proton-proton data at $\sqrt{s} = 7$ and 8 TeV. CMS Physics Analysis Summary CMS-PAS-TOP-14-022, 2015.

[161] G. Degrassi et al. Higgs mass and vacuum stability in the Standard Model at NNLO. *JHEP*, 08:098, 2012.

[162] J. R. Espinosa et al. The cosmological Higgstory of the vacuum instability. *JHEP*, 09:174, 2015.

[163] CMS Collaboration. Constraints on the Higgs boson width from off-shell production and decay to Z-boson pairs. *Phys. Lett.*, B736:64–85, 2014.

[164] Projected performance of an upgraded CMS detector at the LHC and HL-LHC: Contribution to the Snowmass process. In *Community Summer Study 2013: Snowmass on the Mississippi (CSS2013) Minneapolis, MN, USA, July 29-August 6, 2013*, 2013.

[165] CMS Collaboration. Search for lepton-flavour-violating decays of the Higgs boson. *Phys. Lett.*, B749:337–362, 2015.

[166] ATLAS Collaboration. Search for lepton-flavour-violating $H \to \mu\tau$ decays of the Higgs boson with the ATLAS detector. *JHEP*, 11:211, 2015.

[167] CMS Collaboration. A combination of searches for the invisible decays of the Higgs boson using the CMS detector. CMS Physics Analysis Summary CMS-PAS-HIG-15-012, 2015.

[168] CMS Collaboration. Summary results of high mass BSM Higgs searches using CMS run-I data. CMS Physics Analysis Summary CMS-PAS-HIG-16-007, 2016.

[169] G. Degrassi and others. Towards high precision predictions for the MSSM Higgs sector. *Eur. Phys. J.*, C28:133–143, 2003.

[170] CMS Collaboration. Standard model physics - CMS results. `https://twiki.cern.ch/twiki/bin/view/CMSPublic/PhysicsResultsSMP`, 2016.

[171] CMS Collaboration. CMS top physics results. `https://twiki.cern.ch/twiki/bin/view/CMSPublic/PhysicsResultsTOP`, 2016.

[172] ATLAS, CDF, CMS and D0 Collaborations. First combination of Tevatron and LHC measurements of the top-quark mass. 2014. arXiv:1403.4427.

[173] CMS Collaboration. Summary of CMS cross section measurements. `https://twiki.cern.ch/twiki/bin/view/CMSPublic/PhysicsResultsCombined`, 2016.

[174] CMS Collaboration. Search for dark matter, extra dimensions, and unparticles in monojet events in proton-proton collisions at $\sqrt{s} = 8$ TeV. *Eur. Phys. J.*, C75(5):235, 2015.

[175] CMS Collaboration. Search for dark matter with jets and missing transverse energy at 13 TeV. CMS Physics Analysis Summary CMS-PAS-EXO-15-003, 2015.

[176] CMS Collaboration. CMS supersymmetry physics results. `https://twiki.cern.ch/twiki/bin/view/CMSPublic/PhysicsResultsSUS`, 2016.

[177] CMS Collaboration. Summary of comparison plots in simplified models spectra for the 8 TeV dataset. `https://twiki.cern.ch/twiki/bin/view/CMSPublic/SUSYSMSSummaryPlots8TeV`, 2015.

[178] CMS Collaboration. CMS exotica public physics results. `https://twiki.cern.ch/twiki/bin/view/CMSPublic/PhysicsResultsEXO`, 2016.

[179] CMS Collaboration. Search for new physics in high mass diphoton events in proton-proton collisions at $\sqrt{s} = 13$ TeV. CMS Physics Analysis Summary CMS-PAS-EXO-15-004, 2015.

[180] ATLAS Collaboration. Search for resonances decaying to photon pairs in 3.2 fb^{-1} of pp collisions at $\sqrt{s} = 13$ TeV with the ATLAS detector. ATLAS Conference Note ATLAS-CONF-2015-081, 2015.

[181] M. Bicer et al. First Look at the Physics Case of TLEP. *JHEP*, 01:164, 2014.

[182] N. Arkani-Hamed et al. Physics opportunities of a 100 TeV proton-proton collider. Technical Report arXiv:1511.06495. PITT-PACC 1515. CERN-PH-TH-2015-259, Nov 2015.

[183] J. L. Abelleira Fernandez et al. A large hadron electron collider at CERN: Report on the physics and design concepts for machine and detector. *J. Phys.*, G39:075001, 2012.

[184] K. Fujii et al. Physics case for the International Linear Collider. 2015. arXiv:1506.05992.